Dissertation zur Erlangung des Doktorgrades

der Fakultät für Chemie und Pharmazie

der Ludwig-Maximilians-Universität München

Towards a cell-biological understanding of the formation and dissociation of neurotoxic protein aggregates

Victoria Anne Trinkaus

aus

Dortmund, Deutschland

2022

Erklärung

Diese Dissertation wurde im Sinne von § 7 der Promotionsordnung vom 28. November 2011 von Herrn Prof. Dr. F.-Ulrich Hartl betreut.

Eidesstattliche Versicherung

Diese Dissertation wurde eigenständig und ohne unerlaubte Hilfe erarbeitet.

München, den 02.12.2022

Victoria Anne Trinkaus

Dissertation eingereicht am 12.12.2022

1. Gutacher: Prof. Dr. F.-Ulrich Hartl

2. Gutachter: Prof. Dr. R. Fernández-Busnadiego

Mündliche Prüfung am 20.01.2023

“Nothing in life is to be feared, it is only to be understood.

Now is the time to understand more, so that we fear less.”

- Marie Curie

Acknowledgments

First of all, I would like to thank my mentor and PhD supervisor Ulrich Hartl for guiding me through the different projects we have worked on. I would like to express my deep gratitude for his constant support in scientific, career-related and personal concerns.

Additionally, I would like to thank Ruben Fernández-Busnadiego for supporting me in cryo-EM related questions as well as personal concerns and for supervising my cryo-ET projects since my Master's thesis time.

I also want to thank Wolfgang Baumeister for providing an amazing scientific environment and Jürgen Plitzko for helping me with microscope problems on weekends or late in the night.

I would also like to thank Mark Hipp, Andreas Bracher, Irina Dudanova, Dieter Edbauer and Konstanze Winklhofer for many fruitful discussions and constant scientific support. I want to express my gratitude towards the anonymous tissue donor and his family and to Thomas Arzberger, who selected the case and provided us with tissue material.

None of the projects would have gone so smoothly without the help of the technical support of the labs and the core facility. This includes the tech staff of the biochemistry lab, Nadine Wischnewski, Silvia Gärtner and Romy Lange, of the EM lab and workshop, Günter Pfeiffer, Stefan Bohn, Inga Wolf and Florian Beck and of the core facility, Markus Oster. Here, I would also like to thank Darija Pompino and Emmanuel Burghardt for their organizational work in the department.

I would also like to thank my collaborators from the neurobiology lab, Irene Riera-Tur and Dennis Feigenbutz. I additionally want to express my gratitude towards the students that I had the pleasure to supervise, Carolin Klose, Kenneth Ehses and Annika Elimelech.

The many collaborations with fellow PhD students and postdocs made my time at the MPI-B especially exciting – here I would like to thank Antonio Martinez-Sanchez, Qiang Guo, Felix Bäuerlein, Patricia Yuste-Checa, Itika Saha, Hauke Holthusen, Maximilian Garhammer and Gopal Jayaraj.

I am beyond measure thankful for the collaboration with Cole Sitron, who was the driving force that moved our shared project forward at an incredible speed.

Many more people made my time in Martinsried unforgettable. Here, I would like to thank Maria Salfer, Javier Collado, Christos Papantoniou, Matthias Pöge, Markus und Nicole Eisele, Laura Burbaum and Fabian Cerda, Sven Klumpe, Jonathan Schneider, Hugo van den Hoek, Marcel Dickmanns, Manon Demulder, Sagar Khavnekar, William Wan, Anna Bieber, Cristina Capitanio, Jonathan Wagner, Johann Brenner, Oda Schioetz and Christoph Kaiser. I would additionally like to thank Marco Dombrowski, Johanna Brüggenthies, Andrea Seiwert, Ina Wendland, Huping Wang, Rongqin Li and Peng Xu.

Finally, I would like to thank my family, Marion Trinkaus and Ilse and Walter Stoll for their unconditional love; and my partner, Sebastian Michalski, for carrying me through the deepest valleys of this journey, for lifting me up again and for believing in me when I was not able to do so.

Table of contents

Publications

List of publications covered in this thesis:

Yuste-Checa P, **Trinkaus VA**, Riera-Tur I, Imamoglu R, Schaller TF, Wang H, Dudanova I, Hipp MS, Bracher A, Hartl FU. The extracellular chaperone Clusterin enhances Tau aggregate seeding in a cellular model. Nat Commun. 2021 Aug 11;12(1):4863. doi: 10.1038/s41467-021-25060-1. PMID: 34381050; PMCID: PMC8357826.

Trinkaus VA, Riera-Tur I, Martínez-Sánchez A, Bäuerlein FJB, Guo Q, Arzberger T, Baumeister W, Dudanova I, Hipp MS, Hartl FU, Fernández-Busnadiego R. In situ architecture of neuronal α-Synuclein inclusions. Nat Commun. 2021 Apr 14;12(1):2110. doi: 10.1038/s41467-021-22108-0. PMID: 33854052; PMCID: PMC8046968.

Schneider MM, Gautam S, Herling TW, Andrzejewska E, Krainer G, Miller AM, **Trinkaus VA**, Peter QAE, Ruggeri FS, Vendruscolo M, Bracher A, Dobson CM, Hartl FU, Knowles TPJ. The Hsc70 disaggregation machinery removes monomer units directly from α-synuclein fibril ends. Nat Commun. 2021 Oct 14;12(1):5999. doi: 10.1038/s41467-021-25966-w. PMID: 34650037; PMCID: PMC8516981.

Itika Saha, Patricia Yuste-Checa, Miguel Da Silva Padilha, Qiang Guo, Roman Körner, Hauke Holthusen, **Victoria A. Trinkaus**, Irina Dudanova, Rubén Fernández-Busnadiego, Wolfgang Baumeister, David W. Sanders, Saurabh Gautam, Marc I. Diamond, F. Ulrich Hartl, Mark S. Hipp. The AAA+ chaperone VCP disaggregates Tau fibrils and generates aggregate seeds. bioRxiv 2022.02.18.481043; doi: https://doi.org/10.1101/2022.02.18.481043

Summary

Most neurodegenerative diseases, including Alzheimer's disease (AD) and Parkinson's disease (PD), have protein aggregates in neurons, glial cells or the extracellular space as common histopathological hallmark. In AD, the proteins tau and amyloid-β (Aβ) form intracellular and extracellular aggregates, respectively. In PD, the protein α-synuclein (α-syn) aggregates and forms intracellular neuronal inclusions, called Lewy bodies (LBs).

Cellular processes regarding aggregate formation, cellular toxicity induced by protein aggregates as well as cellular disaggregation mechanisms remain poorly understood. Our work aims to shed light on the 'aggregate cycle' of neurotoxic aggregates formed by the proteins tau and α-syn: In four studies, we investigated the mechanisms of aggregate seeding, analyzed cellular interactions of neuronal aggregates at the ultrastructural level and followed the dissociation of amyloid aggregates *in vitro* and *in cellulo*.

In our first study, we focused on the effect of the extracellular chaperone Clusterin (Clu) on seeded aggregation of tau and α-syn. We found that Clu strongly enhances tau seeded aggregation, while it is mitigating the seeding of α-syn. We showed that Clu stabilizes tau oligomers and that tau/Clu seeds enter cells via endocytosis. The seeds subsequently compromise the endolysosomal compartment, resulting in endolysosomal escape and transfer to the cytoplasm (Yuste-Checa *et al.*, 2021).

Our second study focused on the ultrastructural analysis of neuronal α-syn inclusions *in situ*. By using cryo-electron tomography (cryo-ET), we investigated neuronal α-syn aggregates, seeded with *in vitro* formed fibrils or patient-derived aggregate material. We observed that these aggregates consist of both, amyloid α-syn fibrils and membranous organelles. We performed detailed analyses of fibril and membrane interactions and showed that α-syn fibrils do not interact with membranes directly, and that membranes do not cluster within α-syn aggregates. By using gold-labeled aggregate seeds, we observed seeding events *in situ* and characterized seed size as well as the growth direction of the newly formed α-syn fibrils (Trinkaus *et al.*, 2021).

The third study focused on the disaggregation of α-syn fibrils by chaperones of the Hsp70 (Heat shock protein 70) family. By combining *in vitro* microfluidics and chemical

kinetic measurements, we showed that Hsc70 (Hsp70 cognate) together with co-chaperones DnajB1 and Apg2 is able to disaggregate α-syn fibrils completely. The Hsp70 chaperone system removes α-syn monomer units from the fibril ends and fibril fragmentation contributes only little to the overall disaggregation reaction (Schneider *et al.*, 2021).

The fourth study focused on the disaggregation of cellular tau aggregates by the AAA+ ATPase VCP (Vasolin Containing Protein). In a mass spectrometric analysis of cellular tau aggregates, VCP and its cofactors were found to be present on the aggregates. Interestingly, the inhibition of VCP resulted in an increased size of the aggregates, indicating an involvement of VCP in tau aggregate dissociation. Our subsequent biochemical and cell-biological work showed that indeed VCP is disaggregating tau fibrils, thereby producing monomers that are degraded by the proteasome, as well as larger fibril fragments that can serve as new seeds during aggregate propagation (Saha *et al.*, 2022).

Altogether, our studies provide new clues about the series of events in the ‘life cycle’ of a neurotoxic aggregate: We follow aggregate formation, analyze aggregate architecture and cellular interactions of aggregates and elucidate cell-biological mechanisms required for aggregate dissociation.

Prologue: The central dogma of molecular biology

Cells are the elementary units of life. They are enclosed compartments with a lipid membrane forming a barrier between the intracellular area, the cytoplasm, and the extracellular environment. Although mainly separated, an active exchange between these two areas takes place. The cell is able to export material from the intracellular space and internalize material from the extracellular environment.

The main molecular building blocks, which are needed to form a functional cell, are lipids, nucleic acids and proteins: Lipids form membranes and help to compartmentalize the cell's interior by forming organelles. Every organelle has a specific purpose and houses a different repertoire of chemical reactions. Oxidative phosphorylation in mitochondria generates cellular energy in form of adenosine-tri-phosphate (ATP). In lysosomes, misfolded proteins can be degraded by proteases using acidic lysis. The endoplasmic reticulum (ER) in combination with the Golgi apparatus transports proteins through the cell, modifies and releases them into the extracellular space subsequently.

Nucleic acids are the basic carriers of genetic information and can be divided into two classes: Deoxyribonucleic acids (DNA) and ribonucleic acids (RNA). DNA molecules are composed of two polynucleotide chains forming a double helix. In prokaryotic cells, the DNA is solely localized in the cytoplasm. In eukaryotic cells, however, the genomic DNA is held in its own compartment, the nucleus. All genetic information of a cell is stored in form of genes on its DNA. Genes can be transcribed into messenger RNA (mRNA), which is composed of a single polynucleotide chain. mRNA carries all the information needed for translating genes into proteins.

To express proteins, the mRNA is read and translated into a polypeptide chain. For that purpose, amino acids get linked covalently to each other in a specific sequence instructed by the mRNA. The translation of the mRNA is mediated by a ribonucleoprotein complex, the ribosome. Subsequently, the polypeptide chain must adopt a defined three-dimensional structure to become a fully functional protein in a process termed 'protein folding'. The sequential, irreversible flow of information 'DNA makes RNA makes proteins' is referred to as the 'central dogma of molecular biology' (Crick, 1958).

1 Introduction

1.1 Protein folding

Almost all functions of a living cell are executed by proteins, the most complex macromolecules. Proteins facilitate enzymatic reactions, transduce intra- or intercellular signals, serve structural roles and are involved in immune responses against pathogens (Alberts *et al.*, 2002). In order to fulfil this vast array of functions, proteins have to fold into their specific three-dimensional conformation (Dobson, Šali and Karplus, 1998; Kim *et al.*, 2013; Balchin, Hayer-Hartl and Hartl, 2016)

How protein folding is achieved with high efficiency, is one of the most fundamental problems in biology. The complexity of this process is summarized in a thought experiment, known as the Levinthal paradox (Levinthal, 1968). It states that even if each peptide bond in a protein were to occur in only 2 different conformations, a polypeptide chain of 150 amino acids could adopt 2^{149} possible conformations. Assuming that every conformational change takes ~10^{-13} seconds, it would take the polypeptide chain around 10^{24} years to go through all these conformations in order to find the correct one – longer than the existence of the universe (Levinthal, 1968; Zwanzig, Szabo and Bagchi, 1992; Dobson, Šali and Karplus, 1998).

However, polypeptide chains fold within seconds to minutes, indicating that mechanisms, such as defined folding pathways, limit the amount of potential structural conformations during the folding process (Kim *et al.*, 2013). Folding reactions are driven by a combination of relatively weak interactive forces of polar, ionic or hydrophobic nature. Specifically, the hydrophobic effect is a major driver of the folding of globular proteins (Kauzmann, 1959; Dill, 1990; Bolen and Rose, 2008):

Protein folding is a chemical reaction, in which the concentrations of the reactant (the unfolded polypeptide chain [U]) and the product (the folded protein [F]) exist in equilibrium:

$$K_{eq} = \frac{[F]}{[U]}$$

The equilibrium constant is used to calculate the change in Gibb's free energy, ΔG, of the folding reaction, with R being the ideal gas constant and T the temperature:

$$\Delta G = -RTlnK_{eq}$$

A negative ΔG value implies that the reaction is energetically favorable, and that the protein will adopt its folded state. The change in Gibb's free energy can also be expressed as a measure of enthalpy and entropy, with ΔH as the change in enthalpy and ΔS as the change in entropy:

$$\Delta G = \Delta H - T\Delta S$$

ΔS describes the change of entropy before (initial) and after the reaction (final) with a large positive ΔS implying an overall increase of entropy:

$$\Delta S = S(final) - S(initial)$$

If the change in entropy is large and dominant over the change in enthalpy, the reaction is energetically favored.

The hydrophobic effect, as the main driving force of folding, is based on the gain of entropy through the rearrangement of water molecules during the protein's folding process: Water molecules assemble into ordered cages around non-polar molecules, e.g. unfolded polypeptide chains. During protein folding, the hydrophobic polypeptide stretches become buried in the protein core, which reduces the protein's surface area. Burying these hydrophobic stretches decreases the amount of water molecules that must assemble around the protein's surface. This results in a gain of entropy and the folding of the protein is favored (Kauzmann, 1959; Dill, 1990).

A protein that has folded into its three-dimensional conformation contains different structural elements depending on its amino acid sequence. The most common structures are α-helices and β-sheet motifs (Ramachandran, Ramakrishnan and Sasisekharan, 1963): The α-helical element is a helix that is stabilized by hydrogen-bonds (H-bonds) between amino acids within the motif (Pauling, Corey and Branson, 1951). The β-sheet is formed between two polypeptide chains that align either parallel or antiparallel to each other and are also interacting through H-bonds (Pauling and Corey, 1951) (Figure 1).

More than 30 % of all proteins in the eukaryotic proteome contain large unstructured regions (Dunker *et al.*, 2001). These regions do not adopt any specific conformation and are defined as disordered. Proteins containing such disordered stretches are termed ‘intrinsically disordered proteins’ (IDPs) (Dunker *et al.*, 2001). Proteins involved in neurodegenerative protein misfolding diseases, such as α-synuclein (α-syn) and tau (microtubule-associated protein tau), belong to the group of IDPs and the disordered regions facilitate their aggregation into amyloid-like fibrils (Uversky, 2015).

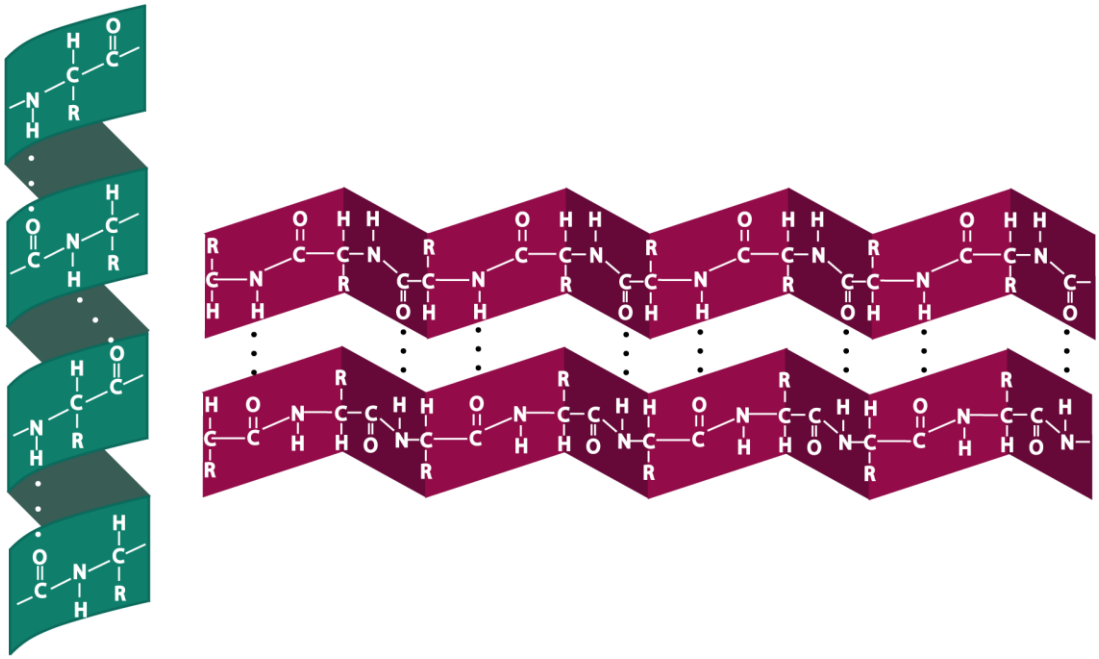

Figure 1 The two most common secondary structures. Schematic of a right-handed α-helix (left) and a β-sheet (right). α-Helices as well as β-sheets are stabilized via H-bonds between the negatively charged oxygen and the positively charged hydrogen atoms of two peptide bonds.

1.2 Molecular chaperones

Since protein folding is a highly complex process, which is often error-prone, the cell has developed several strategies to avoid protein misfolding and aggregation, and to ensure the rapid degradation of dysfunctional and potentially toxic proteins (Hipp, Kasturi and Hartl, 2019): During protein biogenesis, the nascent polypeptide chain emerges from the ribosome and adopts an unstable intermediate folding state (Brockwell and Radford, 2007). To stabilize this state and avoid aggregation, specific

proteins known as ‘molecular chaperones’ assist the folding of the newly synthesized protein (Kim *et al.*, 2013).

Different classes of molecular chaperones and components of pathways involved in protein degradation form the protein quality control (PQC) network, which functions to maintain protein homeostasis (proteostasis) (Balch *et al.*, 2008; Hipp, Kasturi and Hartl, 2019). Molecular chaperones are proteins that bind to other proteins in their non-native conformations, assisting correct folding and/or assembly by reducing non-native intra- and intermolecular interactions (Balchin, Hayer-Hartl and Hartl, 2016). Chaperones represent a remarkably versatile group of intracellular as well as extracellular proteins exhibiting highly conserved mechanisms (Hartl, 1996). Especially two chaperone systems were found to be important in maintaining neuronal proteostasis and preventing the formation of neurotoxic protein aggregates: The Hsp70 chaperone system and the small heat shock proteins (sHsps) (Vos *et al.*, 2008; Bakthisaran, Tangirala and Rao, 2015).

1.2.1 The Hsp70 machinery

Many chaperones belong to the family of heat shock proteins (Hsp), a group of proteins that are transcriptionally upregulated following heat stress. Hsp70 (DnaK in *E. coli*) is a central player of the proteostasis network. Humans have 13 homologs of Hsp70, although not all of them are constitutively expressed (Daugaard, Rohde and Jäättelä, 2007; Rosenzweig *et al.*, 2019). Hsp70 proteins are present in the cyotosol, but can also translocate across membranes into organelles, such as the nucleus, mitochondria and the ER (Rosenzweig *et al.*, 2019). Among stabilizing and preventing the misfolding of newly synthesized proteins, the Hsp70 chaperone machinery was also found to dissociate protein aggregates and target misfolded proteins for degradation. Specialized Hsp70 proteins translocate proteins across the ER and mitochondrial membrane (Ryan and Pfanner, 2001; Young, Barral and Hartl, 2003; Mayer and Bukau, 2005).

Proteins belonging to the Hsp70 family consist of an N-terminal nucleotide binding domain (NBD) and a C-terminal substrate binding domain (SBD) (Bukau and Horwich, 1998). The SBD consists of an α-helical lid segment (SBDα) and an eight-stranded β-sandwich subdomain (SBDβ), in which the substrate binding site is located (Bukau

and Horwich, 1998). The SBD can bind up to seven, mostly hydrophobic residues of an unfolded polypeptide chain by forming H-bonds with the peptide backbone and van der Waals interactions with hydrophobic amino acid side chains (Bukau and Horwich, 1998; Mayer, 2010; Kim *et al.*, 2013).

Hsp70 proteins are ATP-dependent enzymes (Zhuravleva and Gierasch, 2011; Kim *et al.*, 2013): ATP binding to the NBD causes the opening of SBDα. Subsequently, the substrate binding site of SBDβ becomes accessible, which allows client proteins to bind. Upon ATP hydrolysis, the SBDα closes and the client protein is bound (Zhuravleva and Gierasch, 2011; Kim *et al.*, 2013). The SBD shields the client's hydrophobic polypeptide chain from its surrounding environment, preventing its misfolding or inappropriate interactions with other macromolecules in the cell (Rosenzweig *et al.*, 2019). Upon exchange of ADP to ATP, the SBDα lid domain opens again and the client protein's folding attempt continues. If the client protein is unable to fold upon release from the Hsp70 chaperone system, it can re-bind to it, is transferred to other chaperone systems or is degraded (Kim *et al.*, 2013) (Figure 2).

Hsp70s generally cooperate with Hsp40 co-chaperones (DnaJ in *E. coli*) as well as nucleotide exchange factors (NEFs, GrpE in *E. coli*) (Kampinga and Craig, 2010; Hartl, Bracher and Hayer-Hartl, 2011): More than 40 members of the Hsp40 protein family are expressed in humans. Hsp40 proteins function as molecular chaperones on their own and can additionally recruit Hsp70 to non-native client proteins (Kampinga and Craig, 2010; Kim *et al.*, 2013). All Hsp40 proteins contain a J-domain, which can interact with the NBD of Hsp70 and facilitate the hydrolysis of ATP (Jiang *et al.*, 2007; Mayer, 2010) (Figure 2).

While *E. coli* expresses only one Hsp70-specific NEF (GrpE), mammalian cells were found to express different families of NEFs, which are structurally unrelated. The most abundant NEF proteins in mammalian cells are the Hsp110 proteins (Dragovic *et al.*, 2006; Raviol *et al.*, 2006; Kim *et al.*, 2013). Interaction of Hsp110 with Hsp70 results in the stabilization of the open conformation of the Hsp70 NBD, resulting in increased nucleotide exchange kinetics (Polier *et al.*, 2008; Schuermann *et al.*, 2008; Kim *et al.*, 2013).

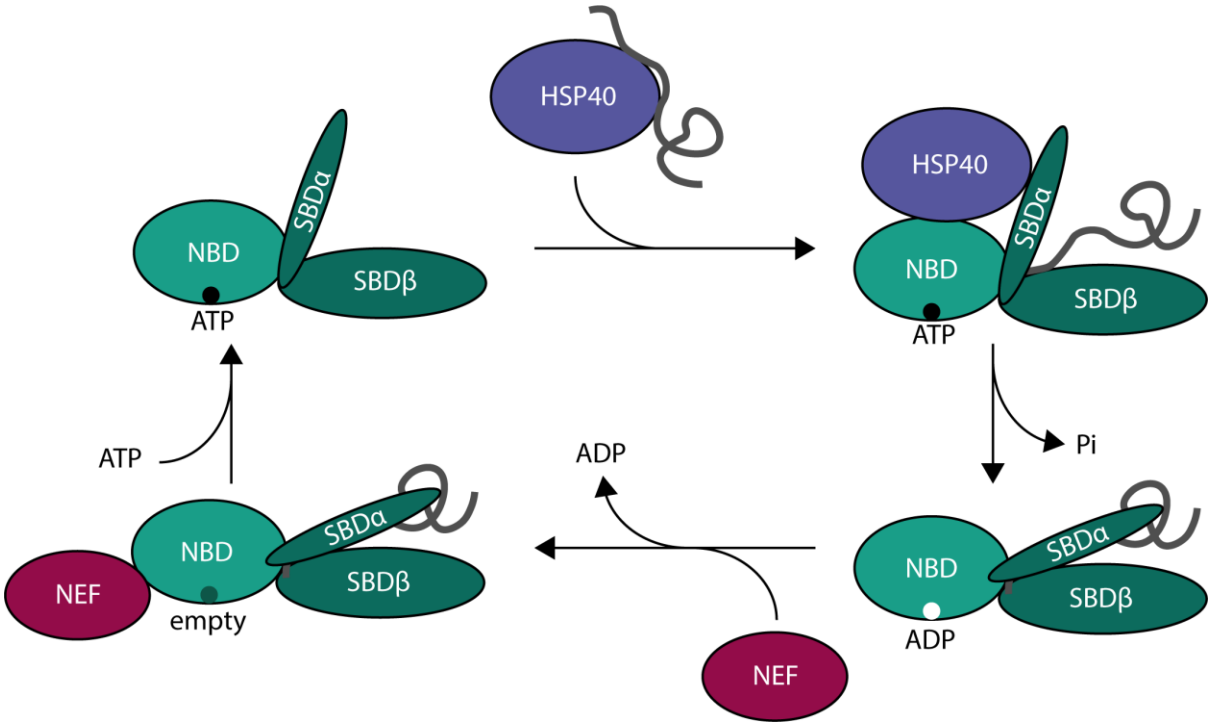

Figure 2 Reaction cycle of the chaperone Hsp70. Hsp40 transfers the client to the SBD of ATP-bound Hsp70. Upon hydrolysis of ATP, Hsp70 binds tightly to the client's peptide chain. NEFs can remove ADP from the NBD and a new ATP molecule can bind subsequently. Adapted from (Shiber and Ravid, 2014).

1.2.2 Small heat-shock proteins

sHsps are molecular chaperones of 12 to 43 kDa that act in an ATP-independent manner. All sHsps have a 80 amino acid (aa) long α-crystalline core domain (ACD) (de Jong, Caspers and Leunissen, 1998; Haslbeck, Weinkauf and Buchner, 2015). 10 different sHsps are expressed in mammals, although the expression pattern can vary between tissues. In the mammalian brain, mainly four sHsps are expressed – HspB1, HspB5, HspB6 and HspB8 (Quraishe *et al.*, 2008; Kampinga *et al.*, 2009).

sHsps contain flexible hydrophobic surface stretches to interact with their client proteins during chaperone action (Carver *et al.*, 2017; Webster *et al.*, 2019). Since these hydrophobic stretches imply a risk for unwanted protein-protein interactions, sHsps accumulate in dormant oligomeric structures with a dimeric substructure, which dissociate upon cellular stress (Santhanagopalan *et al.*, 2018). Interaction with the client protein leads to dissociation of the oligomers and subsequent binding of the chaperone (Freilich *et al.*, 2018; Santhanagopalan *et al.*, 2018).

Since sHsps are not capable of refolding the client protein themselves, they mainly bind to it, thereby preventing protein misfolding (‘holdase’ activity). In contrast, Hsp70 and other ATP-dependent chaperone complexes can subsequently refold the sHsp-bound client protein (Haslbeck *et al.*, 2005).

Notably, various sHsps prevent protein aggregation by interacting with aggregation-prone proteins directly (Golenhofen and Bartelt-Kirbach, 2016; Webster *et al.*, 2019). Some reports also describe an aggregate-stabilizing role for sHsps (Walther *et al.*, 2015; Shelton *et al.*, 2017).

1.3 Protein degradation pathways

During cellular stress or aging, when protein misfolding is increased and exceeds the available chaperone capacity, protein degradation becomes critical in preventing proteostasis collapse (Hipp, Kasturi and Hartl, 2019).

Proteins targeted for proteasomal or autophagic degradation are covalently modified with ubiquitin, a 76 aa protein (Goldstein *et al.*, 1975; Ciechanover *et al.*, 1980; Hershko *et al.*, 1980; Hershko and Ciechanover, 1998). The carboxyl terminus of ubiquitin is conjugated mainly to the ε-amino group of lysine residues, leading to an *iso*-peptide bond (Goldknopf and Busch, 1977; Swatek and Komander, 2016). Ubiquitin can also be linked to other free nucleophiles on a protein, including the N-terminus, serine and threonine hydroxyl groups and cysteine thiol groups (McDowell and Philpott, 2013).

Ubiquitination is performed by ubiquitinating enzymes in a three-step-process. Three different types of ubiquitin ligases are required for the ubiquitination process: The E1 ligase (ubiquitin activating enzyme) binds to the carboxyl group of ubiquitin via an ATP-dependent thioester linkage (Scheffner, Nuber and Huibregtse, 1995; Metzger, Hristova and Weissman, 2012). Subsequently, ubiquitin is transferred onto an E2 ligase (ubiquitin conjugating enzyme) and finally linked to the substrate via an interaction with an E3 ligase (ubiquitin ligating enzyme) (Metzger, Hristova and Weissman, 2012). While there are only two E1 and around 40 E2 enzymes in mammals, more than 600 E3 ligases have been identified so far, which ensure a high

degree of substrate specificity (Komander, 2009). E3 ligases are divided into two main groups: the *HECT* (Homologous to the EAP6 Carboxyl Terminus) (Huibregtse *et al.*, 1995) and the *RING* (Really Interesting New Gene) families (Lorick *et al.*, 1999; Metzger, Hristova and Weissman, 2012). While the *RING* E3 ligases only mediate the ubiquitin transfer from the E2 enzyme onto the substrate, the *HECT* E3 ligases bind ubiquitin in an intermediate step through a thioester bond (Metzger, Hristova and Weissman, 2012) (Figure 3 A).

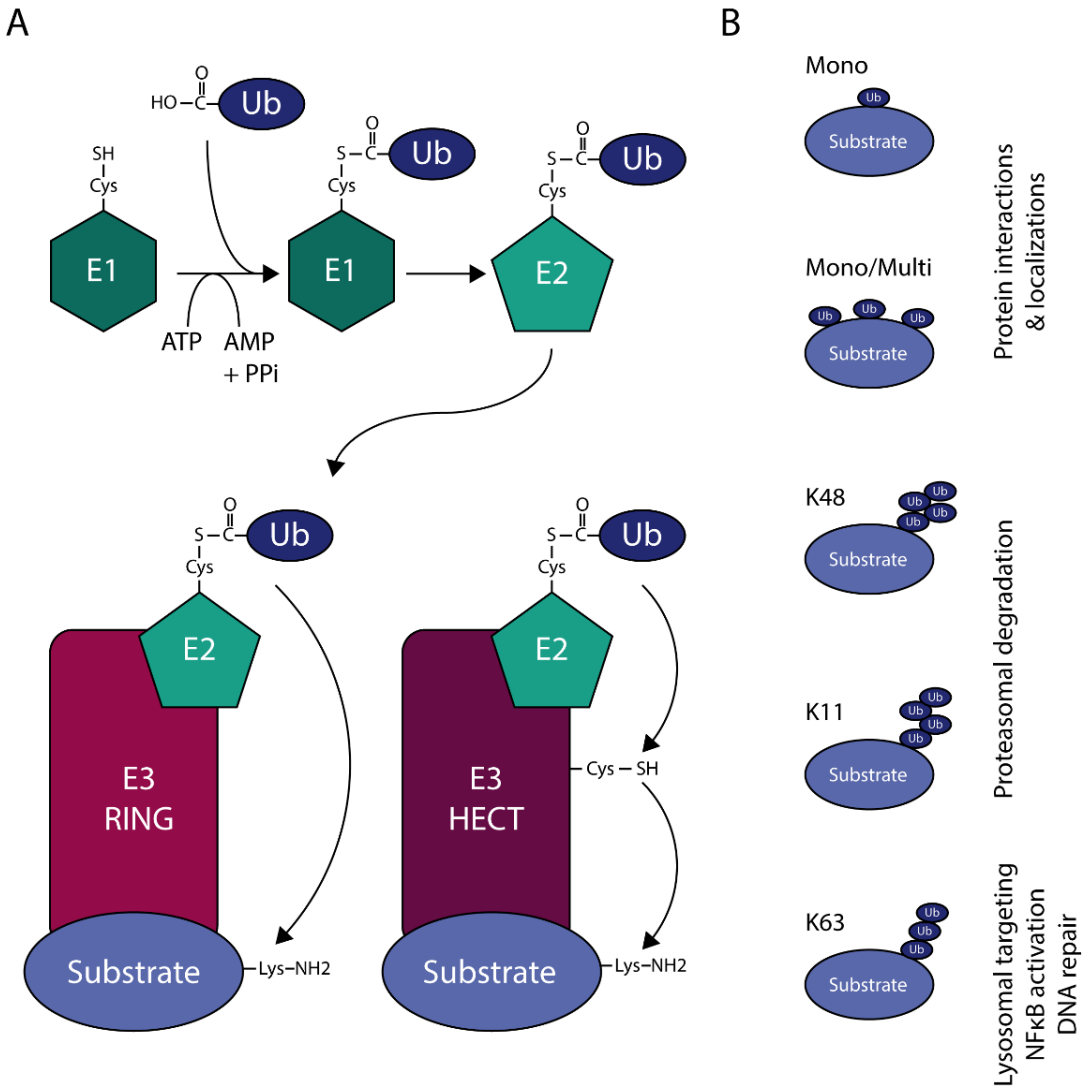

Figure 3 Reaction cycle of ubiquitin ligases. Ubiquitin (Ub) is conjugated to an E1 ligase via a thioester bond in an ATP-dependent manner. The ubiquitin is subsequently conjugated to E2 and E3 ligases (A). Different ubiquitination patterns define the fate of the client protein (B). Mono- and multi-ubiquitination can influence protein interactions and localization, K11 and K48 ubiquitination lead to proteasomal degradation and K63 ubiquitination leads to degradation through the autophagosomal-lysosomal system. Adapted from (Darwin, 2009).

Substrates of ubiquitin ligases can either be monoubiquitinated or polyubiquitinated. Depending on the type of ubiquitination, the substrate faces a different fate (Figure 3 B). Polyubiquitination via the N-terminal methionine (M1 linear ubiquitination) can serve as a signal for the regulation of immune responses as well as quality control (Dittmar and Winklhofer, 2020). Polyubiquitiniation via the seven lysine residues of ubiquitin (K6, K11, K27, K29, K33, K48, or K63) can lead to a plethora of cellular responses. The degradation of target proteins by the ubiquitin-proteasome system (UPS) or selective autophagy is mediated by polyubiquitination (Komander, 2009):

A polyubiquitination pattern of K11 or K48 linked ubiquitins results in the degradation of the substrate by the proteasome (Chau *et al.*, 1989; Jin *et al.*, 2008; Grice and Nathan, 2016). The eukaryotic 26S proteasome consists of a 19S regulatory subunit and a 20S core particle. The 20S core particle has a barrel-shaped structure that is formed by four heptameric rings, two α- and two β-rings (Gerards *et al.*, 1998). The α-rings guide the unfolded polypeptide chain towards the β-rings that are located in the center of the barrel and have proteolytic activity. Inside the center of the barrel, the polypeptide chain is cleaved into small fragments that are 3 to 22 amino acids long (Groll *et al.*, 1997; Kisselev *et al.*, 1999; Adams, 2003).

The 19S regulatory subunit, which is located on top of the 20S particle, contains the hexameric AAA-ATPase (ATPase Associated with diverse cellular Activities) Rpt1-6 (Regulatory Particle of Triple-ATPase) that unfolds the substrate and pulls it into the proteasome barrel (Walz *et al.*, 1998) (Figure 4A). The ubiquitinated substrate is recognized by other components of the 19S regulatory subunit, such as Rpn10 and Rpn13 (Regulatory Particle of Non-ATPase) that contain ubiquitin interacting motifs (Elsasser *et al.*, 2002, 2004; Nickell *et al.*, 2007; Collins and Goldberg, 2017). The UPS degrades around 80 % of all proteins that are targeted for degradation. Such proteins can be either short lived and undergo rapid turnover or are irreversibly misfolded (Collins and Goldberg, 2017).

An alternative degradation pathway is selective autophagy, which is induced by K48 or K63 ubiquitination patterns (Tan *et al.*, 2008; Dikic and Elazar, 2018). Autophagy receptors, such as p62 (ubiquitin-binding protein p62 or Sequestosome-1) or NBR1 (Neighbor of BRCA1 gene 1 protein) bind to the ubiquitin chain via their ubiquitin associated (UBA) domain (preferentially K63 linked ubiquitin) and guide the complex

to membrane bound LC3/GABARAP (Light Chain 3, Gamma-aminobutyric acid Receptor-Associated Protein; ATG8 and ATG12 in *S. cerevisiae*) via their LC3 interacting region (LIR) (Zatloukal *et al.*, 2002; Kirkin *et al.*, 2009; Dikic and Elazar, 2018). LC3 is located in the membrane of the phagophore and is required for its expansion. The phagophore is an open double membrane structure that is engulfing the cargo. Once the phagophore closes and forms an autophagosome, the cargo-membrane structure can undergo fusion with the lysosome. Subsequently, lysosomal proteases degrade the cargo at acidic pH (Pankiv *et al.*, 2007; Dikic and Elazar, 2018) (Figure 4B).

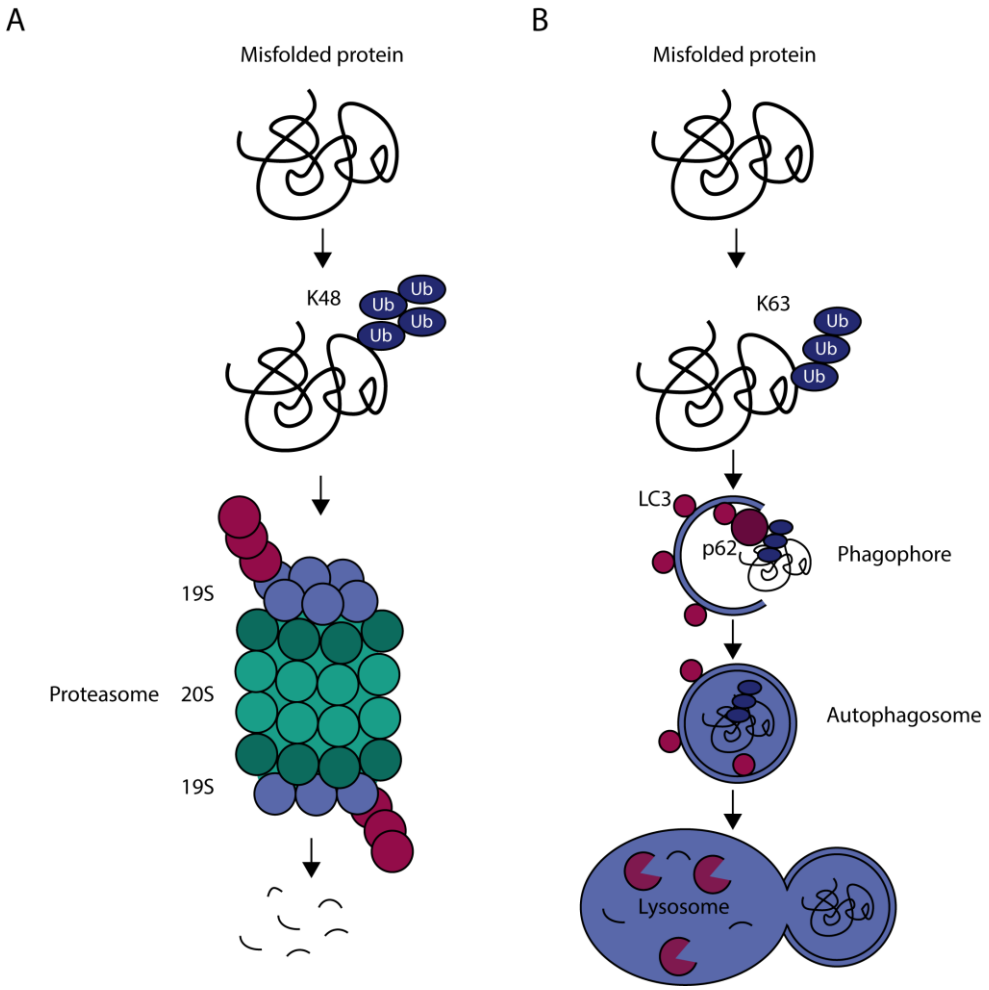

Figure 4 Two types of protein degradation. K48 labeled proteins are targeted for proteasomal degradation (A). The proteasome consists of a core particle (20S) and a regulatory subunit (19S). K63 labeled proteins undergo clearance by autophagy (B). p62 binds to the K63 ubiquitination pattern and mediates binding to LC3, a membrane bound protein of the phagophore. The phagophore elongates around the client protein and forms an autophagosome, which subsequently fuses with the lysosome. In the lysosome, acidic lysis degrades the client protein.

1.4 Protein misfolding

When misfolded or partially unfolded proteins are not refolded by chaperones or their degradation fails, potentially toxic protein aggregates may form (Hipp, Kasturi and Hartl, 2019). Proteins can aggregate during the folding process as they travel downhill on the potential free-energy surface towards their thermodynamically most favorable state (Balch *et al.*, 2008; Balchin, Hayer-Hartl and Hartl, 2016) (Figure 5).

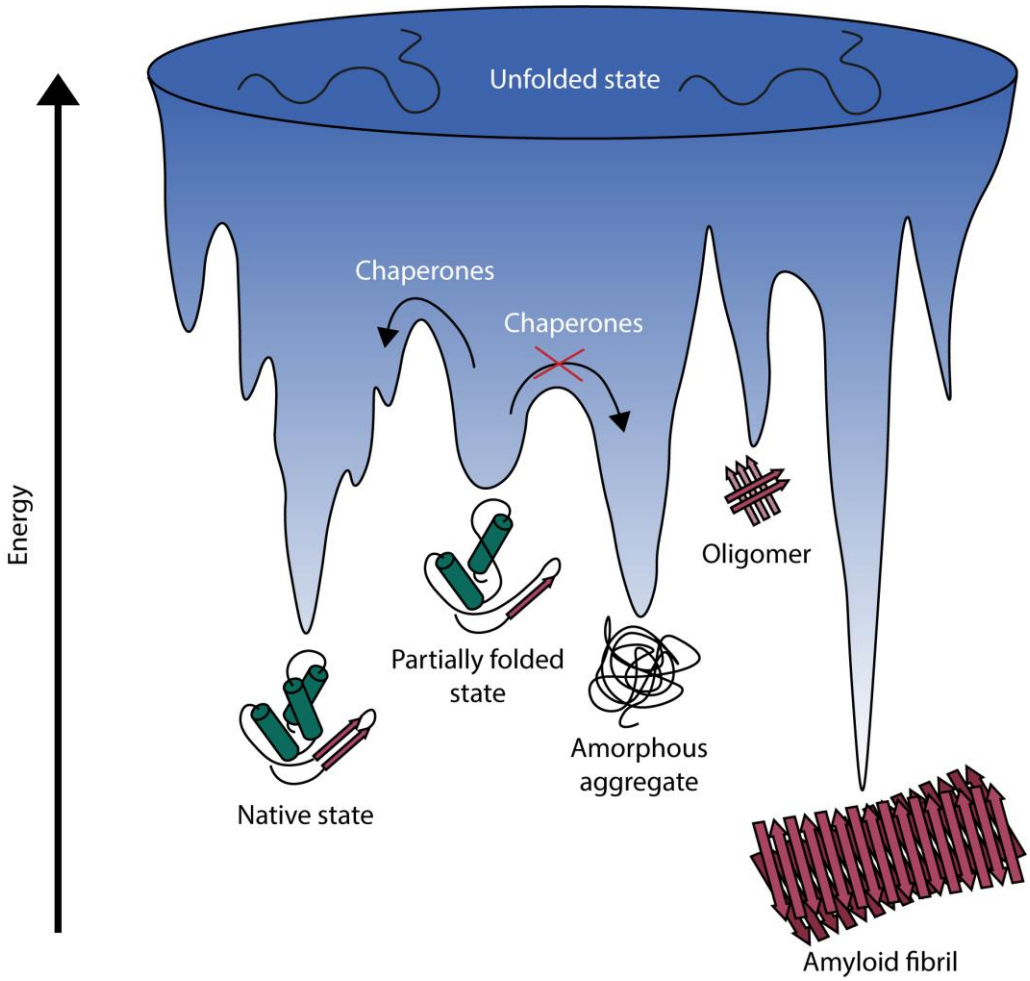

Figure 5 Energy landscape of protein folding. During folding into its native state, the partially folded polypeptide chain can adopt unstable intermediate states. When such intermediates are kinetically trapped and accumulate and exceed the available chaperone capacity, amorphous, oligomeric or amyloid aggregates can form.

If the protein is kinetically trapped in an off-pathway intermediate state and exposes hydrophobic amino acids to the solvent, amorphous, oligomeric or amyloid structures may form (Hipp, Kasturi and Hartl, 2019). The amyloid aggregate is thermodynamically

the most stable conformation of a protein, which makes disaggregation by molecular chaperones difficult (Hipp, Kasturi and Hartl, 2019).

Amyloid aggregates consist of amyloid fibrils. These fibrils have a diameter of 5 to 15 nm and can contain several protofilaments (Toyama and Weissman, 2011). As a hallmark, amyloid fibrils can be stained with fluorescent dyes, such as Congo Red, Thioflavin T (ThT) or Thioflavin S (Bennhold, 1922; LeVine, 1993). Amyloid dyes intercalate between the fibril's β-strands, which align along the fibril axis with a regular spacing of 0.47 nm (Sunde *et al.*, 1997) (Figure 6A). The aggregating protein molecules arrange in specific β-sheet folds, which interact with each other via H-bonds. These β-sheet folds become apparent by visualizing the fibril from the top (Makin and Serpell, 2005; Diaz-Espinoza, 2021). The arrangement of the β-sheets in amyloid fibrils is also referred to as the 'Greek-key topology' due to its similarity to the ancient Greek geometrical pattern (Diaz-Espinoza, 2021) (Figure 6B).

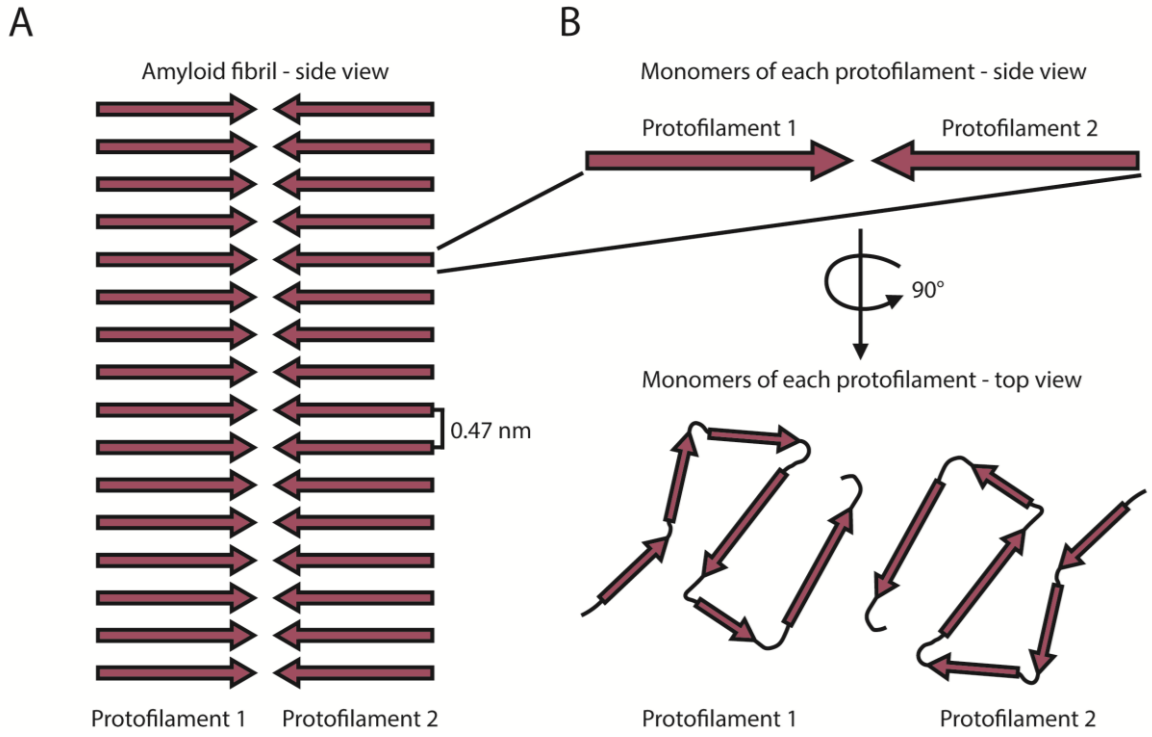

Figure 6 Amyloid fibril structure. Amyloid fibrils consist of one to several protofilaments (in the schematic example, two protofilaments are shown). The protein monomers align perpendicular to the fibril axis with an even spacing of 0.47 nm (A). Every protofilament has a specific protofilament fold that is defined by the β-sheet pattern that is formed by the aggregating protein monomers. The protofilament fold becomes apparent by visualizing the amyloid fibril from the top (B).

In contrast to amyloid fibrils, amorphous aggregates do not adopt a structured fold and lack long-range order, although they can still be rich in β-sheet content. One example of a protein adopting an amorphous aggregated state is αB-crystallin, invovled in proteostasis of the eye lens (Grosas *et al.*, 2020).

Oligomeric aggregates are often considered as toxic aggregation intermediates, due to their highly dynamic nature (Alam *et al.*, 2019). Oligomers can engage proteins as well as membranes in aberrant interactions. This results in protein dysfunction or damage of organelles (Winner *et al.*, 2011). In contrast to amyloid fibrils, oligomers do not necessarily have cross-β content. Some oligomers are thought to adopt an α-helical fold (Fonseca-Ornelas *et al.*, 2017).

Insterestingly, biologically functional aggregates consisting of amyloid fibrils have also been described: The amyloid fibril was found to be the storage form of peptide hormones in pituitary secretory granules (Maji *et al.*, 2009) and the eggshell of the silk moths contains amyloid fibrils, most likely increasing its stability to protect the embryo (Benaki *et al.*, 1998).

1.5 Prion-like propagation of amyloid aggregates

The kinetics of amyloid fibril formation can be monitored *in vitro* by using the amyloid dye ThT (LeVine, 1993; Nilsson, 2004): The aggregation reaction starts when an unfolded monomer adopts an amyloidogenic conformation and forms an early aggregate with additional monomers. As soon as the first aggregate nuclei form, the reaction accelerates and larger fibrils start to grow. When all monomers are consumed in fibrils, the reaction slows down, ending in a saturation phase (Ilie and Caflisch, 2019). Besides *de novo* aggregation, amyloid fibrils can also form upon secondary nucleation. During this event, the surface of fibril fragments provides new aggregation hubs for unfolded or partially misfolded monomers. These subsequently aggregate, which results in an increasing amount of amyloid fibrils (Nilsson, 2004; Meisl *et al.*, 2016) (Figure 7).

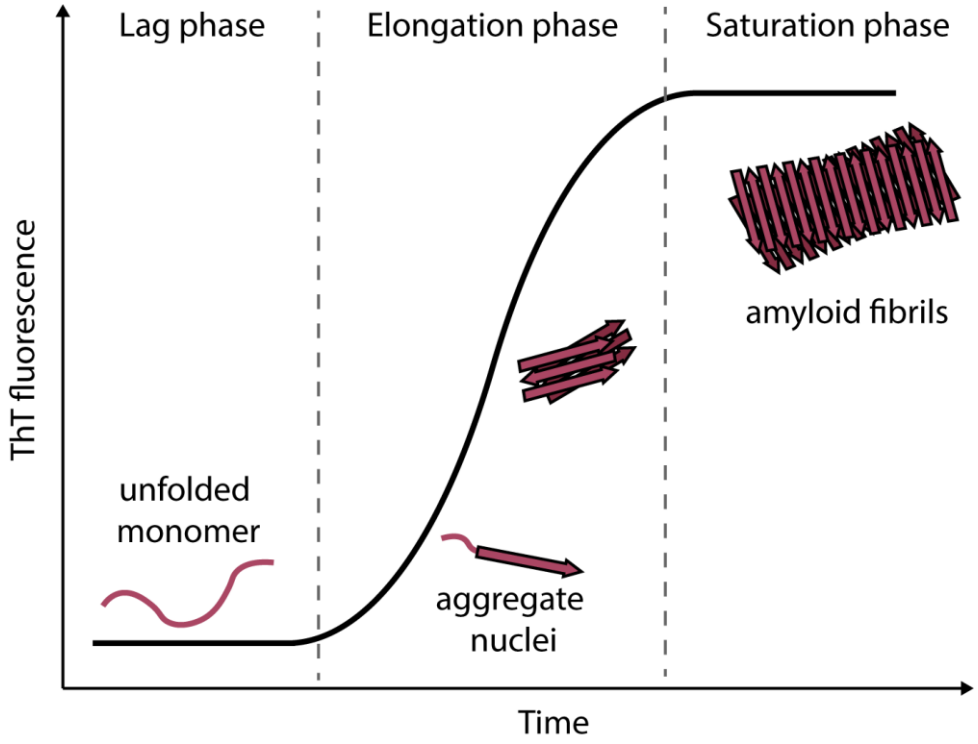

Figure 7 Formation of amyloid fibrils monitored by ThT. In the beginning of the reaction, the amyloidogenic protein is present as unfolded monomer (lag phase). As soon as the first aggregate nuclei form, the reaction rate increases and longer fibrils form (elongation phase). Once all monomers are consumed in amyloid fibrils, the reaction slows down and reaches a saturation phase. Adapted from (Ilie and Caflisch, 2019).

Neurodegenerative diseases, which feature the infectious spreading of amyloid fibrils throughout the brain are classified as prion (prion = proteinaceous infectious particle) diseases. In prion diseases, such as Creutzfeld-Jakob-disease (CJD) in humans and scrapie in sheep, the prion protein PrP^{C} (Prion Protein cellular) forms amyloid fibrils (PrP^{SC} for PrP scrapie form) (Ghetti *et al.*, 1996). During disease spreading, amyloid PrP^{SC} fibrils break into smaller pieces, resulting in secondary nucleation events and facilitating new fibril growth. This leads to a constantly increasing aggregate load. PrP^{SC} aggregates can spread intercellularly, resulting in a transmission of aggregates through interconnected brain regions (Kordek *et al.*, 1999). CJD results in the degeneration of the brain and the death of the patient. Around 77 cases were diagnosed in Germany in the year 2019 (Robert Koch Institute). Mutations in the *PRNP* (prion protein) gene or an older age of the patient can increase the probability of falling ill with CJD (Ladogana and Kovacs, 2018).

Contaminated tissues in the form of tissue grafts (e.g. cornea transplantation) or the consumption of meat from cows affected by bovine spongiform encephalopathy (BSE) can result in transmission of CJD (Will *et al.*, 1996; Will, 2004). This corroborates CJD as an infectious disease, in which amyloid prion fibrils cannot only be transmitted from human to human, but also between different mammalian species.

Not only metazoan organisms can harbor self-replicating amyloid aggregates. *S. cerevisiae* has heritable elements that are transmitted via prions. Known prions in yeast include *[URE3]* and *[PSI+]*, which are the prion forms of the proteins Ure2p (Transcriptional Regulator URE2) and Sup35p (Eukaryotic peptide chain release factor GTP-binding Subunit) (Wickner, 2016). So far, yeast prions are considered benign and represent a specific form of inheritance that is governed by protein conformation and not by DNA sequence (Liebman and Chernoff, 2012).

Evidence is emerging that other amyloid proteins are also able to spread in a prion-like manner (Purro *et al.*, 2018): Spreading of Amyloid-β (Aβ), usually found in plaques of Alzheimer's disease (AD) patient's brains, has been observed in a cohort of young patients in Great Britain, who were treated with preparations of growth hormone in their childhood. Depending on the purification method used, some of the preparations were contaminated with Aβ aggregates. Shortly after the treatment, Aβ plaques formed in the brain of the patients, resulting in typical symptoms of AD and CJD (Purro *et al.*, 2018). In addition to PrP^C and Aβ, also α-syn and tau have been found to aggregate into amyloid fibrils and spread in a prion-like manner in patient brains (Vasili, Dominguez-Meijide and Outeiro, 2019).

The structures of α-syn and tau, the diseases related to their aggregation, as well as the processes of aggregation and spreading will be discussed in detail below.

1.6 α-Synuclein

α-Syn, encoded by the *SNCA* gene, is an IDP with a total length of 140 aa (Uéda *et al.*, 1993; Masliah *et al.*, 1996; Villar-Piqué, Lopes da Fonseca and Outeiro, 2016), which is primarily localized to presynaptic terminals of neurons (Clayton and George, 1998; Burré, 2015). It has two homologues, β-synuclein and γ-synuclein (*SNCB* and

SNCG), that are also expressed in brain tissue. However, not much is known about the function of these two other synuclein proteins. A recent study suggests that the binding of β-syn or γ-syn to α-syn modulates α-syn activity at the pre-synapse (Carnazza *et al.*, 2020).

α-Syn runs as a 16 kDa protein in sodium dodecylsulfate polyacrylamide gel electrophoresis (SDS-PAGE). However, it shows characteristics of a 57 to 60 kDa protein under native conditions, e.g. in size exclusion chromatography. Therefore, it is assumed that α-syn occurs in an unfolded conformation with an increased hydrodynamic radius (Weinreb *et al.*, 1996; Eliezer *et al.*, 2001; Lashuel *et al.*, 2013).

α-Syn consists of three domains (Emanuele and Chieregatti, 2015) (Figure 8). Its N-terminal region, ranging from aa 1 to 60, contains seven imperfect repeats containing the motif KTKEGV. This amphipathic region is able to adopt α-helical structures, which allow the interaction with lipid bilayers (Eliezer *et al.*, 2001; Emanuele and Chieregatti, 2015; Fusco *et al.*, 2017). Due to this ability and its high abundance at the pre-synapse, it has been hypothesized that α-syn plays a role in vesicle fusion during transmission of neuronal signals. While some studies suggest the involvement of α-syn in neurotransmitter release, others describe an inhibitory effect of α-syn at the pre-synapse (Emanuele and Chieregatti, 2015).

The α-helical fold of α-syn has furthermore been linked to multimerization. In 2011, Bartels *et al.* and Wang *et al.* have shown that upon crosslinking, α-syn occurs as a homotetrameric α-helical protein, rather than an unfolded monomeric one (Bartels, Choi and Selkoe, 2011; Wang *et al.*, 2011; Lashuel *et al.*, 2013). This observation, however, could not be reproduced (Burré *et al.*, 2013; Lashuel *et al.*, 2013).

Most mutations of α-syn that induce familial forms of Parkinson's disease (PD) occur in the N-terminal region (Srinivasan *et al.*, 2021), including A18T, A29S (Hoffman-Zacharska *et al.*, 2013), A30P (Krüger *et al.*, 1998), E46K (Zarranz *et al.*, 2004), A53E (Pasanen *et al.*, 2014), A53T (Polymeropoulos *et al.*, 1997), H50Q (Appel-Cresswell *et al.*, 2013) and G51D (Lesage *et al.*, 2013).

The second domain, the so-called 'non-Aβ-component of AD amyloid' (NAC) domain, is the part of α-syn that is involved in amyloid fibril formation and forms the major part of the amyloid fibril core (Giasson *et al.*, 2001). The term 'non-Aβ-component of AD

amyloid' originated from the observation that this domain of α-syn, ranging from aa 61 to 95, was reported to be found in Aβ plaques as a component other than the Aβ protein itself (Uéda *et al.*, 1993). However, later works failed to reproduce this observation and could not detect any α-syn in Aβ plaques (Culvenor *et al.*, 1999). The NAC domain is highly hydrophobic and crucial for aggregation of α-syn into amyloid fibrils. Upon deletion of large parts of the NAC domain, α-syn loses its ability to aggregate *in vitro* (Giasson *et al.*, 2001) and *in cellulo* (Luk *et al.*, 2009; Lashuel *et al.*, 2013).

The C-terminal region of α-syn, ranging from aa 96 to 140, contains predominantly negatively charged as well as proline residues (Breydo, Wu and Uversky, 2012; Villar-Piqué, Lopes da Fonseca and Outeiro, 2016). It was discovered that α-syn can bind Ca^{2+} ions via its C-terminus (Nielsen *et al.*, 2001), which increases its lipid-binding capacity and mediates its localization to the pre-synaptic terminal (Lautenschläger *et al.*, 2018). Additionally, the C-terminus has an aggregation preventing role, as α-syn becomes more aggregation prone upon partial truncation (aa 115 to 140) (Sorrentino *et al.*, 2018).

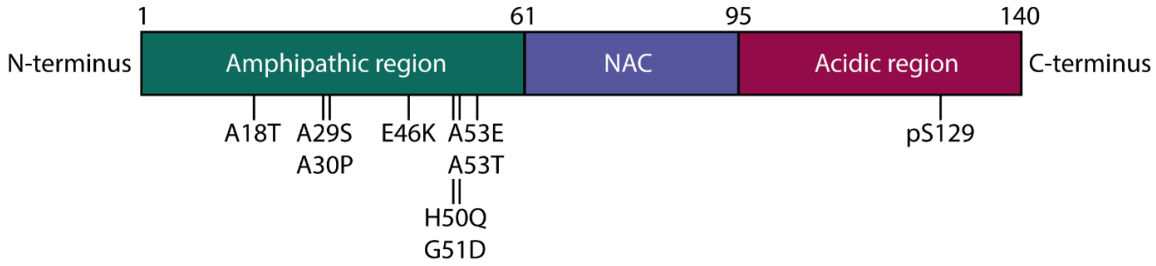

Figure 8 Structure of α-syn. α-Syn consists of three domains: An amphipathic region is located at the N-terminus, in which most of the disease-causing mutations are found. The second domain 'NAC' is needed for fibrillogenesis of α-syn. An acidic region at the C-terminus allows Ca^{2+} binding and modulates lipid binding. Adapted from (Emanuele and Chieregatti, 2015).

Several sites for post-translational modifications (PTMs) are found at the C-terminus (Emanuele and Chieregatti, 2015): Nitration occurs on Y125, Y133 and Y136 and kinases phosphorylate Y125, Y133 and Y135 (Schmid *et al.*, 2013). Notably, more than 90 % of aggregated α-syn gets phosphorylated at S129, which makes phospho-α-syn(S129) a specific marker for aggregated α-syn (Fujiwara *et al.*, 2002).

1.7 α-Synucleinopathies

Neurodegenerative diseases, which feature the deposition of aggregated α-syn in neurons or glial cells as a histopathological hallmark, belong to the group of α-synucleinopathies (Figure 9). α-Synucleinopathies include diseases such as PD, dementia with Lewy bodies (DLB) and multiple system atrophy (MSA) (Peng, Gathagan and Lee, 2018).

1.7.1 Parkinson's disease

PD is the second most prevalent neurodegenerative disorder, which affects 1 of 100 people above an age of 60 years (Tysnes and Storstein, 2017). As a degenerative disorder of the nervous system, the symptoms emerge slowly and become eventually more severe, resulting in the death of the patient. The main symptoms at an early stage are motor symptoms, such as tremor, rigidity, postural instability and slowness of moving. During disease progression, other symptoms like depression and anxiety appear (Hoehn and Yahr, 1967; Pollanen, Dickson and Bergeron, 1993; Tanner and Goldman, 1996).

A main cause for the described motor symptoms is the loss of dopaminergic neurons in the basal ganglia of the *substantia nigra pars compacta*, which function as control center for voluntary motor movements (Benazzouz *et al.*, 2014). So far, the exact cause for the loss of dopaminergic neurons remains unclear. However, it has been shown that most PD patients exhibit α-syn aggregates in neurons of the affected brain regions, which are called Lewy bodies (LBs) (Lewy, 1912; Spillantini et al., 1997). Although LBs are not found in every patient that presents with Parkinsonism (Johansen *et al.*, 2018), a clear link between mutations in the *SNCA* gene, which make α-syn more aggregation prone, as well as *SNCA* triplication and an early onset of PD has been found in genome-wide association studies (GWAS) (Singleton *et al.*, 2003; Blauwendraat *et al.*, 2019).

It is noteworthy that besides the *SNCA* gene, also other genes, such as *LRRK2* (Leucin Rich Repeat Kinase 2), *GBA1* (Glucosylceramidase Beta 1) *PRKN* (Parkin RBR E3 Ubiquitin Protein Ligase), *PINK1* (PTEN-induced putative Kinase 1), *DJ-1*

(Daisuke-Junko-1) and *VPS35* (Vacuolar Protein Sorting 35) have been identified as PD risk factor genes (Billingsley *et al.*, 2018; Lunati, Lesage and Brice, 2018).

Because PD is a degenerative disease and no cure has been found so far, only symptomatic treatment can be offered to the patients. This treatment includes the application of Levodopa (L-DOPA), a precursor molecule of dopamine, or dopamine agonists (Armstrong and Okun, 2020). Besides the application of chemical compounds, patients can also be treated by deep brain stimulation (DBS). In this case, electrodes are implanted into the patient's brain. These electrodes constantly apply electrical impulses leading to a stimulation of the affected brain areas and a reduction of the occurring symptoms (Armstrong and Okun, 2020). The exact mode of action of DBS, however, is still not understood.

1.7.2 Dementia with Lewy bodies

Patients suffering from DLB show similar motor symptoms as observed in PD. Additionally, severe cognitive defects, such as confusion, loss of speech or poor attention may occur. Many DLB patients present with a rapid eye movement (REM) sleep behavior disorder, which results in exhaustion (Capouch, Farlow and Brosch, 2018).

The pathophysiology of DLB is characterized by LBs and loss of dopaminergic and cholinergic neurons in the tegmentum and the basal forebrain. Besides α-syn accumulations, tau aggregates (Neurofibrillary tangles, NFT) and Aβ plaques may also be present, which are otherwise typically found in AD (Taylor *et al.,* 2017; Irwin and Hurtig, 2018)

1.7.3 Multiple System Atrophy

MSA, in contrast to PD and DLB, is histopathologically characterized by α-syn aggregates in glial cells, which are called glial cell cytoplasmic inclusions (GCIs) or Papp-Lantos bodies (Papp, Kahn and Lantos, 1989; Gai *et al.*, 2003). Although a different cell type is affected in MSA compared to PD, the same brain areas degenerate over time. The progressing degeneration results in a similar symptomatic phenotype. Interestingly, however, L-DOPA has been found to be ineffective in MSA

patients (Wolf, 2012). In comparison to PD, MSA is more aggressive, leading to the death of the patients within 8 to 11 years after diagnosis (Wenning *et al.*, 2013).

It has been shown that α-syn aggregates purified from *post mortem* material of patients having suffered from PD and MSA have different structural and biochemical characteristics, which may underlie the different clinical phenotypes observed in the two diseases (Peng *et al.*, 2018). Clinically, MSA cases are divided into MSA-P, which predominantly show a Parkinsonian phenotype, and MSA-C, which show cerebellar ataxia (Köllensperger *et al.*, 2010).

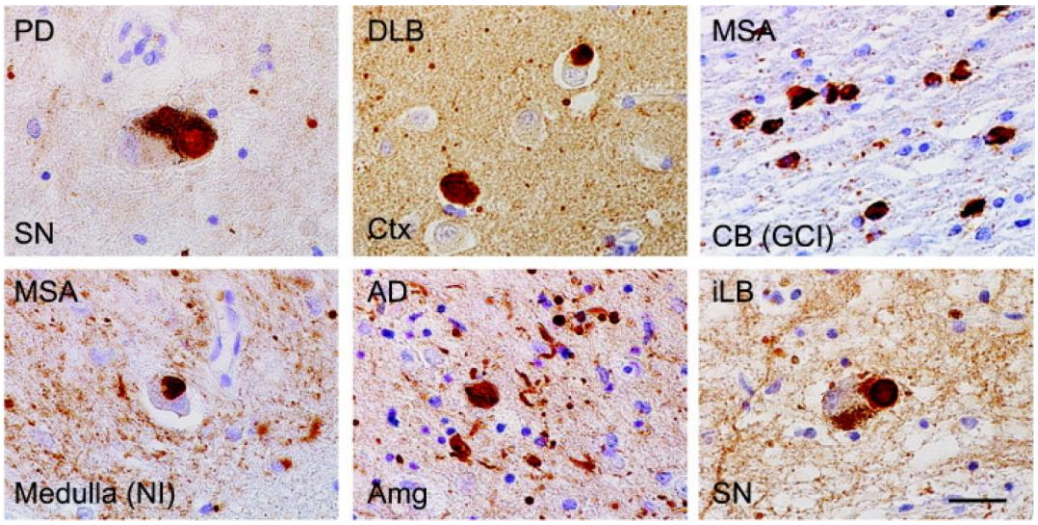

Figure 9 α-Syn pathology in different neurodegenerative diseases. Aggregated α-syn is present in various synucleinopathies, like PD, DLB, MSA and incidental Lewy body disease. Although α-syn aggregates are mainly found in neurons, they also occur as GCIs in the case of MSA. Different brain areas are affected in different diseases: SN - *substantia nigra;* Ctx - cortex; CB - cerebellum; Amg - amygdala; Scale bar: 25 µm (Peng, Gathagan and Lee, 2018).

1.8 α-Synuclein aggregation

α-Syn aggregation is thought to be causally related to the occurrence of synucleinopathies, such as PD or MSA. The exact connection between α-syn aggregation and cellular toxicity, however, is still not clear.

In a healthy cell, the level of α-syn is tightly regulated (Lashuel *et al.*, 2013). α-Syn is degraded by the UPS, autophagy (Webb *et al.*, 2003) or direct proteolysis (Iwata *et al.*, 2003). If one of these degradation mechanisms fails, less α-syn is degraded, resulting in an increased intracellular concentration, which subsequently favors the

aggregation reaction. *SNCA* gene mutations and triplications, toxins, oxidative stress as well as PTMs were found to be additional regulators of aggregation (Paleologou *et al.*, 2010; Lashuel *et al.,* 2013; Manzanza, Sedlackova and Kalaria, 2021).

The major part of α-syn in LBs as well as GCIs occurs most likely in form of amyloid fibrils (Spillantini *et al.*, 1997; M. G. Spillantini *et al.*, 1998; Gai *et al.*, 2003), possibly representing an attempt of the cell to sequester toxic aggregated material in a stable and less dynamic form (Lashuel *et al.*, 2013).

1.8.1 α-Synuclein oligomers

Oligomeric α-syn species are structurally highly diverse and dynamic (Alam *et al.*, 2019): spheroid, annular- and “chains of spheres”-shaped oligomers have been described, which cannot only interconvert to soluble monomers or amyloid fibrils, but have the ability to adopt other oligomeric structures as well (Stöckl, Zijlstra and Subramaniam, 2013; Cremades, Chen and Dobson, 2017; Alam *et al.*, 2019).

α-Syn oligomers can be toxic for the cell (Alam *et al.*, 2019). They may damage mitochondria (Parihar *et al.*, 2009), lead to lysosomal rupture (Hashimoto *et al.*, 2004; Jiang *et al.*, 2017) and result in Ca^{2+} influx and cell death (Danzer *et al.*, 2007). *In vivo* studies found that toxic oligomers result in a dramatic loss of dopaminergic neurons in the *substantia nigra* by potential disruption of membranes (Winner *et al.*, 2011; Lashuel *et al.*, 2013).

Oligomers cannot only interconvert, but also recruit monomeric α-syn into amyloid fibrils (Chen *et al.*, 2015). Interestingly, α-syn fibrils may release oligomeric species, which subsequently lead to neuronal dysfunction (Cascella *et al.*, 2021).

1.8.2 α-Synuclein amyloid fibrils

While the structure of oligomers is difficult to determine, several structures of α-syn amyloid fibrils have been solved by nuclear magnetic resonance (NMR) spectroscopy or cryo-electron microscopy (cryo-EM) single particle analysis. The first cryo-EM structure of an *in vitro* formed α-syn fibril was solved by Guerrero-Ferreira *et al.* at an overall resolution of 3.4 Å. For this study, truncated wild type (wt) α-syn (aa 1-121) was used and amyloid fibril formation was facilitated *in vitro* by constant agitation in Dulbecco’s buffered saline (DPBS) at 37 °C (Guerrero-Ferreira *et al.*, 2018).

Wt α-syn(1-121) assembles into a symmetrical, polar fibril, composed of two protofilaments that contain staggered β-strands with a spacing of 4.9 Å. The fibril core ranges from residues L38 to V95. Within one protofilament, eight in-register parallel β-strands wind around a hydrophobic valine and alanine rich intra-molecular core (residues 48 – 91), which likely stabilizes the protofilament (Guerrero-Ferreira *et al.*, 2018).

The authors found that the two protofilaments interact with each other via a hydrophobic steric zipper topology within β-sheet 3, ranging from aa 51 to 56. In this region, A53 and V55 form an inter-molecular surface, which is additionally stabilized by a salt bridge between E57 and H50. Notably, three PD associated mutations, H50Q, G51D and A53T, are located at the protofilament interface. One hypothesis that could explain the aggregation-prone character of A53T mutant α-syn, is the position of the threonine at the interface. A polar amino acid may lead to an overall destabilization of the zipper topology, resulting in increased fibril breakage and enhanced secondary nucleation (Guerrero-Ferreira *et al.*, 2018).

Since publication of the first cryo-EM structure, more structures of *in vitro* formed α-syn fibrils have been reported. Different research groups studied wt fibrils aggregated in different buffers, supplemented with various additives (B. Li *et al.*, 2018), mutant fibrils (e.g. H50Q) (Boyer *et al.*, 2019) or fibrils that contained PTMs (e.g. N-terminal acetylation) (Y. Li *et al.*, 2018). Interestingly, however, none of the *in vitro* aggregated fibril structures resembles the one purified from *post mortem* patient brain material (Schweighauser *et al.*, 2020).

In 2020, Schweighauser *et al.* solved the structure of α-syn fibrils purified from the putamen of MSA patients. The protofilaments of the two structures they determined (from a total of five cases) show an asymmetrical arrangement. One of the protofilaments contains additional β-sheets at the N-terminus, which results in a total of 12 β-sheets.

Another difference between the MSA fibrils and fibrils formed *in vitro* is an additional density that is not connected to the polypeptide chain and is surrounded by side chains K43, K45 and H50. Although the exact composition of the density remains unknown, Schweighauser *et al.* hypothesized that this molecule is highly negatively charged and of non-proteinacious nature (Schweighauser *et al.*, 2020) (Figure 10).

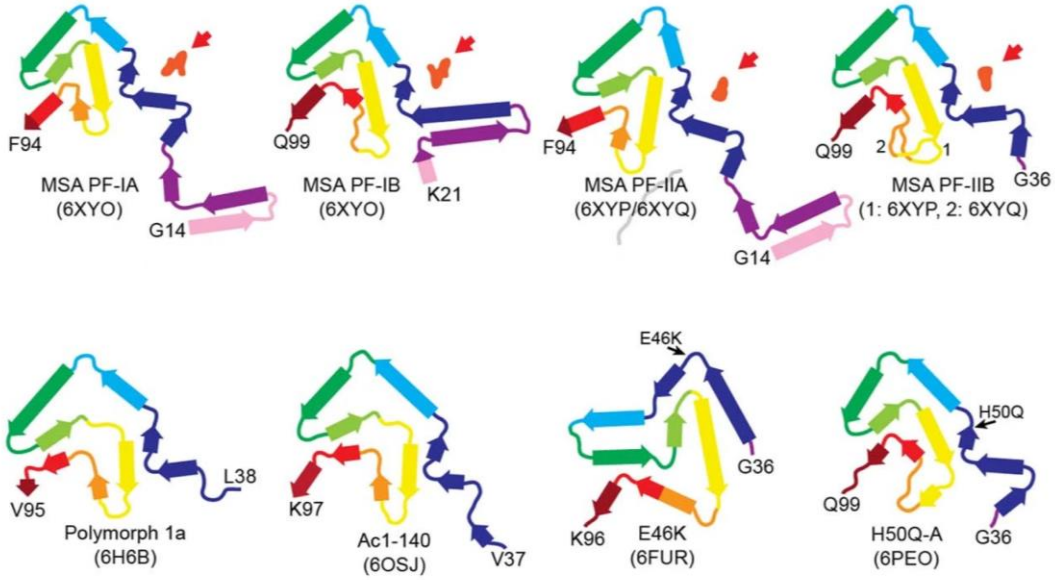

Figure 10 Schematic of β-sheet arrangements in different α-syn protofilament cores. α-Syn fibrils purified from patient brain material show different β-sheet arrangements (upper row) and presence of additional non-proteinaceous molecules (orange), compared to *in vitro* formed α-syn fibrils (lower row). Polymorph 1a is formed by wt α-syn, Ac1-140 is additionally N-terminally acetylated, E46K and H50Q are α-syn mutations found in familial forms of PD. Adapted from (Schweighauser *et al.*, 2020).

1.8.3 α-Synuclein aggregates in neurons and glial cells

LBs are neuronal cytoplasmic inclusions, first described by Heinrich Lewy in 1912 (Lewy, 1912). Until today, the molecular architecture of LBs has not finally been clarified, as methods for the unperturbed ultrastructural imaging of native human brain tissue are still lacking.

Early conventional EM work suggested that LBs are proteinaceous accumulations, consisting of fibrillar material that in some cases adopts a multilaminated structure. Although LBs from different areas of the brain vary in their appearance, all of them contain fibrils as a hallmark (Forno, 1996).

Ubiquitin, neurofilament (Goldman *et al.*, 1983; Kuzuhara *et al.*, 1988) and α-syn were the first proteins identified as components of LBs (Spillantini *et al.*, 1997; M. G. Spillantini *et al.*, 1998; Trojanowski and Lee, 1998). Early immuno-gold labeling experiments of brain slices suggested that the filamentous components of LBs are either composed of α-syn directly, or that α-syn binds to the observed fibrils (Arima *et*

al., 1998). Purification of fibrils from PD patient brain and subsequent immuno-gold staining proved that the purified fibrils are indeed formed by α-syn (M. Spillantini *et al.*, 1998).

However, in 2019 Shahmoradian *et al.* suggested that LB pathology is rather a lipidopathy than a proteinopathy: Upon examination of 17 different LBs by room temperature correlative-light electron microscopy (CLEM), they found that all of the analyzed LBs mainly consisted of membranous organelles, rather than fibrils. Although the authors also observed fibrillar material in 14 of the LBs, they subsequently questioned the existence of α-syn fibrils in LBs (Shahmoradian *et al.*, 2019; Lashuel, 2020).

This claim led to a conflict in the scientific community (Lashuel, 2020). A study that was able to replicate LB-like aggregates in primary mouse neurons and analyzed them with conventional EM, came to the conclusion that indeed significant amounts of membranous organelles are present in LBs. However, the authors could additionally observe filaments, which resembled α-syn fibrils, as observed in the early EM studies performed on human brain material (Mahul-Mellier *et al.*, 2020).

In contrast to LBs, GCIs occur mainly in oligodendrocytes. GCIs are composed of α-syn fibrils, which contain phospho-α-syn(S129) (Gai *et al.*, 2003) and are localized to the cytoplasm as well as to the nucleus. In MSA, α-syn-positive inclusions can also be found in neurons, albeit to a lesser extent (Papp and Lantos, 1994). The brain areas affected by GCIs are the *substantia nigra*, the striatum, the pontine nucleus, the cerebellum and the spinal cord. These regions show a characteristic neurodegeneration, which is most probably due to the loss of oligodendrocytes, as the primary lesion (Ozawa *et al.*, 2004).

1.9 Tau

The microtubule binding protein tau is an IDP that is highly expressed throughout the whole central nervous system (CNS) and consists of four domains: The N-terminal acidic projection domain, the proline-rich domain, the microtubule-binding domain (MTBD) and a C-terminal tail (Strang, Golde and Giasson, 2019).

Alternative splicing of exon 2, 3 and 10 can give rise to six different isoforms in the CNS, resulting in proteins of 352 to 441 aa lengths: Tau isoforms with zero, one or two N-terminal repeats (0N, 1N, 2N) are the result of alternative splicing of exon 2 and 3. The splicing of exon 10 generates tau isoforms that contain three or four MT-binding repeats (3R or 4R) (Strang, Golde and Giasson, 2019) (Figure 11). Each N-terminal insert is 29 aa long and each repeat in the MTBD is 30 or 31 aa long (Guo, Noble and Hanger, 2017). Although the ratio between 3R to 4R tau is very similar in the healthy adult brain, it may vary in the brain of patients suffering from tauopathies (Liu and Gong, 2008). The distribution of the N-terminal isoforms is irregular: 0N tau comprises 37 %, 1N tau 54 % and 2N tau 9% of all the tau isoforms (Goedert and Jakes, 1990; Hong *et al.*, 1998; Hanes *et al.*, 2009).

It was found that tau can fold into a ‘paperclip’-like structure, where N- and C-terminus interact with each other (Jeganathan *et al.*, 2006). Mutations, truncation or PTMs may disturb this interaction, leading to more unfolded tau in the cell, which increases the probability of tau aggregation (Strang, Golde and Giasson, 2019).

The primary function of tau is to bind to and assemble microtubules (MTs) by binding to the interface between α- and β-tubulin heterodimers (Kadavath *et al.*, 2015; Strang, Golde and Giasson, 2019). *In vitro* experiments showed that 4R tau interacts with MTs with a higher affinity than 3R tau and results in increased MT stability (Panda *et al.*, 2003).

Besides MTs, tau interacts with other proteins, such as dynactin, which is a regulator of the MT motor protein dynein (Magnani *et al.*, 2007). Furthermore, tau is involved in axonal transport and neurite outgrowth (Caceres and Kosik, 1990; Strang, Golde and Giasson, 2019).

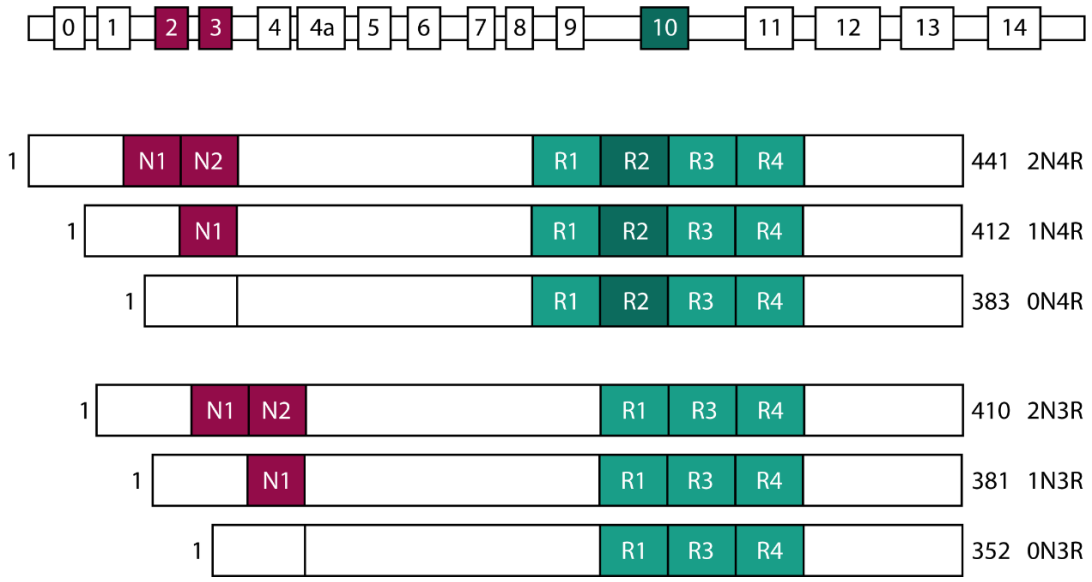

Figure 11 Isoforms of human brain tau. In the CNS, six different tau isoforms are generated by alternative mRNA splicing of exon 2, 3 (red) and 10 (green). These isoforms are 352 to 441 aa long. Depending on the splicing pattern, tau with zero, one or two N-terminal repeats (red) and three or four MTBD (green) is expressed. Adapted from (Guo, Noble and Hanger, 2017).

1.10 Tauopathies and Tau aggregation

Tauopathies are neurodegenerative diseases that have tau deposits as histopathological hallmark. Tau aggregates intracellularly into amyloid neurofibrillary or gliofibrillary tangles that are hyperphosphorylated (Van Swieten *et al.*, 1999). Tau hyperphosphorylation likely occurs prior to the aggregation, leading to an electrostatic conflict that favors dissociation of tau from MTs (Grundke-Iqbal *et al.*, 1986; Despres *et al.*, 2017; Goedert, Eisenberg and Crowther, 2017).

1.10.1 AD and FTDP-17

The most common tauopathy is AD. In addition to intracellular tau aggregates, insoluble extracellular aggregates of Aβ (senile plaques) can be found in AD patient brains (Spires-Jones, Attems and Thal, 2017). AD is characterized by dementia as well as language problems, disorientation, mood swings and behavioral changes (Bature *et al.*, 2017). Although AD is described as sporadic disease, 1 to 2 % of the cases are inherited. Genes associated with autosomal dominant AD are *APP* (Aβ precursor protein), *PSEN1* and *2* (Persenilin 1 and 2) (Dai *et al.*, 2017). Genes involved

in late onset AD (LOAD) are - among others - *APOE* (Apolipoprotein E) as well as *CLU* (Clusterin, Clu) (dos Santos *et al.*, 2020).

Interestingly, dominant mutations in the *MAPT* (Microtubule-Associated Protein Tau) gene (e.g. P301L or V337M) have been identified that result in frontotemporal dementia with Parkinsonism linked to chromosome 17 (FTDP-17) (Goedert and Jakes, 2005). In comparison to wt tau, tau P301L aggregates faster *in vitro* and *in cellulo* (Elbaum-Garfinkle *et al.*, 2014; Strang *et al.*, 2018). Both mutations, P301L and V337M, decrease tau binding to MTs, which results in more unbound tau in the cell, favoring its aggregation (Hong *et al.*, 1998). Over 100 families with 32 different tau mutations have been identified so far. However, symptoms and phenotype do not only vary between the different families, but also between different individuals carrying the same mutation (Goedert and Jakes, 2005).

1.10.2 Tau amyloid fibrils

All six tau isoforms are found in NFTs in AD. The fibrils are therefore either formed by tau containing 3 MTBDs (3R tau) or 4 MTBDs (4R tau). AD tau fibrils can adopt two different overall filament structures: either paired helical filaments (PHFs) or straight filaments (SFs) (Kidd, 1963; Berriman *et al.*, 2003; Goedert and Jakes, 2005).

Cryo-EM studies of PHFs and SFs purified from *post mortem* AD brain revealed that the number of protofilaments as well as their arrangement can differ within the same sample. Although PHFs and SFs have the same protofilament fold, the protofilaments arrange differently to each other, changing the overall structure of the fibrils (Fitzpatrick *et al.*, 2017).

The protofilament core of AD fibrils encompasses MTBD 3 and 4, as well as a part of the C-terminus. This core contains 8 β-sheets, which arrange in a C-shaped form (Fitzpatrick et al., 2017). A similar protofilament fold has been observed for fibrils purified from *post mortem* brain of patients suffering from chronic traumatic encephalopathy (CTE) (Falcon *et al.*, 2019).

The β-fold for the 3R isoforms of AD and CTE fibrils starts at G273 or K274 and for the 4R isoforms it starts at G304 or S305. This fold then ends at E380 or R379. While the overall fold between AD and CTE fibrils appears similar, CTE fibrils show a cavity between β-sheet 4 and 6, where an additional density is located, most likely

representing a different type of molecule. This molecule is most probably of hydrophobic and non-proteinaceous nature (Figure 12) (Falcon *et al.*, 2019).

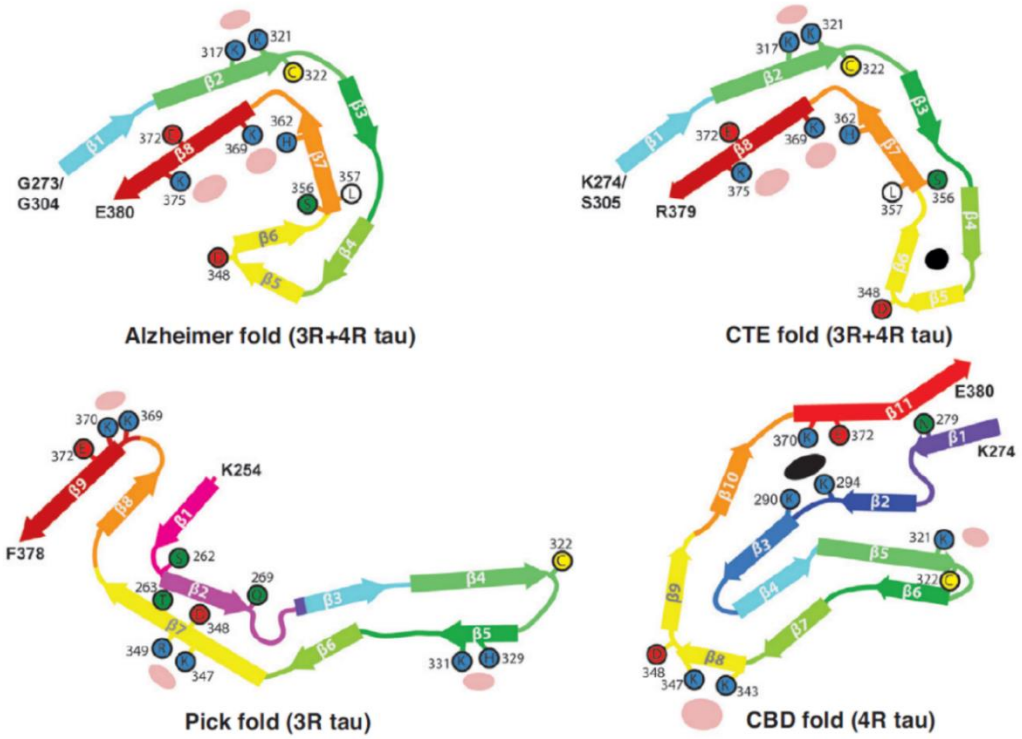

Figure 12 Schematic models of protofilament folds of tau fibrils of different diseases. The protofilament folds of AD and CTE, both formed by either 3R or 4R tau, appear very similar. The folds of PiD and CBD appear significantly different, with more β-sheets being included in the core (Scheres *et al.*, 2020).

In Pick's disease (PiD), which is a 3R tauopathy, not only MTBD 3 and 4 are part of the protofilament core, but also a short sequence of R1 (Falcon *et al.*, 2018). In the 4R tauopathy corticobasal degeneration (CBD), the protofilament core comprises MTBDs 3, 4 and parts of 2 (Zhang *et al.*, 2020).

The PiD and the CBD folds differ significantly from those observed in AD and CTE fibrils. In PiD, the protofilament core is formed by 9 β-sheets that arrange into a J-shaped fold, starting at K254 in R1 and ending at F378 in the C-terminal tail. CBD protofilaments adopt a four layered fold, formed by 11 β-sheets. The CBD fibril core ranges from K274 to E380 at the C-terminus (Falcon *et al.*, 2018; Zhang *et al.*, 2020). It is important to note that the structure of *in vitro* formed heparin induced fibrils differs significantly from the fibrils purified from *post mortem* material (Scheres *et al.*, 2020).

1.11 Transmission of α-Syn and Tau aggregates in neurodegenerative diseases

The spatial distribution of protein deposits involved in neurodegenerative diseases follows a disease-specific pattern (Peng, Trojanowski and Lee, 2020). In PD, α-syn aggregates are first found in the olfactory bulb and the brain stem. During disease progression, the pathology emerges via the midbrain to the cortex (Braak *et al.*, 2003). In AD, the tau pathology originates in the entorhinal region and spreads via the hippocampus to the neocortical region (Braak and Braak, 1991; Peng, Trojanowski and Lee, 2020).

One hypothesis that may explain the disease-specific pathology pattern is the cell-to-cell transmission of toxic protein aggregates between interconnected brain regions (Peng, Trojanowski and Lee, 2020). Strong evidence for the intercellular spread of α-syn aggregates comes from studies that observed the transmission of α-syn aggregates from diseased patient brain into healthy transplanted human fetal-brain-derived graft neurons (Kordower *et al.*, 2008).

The spread of protein aggregates can also be studied in animal models. Transgenic mice, expressing human A53T α-syn, as well as wt mice develop α-syn pathology upon injection of synucleinopathy patient brain homogenate, brain homogenate of diseased mice or *in vitro* formed α-syn fibrils (preformed fibrils, PFFs) (Luk *et al.*, 2012; Masuda-Suzukake *et al.*, 2013). Similar observations have been made in tau mouse models. Injection of patient brain material induces tau pathology in wt mice and *in vitro* formed tau fibrils result in tau aggregation in transgenic mice that express human P301L tau (Peeraer *et al.*, 2015; Guo *et al.*, 2016).

Protein aggregates that result in a templated misfolding of the endogenously expressed proteins are termed ‘seeds’ and the process of templated misfolding is referred to as ‘seeding’. Several hypotheses have been proposed regarding seed release and uptake (Peng, Trojanowski and Lee, 2020) (Figure 13).

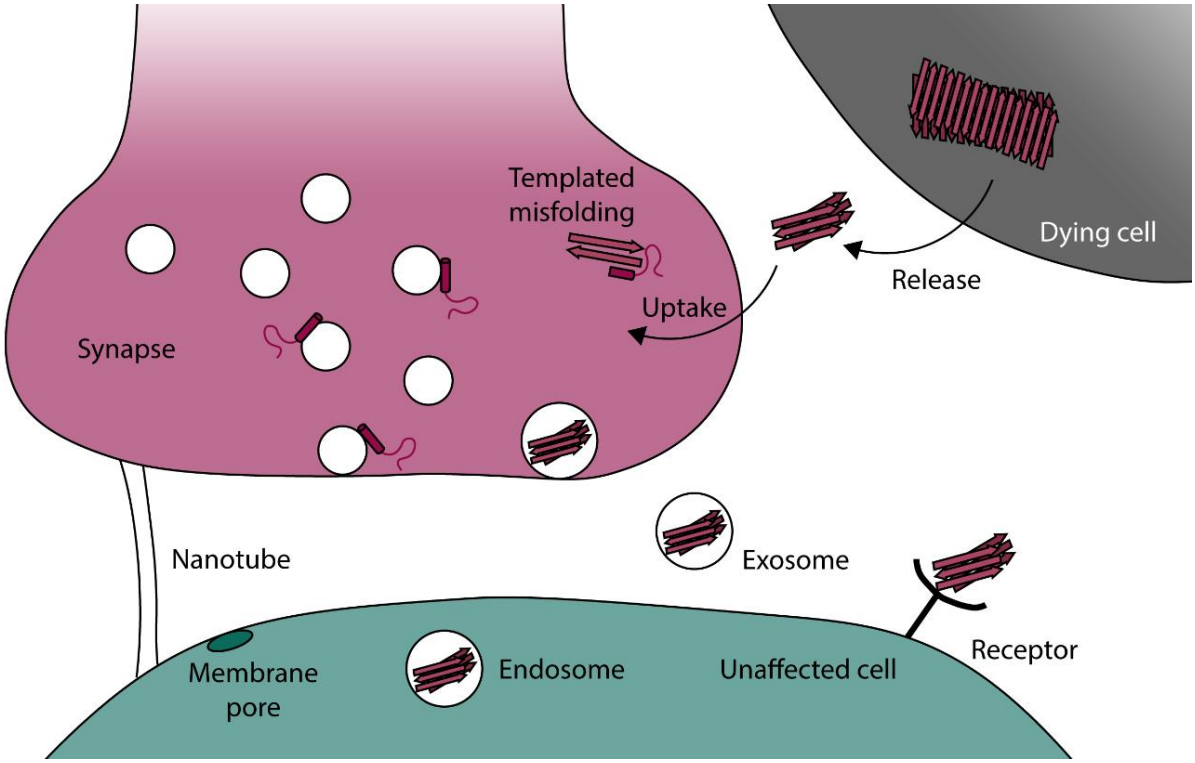

Figure 13 Schematic of various models of intercellular α-syn seeding. In healthy cells, α-syn is bound to membranes in the pre-synapse (pink cell). Upon uptake of seeds, templated misfolding takes place and aggregates form. Smaller aggregates can be transmitted to neighboring cells via nanotubes, exosomes / endosomes or receptor-mediated uptake (green cell). The release of seeds from dying cells has not been observed in patient brains so far (grey cell).

It is likely that α-syn and tau aggregates are released through exosomes, as the amount of exosomal α-syn and tau is significantly increased in PD and AD patients compared to healthy controls (Saman *et al.*, 2012; Shi *et al.*, 2014; Peng, Trojanowski and Lee, 2020). Interestingly, injection of exosomes purified from DLB patients results in α-syn seeding and aggregation in wt mice (Ngolab *et al.*, 2017; Peng, Trojanowski and Lee, 2020). A different hypothesis proposes that seeds are released by dying cells and subsequently diffuse through the extracellular space. However, no evidence in patient brain has been found so far that is supporting this idea (Peng, Trojanowski and Lee, 2020).

For α-syn seeds, dynamin-dependent endocytosis has been described as a general pathway of aggregate uptake (Hansen *et al.*, 2011; Grozdanov and Danzer, 2018). Additionally, heparan sulfate proteoglycan (HSPG)-mediated macropinocytosis mediates at least partially the uptake of α-syn as well as tau seeds. Incubation of cells

with heparin prior to seed addition prevents the seed uptake (Holmes *et al.*, 2013; Peng, Trojanowski and Lee, 2020). A third way of seed uptake, proposed by the Dawson group and colleagues, is receptor-mediated endocytosis of α-syn. They found that α-syn seeds are internalized into primary neurons after binding to the plasma membrane receptors APLP1 (Amyloid Precursor-Like Protein 1) and LAG3 (Lymphocyte Activation Gene 3) (Mao *et al.*, 2016; Zhang *et al.*, 2021). Later studies, however, failed to find any evidence for LAG3 expression in brain cells (Emmenegger *et al.*, 2021). To allow cellular release and uptake via the discussed pathways, the size of α-syn and tau seeds needs to be sufficiently small. This size constraint makes sonication and thereby fragmentation of PFFs crucial for *in vitro* seeding experiments (Volpicelli-Daley, Luk and Lee, 2014).

More evidence is accumulating that pathological seeds can occur in more than one conformation. Fibrils purified from *post mortem* brain material of different neurodegenerative diseases have distinct folds (Scheres *et al.*, 2020; Schweighauser *et al.*, 2020) and *in vitro* seeding experiments showed that the cerebrospinal fluid (CSF) of patients suffering from PD or MSA has disease-specific seeding properties, which propagate through several cycles of protein misfolding cyclic amplification (PMCA) reactions (Shahnawaz *et al.*, 2020). Notably, not only fibril structure (Long *et al.*, 2021), but also aggregate morphology is propagated in tau seeding experiments *in cellulo* and *in vivo* (Sanders *et al.*, 2014).

The different conformations of the protein seeds are termed ‘strains’ and the propagation of the conformation is considered as ‘prion-like’ (Peng, Trojanowski and Lee, 2020). However, not only the seed, but also the cell type seems to play an important role in the propagation of an aggregate strain: Peng *et al.* found that the cellular milieu of oligodendrocytes favors the conversion of α-syn aggregates into an MSA-like aggregate strain, whereas neurons were not able to convert aggregates into a PD-like strain (Peng *et al.*, 2018).

1.12 Effects of molecular chaperones on toxic protein aggregates

1.12.1 The effect of Clusterin on amyloid fibril formation and seeding

The multicellularity of higher eukaryotes creates a complex architecture of both, the cells themselves and the space between them - the extracellular space (ECS). The ECS is filled with extracellular fluid that contains metabolites, ions, proteins and molecules, such as neurotransmitters or hormones. To maintain proteostasis in the ECS, an extracellular chaperone network has evolved. One of the first extracellular chaperones that was discovered is Clusterin (Clu) that is also called ApoJ (Apolipoprotein J) (Michel *et al.*, 1997). To become a functional chaperone, translated Clu is cleaved into an α- and β-subunit, which are connected by disulfide bonds, and is subsequently translocated via the Golgi into the ECS (Collard and Griswold, 1987; De Silva *et al.*, 1990; Yuste-Checa, Bracher and Hartl, 2022). Various rare genetic mutations have been described that are affecting Clu secretion, alternative splicing and expression (Szymanski *et al.*, 2011; Bettens *et al.*, 2015; Padhy *et al.*, 2017).

Surprisingly, in 2009, the *CLU* gene was found in two independent GWAS as a risk gene for LOAD (Harold *et al.*, 2009; Lambert *et al.*, 2009). Biomarker studies hint towards a link between Clu and AD, as Clu levels are increased in the plasma of AD patients (Weinstein *et al.*, 2016). Additionally, Clu expression is upregulated in the hippocampus and cortex of AD patient brains (May *et al.*, 1990) and Clu was found to co-localize with Aβ plaques and tau aggregates (Calero *et al.*, 2000; Foster *et al*., 2019).

To understand the role of Clu in protein aggregation, several *in vitro* studies have been conducted. Clu can fulfill ATP-independent chaperone functions, similar to those of sHsps (Michel *et al.*, 1997; Poon *et al.*, 2000). Clu, as a holdase chaperone, can efficiently prevent the *de novo* aggregation of amyloid proteins, such as Aβ or α-syn at substoichiometric ratios (Yerbury *et al.*, 2007). Notably, the ratio of Clu and the

aggregating protein seems to be important. At Clu:substrate ratios of 1:10 or greater, Clu can directly interact with prefibrillar, oligomeric species, stop the ongoing aggregation and provide substantial cytoprotection (Yerbury *et al.*, 2007).

Additionally, a molar ratio of Clu:α-syn of 1:100 during a co-aggregation reaction reduces α-syn-induced permeabilization of lipid bilayers (Whiten *et al.*, 2018). Similar observations have been made *in cellulo*: Clu reduces the uptake of α-syn aggregates into mouse and human astrocytes, indicating a protective effect of Clu (Filippini *et al.*, 2021).

Clu has furthermore been linked to a decreased aggregate load of Aβ and tau in AD mouse models. Viral overexpression of Clu in APP/PS1 mice (transgenic *APP* KM670/671NL and *PSEN1* L116P) leads to a reduced accumulation of amyloid aggregates and subsequently reduced gliosis (Wojtas, Sens, *et al.*, 2020). Tau overexpression in *CLU*-knock out (KO) mice leads to a higher aggregate load compared to wt mice and results in anxiety-like behavior (Wojtas, Carlomagno, *et al.*, 2020).

Interestingly and also contrary to the studies discussed above, earlier studies observed a cytotoxic effect of Clu: Binding of Clu to synthetically produced $A\beta_{42}$ oligomers and their subsequent stabilization was found to increase the production of reactive oxygen species (ROS) in PC12 cells and decreased cellular viability (Oda *et al.*, 1995). Additionally, KO of Clu in PDAPP (transgenic *APP* V717F) mice was found to decrease the amount of fibrillar Aβ deposits (DeMattos *et al.*, 2002). The contradictory results may therefore point towards a Janus-faced effect of Clu on the emergence and progression of neurodegenerative diseases (Yuste-Checa, Bracher and Hartl, 2022).

1.12.2 Hsp70-mediated disaggregation of α-synuclein fibrils

Molecular chaperones do not only interact with aggregation-prone proteins to prevent their misfolding and aggregation. They are additionally involved in the active disaggregation of preexisting amyloid fibrils.

In vitro studies by the Bukau group reported an efficient fragmentation and depolymerization of α-syn fibrils by the Hsp70 machinery, which they reconstituted with Hsc70 (Heat Shock Cognate 71 kDa Protein, Hsp70), DnaJB1 (DnaJ Heat Shock

Protein Family Member B1, Hsp40) and Apg2 (Heat Shock 70-Related Protein APG-2, Hsp110, NEF) (Gao *et al.*, 2015). Notably, heat-inducible Hsp70 (*HSPA1A*) disaggregates amyloid fibrils less efficiently than the constitutively expressed Hsc70. They also found that Hsp110 has to be present in substoichiometric ratios, since a 1:1 ratio decreases chaperone activity relative to the substoichiometric regime (Duennwald, Echeverria and Shorter, 2012; Gao *et al.*, 2015). The ATP-dependent disaggregation reaction results in monomeric α-syn species that are less toxic to neuroblastoma cells than the original PFFs (Gao *et al.*, 2015).

In 2020, Wentink *et al.* described the mechanism of α-syn fibril disaggregation by the Hsp70 machinery in greater detail (Figure 14) (Wentink *et al.*, 2020).

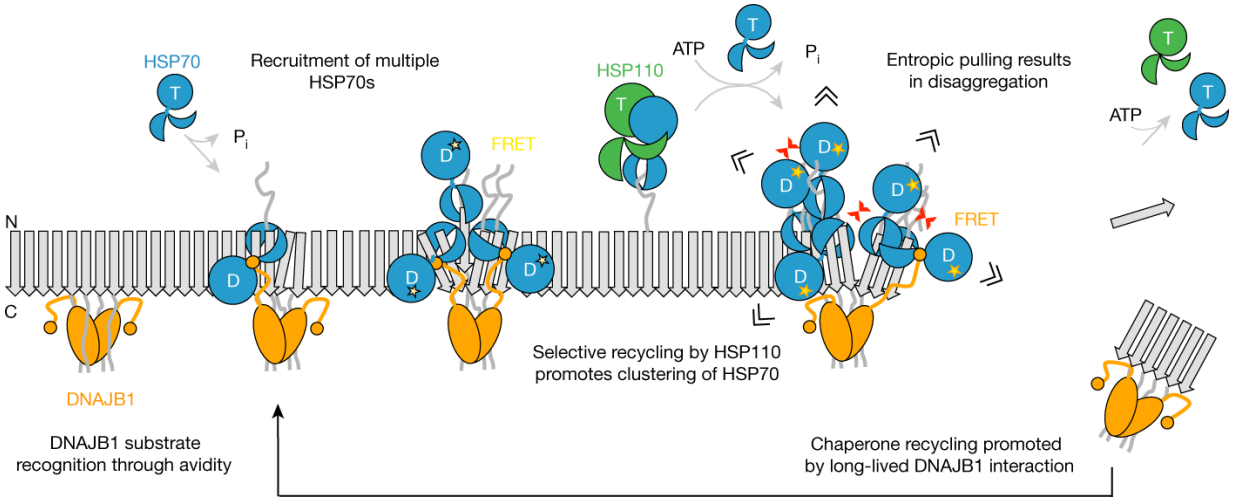

Figure 14 Schematic of α-syn fibril disaggregation by the Hsp70 chaperone machinery. DnaJB1 recognizes the C-terminus of α-syn. Hsp70 binds subsequently to DnaJB1 leading to molecular crowding. Finally, entropic forces result in the disaggregation of the α-syn fibril (Wentink *et al.*, 2020).

The authors found that DnaJB1 binds through multivalent interactions to the C-terminal region (aa 123-129) of α-syn, which is not part of the amyloid core, but sticks out of the fibril, forming a 'fuzzy coat'. In multiple recruitment cycles, DnaJB1 assists the binding of Hsp70 to the site of action. The high amount of bound Hsp70s leads to molecular crowding, which is energetically unfavorable. However, the high affinity of Hsp70 to DnaJB1 allows an increased accumulation of Hsp70 proteins. To avoid non-productive Hsp70 loading, Hsp110 performs rounds of selective reshuffling of Hsp70 proteins, which clusters more Hsp70s at the site of action. Eventually, the molecular

crowding becomes so high that entropic forces pull the α-syn subunits apart, resulting in amyloid fibril disaggregation (Wentink *et al.*, 2020).

1.12.3. AAA+ ATPase-mediated disaggregation of amyloid fibrils

One of the best studied protein disaggregases is the yeast Hsp104 complex (Sanchez and Lindquist, 1990). Hsp104 (in *E. coli*: ClpB, Caseinolytic peptidase B protein homolog) is a member of the homohexameric AAA+ ATPase family (Parsell *et al.*, 1994; Wendler *et al.*, 2009). The six monomers of the Hsp104 complex form a ring-like protein structure with an axial channel in the center. Hsp104 consists of an N-terminal domain (NTD), NBD1, a middle domain (MD), NBD2 and a C-terminal domain (CTD). Both NBDs contain Walker A and B motifs, which harbor an arginine finger that is required for ATP hydrolysis (Sweeny and Shorter, 2016).

During Hsp104-mediated disaggregation of amorphous or amyloid protein aggregates, ATP is hydrolyzed and a pulling force is generated on the polypeptide chain of the aggregated protein. The polypeptide chain is subsequently threaded through the chaperone's AAA+ ring resulting in a dissociation of aggregated protein assemblies (Wendler *et al.*, 2009).

Hsp104 works in close collaboration with the Hsp70/Hsp40 chaperone system in protozoans and bacteria. The complex is therefore termed the 'Hsp70/Hsp104 bi-chaperone machinery' (Mogk, Bukau and Kampinga, 2018).

Interestingly, Hsp104 governs the inheritance of a yeast strain's prion status. Hsp104 disassembles yeast prion fibrils, such as Sup35 fibrils, into smaller oligomers that serve as seeds for conformational replication (propagons) (Chernova, Wilkinson and Chernoff, 2017). If Hsp104 is inhibited, no seeding competent propagons are formed. This results in long 'dead end' fibers, which are diluted out during cell division. Over time, the yeast strain's prion status gets lost. At the same time, if an increased amount of Hsp104 is active on the prions, the fibrils will be disassembled into non-transmissible fragments, most likely monomers. This results, as well, in the loss of the yeast strain's prion status (Chernoff *et al.*, 1995).

Metazoan cells do not express Hsp104. However, other AAA+ ATPase proteins have been found to fulfil similar disaggregation functions: Previous studies showed that functional VCP (Vasolin Containing Protein, p97 and Cdc48 in *S. cerevisiae*) is

required to decrease abundance and size of cellular polyglutamine-(polyQ)-expanded huntingtin exon 1 aggregates in HeLa cells (Ghosh *et al.* 2018), and tau aggregates in human embryonic kidney cells (Darwich *et al.*, 2020).

VCP is, similar to Hsp104, a homohexameric protein complex, forming a ring-like structure with a central pore. The VCP monomer consists of three domains, an N-terminal domain (N-domain), and two ATPase domains (D1 and D2) (Wang, Song and Li, 2004). The N-domain is required to interact with cofactors and potential substrates. Upon ATP hydrolysis, a force is generated, which results in movement of the N-domain and substrate binding (Cooney *et al.*, 2019; Ferrari *et al.*, 2022).

One of the main functions of VCP is the extraction and segregation of ubiquitinated proteins from protein complexes and membranes, resulting in their subsequent degradation by the proteasome (Stolz *et al.*, 2011). The binding of VCP to the ubiquitinated substrate protein may occur through adaptor proteins. More than 30 different co-factors of VCP have been identified, which modulate VCP function (Meyer and Weihl, 2014). Among these cofactors are the proteins Ufd1 (Ubiquitin fusion degradation protein 1 homolog) and Npl4 (Nuclear protein localization protein 4 homolog), various UBX (ubiquitin X regulatory)-domain containing proteins, ubiquitin ligases and deubiquitinating enzymes (Ferrari *et al.*, 2022).

VCP fulfils additional functions in various PQC pathways, such as ER-associated degradation (ERAD) (Stolz *et al.*, 2011; Meyer and Weihl, 2014), mitochondria-associated degradation (MAD) (Heo *et al.*, 2010) and ribosome-associated degradation (RAD) (Verma *et al.*, 2013; Ferrari *et al.*, 2022). Unsurprisingly, *VCP* gene mutations are linked to protein misfolding diseases, such as AD, PD, multisystem proteinopathies (MSPs), inclusion bodies myopathy Paget disease and frontotemporal dementia (IBMPFD) and frontotemporal degeneration (FTD) (Tang and Xia, 2016; Darwich *et al.*, 2020).

2 Publications

2.1 Publication 1: The extracellular chaperone Clusterin enhances Tau aggregate seeding in a cellular model

Aim and key results of the study:

The extracellular chaperone Clu has been identified as a risk factor for LOAD. It was therefore of interest to study the effect of Clu on the formation of amyloid aggregates of proteins involved in AD.

To investigate the effect of Clu on *de novo* aggregation of tau and α-syn, we added Clu to *in vitro* aggregation reactions. For both, tau and α-syn, Clu delayed the aggregation. Next, we sought to test the effect of Clu on seeded aggregation and applied the co-aggregated tau/Clu and α-syn/Clu fibrils to reporter cell lines, expressing fluorescently tagged tau and α-syn. Interestingly, while α-syn/Clu fibrils showed a decreased seeding property compared to α-syn fibrils alone, tau/Clu fibrils showed a reversed effect: seeding with tau fibrils that were co-aggregated with Clu resulted in an increased amount of aggregate formation within cells compared to seeding with tau fibrils alone.

Upon further biochemical and biophysical characterization of the seeds, we found that Clu stabilizes soluble, highly seeding competent tau species, which enter the cell via endocytosis. The seeds subsequently compromise the endolysosomal system and enter the cytoplasm, where seeded aggregation of the endogenously expressed tau monomers occurs.

Contribution:

V.A.T. conducted α-syn experiments, including protein purification and fibrilization of α-syn as well as membrane retention assays, cell-biological work, generation of stable human neuroblastoma and embryonic kidney cell lines, seeding experiments, analyses by fluorescence microscopy and the quantification of the images, as well as negative stain electron microscopy experiments.

nature COMMUNICATIONS

ARTICLE

https://doi.org/10.1038/s41467-021-25060-1 OPEN

The extracellular chaperone Clusterin enhances Tau aggregate seeding in a cellular model

Patricia Yuste-Checa[1,2], Victoria A. Trinkaus[1,2,3], Irene Riera-Tur[4,5], Rahmi Imamoglu[1], Theresa F. Schaller[1,6], Huping Wang[1], Irina Dudanova[4,5], Mark S. Hipp[1,7,8], Andreas Bracher[1] & F. Ulrich Hartl[1,2,3]✉

Spreading of aggregate pathology across brain regions acts as a driver of disease progression in Tau-related neurodegeneration, including Alzheimer's disease (AD) and frontotemporal dementia. Aggregate seeds released from affected cells are internalized by naïve cells and induce the prion-like templating of soluble Tau into neurotoxic aggregates. Here we show in a cellular model system and in neurons that Clusterin, an abundant extracellular chaperone, strongly enhances Tau aggregate seeding. Upon interaction with Tau aggregates, Clusterin stabilizes highly potent, soluble seed species. Tau/Clusterin complexes enter recipient cells via endocytosis and compromise the endolysosomal compartment, allowing transfer to the cytosol where they propagate aggregation of endogenous Tau. Thus, upregulation of Clusterin, as observed in AD patients, may enhance Tau seeding and possibly accelerate the spreading of Tau pathology.

[1] Department of Cellular Biochemistry, Max Planck Institute of Biochemistry, Martinsried, Germany. [2] Aligning Science Across Parkinson's (ASAP) Collaborative Research Network, Chevy Chase, MD, USA. [3] Munich Cluster for Systems Neurology (SyNergy), Munich, Germany. [4] Department of Molecules—Signaling—Development, Max Planck Institute of Neurobiology, Martinsried, Germany. [5] Molecular Neurodegeneration Group, Max Planck Institute of Neurobiology, Martinsried, Germany. [6] Present address: Institute for Molecular Medicine, University Medical Center of the Johannes Gutenberg-University Mainz, Mainz, Germany. [7] Present address: Department of Biomedical Sciences of Cells and Systems, University Medical Center Groningen, University of Groningen, Groningen, The Netherlands. [8] Present address: School of Medicine and Health Sciences, Carl von Ossietzky University Oldenburg, Oldenburg, Germany. ✉email: uhartl@biochem.mpg.de

Progression of several neurodegenerative diseases, prominently including tauopathies such as frontotemporal dementia (FTD) and Alzheimer's disease (AD), is driven by the spreading of aggregate pathology across brain regions in a prion-like seeding mechanism[1–5]. Tau aggregate spreading involves the exposure of aggregate seeds to the extracellular milieu[6,7], suggesting that extracellular protein quality control factors may modulate disease progression[8]. Clusterin (Clu; apolipoprotein J) is a ~70 kDa glycoprotein with chaperone-like properties found abundantly in plasma and extracellular fluid[8–10]. During its passage through the secretory pathway, immature Clu is extensively N-glycosylated and cleaved into α and β-chains, which remain linked by disulfide bonds (Supplementary Fig. 1a). Although mainly a secreted chaperone, Clu is also found intracellularly under stress conditions[9]. Clu stabilizes unfolded proteins against aggregation and can inhibit fibril formation of amyloid β (Aβ) and other amyloidogenic proteins in vitro, consistent with the function of an ATP-independent "holdase" chaperone[10–15].

The *CLU* gene ranks third among genetic risk factors for late-onset AD[16,17]. However, the mechanism by which Clu modulates AD pathology remains unclear, as Clu has been associated with both neuroprotective and neurotoxic effects in AD[15,18–25]. Clu protein expression is upregulated in AD patient brain and cerebrospinal fluid[26,27], localizing with Aβ deposits in senile plaques[28–30]. Evidence has been presented that Clu can mediate uptake of Aβ by microglia via the endosomal pathway and is involved in clearance of Aβ via the blood-brain barrier[31–33]. On the other hand, enhancement of Aβ toxicity by Clu has also been reported[24,25] and elevated plasma levels of Clu were found to be associated with rapid progression of AD, suggesting that Clu could be a driver of pathology[34,35]. Little is known about the possible role of Clu in the progression of Tau pathology, which strongly correlates with the severity of AD[36–38]. Interestingly, Clu was identified as an interactor of soluble Tau in AD brain[39]. More recently, it was shown that Clu also colocalizes with intracellular Tau aggregates and may provide a protective function by inhibiting fibril formation[40]. Given the predominant role of extracellular Clu as the chaperone active form, it remains to be understood whether Clu modulates transcellular Tau seeding and influences overall pathology.

Here we analyzed the effect of Clu on the seeding competence of Tau aggregates formed in vitro and in cells. Our results show that Clu can strongly enhance Tau aggregate propagation by binding and stabilizing seeding active Tau species for cellular uptake. Thus, upregulation of Clu in AD has the potential to accelerate disease progression by enhancing the seeding competence of Tau aggregates.

Results

Clusterin potentiates seeding of Tau aggregates. To test whether Clu interferes with aggregate seeding of Tau,[10,14], we purified chaperone-active Clu upon recombinant expression in HEK293-EBNA cells (Supplementary Fig. 1b, c). We measured aggregate seeding with TauRD-YT cells, a HEK293T cell line stably co-expressing the repeat domain of Tau (TauRD; residues 244-372 with FTD mutations P301L/V337M) fused to YFP or mTurquoise2, whose co-aggregation during fibril formation results in fluorescence resonance energy transfer (FRET)[41] (Fig. 1a). Seed aggregates were generated with recombinant, cysteine-free TauRD (Tau residues 244-371, C291A/P301L/C322A/V337M) to avoid the use of reducing agents that might interfere with Clu function. Mutation of the two cysteines in TauRD avoids the formation of intramolecular disulfide bonds that slows fibril formation[42]. Lipofectamine was used to render seed uptake independent of cellular machinery for internalization. The TauRD is critical for aggregation and forms the core of Tau fibrils[43,44].

TauRD rapidly formed thioflavin T (ThT)-positive fibrillar aggregates in vitro, induced by heparin[45] (Fig. 1b, Supplementary Fig. 2a). The addition of Clu at an equimolar ratio to TauRD extended the lag phase and slowed fibril elongation[46,47] but did not prevent fibril formation (Fig. 1b, Supplementary Fig. 2a). To observe seeding, we next transferred small quantities of TauRD (0.05 ng to 14 ng with lipofectamine) after different times of in vitro aggregation to TauRD-YT cells, followed by an analysis of endogenous aggregate formation by flow cytometry of FRET positive cells and fluorescence microscopy (Fig. 1a, c, d, Supplementary Fig. 2b). Seeding competent TauRD accumulated with kinetics similar to the formation of ThT-positive aggregates (Fig. 1b, c). The presence of Clu in the aggregation reaction delayed the appearance of seed material (0% FRET positive cells after 1 h aggregation time, Fig. 1c, d). However, once ThT-positive aggregates formed (from 2 h on, Fig. 1b), the Clu-containing aggregation reaction surprisingly presented a markedly increased seeding potency resulting in ~80% FRET-positive cells (exceeding the linear range of the assay) compared to ~30% FRET-positive cells with TauRD aggregates alone (Fig. 1c, d, Supplementary Fig. 2b). When aggregation reactions were diluted 280-fold, seeding without Clu was virtually abolished, but was still measurable in the presence of Clu, resulting in ~25% of aggregate containing cells (Fig. 1c). Again, the kinetics of seed formation correlated with the delayed formation of ThT-positive aggregates (Fig. 1b, c). The FRET-positive inclusions formed in cells with and without Clu were morphologically similar and stained with the amyloid dye X34 (Fig. 1d, Supplementary Fig. 2c). Clu alone neither formed ThT-positive species nor induced Tau aggregation when added to cells (Supplementary Fig. 2d). Titration experiments using seed material from the plateau phase of aggregation (Fig. 1b) showed that Clu increased seeding potency ~25-fold (defined as % FRET-positive cells/ng TauRD) (Fig. 1e, Supplementary Fig. 2e). To test the effect of Clu on seeding in cells with the unperturbed plasma membrane, we omitted the transfection reagent. Under these conditions, Clu still increased the seeding potency of TauRD aggregates approximately eightfold (Supplementary Fig. 3). However, as expected, higher amounts of TauRD and TauRD/Clu aggregates were necessary to observe aggregate seeding.

The effect of Clu on TauRD aggregation and seeding is concentration-dependent, since increasing the ratio of Clu relative to TauRD further delayed amyloid formation in vitro and increased seeding potency (Supplementary Fig. 4a, b). However, the effect on seeding potency is saturated at a 1:1 molar ratio of TauRD:Clu (Supplementary Fig. 4b).

As TauRD is a highly charged protein (21 positively and 10 negatively charged amino acids), we tested whether the effect of Clu on TauRD seeding is dependent on electrostatic interactions. TauRD and TauRD/Clu aggregates (Fig. 1a) were incubated with PBS or high salt buffer (PBS/500 mM NaCl) prior to addition to TauRD-YT cells. Incubation with high salt buffer resulted in a general increase in seeding (Supplementary Fig. 4c), suggesting that high ionic strength may stabilize seeding competent TauRD species. Importantly, Clu increased seeding potency both in PBS and in the high salt buffer (Supplementary Fig. 4c), consistent with hydrophobic forces playing a role in the Clu-TauRD interaction.

In order to test the effect of Clu on preformed Tau aggregates, Clu was added to the aggregation reaction once the ThT plateau was reached (at 1 h or 24 h after initiating aggregation, Supplementary Fig. 4d). When added at an equimolar ratio to TauRD aggregates, Clu amplified seeding competence ~3–4-fold

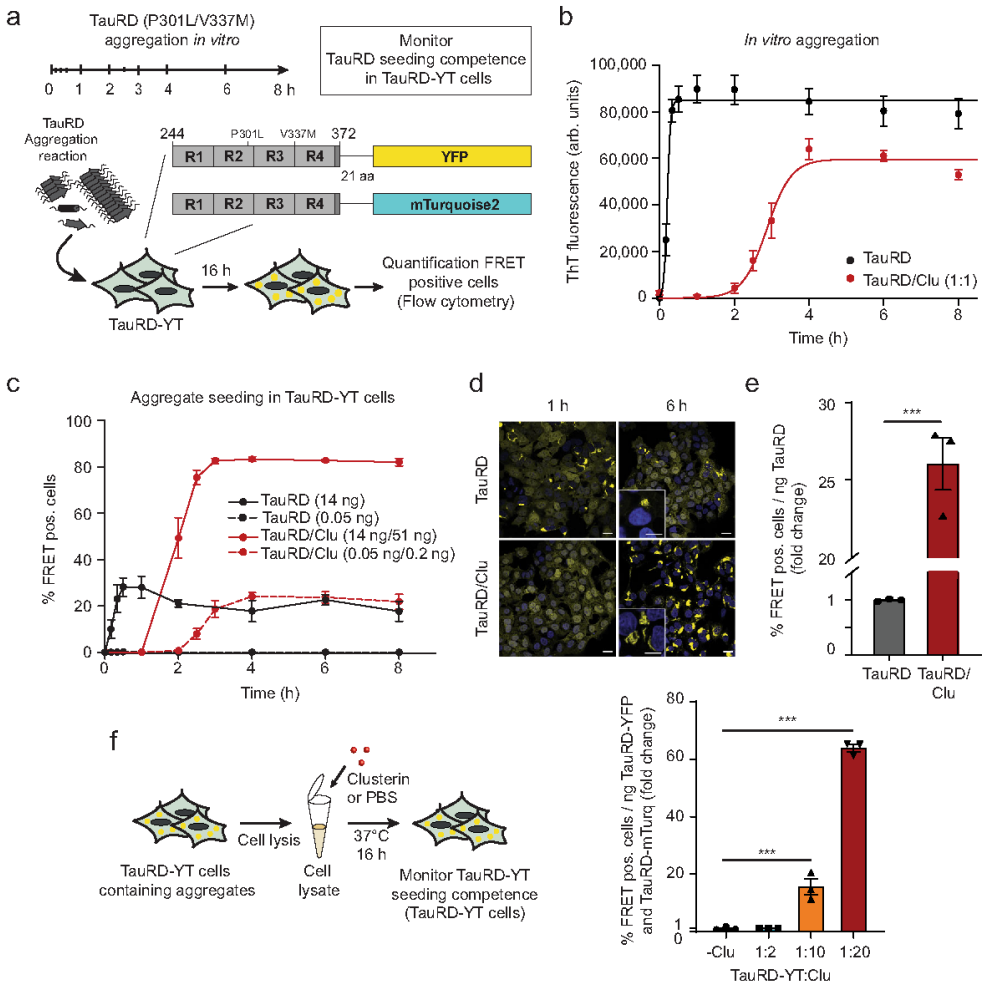

Fig. 1 Clusterin potentiates seeding of Tau aggregates. a Workflow of the seeding experiment. At the times indicated, samples were removed from TauRD aggregation reactions with or without Clu, and added with or without transfection reagent (lipofectamine) to reporter cells co-expressing TauRD fused to the FRET pair of YFP and mTurquoise2 (TauRD-YT). The fraction of cells containing FRET-positive (pos.) aggregates was quantified by flow cytometry. **b** TauRD amyloid formation in aggregation reactions of 10 µM TauRD without (black) or with equimolar Clu (red) as monitored by ThT fluorescence. Averages ± SEM ($n = 10$ independent experiments). arb.units, arbitrary units. **c** Effect of Clu on the formation of seeds that induce aggregation of endogenous TauRD in cells. Seed formation was analyzed as described in (**a**). Reporter cells were transfected with aggregation reactions containing 14 ng (solid lines) or 0.05 ng (dashed lines) TauRD and 51 ng (solid lines) or 0.2 ng (dashed lines) Clu, respectively (molar ratio Clu:TauRD 1:1). Averages ± SEM ($n = 3$ independent experiments). **d** Representative fluorescence microscopy images of TauRD-YT cells seeded with TauRD (14 ng TauRD) from the plateau phase of aggregation (TauRD, 1 h reaction time; TauRD/Clu, 6 h reaction time (**b**)). TauRD-YFP and DAPI nuclear staining signals are shown in yellow and blue, respectively. Scale bars, 20 µm for overview panels and 10 µm for insets. **e** Fold change of seeding potency of TauRD aggregation reactions containing Clu (red) compared to control reactions without Clu (gray). Bar graphs represent the average slope ± SEM ($n = 3$ independent experiments) from the linear regression analyses described in Supplementary Fig. 2e. $^{***}p < 0.001$ ($p = 1.2 \times 10^{-4}$) by two-tailed Student's t-test. **f** Effect of Clu on seeding potency of TauRD-YT cell lysates containing TauRD-YT aggregates. Whole-cell lysates of FRET-positive (pos.) TauRD-YT cells were incubated with or without Clu. Fold change of TauRD seeding potency expressed per ng of TauRD-YT in cell lysates upon treatment with increasing Clu (molar ratios TauRD-YT:Clu 1:2, 1:10 and 1:20). Bar graphs represent the average slope ± SEM ($n = 3$ independent experiments) from the linear regression analyses shown in Supplementary Fig. 4e. $^{***}p < 0.001$ (-Clu vs. TauRD-YT:Clu 1:10 $p = 8 \times 10^{-4}$; -Clu vs. TauRD-YT:Clu 1:20 $p = 1.1 \times 10^{-8}$) by one-way ANOVA with Bonferroni post hoc test.

(Supplementary Fig. 4d), similar to when present during aggregation (Fig. 1c). Thus, Clu may act on preexistent fibrils or on aggregate species present in equilibrium.

The use of heparin in seed production results in a non-physiological conformation of Tau fibrils[44]. To exclude that the observed effect on TauRD seeding is dependent on heparin, we, therefore, investigated the effect of Clu on seeding by TauRD aggregates produced in cells. Cells were lysed under mild conditions in the presence of non-ionic detergent (0.05% Triton X-100) without sonication to preserve the structural properties of the aggregates. Lysates from TauRD-YT cells containing aggregates were incubated with increasing concentrations of Clu

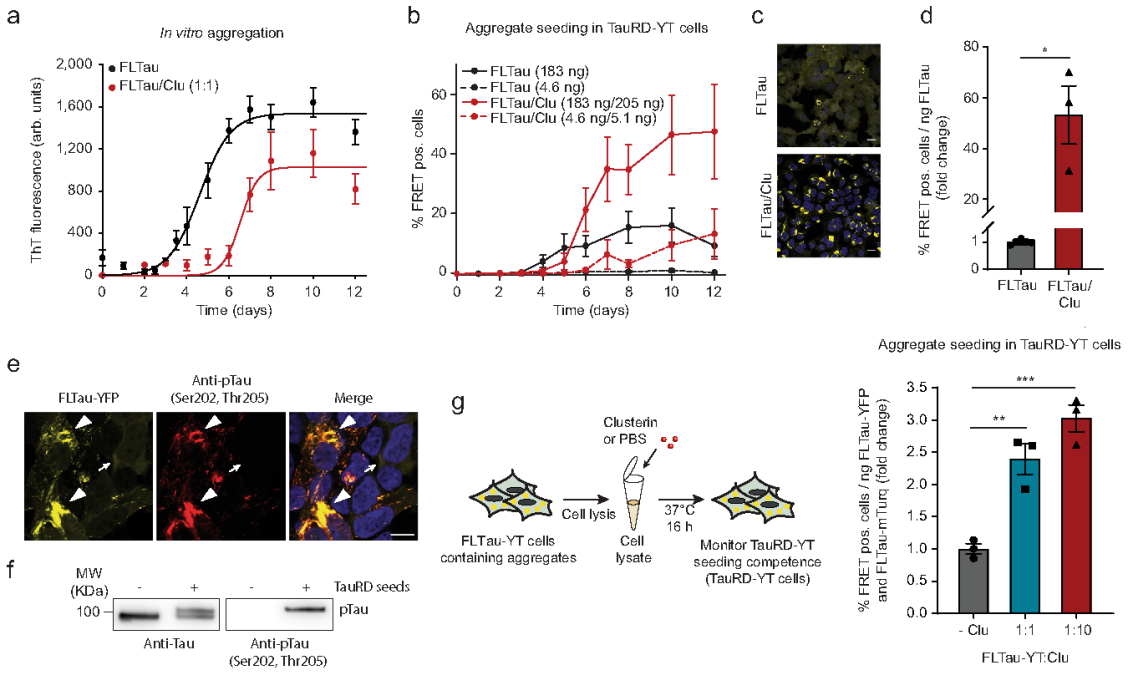

Fig. 2 Clusterin enhances the seeding potency of FLTau aggregates. a Effect of Clu on the kinetics of aggregation of full-length (FL) Tau (10 μM) monitored by ThT fluorescence. FLTau/Clu molar ratio was 1:1. Averages ± SEM ($n = 5$ independent experiments). arb.units, arbitrary units. **b** Formation of seeds in FLTau aggregation reactions without (black) or with Clu (10 μM, red) as described in (**a**). Reporter cells were transfected with aggregation reactions containing 183 ng (solid lines) or 4.6 ng (dashed lines) FLTau and 205 ng (solid lines) or 5.1 ng (dashed lines) Clu, respectively (molar ratio Clu: FLTau 1:1). Averages ± SEM ($n = 3$ independent experiments). **c** Representative fluorescence microscopy images of TauRD-YT cells seeded with FLTau aggregation reactions (183 ng FLTau) after reaching the plateau of aggregation (10 days, (**a**)). TauRD-YFP and DAPI nuclear staining signals are shown in yellow and blue, respectively. Scale bars, 20 μm. **d** Fold change of seeding potency of FLTau aggregation reactions containing Clu (red) compared to control reactions without Clu (gray). Bar graphs represent the average slope ± SEM ($n = 3$ independent experiments) from the linear regression analyses described in Supplementary Fig. 5a. $^{*}p < 0.05$ ($p = 0.0106$) by two-tailed Student's *t*-test. Lipofectamine was used as a transfection reagent. **e**, **f** Seeded aggregates of FLTau-YT contain phospho-Tau. ($n = 3$ independent experiments) **e** Fluorescence microscopy images of FLTau-YT cells seeded with TauRD aggregates. FLTau-YFP and immunostaining of phospho-Tau (pTau, AT8 antibody) are shown in yellow and red, respectively. The AT8 antibody recognizes Tau phosphorylation at both serine 202 and threonine 205 and is widely used to detect Tau paired helical fibrils[36,49]. DAPI nuclear staining signal is additionally shown in blue in the merge. Arrowheads indicate aggregates. The small arrow indicates a cell without aggregates. Scale bar, 10 μm. **f** Representative immunoblot analysis showing Tau (Tau/Repeat Domain antibody) and phospho-Tau (pTau, AT8 antibody) in FLTau-YT cell lysates from cells treated with or without TauRD seeds. Molecular weight (MW) standards are indicated. **g** Clu enhances the seeding potency of FLTau aggregates formed in FLTau-YT cells. Whole-cell lysates of FRET-positive (pos.) FLTau-YT cells were incubated without or with Clu (molar ratios FLTau-YT:Clu 1:1 and 1:10). Bar graphs represent the average slope ± SEM from the linear regression analyses described in Supplementary Fig. 5e. Data represent the mean ± SEM ($n = 3$ independent experiments). $^{**}p < 0.01$ (−Clu vs. FLTau-YT:Clu 1:1 $p = 0.0058$); $^{***}p < 0.001$ (−Clu vs. FLTau-YT:Clu 1:10 $p = 7.9 \times 10^{-4}$) by one-way ANOVA with Bonferroni post hoc test. Lipofectamine was used as a transfection reagent.

(Fig. 1f). A strong increase in seeding potency (up to ~60-fold) was observed upon Clu addition (Fig. 1f and Supplementary Fig. 4e). In this case, higher amounts of Clu relative to TauRD (up to ~20-fold excess) were effective, presumably due to lysate proteins competing for Clu binding with the aggregates.

To exclude the possibility that our findings are limited to the isolated repeat domain of Tau, we next performed experiments with full-length Tau (FLTau 2N4R) aggregates as seeds in cells expressing either TauRD or FLTau FRET constructs. As expected, in vitro amyloid formation of FLTau was slow[42] ($t_{1/2} \sim 4.6$ days, Fig. 2a) and was further delayed in the presence of Clu ($t_{1/2} \sim 6.6$ days, Fig. 2a). Clu dramatically enhanced (~55-fold) the potency of FLTau aggregates to seed TauRD-YT aggregates (Fig. 2b–d and Supplementary Fig. 5a). An even greater potentiation of FLTau seeds (~100-fold) was observed with cells stably co-expressing FLTau (P301L/V337M) fusion proteins with YFP or mTurquoise2 (FLTau-YT cells), forming FLTau aggregates (Supplementary Fig. 5b–d).

As Tau aggregates in the patient brain typically contain highly phosphorylated Tau[48], we also tested the effect of Clu using cell lysates containing phosphorylated FLTau-YT aggregates as seeds[36,49] (Fig. 2e–g and Supplementary Fig. 5e). Phosphorylated FLTau-YT aggregates were obtained by seeding naïve FLTau-YT cells with TauRD aggregates formed in vitro (Fig. 1b). Phosphorylation of the resulting aggregates was confirmed by the AT8 antibody[36,49] (Fig. 2e, f). Clu enhanced the seeding competence of these phospho-Tau aggregates up to threefold (Fig. 2g and Supplementary Fig. 5e). The lower effect of Clu on the seeding potency of cellular FLTau aggregates compared to TauRD aggregates (Figs. 1f and 2g) may be due to the "fuzzy coat" around the core of FLTau fibrils[50], which may limit Clu binding, or to differential posttranslational modifications, including phosphorylation.

Physical interaction between Clu and phospho-FLTau containing aggregates was confirmed by co-immunoprecipitation using the AT8 antibody (Supplementary Fig. 5f). However, the AT8 antibody also precipitated unmodified, apparently co-aggregated FL-Tau and thus a direct interaction of Clu with phospho-Tau remains to be demonstrated.

In summary, Clu robustly enhances the potency of TauRD and FLTau aggregates to seed aggregation in cells expressing TauRD or FLTau. This effect is independent of whether Clu is present during initial aggregation or added to preformed aggregates produced in vitro or in cells.

Clusterin stabilizes oligomeric Tau seeds. To biochemically characterize the seeding competent TauRD species, we fractionated the in vitro aggregation reaction by centrifugation. In the absence of Clu, aggregated TauRD was apparently insoluble after 1 h of aggregation (Fig. 3a, upper panel). When increasing amounts of the supernatant fraction (×10, ×20, ×30 the amount loaded in the upper panel) (Fig. 3a, lower panel) were analyzed, we found ~1.5% of total TauRD to be soluble. The amount of soluble TauRD increased to ~14% of the total in the presence of equimolar Clu (Fig. 3a, lower panel). Approximately 13% of Clu was recovered in the pellet fraction (Fig. 3a, upper panel), suggesting a weak association with insoluble fibrils. The seeding competence of the soluble and insoluble TauRD was compared by measuring the fraction of FRET positive cells per ng of TauRD in the seed material as determined by quantitative immunoblotting (Fig. 3a). The soluble fraction of the aggregation reaction had a much higher specific seeding capacity in the cellular assay than the resuspended pellet (Fig. 3b), indicating that soluble TauRD species are more seeding competent[51,52]. Notably, the specific seeding activity of the Clu-containing supernatant was ~40-fold higher than that in the absence of Clu (Fig. 3b), suggesting that Clu not only increased the amount of soluble TauRD aggregates but also enhanced their intrinsic seeding activity. To test this possibility directly, we added Clu to the seeding-active, soluble fraction of a TauRD aggregation reaction generated in the absence of Clu. This resulted in an approximately fivefold increase in seeding capacity (Fig. 3c). Thus, Clu not only increases the amount of soluble TauRD seeds when present during aggregation but also enhances the intrinsic seeding activity of preexisting, soluble TauRD species.

The addition of Clu 6 h after initiating TauRD aggregation still produced a small, but detectable amount of soluble TauRD (Supplementary Fig. 6a), in line with enhanced seeding when Clu is added to preformed aggregates (Fig. 1f, Fig. 2g, and Supplementary Fig. 4d). Surprisingly, a small amount of soluble TauRD was also generated when Clu was added to the resuspended pellet fraction (Supplementary Fig. 6b). In both cases, ~4–5% of total Clu is associated with the insoluble TauRD aggregates (Supplementary Fig. 6a–c). Thus, Clu binding to preexistent, insoluble TauRD aggregates generates seeding competent, soluble TauRD.

To determine when during the aggregation reaction Clu interacts with TauRD, we utilized dual-color fluorescence cross-correlation spectroscopy (dcFCCS). To this end, we generated the cysteine mutant I260C in otherwise cysteine-free TauRD and labeled the protein with Alexa Fluor 532 (TauRD-A532). Residue 260 is situated outside the fibril core[44,53]. Both Clu chains were labeled N-terminally with Alexa Fluor 647 (Clu-A647). Labeled TauRD at 1 μM was added to an aggregation reaction of unlabeled TauRD (9 μM). Labeling did not substantially affect aggregation kinetics or seeding properties of the resulting aggregates (Supplementary Fig. 7a, b, labeled TauRD; Fig. 1b, c, unlabeled TauRD) and labeled Clu (1.25 μM) enhanced seeding to a similar extent as observed with the unlabeled proteins (Supplementary Fig. 7b, labeled proteins; Supplementary Fig. 4b, unlabeled proteins; TauRD:Clu 8:1). A clear fluorescence cross-correlation signal between TauRD-A532 and Clu-A647 was only detectable at 1.5–2 h after initiation of aggregation (Fig. 3d), when ThT-positive and seeding competent TauRD species had formed (Fig. 3e). Apparently, Clu does not bind to monomeric TauRD but interacts with TauRD aggregates. Based on their diffusion time (~16.5 ± 1.3 ms; Supplementary Fig. 7c), the TauRD/Clu complexes formed are on average ~5000 kDa in size, equivalent to Clu bound to TauRD fibrils comprising ~300 TauRD units.

To characterize the interaction of Clu with the soluble, highly seeding competent TauRD, we next measured the FCCS signal between Clu-A647 and TauRD-A532 in the soluble fraction of aggregation reactions. Clu did not interact with monomeric TauRD (0 h; Fig. 3f), but strong interaction with soluble TauRD was detected after aggregation had reached the plateau phase (6 h; Fig. 3f, Supplementary Fig. 7a). The average size of the soluble TauRD/Clu complexes was ~320 kDa (diffusion time ~4.95 ± 0.19 ms; Supplementary Fig. 7c), consistent with one or more Clu stabilizing small TauRD oligomers. The interaction between Clu and TauRD is dynamic, as the FCCS signal was rapidly reduced upon the addition of excess unlabeled Clu (Supplementary Fig. 7d, e). Together these data show that Clu binds and stabilizes soluble Tau oligomers, either when present during ongoing aggregation or when added to preexistent aggregates. These soluble species are highly competent for cellular uptake and seeding of endogenous aggregation.

Seeding competent Tau/Clu species enter cells by endocytosis. To test whether cells incorporate TauRD/Clu seeds by endocytosis, as described for Tau alone[54–58], we incubated TauRD-YT cells during seeding with Bafilomycin, an inhibitor of the lysosomal H^+ ATPase[59], or leucyl-leucyl-O-methylester (LLOME), an agent that accumulates in acidic membrane compartments inducing their rupture[60]. A reduced amount of Tau/Clu aggregates compared to TauRD aggregates was applied to the TauRD-YT cells in order to obtain comparable seeding efficiencies. Both compounds increased seeding by TauRD and TauRD/Clu aggregates (in the absence of transfection reagent) to a similar extent and in a concentration-dependent manner (Fig. 4a, b). Thus, seed internalization occurs via endocytosis, with a fraction of seed material presumably undergoing lysosomal degradation in the absence of Bafilomycin or LLOME.

Heparan sulfate proteoglycans (HSPGs) are involved in cell surface binding and internalization of Tau seeds[61], as well as in the clearance of aberrant extracellular proteins mediated by Clu[31]. To test the role of this internalization mechanism in Tau/Clu seed uptake, TauRD-YT cells were incubated with increasing concentrations of heparin, an HSPG blocker, and treated with Tau aggregates formed in the presence or absence of Clu. In both cases the number of FRET positive cells strongly decreased in a manner dependent on heparin concentration (Fig. 4c), suggesting that TauRD and TauRD/Clu aggregates are internalized via HSPGs. We next investigated whether Clu and TauRD seeds enter cells together. To this end, we incubated HEK293T cells stably expressing TauRD (P301L/V337M)-mTurquoise2 (TauRD-T cells) with fluorescence-labeled soluble TauRD-A532/Clu-A647 seeds (Supplementary Fig. 7a, b) for 24 h. Clu-A647 and TauRD-A532 entered the cells as a complex (Fig. 4d–g and Supplementary Fig. 8) and in several cases co-localized with CHMP2a (Fig. 4d and Supplementary Fig. 8a), a subunit of the endosomal sorting complexes required for transport (ESCRT) machinery[62]. Some seed material also co-localized with the

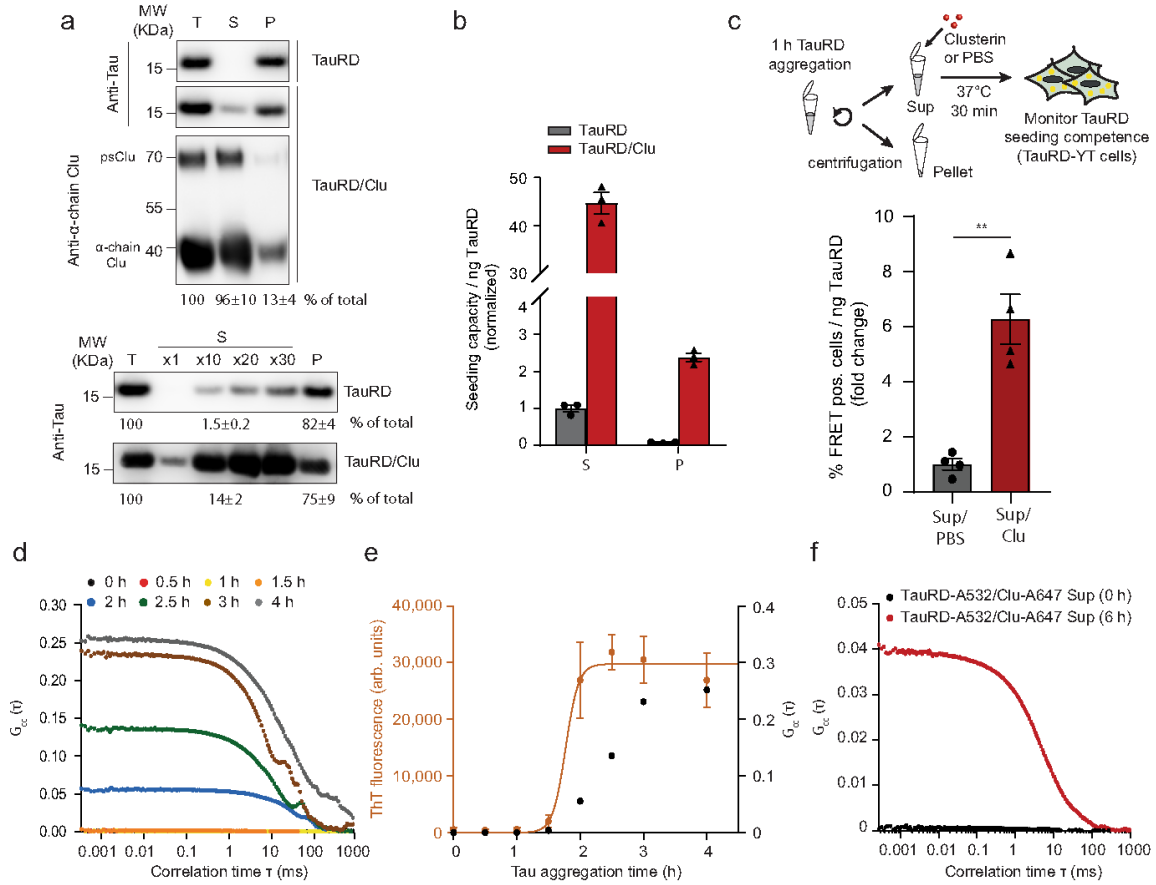

Fig. 3 Clusterin binds to aggregates and stabilizes oligomeric Tau seeds. a Fractionation by sedimentation of TauRD aggregation reactions without or with Clu (TauRD/Clu). Representative immunoblots of total (T), supernatant (S), and pellet (P) fractions. The small amount of soluble TauRD was visualized and quantified by analyzing increasing amounts of the supernatant fraction (lower panel, ×10, ×20, ×30 times the amount loaded in upper panel, ×1). psClu: pre-secretory Clu. TauRD ($n = 6$ independent experiments) and Clu ($n = 3$ independent experiments) were quantified by densitometry with the amounts in total fractions set to 100%. Averages ± SEM. Molecular weight (MW) standards are indicated. **b** Seeding potency of soluble (S) and pellet (P) fractions of TauRD aggregation reactions formed without (gray) or with Clu (red). Lipofectamine was used as a transfection reagent. Seeding by soluble TauRD without Clu was set to 1. Averages ± SEM ($n = 3$ independent experiments). **c** Effect of Clu on the seeding potency of the soluble fraction of aggregation reactions without Clu. The soluble fraction was incubated for 30 min either with Clu or with PBS prior to addition to cells. Lipofectamine was used as a transfection reagent. Titration of seeding potency was performed as described in Supplementary Fig. 2e. Bar graphs represent the average slope ± SEM from the linear regression analyses ($n = 4$ independent experiments). $^{**}p < 0.01$ ($p = 0.0013$) by two-tailed Student's *t*-test. **d**, **e** Dual-color fluorescence cross-correlation spectroscopy (dcFCCS) analysis of the interaction of TauRD with Clu during aggregation. Aggregation reactions contained 1 µM Alexa Fluor 532 labeled TauRD (TauRD-A532) and 9 µM unlabeled TauRD in the presence of Alexa Fluor 647 labeled Clu (Clu-A647; 1.25 µM). Representative experiments are shown ($n = 4$ independent experiments). **e** Kinetic development of FCCS signal in (**d**) (right *y*-axis; black) relative to the formation of ThT positive aggregates (left *y*-axis; orange, Supplementary Fig. 7a, data represent the mean ± SEM ($n = 3$ independent experiments)). arb. units, arbitrary units. **f** Clu interacts with soluble oligomeric TauRD species. dcFCCS analysis of TauRD-A532 and Clu-A647 interaction in the soluble fraction of the aggregation reaction immediately upon initiation of aggregation (0 h, black) and after reaching the plateau of ThT positive aggregate formation (6 h, red, Supplementary Fig. 7a). Representative data are shown ($n = 3$ independent experiments).

danger receptor galectine-8 (GAL-8) (Fig. 4e and Supplementary Fig. 8b), a marker of ruptured endomembranes[63]. After incubation for a further 24 h, we observed incorporation of TauRD-A532 and Clu-A647 into aggregates formed by endogenous TauRD-mTurquoise2 (TauRD-mTurq) (Fig. 4f, g and Supplementary Fig. 8c–f). The level of colocalization of the three fluorophores in seeded TauRD-mTurq aggregates was quantified by plotting their relative intensity profile, extracted from lines manually drawn in mid focal planes (Fig. 4g and Supplementary Fig. 8d, f). Co-localization of Tau-A532/Clu-A647 seeds with CHMP2a, Gal-8, and endogenous aggregates was not detected frequently enough to be reliably quantified.

Thus, following uptake by endocytosis, TauRD/Clu seeds presumably induce vesicle damage[54,58], allowing their escape into the cytosol where they template aggregation of endogenous TauRD.

Clusterin interferes with seeding of α-Synuclein aggregates. To test whether the effect of Clu on aggregate seeding is Tau specific, we next performed experiments with α-Synuclein (α-Syn), which

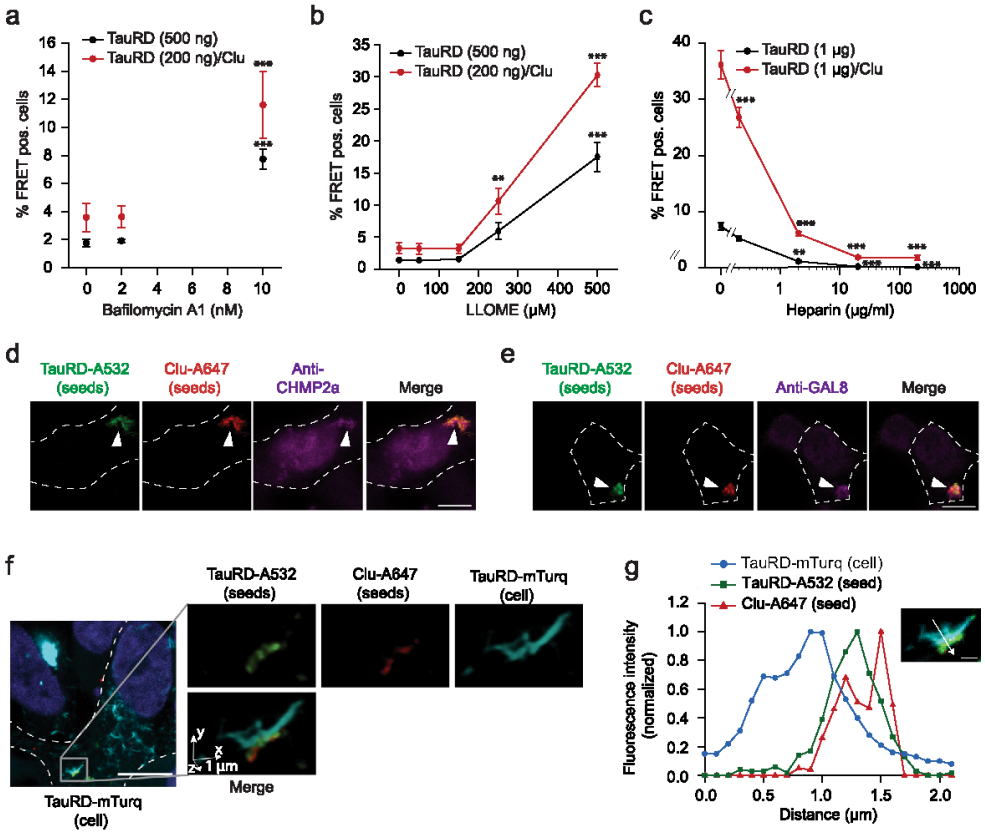

Fig. 4 Uptake of Clusterin-associated, seeding competent Tau aggregates by endocytosis. a, **b** Effect of inhibition of lysosomal H^+ ATPase by Bafilomycin A1 (**a**) and permeabilization of acidic membrane compartments with LLOME (**b**) on seeding potency of TauRD aggregates formed with or without Clu. TauRD-YT cells were treated with increasing concentrations of the inhibitors in combination with 500 ng TauRD seeds or 200 ng TauRD/Clu seeds without a transfection reagent. FRET positive (pos.) cells were analyzed after 48 h. Data represent the mean ± SEM ($n = 5$ independent experiments). Significance is represented relative to control cells treated with the vehicle without Bafilomycin A1 or LLOME. $^{**}p < 0.01$, $^{***}p < 0.001$ by two-way ANOVA with Sidak post hoc test (TauRD vehicle vs. TauRD 10 nM Bafilomycin A1 $p = 2.9 \times 10^{-5}$; TauRD/Clu vehicle vs. TauRD/Clu 10 nM Bafilomycin A1 $p = 3.9 \times 10^{-4}$; TauRD vehicle vs. TauRD 500 μM LLOME $p = 4 \times 10^{-10}$; TauRD/Clu vehicle vs. TauRD/Clu 250 μM LLOME $p = 0.002$; TauRD/Clu vehicle vs. TauRD/Clu 500 μM LLOME $p < 1 \times 10^{-15}$). **c** Heparan sulfate proteoglycan (HSPG) mediated internalization of TauRD and TauRD/Clu aggregates. TauRD-YT cells were treated with increasing concentrations of heparin in combination with 1 μg TauRD seeds or TauRD/Clu seeds without a transfection reagent. FRET positive (pos.) cells were analyzed after 48 h. Data represent the mean ± SEM ($n = 4$ independent experiments). Significance is represented relative to control cells treated with the vehicle without heparin. $^{**}p < 0.01$, $^{***}p < 0.001$ by two-way ANOVA with Sidak post hoc test (TauRD vehicle vs. TauRD 2 μg/ml heparin $p = 0.0017$; TauRD vehicle vs. TauRD 20 μg/ml heparin $p = 3 \times 10^{-4}$; TauRD vehicle vs. TauRD 200 μg/ml heparin $p = 2.5 \times 10^{-4}$; TauRD/Clu vehicle vs. TauRD/Clu 0.2 μg/ml heparin $p = 4.4 \times 10^{-6}$; TauRD/Clu vehicle vs. TauRD/Clu 2 μg/ml heparin, TauRD/Clu vehicle vs. TauRD/Clu 20 μg/ml heparin and TauRD/Clu vehicle vs. TauRD/Clu 200 μg/ml heparin $p < 1 \times 10^{-15}$). **d**, **e** Colocalization of TauRD/Clu seeds (TauRD-A532 in green, Clu-A647 in red) (arrowheads) with the endocytosis marker CHMP2a (magenta) (**d**) and the marker of ruptured endomembranes, galectin-8 (GAL8; magenta) (**e**) in TauRD-T cells. A representative result of confocal imaging is shown. The cell outline is indicated by a white dashed line. Scale bar, 10 μm. ($n = 3$ independent experiments). **f**, **g** Colocalization of TauRD/Clu seeds with endogenous TauRD-mTurquoise2 (TauRD-mTurq) aggregates. **f** A representative slice from a confocal stack is shown (scale bar, 10 μm) where cells are outlined with a white dashed line. One aggregate region, marked with a square in the slice, is represented by volume rendering (1 μm scale bars indicated by arrows). Channels are also displayed separately. TauRD-A532 seed in green, Clu-A647 in red, endogenous TauRD aggregate in turquoise. ($n = 3$ independent experiments). **g** Quantification of relative fluorescence intensity in the aggregate shown in the inset. TauRD-mTurq (blue), TauRD-A532 (green) and Clu-A647 (red). The colocalization line profile on a mid focal plane (inset image) along the white arrow is shown. Scale bar, 1 μm.

undergoes prion-like aggregate propagation in Parkinson's disease (PD)[1]. Clu also delayed the formation of ThT-positive aggregates of α-Syn (with early-onset-PD mutation A53T), even at very low molar ratios to α-Syn[14,64] (Fig. 5a). However, as in the case of Tau, α-Syn fibrils were nevertheless assembled (Supplementary Fig. 9a, b) and similar amounts of aggregates were generated in the absence and presence of Clu, as demonstrated by filtration assay (Supplementary Fig. 9b). Seeding competent α-Syn species formed slightly before the accumulation of ThT-positive aggregates, as analyzed in HEK293T cells stably expressing GFP-α-Syn(A53T) (Fig. 5a–c). Lipofectamine was used to render seed uptake independent of cellular machinery for internalization. In the absence of Clu, seeding with α-Syn(A53T) resulted in ~60% of cells with aggregates. Seeding was markedly suppressed by sub-stoichiometric amounts of Clu at ratios of Clu:α-Syn of 1:1,000 to 1:100 (Fig. 5b, c). This effect was also confirmed with

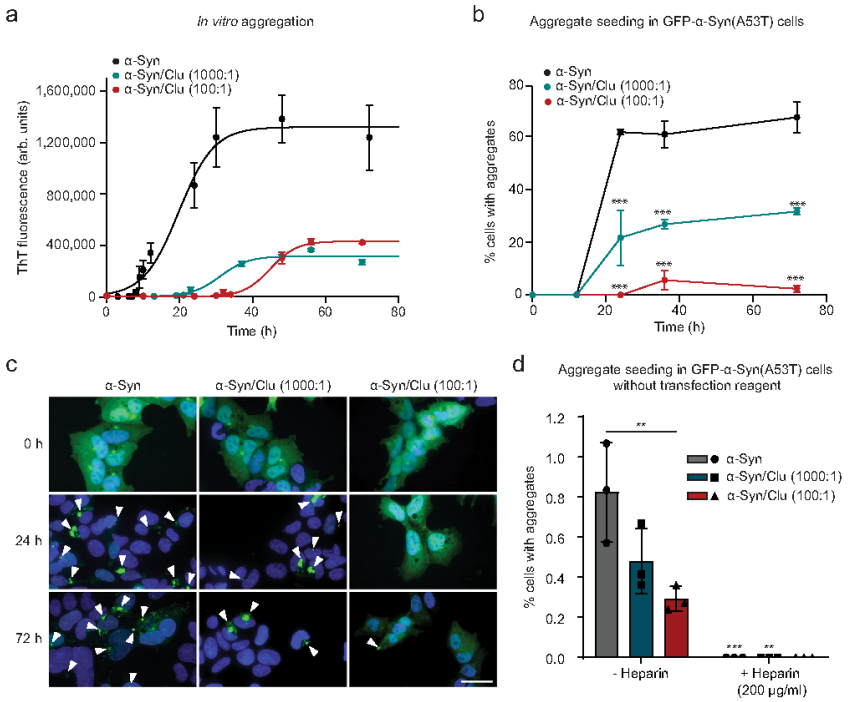

Fig. 5 Effect of Clusterin on α-Synuclein aggregation and seeding. a Aggregation of α-Syn (300 μM) without (black) or with Clu (0.3 μM and 3 μM in cyan and red, respectively) was monitored by ThT fluorescence. Molar ratios of α-Syn:Clu are indicated. arb.units, arbitrary units. Averages ± SEM ($n = 4$ independent experiments). **b** Effect of Clu on seeding potency of α-Syn aggregation reactions as in (**a**). Seeding was measured by quantifying the fraction of HEK293T cells stably expressing GFP-α-Syn(A53T) that contained aggregates after 24 h of seeding (200 ng α-Syn) with lipofectamine. Molar ratios of α-Syn:Clu are indicated. Significance is represented relative to α-Syn alone at each time point. Averages ± SEM ($n =$ at least 100 cells examined over three independent experiments). $^{***}p < 0.001$ by two-way ANOVA with Sidak post hoc test. (α-Syn 24 h vs. α-Syn/Clu 1000:1 24 h $p = 1.9 \times 10^{-8}$; α-Syn 24 h vs. α-Syn/Clu 100:1 24 h $p = 8.4 \times 10^{-13}$; α-Syn 36 h vs. α-Syn/Clu 1000:1 36 h $p = 4.5 \times 10^{-7}$; α-Syn 36 h vs. α-Syn/Clu 100:1 36 h $p = 1.3 \times 10^{-11}$; α-Syn 72 h vs. α-Syn/Clu 1000:1 72 h $p = 1.8 \times 10^{-7}$; α-Syn 72 h vs. α-Syn/Clu 100:1 72 h $p = 2.3 \times 10^{-13}$). **c** Representative images of HEK 293 T GFP-α-Syn(A53T) cells seeded with aggregation reactions (200 ng α-Syn after 0 h, 24 h and 72 h aggregation (**a**)) with or without Clu. GFP-α-Syn(A53T) and DAPI nuclear staining are shown in green and blue, respectively. Arrowheads indicate aggregates. Scale bar, 30 μm. **d** Heparan sulfate proteoglycan (HSPG) mediated internalization of α-Syn and α-Syn/Clu aggregates. Seeding was measured by quantifying the fraction of GFP-α-Syn(A53T) cells that contained aggregates after 72 h of seeding (50 μg α-Syn after 72 h aggregation (**a**)) without lipofectamine (−Heparin). GFP-α-Syn(A53T) cells were also treated with α-Syn and α-Syn/Clu aggregates (50 μg) in combination with heparin (200 μg/ml). Molar ratios of α-Syn:Clu are indicated. Data represent the mean ± SEM ($n =$ at least 1000 cells examined over three independent experiments). $^{**}p < 0.01$, $^{***}p < 0.001$ by two-way ANOVA with Sidak post hoc test (−Heparin α-Syn vs. −Heparin α-Syn/Clu 100:1 $p = 0.003$; −Heparin α-Syn vs. +Heparin α-Syn $p = 4.8 \times 10^{-5}$; −Heparin α-Syn/Clu 1000:1 vs. +Heparin α-Syn/Clu 1000:1 $p = 0.007$). The significance of +Heparin reactions is relative to the respective −Heparin control.

neuroblastoma SH-SY5Y cells stably expressing GFP-α-Syn (A53T) (Supplementary Fig. 9c, d), however higher amounts of seeding material (10 μg α-Syn for SH-SY5Y cells, 200 ng α-Syn for HEK293T) were necessary to obtain comparable seeding efficiencies. The observed decrease in α-Syn seeding in the presence of Clu does not appear to be due to reduced formation of insoluble fibrils (Supplementary Fig. 9b), but rather to changes in the effective concentration of other seeding competent species. Note that Clu increased the seeding potency of TauRD aggregates approximately twofold even when used at a low Clu:TauRD ratio of 1:100 (Supplementary Fig. 9e). Thus, while having similar effects on aggregation kinetics in vitro, Clu has opposite effects on the seeding activity of Tau and α-Syn aggregates in the cellular assay, enhancing the former and suppressing the latter.

To test the effect of Clu on α-Syn seeding in cells with the unperturbed plasma membrane, we omitted the transfection reagent. Under these conditions, Clu still clearly suppressed α-Syn seeding (Fig. 5d). Consistent with the notion that HSPGs are also involved in α-Syn internalization[57], aggregate seeding by α-Syn and α-Syn/Clu was completely suppressed in the presence of heparin (200 μg/ml, Fig. 5d). Thus, HSPGs participate in the internalization of both α-Syn and TauRD seeds, independent of the presence of Clu.

Clusterin enhances Tau seeding and toxicity in neurons. To extend our findings to neuronal cells, we used primary mouse neurons transduced with TauRD (residues 244-372, P301L/V337M) fused to YFP (TauRD-Y). We incubated neurons with either aggregates of TauRD, TauRD/Clu, or buffer control without transfection reagent and after 4 days monitored the formation of aggregates of endogenous TauRD-Y by fluorescence microscopy (Fig. 6a–c). Incubation with TauRD seeds alone induced the formation of TauRD-Y inclusions in ~12% of neurons, while TauRD/Clu induced aggregation in ~45% of neurons (Fig. 6b, c). While there was no difference in neuronal viability 4 days after seeding, treatment with TauRD/Clu resulted in a ~30% decrease in viability 7 days after seeding compared to cells seeded with

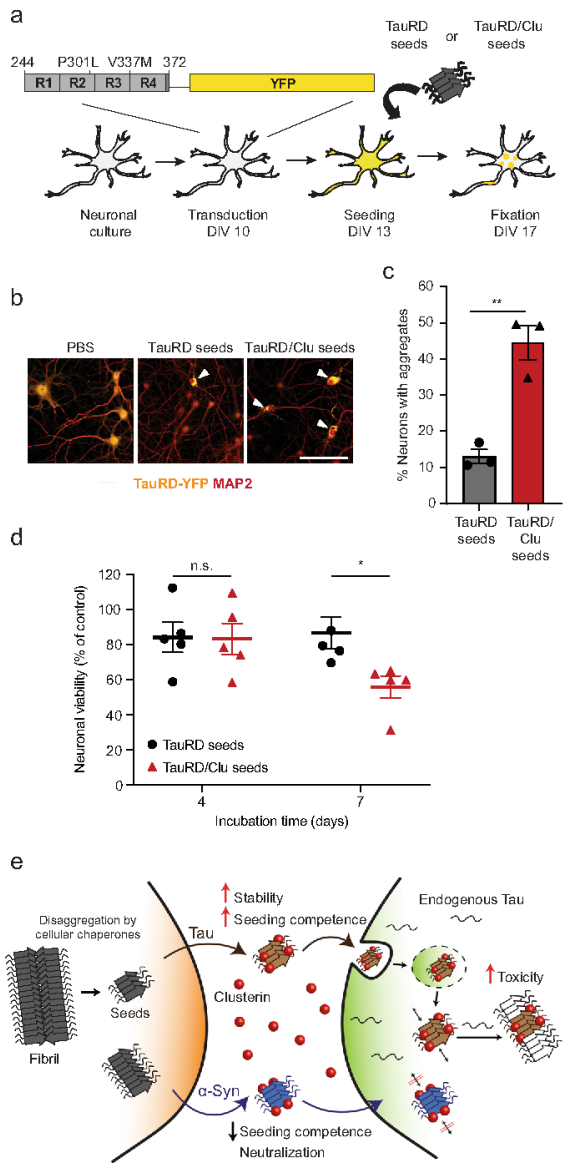

Fig. 6 Clusterin enhances Tau seeding and toxicity in neurons. a Workflow for TauRD aggregate seeding experiments with primary mouse neurons. DIV, days in vitro. **b** Representative fluorescence microscopy images of primary mouse neurons expressing TauRD-YFP (yellow) incubated with PBS, TauRD seeds or TauRD/Clu seeds (70 ng TauRD). Neurons were stained with an antibody against the neuronal marker MAP2 (red). Arrowheads indicate aggregates. Scale bar, 20 µm. **c** Comparison of seeding competence of TauRD (gray) and TauRD/Clu (red) seeds (70 ng TauRD) in primary mouse neurons. The fraction of neurons containing YFP-positive aggregates by fluorescence microscopy imaging was quantified. Data represent the mean ± SEM (n = at least 800 cells examined over 3 independent experiments). $^{**}p < 0.01$ ($p = 0.0038$) by two-tailed Student's t-test. **d** Viability of neurons expressing TauRD-YFP at 4 and 7 days after incubation with TauRD (black) or TauRD/Clu (red) seeds (11 ng TauRD). Data from MTT assays are normalized to the control sample incubated with PBS (100%) and represent the mean ± SEM ($n = 5$ independent experiments). $^{*}p < 0.05$ ($p = 0.034$); n.s., not significant ($p = 0.99$) by two-way ANOVA with Sidak post hoc test. **e** Hypothetical model for the role of Clu (red) in amyloid seeding of Tau (brown) and α-Synuclein (α-Syn) (blue). Tau and α-Syn seeding competent species, partially produced by chaperone-mediated disaggregation, are released to the extracellular space from cells containing amyloid aggregates (gray). Clu (red) interacts with these species increasing seeding competence for Tau upon uptake by neighboring cells via the endosomal pathway. In contrast, Clu inhibits seeding for α-Syn. Tau/Clu seeds efficiently template aggregation of endogenous Tau, resulting in cytotoxicity, while α-Syn/Clu seeds are unable to template aggregation of endogenous α-Syn.

TauRD alone (Fig. 6d). This suggests that the higher endogenous aggregate load produced by the Clu-stabilized TauRD seeds is associated with significant neuronal toxicity.

Discussion

Extensive evidence links Clusterin with AD, and both neuroprotective and pathology-enhancing functions have been ascribed to this abundant extracellular chaperone[15–27,31–33]. While these previous investigations focused on the effects of Clu on Aβ aggregation and toxicity, our results suggest the possibility that Clu can modulate the Tau component of AD by accelerating Tau aggregate seeding. Using cellular models, we show that Clu binds and stabilizes soluble Tau species in a state highly competent in seeding aggregation of endogenous Tau upon uptake by recipient cells (Fig. 6e). The structural properties of these Tau species remain to be defined. Within the cell, clearance of aggregates by intracellular chaperones such as the Hsp70 system[65] may generate seeding competent Tau species, which could be a substrate for stabilization by Clu after release into the extracellular space (Fig. 6e). Although the exact mechanism by which Tau species are released from cells remains unclear[7], seeding competent, high-molecular-weight Tau that could be acted on by Clu, has been detected in the cerebrospinal fluid of AD patients[66]. TauRD enters target cells in complex with Clu, apparently by endocytosis (Fig. 6e). However, TauRD/Clu seeds induce vesicle rupture and escape from endosomes to the cytosol, as described for Tau alone and other amyloidogenic proteins[54,58] (Fig. 6e), enabling them to induce aggregation of endogenous Tau. Thus, Clu fails to mediate efficient lysosomal degradation of Tau, in contrast to other Clu-bound misfolded proteins[31,32]. Seed uptake and permeation of endolysosomal membranes may be facilitated by the relatively small size of the Tau species stabilized by Clu.

In contrast to a possible role of extracellular Clu in promoting Tau pathology, intracellular Clu, accumulating under stress conditions[9], may be protective by interfering with de novo Tau aggregation. The latter activity would be consistent with a recent study reporting colocalization of Clu with intracellular Tau tangles in the brain of mice overexpressing human Tau (P301L) and exacerbated Tau pathology in CLU knock-out animals[40]. However, aggregate spreading was not explicitly assessed. It also remains to be investigated whether other apolipoproteins including ApoE, which also influences Tau pathology[67–70], may compensate for the loss of extracellular Clu[71–74]. Whether Clu ultimately delays or promotes Tau pathology may depend on the stage of the disease and multiple other factors.

The seeding-enhancing effect of Clu appears to be Tau specific. In the case of α-Syn, another amyloidogenic protein that undergoes prion-like aggregate spreading[1], Clu blocked both aggregation and seeding (Fig. 6e), consistent with recent observations[64,75,76]. Indeed, Clu is upregulated in PD and other synucleinopathies[77]. Interestingly, progressive PD in older patients is often associated with mixed brain pathologies,

including Tau aggregation[78,79], raising the possibility of a tug of war between protective functions of Clu and collateral damage incurred. Thus, the ability of Clu to modulate transcellular Tau aggregate seeding may be broadly relevant in understanding the progressive nature of neurodegenerative pathologies.

Methods

Plasmids. The N1-TauRD (P301L/V337M)-EYFP construct and the mTurquoise2N1 plasmid were gifts from Marc Diamond and Michael Davidson, respectively (Addgene #54843[80]). The N1-TauRD (P301L/V337M)-mTurquoise2 plasmid for TauRD-mTurquoise2 expression in HEK293T cells was constructed by cloning the TauRD sequence (Tau amino acids 244-372, containing the disease-related mutations P301L and V337M) from N1-TauRD (P301L/V337M)-EYFP into the mTurquoise2N1 plasmid using the EcoRI and NheI restriction sites. The N1-PLTau (0N4R, P301L/V337M)-EYFP and N1-PLTau (0N4R, P301L/V337M)-mTurquoise2 plasmids were constructed by substitution of the TauRD (P301L/V337M) sequence from N1-TauRD (P301L/V337M)-EYFP and N1-TauRD (P301L/V337M)-mTurquoise2 plasmids by the PLTau (0N4R, P301L/V337M) sequence from the pRK5-EGFP-Tau P301L plasmid (a gift from Karen Ashe (Addgene #46908[81])) after introducing the mutation V337M, by Gibson assembly using the Gibson Assembly Master Mix (New England Biolabs). The linker between Tau and the fluorescent protein was composed of 21 amino acids in all cases (YPYGILQSTVPRARDPPVATA/M for YFP and mTurquoise2 plasmids, respectively) to avoid interference of fluorescent protein with fibril formation.

The pHUE-TauRD (P301L/V337M) plasmid was made by inserting the TauRD sequence (Tau amino acids 244-371) in pHUE[82] by Gibson assembly using the Gibson Assembly Master Mix (New England Biolabs). Plasmid pHUE-TauRD (C291A/P301L/C322A/V337M) containing cysteine-free TauRD and pHUE-TauRD (I260C/C291A/P301L/C322A/V337M) containing TauRD-I260C for fluorescent labeling was constructed by mutagenesis of the pHUE-TauRD (P301L/V337M) plasmid using the Q5® Site-Directed Mutagenesis Kit (New England Biolabs).

The Tau/pET29b plasmid used for wild-type PLTau (2N4R) expression and purification was a gift from Peter Klein (Addgene plasmid #16316[83]).

pFhSynW2 and the pVsVg packing plasmids used for lentivirus production were a gift from Dieter Edbauer. The psPAX2 packing plasmid, also used for lentivirus production, was a gift from Didier Trono (Addgene plasmid #12260). pFhSynW2 TauRD (P301L/V337M)-EYFP used for TauRD-EYFP expression in mouse primary neurons was constructed by PCR amplification of the TauRD (P301L/V337M)-EYFP sequence from the N1-TauRD (P301L/V337M)-EYFP plasmid.

The pB-T-PAF vector was a gift from James Rini. The pB-T-PAF-CluStrep plasmid, which was used for Clusterin (Clu) (Clu followed by a strep tag, WSHPQPEK) expression and purification, was constructed by cloning the Clu cDNA sequence amplified from human embryonic kidney 293T (HEK293T) cells into the pB-T-PAF vector. RNA was extracted from the cell pellet using the RNeasy Mini kit (Qiagen). cDNA was then synthesized using the QuantiTect Reverse Transcription Kit (Qiagen) and the Clu cDNA amplified by PCR. The PCR product was then digested and subcloned into the pB-T-PAF vector.

Plasmid pT7-7 α-Syn A53T for the expression and purification of recombinant α-Syn was a gift from Hilal Lashuel (Addgene plasmid #105727[84]) and EGFP-α-SynA53T plasmid for α-Syn expression in HEK293T and SH-SY5Y cells were a gift from David Rubinsztein (Addgene plasmid #40823[85]).

Cell lines. A HEK293-EBNA suspension cell line[86] stably expressing the recombinant protein Clusterin-Strep tag (HEK293E-CluStrep) was generated by using a piggyBac transposon-based expression system[87] employing the pB-T-PAF-CluStrep plasmid.

The monoclonal HEK293T cell line stably expressing two different constructs, TauRD N-terminally fused to either EYFP or mTurquoise2 (TauRD-YT cell line) was generated by transfecting HEK293T cells with N1-TauRD (P301L/V337M)-EYFP and N1-TauRD (P301L/V337M)-mTurquoise2 plasmids using lipofectamine 3000 (Thermo Fisher Scientific). Cells expressing the constructs were selected by 1 mg ml^{-1} G418 antibiotic (Gibco) selection, and monoclonal cell lines were generated by isolating cells expressing both TauRD fusion proteins in a 96 well-plate by cell sorting with a BD FACS Aria III (BD Biosciences) following amplification. A monoclonal cell line allowing Tau aggregation to be monitored by flow cytometry (FRET signal detection) with high efficiency was selected. In a similar way, a monoclonal HEK293T cell line stably expressing PLTau (0N4R, P301L/V337M) fused to either EYFP or mTurquoise2 was generated (PLTau-YT cell line) using the N1-PLTau (0N4R, P301L/V337M)-EYFP and N1-PLTau (0N4R, P301L/V337M)-mTurquoise2 plasmids, as well as monoclonal cell lines expressing just one of the constructs, N1-TauRD (P301L/V337M)-EYFP construct (TauRD-Y cell line), N1-TauRD (P301L/V337M)-mTurquoise2 construct (TauRD-T cell line), N1-PLTau (0N4R, P301L/V337M)-EYFP construct (PLTau-Y cell line) and N1-PLTau (0N4R, P301L/V337M)-mTurquoise2 construct (PLTau-T cell line).

The HEK293T and SH-SY5Y cell lines stably expressing EGFP-α-Syn(A53T)[88] were generated by transfecting HEK293T and SH-SY5Y cells with the EGFP-α-SynA53T plasmid using lipofectamine (Thermo Fisher Scientific). Cells expressing the constructs were selected by 2000 and 1000 μg ml^{-1} G418 antibiotic (Gibco) treatment, respectively. The SH-SY5Y EGFP-α-Syn(A53T) cell line was enriched by selecting cells expressing EGFP-α-SynA53T by cell sorting with a BD FACS Aria III (BD Biosciences) following amplification.

HEK293T and SH-SY5Y cell lines were maintained at 37 °C and 5% CO_2 in Dulbecco's modified Eagle's medium (DMEM, Biochrom KG) supplemented with 10% fetal bovine serum (Gibco), 100 U ml^{-1} penicillin (Gibco), 100 μl ml^{-1} streptomycin sulfate (Gibco) and 2 mM L-glutamine (Gibco). Stable cell lines were maintained in the medium described above supplemented with G418 (200 μg ml^{-1}).

Primary neuronal cultures. Primary mouse neurons were prepared from 15.5 CD-1 wild-type embryos. All experiments involving mice were performed in accordance with the relevant guidelines and regulations. Pregnant females were sacrificed by cervical dislocation, the uterus was removed from the abdominal cavity and placed into a 10 cm sterile Petri dish on ice containing dissection medium, consisting of Hanks' balanced salt solution (HBSS) supplemented with 0.01 M HEPES, 0.01 M $MgSO_4$, and 1% Penicillin/Streptomycin. Each embryo was isolated, heads were quickly cut, and brains were removed from the skull and immersed in an ice-cold dissection medium. Cortical hemispheres were dissected and meninges were removed under a stereomicroscope. Cortical tissue from typically six to seven embryos was transferred to a 15 ml sterile tube and digested with 0.25% trypsin containing 1 mM ethylenediaminetetraacetic acid (EDTA) and 15 μl 0.1% DNAse I for 20 min at 37 °C. The enzymatic digestion was stopped by removing the supernatant and washing the tissue twice with a Neurobasal medium (Invitrogen) containing 5% FBS. The tissue was resuspended in a 2 ml medium and triturated to achieve a single cell suspension. Cells were spun at 130 × *g*, the supernatant was removed, and the cell pellet was resuspended in a Neurobasal medium with 2% B27 (Invitrogen), 1% L-Glutamine (Invitrogen), and 1% Penicillin/Streptomycin (Invitrogen). For immunofluorescence, neurons were cultured in 24-well plates on 13 mm coverslips coated with 1 mg ml^{-1} poly-D-Lysine (Sigma) and 1 μg ml^{-1} laminin (Thermo Fisher Scientific) (100,000 neurons per well). For viability measurements, neurons were cultured in 96-well plates coated in the same way (19,000 neurons per well). Lentiviral transduction was performed at DIV 10. Viruses were thawed and immediately added to a freshly prepared neuronal culture medium. Neurons in 24-well plates received 1 μl of virus per well. Neurons in 96-well plates received 0.15 μl of virus per well. A fifth of the medium from cultured neurons was removed and the equivalent volume of virus-containing medium was added.

Lentivirus production. HEK293T cells for lentiviral packaging (Lenti-X 293T cell line, Takara) were expanded to 70–85% confluency in DMEM Glutamax (+4.5 g l^{-1} D-Glucose, - Pyruvate) supplemented with 10% FBS (Sigma), 1% G418 (Gibco), 1% NEAA (Thermo Fisher Scientific), and 1% HEPES (Biomol). Only low passage cells were used. For lentiviral production, a three-layered T525cm^2 flask (Falcon) was seeded and cells were henceforth cultured in a medium without G418. On the following day, cells were transfected with the pFhSynW2 TauRD (P301L/V337M)-EYFP expression plasmid and the packaging plasmids psPAX2 and pVsVg using TransIT-Lenti transfection reagent (Mirus). The transfection mix was incubated for 20 min at room temperature (RT) and in the meanwhile, cell medium was exchanged. In total, 10 ml transfection mix was added to the flask and left overnight. The medium was exchanged on the next day. After 48–52 h, the culture medium containing the viral particles was collected and centrifuged for 10 min at 1200 × *g*. The supernatant was filtered through 0.45 μm pore size filters using 50 ml syringes, and a Lenti-X concentrator was added (Takara). After overnight incubation at 4 °C, samples were centrifuged at 1500 × *g* for 45 min at 4 °C, the supernatant was removed, and the virus pellet was resuspended in 600 μl TBS-5 buffer (50 mM Tris-HCl pH 7.8, 130 mM NaCl, 10 mM KCl, 5 mM $MgCl_2$). After aliquoting, the virus was stored at −80 °C.

Chemicals and cell treatments. Bafilomycin A1 was purchased from InvivoGen. L-Leucyl-L-Leucine methyl ester (hydrochloride) (LLOME) was purchased from Cayman chemicals. Both compounds were dissolved in DMSO and small aliquots were stored at −20 °C until further use. For non-treated samples, DMSO alone was used as a control. Alexa Fluor 532 C5 maleimide and Alexa Fluor 647 N-hydroxysuccinimide (NHS) ester were purchased from Thermo Fischer Scientific and freshly dissolved in DMSO before protein labeling. Heparin sodium salt from porcine intestinal mucosa was purchased from Merck (H3393).

Sodium dodecyl sulfate-polyacrylamide gel electrophoresis (SDS-PAGE) and immunoblotting. Protein samples were boiled in SDS-PAGE sample buffer for 5 min. Protein samples were separated by electrophoresis on NuPAGE 4–12% Bis-Tris SDS gels (Thermo Fisher Scientific) using NuPAGE MES SDS running buffer (Thermo Fisher Scientific) at 180 V. Coomassie blue staining was performed with InstantBlue (Merck). For immunoblotting, proteins were transferred at 70 V for 2 h onto a nitrocellulose membrane (GE Healthcare) using a wet electroblotting system (BIO-RAD). Membranes were blocked for at least 1 h with 0.05% TBS-Tween and 5% low-fat milk. Immunodetection was performed using mouse monoclonal Tau/Repeat Domain antibody (TECAN, 2B11), anti-Tau-1 antibody (non-phosphorylated Tau, clone PC1C6, Merck, MAB3420), Tau monoclonal antibody (TAU-5,

Total Tau, Thermo Fisher Scientific, MA5-12808), phospho-Tau antibody (Ser202, Thr205, AT8, Thermo Fisher Scientific, MN1020), mouse monoclonal Clu-α antibody (Santa Cruz Biotechnology, sc-5289), recombinant anti-Clusterin antibody (EPR2911, abcam, ab92548) and anti-alpha-Synuclein antibody (LB509, abcam, ab27766). Conjugated goat-anti mouse immunoglobulin G (IgG)-horseradish peroxidase (HRP) (Merck, A4416) or anti-rabbit IgG (whole molecule)–peroxidase antibody produced in goat (Merck, A9169) were used as secondary antibodies. Immobilon Classico Western HRP substrate or Immobilon ECL Ultra Western HRP Substrate (Merck) were used for detection. Quantification by densitometry was performed with AIDA Image Analyzer v.4.27 (Elysia Raytest) or Image J (Rasband, W.S., National Institutes of Health, USA). Pull scan blots are provided in the Source Data file.

Protein purification. Seed aggregates for addition to cells were generated with purified recombinant cysteine-free TauRD (Tau residues 244-371, C291A/P301L/C322A/V337M) to avoid the use of reducing agents that might interfere with Clu function (Supplementary Fig. 1a). Mutation of the two cysteines in TauRD avoids the formation of intramolecular disulfide bonds that slows fibril formation[42]. Cysteine-free TauRD and TauRD-I260C were expressed as N-terminal His_6-ubiquitin fusion proteins in *Escherichia coli* BL21(DE3) cells transformed with the respective pHUE-TauRD plasmids via IPTG induction. The cell pellet from a 2 l culture was resuspended in 50 ml lysis buffer (50 mM PIPES-NaOH pH 6.5, 250 mM NaCl, 10 mM imidazole, 2 mM β-mercaptoethanol (βME)) supplemented with 1 mg ml^{-1} lysozyme, Complete EDTA-free protease inhibitor cocktail (MERK) and benzonase, and incubated while gently shaking at 4 °C for 30 min. Cells were lysed by ultrasonication, and the lysate was cleared by centrifugation (1 h, 40,000 × *g* at 4 °C). The supernatant was loaded onto a Ni-NTA column equilibrated with lysis buffer. The column was washed with high salt buffer (50 mM PIPES-NaOH pH 6.5, 500 mM NaCl, 10 mM imidazole, 2 mM βME) and wash buffer (50 mM PIPES-NaOH pH 6.5, 250 mM NaCl, 50 mM imidazole, 2 mM βME), and His_6-ubiquitin-TauRD was eluted with elution buffer (50 mM PIPES-NaOH pH 6.5, 50 mM NaCl, 250 mM imidazole, 2 mM β-ME). The eluted fractions were collected and the salt concentration was reduced by diluting the sample (1:5) with PIPES buffer (50 mM PIPES-NaOH pH 6.5, 2 mM βME), followed by incubation with Usp2 ubiquitin protease (0.5 mg) overnight at 4 °C in order to cleave the His_6-ubiquitin tag. The cleavage mixture was applied to a Source30S cation exchange column and the TauRD protein was eluted with a 0–500 mM NaCl gradient in PIPES buffer. The TauRD protein was further purified by size exclusion chromatography (SEC) on Superdex-75 in phosphate-buffered saline (PBS). For TauRD-I260C, the buffer used for SEC contained 1 mM tris(2-carboxyethyl) phosphine (TCEP) in order to prevent the formation of disulfide bonds. Fractions containing pure protein were combined, aliquoted, and flash-frozen in liquid nitrogen for storage at −80 °C. A more detailed protocol can be found here, https://edmond.mpdl.mpg.de/imeji/collection/3psV1MQj0fmYu5KS.

Wild type FLTau (2N4R) was expressed in *E. coli* BL21(DE3) transformed with the Tau/pET29b plasmid via IPTG induction. The cell pellet from 6 l of culture was resuspended in 180 ml lysis2 buffer (50 mM MES-NaOH pH 6.8, 20 mM NaCl, 1 mM $MgCl_2$, 5 mM DTT), applied to a French press cell disruptor, and subsequently boiled for 20 min. The lysate was cleared by centrifugation (1 h, 40,000 × *g* at 4 °C), and the supernatant was loaded onto a Source30S cation exchange column equilibrated with lysis2 buffer. The protein was eluted with a 0–500 mM NaCl gradient and further purified by SEC on Sephacryl S-200 in 20 mM MES-NaOH pH 6.8, 20 mM NaCl, 10% glycerol. Fractions containing pure protein were combined, aliquoted, and flash-frozen in liquid nitrogen for storage at −80 °C.

Recombinant Clu (CluStrep) was purified as described (https://doi.org/10.17504/protocols.io.bvvkn64w). Strep-tagged Clu was expressed and secreted by HEK293E-CluStrep cells cultured in FreeStyle 293 Expression Medium (Thermo Fisher Scientific) for 4 days. The conditioned medium was then separated from the cells by centrifugation. For chromatographic purification, the medium was first dialyzed against wash buffer (20 mM Na acetate pH 5.0). After removal of the precipitate by centrifugation, the supernatant was passed over a HiTrap SP XL cation exchange column. The column was washed with 10 column volumes (CV) denaturing buffer (20 mM Na acetate pH 5.0, 6 M urea), followed by 5 CVs wash buffer. For protein elution, a 0–500 mM NaCl gradient in wash buffer was applied. Clu-containing fractions were further purified by SEC on Superdex-200 in 20 mM Na acetate pH 5.0, 100 mM NaCl, 1 mM EDTA. Fractions containing pure Clu were concentrated, and the buffer was exchanged to PBS using a Nap5 (GE Healthcare) column. Aliquots were flash-frozen in liquid nitrogen for storage at −80 °C.

Recombinant human α-Synuclein (α-Syn, A53T) was purified essentially as described[89] (https://doi.org/10.17504/protocols.io.btynnpve). In brief, *E. coli* BL21 (DE3) cells were transformed with the pT7-7 α-Syn A53T plasmid. Protein expression was induced with 1 mM IPTG for 4 h at 37 °C. Bacteria were harvested and the pellet was lysed in high salt buffer (750 mM NaCl, 50 mM Tris-HCl pH 7.6, 1 mM EDTA). The lysate was sonicated for 5 min and boiled subsequently. The boiled suspension was centrifuged, the supernatant dialyzed against 50 mM NaCl, 10 mM Tris-HCl pH 7.6, and 1 mM EDTA and purified by SEC on Superdex 200 in the same buffer. Fractions were collected and those containing α-Syn were combined. The combined fractions were applied onto an anion exchange column (MonoQ). α-Syn was purified by a gradient ranging from 50 mM to 1 M NaCl. Fractions containing α-Syn were combined and dialyzed in 150 mM KCl, 50 mM Tris-HCl pH 7.6. Aliquots were stored at −80 °C.

Deglycosylation. Purified Clu was deglycosylated with PNGase F (glycerol free, NEB), following the manufacturer's instructions.

Rhodanese aggregation assay. Rhodanese (100 μM) was denatured in 6 M guanidinium-HCl, 5 mM DTT for 1 h at 25 °C, and diluted 200-fold into PBS in the absence or presence of Clu (0.5 μM). Bovine serum albumin (BSA) (Thermo Fisher Scientific) (0.5 μM) was used as control. Aggregation was monitored immediately after dilution by measuring turbidity at 320 nm wavelength.

Filter retardation assay. Different amounts of α-Syn aggregation reaction were diluted in PBS and subsequently applied onto a pre-wetted 0.2 μm pore size cellulose acetate membrane in a Hoefer slot-blot apparatus. The membrane was subsequently washed twice with 0.1% Triton-X 100. Immunodetection was performed as described above (Sodium dodecyl sulfate-polyacrylamide gel electrophoresis (SDS-PAGE) and immunoblotting).

Protein labeling. TauRD-I260C and Clu were labeled with Alexa532 C5 maleimide and Alexa647 NHS ester (Thermo Fisher Scientific), respectively. Before the labeling reaction, TauRD-I260C was incubated on ice in the purification buffer containing 2 mM TCEP to reduce the cysteine residue, followed by removal of TCEP by SEC using a Nap5 (GE Healthcare) column pre-equilibrated with PBS buffer. Labeling of TauRD-I260C at an equimolar ratio of the fluorophore was performed in the PBS buffer for 1 h at RT. For the labeling reaction of Clu, PBS buffer was exchanged with 0.1 M sodium bicarbonate buffer (pH 8.3) (N-terminal labeling buffer) using a Nap5 column, and labeling was subsequently performed at a twofold molar excess of fluorophore for 1 h at RT. Free dyes were removed using a Nap5 column, pre-equilibrated with PBS buffer. The labeling efficiency was measured by nanodrop and was typically about 65–70%.

Fluorescence cross-correlation spectroscopy (dcFCCS). dcFCCS measurements were performed on a Micro Time 200 inverse time-resolved fluorescence microscope (PicoQuant) as described previously[90,91]. Samples were diluted 100-fold in PBS (from 1 μM to 10 nM each labeled protein) immediately before each measurement. Autocorrelation was recorded for 30 min. The diffusion time was obtained by fitting the curves with the triplet diffusion equation using Symphotime 64 (PicoQuant). The confocal volume (V_{eff}) was calibrated daily using Atto655 maleimide dye.

Estimation of the average molecular weight of Tau/Clu complexes. To estimate the average size of Tau/Clu complexes, we performed FCS measurements to determine the diffusion coefficient (*D*). Diffusion coefficients (D) were converted into hydrodynamic radii (R_H) via the Stokes–Einstein equation (Eq. (1)), where k_B is the Boltzmann constant, *T* is the temperature (in K) and η is the solvent viscosity. Second, the correlation between R_H and the chain length (in amino acid residues, N) (Eq. (2)) for elongated proteins was applied[92], and this chain length was converted to molecular weight by assuming an average molar mass for amino acids of $m_{aa} = 113$ g/mol (relative to amino acid abundance in eukaryotic proteins).

$$R_H = \left(\frac{k_B T}{6\pi\eta D}\right) \quad (1)$$

$$R_H = (2.21 \pm 1.07) N^{0.57 \pm 0.02} \quad (2)$$

Protein aggregation reactions and thioflavin-T (ThT) fluorescence measurements. Tau aggregation: 100 μl of 10 μM Tau (TauRD or FLTau), 2.5 μM heparin, 2 mM $MgCl_2$ were incubated in the presence or absence of Clu at 37 °C with constant agitation (850 rpm) in a thermomixer (Eppendorf). Aliquots were removed at the indicated time points, flash-frozen in liquid nitrogen, and stored at −80 °C until measurement of ThT fluorescence and seeding activity.

α-Syn aggregation: purified α-Syn (5 mg ml^{-1}, 330 μM) was centrifuged at 100,000 × *g* for 1 h. The supernatant was transferred into a new reaction tube and incubated in the presence or absence of Clu with constant agitation (1000 rpm) at 37 °C in a thermomixer. Aliquots were removed at the indicated time points and stored at −80 °C until measurement of ThT fluorescence and seeding activity.

For monitoring amyloid formation by ThT fluorescence, aliquots from aggregation reactions of Tau or α-Syn were diluted 50 or 100-fold, respectively, into 20 μM ThT in PBS. Excitation and emission wavelengths were 440 nm and 480 nm, respectively. Measurements were performed with a FluoroMax-4 Spectrophotometer (HORIBA) using FluorEssence V3.9 (HORIBA). The emission signal was corrected with the reference signal of the lamp (S1/R1 wavelength, S: emission signal, R: reference signal) and by subtraction of the minimum data point. ThT kinetics were fitted using Sigma plot 14.0 (Sigmoidal dynamic fitting, sigmoid 3 parameter equation). A more detailed protocol can be found here https://edmond.mpdl.mpg.de/imeji/collection/3psV1MQj0fmYu5KS.

Fractionation of in vitro aggregation reactions. TauRD and TauRD/Clu aggregation reactions were centrifuged at 16,100 × *g* and 4 °C for 1 h. The supernatant was collected. The pellet was washed with PBS, centrifuged at 16,100 × *g* and 4 °C for 30 min, and the resulting pellet was resuspended in the initial volume of PBS. The Tau and Clu content was quantified by immunoblotting.

Cell-based seeding assays. Seeding of HEK293T cells: 100,000 cells per well of the HEK293T reporter cell line (TauRD-YT or PLTau-YT) were dispensed into a 12-well plate. For subsequent fluorescence microscopy imaging, a coverslip was placed on the well. In total, 16–24 h later, Tau aggregates were transfected with lipofectamine 3000 (Thermo Fisher Scientific). Specifically, aggregate samples were mixed with a mixture of 50 µl Opti-MEM (Gibco) and 1.6 µl lipofectamine 3000 reagents (Thermo Fisher Scientific) and incubated for 20 min at RT. The mixtures were added to the cells with 0.5 ml of fresh medium. When lipofectamine was not used, the aggregates were mixed with 0.5 ml of fresh medium and added directly to the cells replacing the medium. After 16–20 h (when using lipofectamine) or 48 h (without lipofectamine or when using the PLTau-YT reporter cells), cells were processed for FRET signal analysis by flow cytometry or fluorescence microscopy imaging. When heparin was used to block HSPGs receptors, 1 µg of TauRD or TauRD/Clu aggregates were pre-incubated with different concentrations of heparin in 0.5 ml medium for 16 h at 4 °C[57]. After incubation, mixtures were added to the cells by exchanging the medium and 48 h later the FRET signal of seeded aggregates was analyzed by flow cytometry.

Quantification of FRET positive cells by flow cytometry: cells were harvested with TrypL Express Enzyme (Gibco), washed with PBS once, and resuspended in PBS for analysis with an Attune NxT flow cytometer (Thermo Fisher Scientific). To measure the mTurquoise2 and FRET fluorescence signals, cells were excited with 405 nm laser light and fluorescence was determined using 440/50 and 530/30 filters, respectively. To measure the YFP fluorescence signal, cells were excited at 488 nm and emission was recorded using a 530/30 filter. For each sample, 50,000 single cells were analyzed. Data processing was performed using FlowJo V9 and V10.7.1 software (FlowJo LLC). After gating single cells, an additional gate was introduced to exclude YFP-only cells that show a false-positive signal in the FRET channel due to excitation at 405 nm[93]. The FRET positive gate was set by plotting the FRET fluorescence signal versus the mTurquoise2 fluorescence signal using as reference non-seeded cells (Supplementary Fig. 10).A more detailed protocol and the original .fcs files can be found here, https://edmond.mpdl.mpg.de/imeji/collection/3psV1MQj0fmYu5KS0

Fluorescence microscopy imaging: cells were fixed with 4% paraformaldehyde (PFA) in PBS for 10 min, washed with PBS, and permeabilized with 0.1% Triton-X100/PBS for 5 min. Nuclei were stained with NucBlue Fixed Cell ReadyProbes Reagent (Thermo Fisher Scientific) following the manufacturer's instructions, and the coverslips were mounted with Dako fluorescence mounting medium (Agilent). Confocal imaging was performed as described below (immunofluorescence microscopy).

When lysates from cells containing aggregates were used as seeding material, cell pellets were lysed with 0.05% Triton X-100/PBS, Complete EDTA-free protease inhibitor cocktail (MERK) and benzonase for 20 min on ice, total protein was quantified by Bio-Rad Protein Assay (Bio-Rad) and the amount of Tau protein was quantified by SDS-PAGE and immunoblotting using purified Tau as standard.

Seeding of primary neurons: 70 ng of TauRD aggregates mixed with fresh medium (one-tenth of the medium in the well) were directly added to the neuronal cultures in 24-well plates at DIV 13. After 4 days of incubation (DIV 17), coverslips were processed as described below (immunofluorescence microscopy).

Seeding of α-Syn aggregation: HEK293T and SH-SY5Y cells expressing EGFP-α-Syn(A53T) were seeded in a 24-well plate containing a coverslip and α-Syn aggregates were transfected after 24 h using lipofectamine 2000 (Thermo Fisher Scientific). For HEK293T cells, seed material containing 200 ng of α-Syn was diluted into a mixture of 25 µl Opti-MEM (Gibco) and 1.5 µl lipofectamine. Subsequently, the suspension was added to 0.5 ml of cell culture. For SH-SY5Y cells, seed material containing 10 µg of α-Syn was diluted into a mixture of 25 µl of Opti-MEM (Gibco) and 1.5 µl of lipofectamine. Subsequently, the suspension was added to 0.5 ml of cell culture. After 24 h cells were processed for fluorescence microscopy imaging as described below and confocal imaging was performed (immunofluorescence microscopy). When heparin was used to block HSPGs receptors in seeding experiments without lipofectamine, 50 µg of α-Syn or α-Syn/Clu aggregates were pre-incubated with or without heparin (200 µg/ml) in 0.5 ml medium for 2 h at room temperature, followed by addition to the cells by the medium exchange. The medium was replaced after 24 h to limit the toxicity otherwise observed with 50 µg of α-Syn. After further 48 h cells were processed for fluorescence microscopy as described below and confocal imaging was performed (immunofluorescence microscopy).

Amyloid staining. Cells were fixed with 4% PFA/PBS for 10 min, washed with PBS, and permeabilized with 0.25% Triton-X100/PBS for 30 min. Coverslips were incubated with 1 µM X-34 (Sigma) in 60% PBS, 39% ethanol, 0.02 M NaOH for 15 min, washed three times with 60% PBS, 39% ethanol, 0.02 M NaOH followed by two washes with PBS, and mounted with Dako fluorescence mounting medium (Agilent).

Immunofluorescence microscopy. Cells were fixed with 4% PFA/PBS for 10 min, washed with PBS, and permeabilized with 0.1% Triton-X100/PBS for 5 min. Blocking solution (8% BSA/PBS) was added for 30 min. Coverslips were transferred to a humid chamber and incubated overnight with the primary antibody diluted in 1% BSA/PBS (anti-phospho-Tau AT8, MN1020, Thermo Fisher Scientific, 1:100 dilution; anti-CHMP2A, 10477-1-AP, Proteintech, 1:50 dilution; anti-Galectin 8, ab109519, Abcam, 1:50 dilution). Cells were then washed with 0.1% Tween-20/PBS, incubated with the corresponding secondary antibody (F(ab')2-Goat anti-Mouse IgG Alexa Fluor 633 (A-21053); goat-anti Rabbit IgG Alexa Fluor 405 (A-31556), Thermo Fisher Scientific) diluted in 1% BSA/PBS (1:500) for 1 h, washed with 0.1% Tween-20/PBS and stained with NucBlue Fixed Cell ReadyProbes Reagent (Thermo Fisher Scientific) in the case of using anti-phospho-Tau AT8 antibody. Coverslips were mounted with Dako fluorescence mounting medium (Agilent). The confocal imaging was performed at the Imaging Facility of Max Planck Institute of Biochemistry, Martinsried, on a LEICA TCS SP8 AOBS confocal laser scanning microscope (Wetzlar, Germany) equipped with a LEICA HCX PL APO 63×/NA1.4 oil immersion objective. Images were analyzed with Image J (Rasband, W.S., National Institutes of Health, USA).

To detect colocalization of TauRD-A532/Clu-A647 with endogenous TauRD-mTurq aggregates, a series of z-stack images were acquired and then deconvolved using Huygens Essentials 19.10 (Scientific Volume Imaging). Three-dimensional volume renderings were generated using Volocity V6.3 (Quorum Technologies).

Aggregate formation in primary neurons: neurons were fixed at DIV 17 with 4% PFA/PBS for 20 min; remaining free groups of PFA were blocked with 50 mM ammonium chloride in PBS for 10 min at RT. Cells were rinsed once with PBS and permeabilized with 0.25% Triton X-100/PBS for 5 min. After washing with PBS, a blocking solution consisting of 2% BSA (w/v) (Roth) and 4% donkey serum (v/v) (Jackson Immunoresearch Laboratories) in PBS was added for 30 min at RT. Coverslips were transferred to a light-protected humid chamber and incubated in anti-MAP2 (NB300-213, Novus Biologicals) primary antibody diluted in blocking solution (1:500) for 1 h. Cells were washed with PBS and incubated with the secondary antibody Alexa Fluor 647 AffiniPure Donkey Anti-Chicken IgY (IgG) (703-605-155, Jackson Immunoresearch Laboratories) diluted 1:250 in blocking solution, with 0.5 µg ml^{-1} DAPI added to stain the nuclei. Coverslips were mounted on Menzer glass slides using Prolong Glass fluorescence mounting medium. Confocal images were obtained at an SP8 confocal microscope (Leica).

In the case of α-Syn seeding experiments, HEK293T and SH-SY5Y cells were imaged at a CorrSight microscope (Thermo Fisher) in spinning disc mode with a 63x oil immersion objective. Images were acquired with MAPS software (Thermo Fisher) and afterward analyzed by Image J. Cells were counted manually and α-Syn accumulations with high fluorescence intensity and a diameter larger than 500 nm were considered aggregates. Fractions containing aggregates were calculated by using Origin Pro 2019b.

Immunoprecipitation. PLTau-YT cells were lysed with 0.05% Triton X-100/PBS with Complete, Mini, EDTA-free Protease Inhibitor Cocktail (Merck), PhosSTOP (Merck), and benzonase for 20 min on ice. Total protein was quantified (Bio-Rad protein assay) and the amount of PLTau protein was quantified by SDS-PAGE and quantitative immunoblotting with purified PLTau as standard. Lysates were diluted in PBS (400 µl at 3 mg/ml total protein) and incubated with or without Clu (molar ratio PLTauYT:Clu 1:1) for 16 h at 37 °C. Immunoprecipitation was then performed with Dynabeads Protein G Immunoprecipitation Kit (Sigma-Aldrich) following the manufacturer's instructions. Briefly, 25 µl of magnetic beads were incubated with 5 µg of phospho-Tau antibody (AT8 antibody, MN1020, Thermo Fisher Scientific) in antibody binding and washing buffer with rotation for 30 min at room temperature. The beads were then washed and incubated with cell lysate with rotation for 1.5 h at room temperature. After incubation, the beads were washed 3 times with washing buffer, transferred to a clean tube, and elution was performed by addition of 40 µl sample buffer/100 mM DTT to the beads and incubation at 70 °C for 10 min. 5 µl of 1.5 M Tris pH 8.8 was added to the elution after removal of the magnetic beads. Samples (13 µl of eluate and 2 µl of lysate as input) were subsequently analyzed by SDS-PAGE and immunoblotting as described above (Sodium dodecyl sulfate-polyacrylamide gel electrophoresis (SDS-PAGE) and immunoblotting).

Neuronal viability measurements. At DIV 13, 11 ng of TauRD aggregates mixed with fresh medium (one-tenth of the medium in the well) were directly added to the neuronal cultures in 96-well plates. Viability was determined with the MTT assay using thiazolyl blue tetrazolium bromide (MTT) reagent (Sigma-Aldrich). The cell medium was exchanged for 100 µl of fresh medium. Subsequently, 20 µl of 5 mg ml^{-1} MTT in PBS was added and incubated for 2–4 h at 37 °C, 5% CO_2. Subsequently, 100 µl solubilizer solution (10% SDS, 45% dimethylformamide in water, pH 4.5) was added, and on the following day, absorbance was measured at 570 nm. Each condition was measured in six replicates per experiment and absorbance values were averaged for each experiment.

Electron microscopy. For negative stain analysis, continuous carbon grids (Quantfoil) were glow discharged using a plasma cleaner (PDC-3XG, Harrick) for 30 s. Grids were incubated for 5 min with Tau samples, blotted and stained with

0.5% uranyl acetate solution, dried, and imaged in a Titan Halo (PEI) transmission electron microscope using SerialEM.

In the case of α-Syn, grids were incubated for 1 min with the samples, blotted, and subsequently washed two times with water for 10 s. The blotted grids were stained with 0.5% uranyl acetate solution, dried, and imaged in a Polara cryo-electron microscope (PEI) at 300 kV using SerialEM.

Statistical analysis. Statistical analysis was performed with Sigma Plot 14.0 or GraphPrism6. Sample size (*n*) given in figure legends describe measurements taken from distinct, independent samples. Normality was assessed in all cases. Log-transformation was applied on Bafilomycin treatment data to conform to normal distribution prior to statistical analysis. A two-tailed Student's *t*-test was used for simple comparisons. One-way ANOVA with Bonferroni post hoc test or Two-way ANOVA with Sidak post hoc test was used for multiple comparisons.

Reporting summary. Further information on research design is available in the Nature Research Reporting Summary linked to this article.

Data availability

All data supporting the findings of this study are available within the manuscript. Other data are available from the corresponding author upon reasonable request. Source data are provided with this paper.

Received: 26 January 2021; Accepted: 16 July 2021;
Published online: 11 August 2021

References

1. Peng, C., Trojanowski, J. Q. & Lee, V. M. Protein transmission in neurodegenerative disease. *Nat. Rev. Neurol.* **16**, 199–212 (2020).
2. Jucker, M. & Walker, L. C. Propagation and spread of pathogenic protein assemblies in neurodegenerative diseases. *Nat. Neurosci.* **21**, 1341–1349 (2018).
3. Vaquer-Alicea, J. & Diamond, M. I. Propagation of protein aggregation in neurodegenerative diseases. *Annu. Rev. Biochem.* **88**, 785–810 (2019).
4. Iadanza, M. G., Jackson, M. P., Hewitt, E. W., Ranson, N. A. & Radford, S. E. A new era for understanding amyloid structures and disease. *Nat. Rev. Mol. Cell Biol.* **19**, 755–773 (2018).
5. Sibilla, C. & Bertolotti, A. Prion properties of SOD1 in amyotrophic lateral sclerosis and potential therapy. *Cold Spring Harb Perspect Biol* **9**, https://doi.org/10.1101/cshperspect.a024141 (2017).
6. Wang, Y. et al. The release and trans-synaptic transmission of Tau via exosomes. *Mol. Neurodegener.* **12**, 5 (2017).
7. Brunello, C. A., Merezhko, M., Uronen, R. L. & Huttunen, H. J. Mechanisms of secretion and spreading of pathological tau protein. *Cell Mol. Life Sci.* **77**, 1721–1744 (2020).
8. Chaplot, K., Jarvela, T. S. & Lindberg, I. Secreted chaperones in neurodegeneration. *Front Aging Neurosci.* **12**, 268 (2020).
9. Foster, E. M., Dangla-Valls, A., Lovestone, S., Ribe, E. M. & Buckley, N. J. Clusterin in Alzheimer's disease: mechanisms, genetics, and lessons from other pathologies. *Front. Neurosci.* **13**, 164 (2019).
10. Wyatt, A. R., Yerbury, J. J., Ecroyd, H. & Wilson, M. R. Extracellular chaperones and proteostasis. *Annu Rev. Biochem* **82**, 295–322 (2013).
11. Lee, K. W. et al. Clusterin regulates transthyretin amyloidosis. *Biochem. Biophys. Res. Commun.* **388**, 256–260 (2009).
12. Narayan, P. et al. The extracellular chaperone clusterin sequesters oligomeric forms of the amyloid-beta(1-40) peptide. *Nat. Struct. Mol. Biol.* **19**, 79–83 (2011).
13. Gregory, J. M. et al. Clusterin protects neurons against intracellular proteotoxicity. *Acta Neuropathol. Commun.* **5**, 81 (2017).
14. Yerbury, J. J. et al. The extracellular chaperone clusterin influences amyloid formation and toxicity by interacting with prefibrillar structures. *FASEB J.* **21**, 2312–2322 (2007).
15. Yu, J. T. & Tan, L. The role of clusterin in Alzheimer's disease: pathways, pathogenesis, and therapy. *Mol. Neurobiol.* **45**, 314–326 (2012).
16. Lambert, J. C. et al. Genome-wide association study identifies variants at CLU and CR1 associated with Alzheimer's disease. *Nat. Genet.* **41**, 1094–1099 (2009).
17. Harold, D. et al. Genome-wide association study identifies variants at CLU and PICALM associated with Alzheimer's disease. *Nat. Genet.* **41**, 1088–1093 (2009).
18. DeMattos, R. B. et al. Clusterin promotes amyloid plaque formation and is critical for neuritic toxicity in a mouse model of Alzheimer's disease. *Proc. Natl Acad. Sci. USA* **99**, 10843–10848 (2002).
19. Wojtas, A. M. et al. Loss of clusterin shifts amyloid deposition to the cerebrovasculature via disruption of perivascular drainage pathways. *Proc. Natl Acad. Sci. USA* **114**, E6962–E6971 (2017).
20. Oh, S. B. et al. Clusterin contributes to early stage of Alzheimer's disease pathogenesis. *Brain Pathol.* **29**, 217–231 (2019).
21. Qi, X. M., Wang, C., Chu, X. K., Li, G. & Ma, J. F. Intraventricular infusion of clusterin ameliorated cognition and pathology in Tg6799 model of Alzheimer's disease. *BMC Neurosci.* **19**, 2 (2018).
22. Fernandez-de-Retana, S. et al. Characterization of ApoJ-reconstituted high-density lipoprotein (rHDL) nanodisc for the potential treatment of cerebral beta-amyloidosis. *Sci. Rep.* **7**, 14637 (2017).
23. Montoliu-Gaya, L. et al. Differential effects of apoE and apoJ mimetic peptides on the action of an anti-Abeta scFv in 3xTg-AD mice. *Biochem. Pharm.* **155**, 380–392 (2018).
24. Killick, R. et al. Clusterin regulates beta-amyloid toxicity via Dickkopf-1-driven induction of the wnt-PCP-JNK pathway. *Mol. Psychiatry* **19**, 88–98 (2014).
25. Robbins, J. P. et al. Clusterin is required for beta-amyloid toxicity in human iPSC-derived neurons. *Front Neurosci.* **12**, 504 (2018).
26. May, P. C. et al. Dynamics of gene expression for a hippocampal glycoprotein elevated in Alzheimer's disease and in response to experimental lesions in rat. *Neuron* **5**, 831–839 (1990).
27. Nilselid, A. M. et al. Clusterin in cerebrospinal fluid: analysis of carbohydrates and quantification of native and glycosylated forms. *Neurochem Int.* **48**, 718–728 (2006).
28. Choi-Miura, N. H. et al. SP-40,40 is a constituent of Alzheimer's amyloid. *Acta Neuropathol.* **83**, 260–264 (1992).
29. McGeer, P. L., Kawamata, T. & Walker, D. G. Distribution of clusterin in Alzheimer brain tissue. *Brain Res.* **579**, 337–341 (1992).
30. Giannakopoulos, P. et al. Possible neuroprotective role of clusterin in Alzheimer's disease: a quantitative immunocytochemical study. *Acta Neuropathol.* **95**, 387–394 (1998).
31. Itakura, E., Chiba, M., Murata, T. & Matsuura, A. Heparan sulfate is a clearance receptor for aberrant extracellular proteins. *J Cell Biol* **219**, https://doi.org/10.1083/jcb.201911126 (2020).
32. Yeh, F. L., Wang, Y., Tom, I., Gonzalez, L. C. & Sheng, M. TREM2 binds to apolipoproteins, including APOE and CLU/APOJ, and thereby facilitates uptake of amyloid-beta by microglia. *Neuron* **91**, 328–340 (2016).
33. Bell, R. D. et al. Transport pathways for clearance of human Alzheimer's amyloid beta-peptide and apolipoproteins E and J in the mouse central nervous system. *J. Cereb. Blood Flow. Metab.* **27**, 909–918 (2007).
34. Thambisetty, M. et al. Association of plasma clusterin concentration with severity, pathology, and progression in Alzheimer disease. *Arch. Gen. Psychiatry* **67**, 739–748 (2010).
35. Schrijvers, E. M., Koudstaal, P. J., Hofman, A. & Breteler, M. M. Plasma clusterin and the risk of Alzheimer disease. *JAMA* **305**, 1322–1326 (2011).
36. Braak, H., Thal, D. R., Ghebremedhin, E. & Del Tredici, K. Stages of the pathologic process in Alzheimer disease: age categories from 1 to 100 years. *J. Neuropathol. Exp. Neurol.* **70**, 960–969 (2011).
37. Arriagada, P. V., Growdon, J. H., Hedley-Whyte, E. T. & Hyman, B. T. Neurofibrillary tangles but not senile plaques parallel duration and severity of Alzheimer's disease. *Neurology* **42**, 631–639 (1992).
38. Nelson, P. T. et al. Correlation of Alzheimer disease neuropathologic changes with cognitive status: a review of the literature. *J. Neuropathol. Exp. Neurol.* **71**, 362–381 (2012).
39. Hsieh, Y. C. et al. Tau-mediated disruption of the spliceosome triggers cryptic RNA splicing and neurodegeneration in Alzheimer's disease. *Cell Rep.* **29**, 301–316 e310 (2019).
40. Wojtas, A. M. et al. Clusterin ameliorates tau pathology in vivo by inhibiting fibril formation. *Acta Neuropathol. Commun.* **8**, 210 (2020).
41. Holmes, B. B. et al. Proteopathic tau seeding predicts tauopathy in vivo. *Proc. Natl Acad. Sci. USA* **111**, E4376–E4385 (2014).
42. Barghorn, S. & Mandelkow, E. Toward a unified scheme for the aggregation of tau into Alzheimer paired helical filaments. *Biochemistry* **41**, 14885–14896 (2002).
43. von Bergen, M., Barghorn, S., Biernat, J., Mandelkow, E. M. & Mandelkow, E. Tau aggregation is driven by a transition from random coil to beta sheet structure. *Biochim. Biophys. Acta* **1739**, 158–166 (2005).
44. Scheres, S. H., Zhang, W., Falcon, B. & Goedert, M. Cryo-EM structures of tau filaments. *Curr. Opin. Struct. Biol.* **64**, 17–25 (2020).
45. Goedert, M. et al. Assembly of microtubule-associated protein tau into Alzheimer-like filaments induced by sulphated glycosaminoglycans. *Nature* **383**, 550–553 (1996).
46. Arosio, P., Knowles, T. P. & Linse, S. On the lag phase in amyloid fibril formation. *Phys. Chem. Chem. Phys.* **17**, 7606–7618 (2015).
47. Mok, S. A. et al. Mapping interactions with the chaperone network reveals factors that protect against tau aggregation. *Nat. Struct. Mol. Biol.* **25**, 384–393 (2018).

48. Iqbal, K., Liu, P. & Gong, C. X. Tau and neurodegenerative disease: the story so far. *Nat. Rev. Neurol.* **12**, 15–27 (2016).
49. Goedert, M., Jakes, R. & Vanmechelen, E. Monoclonal antibody AT8 recognises tau protein phosphorylated at both serine 202 and threonine 205. *Neurosci. Lett.* **189**, 167–169 (1995).
50. Wischik, C. M. et al. Structural characterization of the core of the paired helical filament of Alzheimer disease. *Proc. Natl Acad. Sci. USA* **85**, 4884–4888 (1988).
51. Dujardin, S. et al. Tau molecular diversity contributes to clinical heterogeneity in Alzheimer's disease. *Nat. Med.* **26**, 1256–1263 (2020).
52. Dujardin, S. & Hyman, B. T. Tau prion-like propagation: state of the art and current challenges. *Adv. Exp. Med. Biol.* **1184**, 305–325 (2019).
53. Kumar, S. et al. Stages and conformations of the Tau repeat domain during aggregation and its effect on neuronal toxicity. *J. Biol. Chem.* **289**, 20318–20332 (2014).
54. Chen, J. J. et al. Compromised function of the ESCRT pathway promotes endolysosomal escape of tau seeds and propagation of tau aggregation. *J. Biol. Chem.* **294**, 18952–18966 (2019).
55. Falcon, B., Noad, J., McMahon, H., Randow, P. & Goedert, M. Galectin-8-mediated selective autophagy protects against seeded tau aggregation. *J. Biol. Chem.* **293**, 2438–2451 (2018).
56. Rauch, J. N. et al. Tau internalization is regulated by 6-O sulfation on heparan sulfate proteoglycans (HSPGs). *Sci. Rep.* **8**, 6382 (2018).
57. Holmes, B. B. et al. Heparan sulfate proteoglycans mediate internalization and propagation of specific proteopathic seeds. *Proc. Natl Acad. Sci. USA* **110**, E3138–E3147 (2013).
58. Flavin, W. P. et al. Endocytic vesicle rupture is a conserved mechanism of cellular invasion by amyloid proteins. *Acta Neuropathol.* **134**, 629–653 (2017).
59. Yoshimori, T., Yamamoto, A., Moriyama, Y., Futai, M. & Tashiro, Y. Bafilomycin A1, a specific inhibitor of vacuolar-type H(+)-ATPase, inhibits acidification and protein degradation in lysosomes of cultured cells. *J. Biol. Chem.* **266**, 17707–17712 (1991).
60. Thiele, D. L. & Lipsky, P. E. Mechanism of L-leucyl-L-leucine methyl ester-mediated killing of cytotoxic lymphocytes: dependence on a lysosomal thiol protease, dipeptidyl peptidase I, that is enriched in these cells. *Proc. Natl Acad. Sci. USA* **87**, 83–87 (1990).
61. Alavi Naini, S. M. & Soussi-Yanicostas, N. Heparan sulfate as a therapeutic target in tauopathies: insights from zebrafish. *Front Cell Dev. Biol.* **6**, 163 (2018).
62. Hurley, J. H. ESCRTs are everywhere. *EMBO J.* **34**, 2398–2407 (2015).
63. Thurston, T. L., Wandel, M. P., von Muhlinen, N., Foeglein, A. & Randow, F. Galectin 8 targets damaged vesicles for autophagy to defend cells against bacterial invasion. *Nature* **482**, 414–418 (2012).
64. Whiten, D. R. et al. Single-molecule characterization of the interactions between extracellular chaperones and toxic alpha-synuclein oligomers. *Cell Rep.* **23**, 3492–3500 (2018).
65. Nachman, E. et al. Disassembly of Tau fibrils by the human Hsp70 disaggregation machinery generates small seeding-competent species. *J. Biol. Chem.* **295**, 9676–9690 (2020).
66. Takeda, S. et al. Seed-competent high-molecular-weight tau species accumulates in the cerebrospinal fluid of Alzheimer's disease mouse model and human patients. *Ann. Neurol.* **80**, 355–367 (2016).
67. Wang, C. et al. Selective removal of astrocytic APOE4 strongly protects against tau-mediated neurodegeneration and decreases synaptic phagocytosis by microglia. *Neuron*, https://doi.org/10.1016/j.neuron.2021.03.024 (2021).
68. Litvinchuk, A. et al. Apolipoprotein E4 reduction with antisense oligonucleotides decreases neurodegeneration in a tauopathy model. *Ann. Neurol.* **89**, 952–966 (2021).
69. Shi, Y. et al. ApoE4 markedly exacerbates tau-mediated neurodegeneration in a mouse model of tauopathy. *Nature* **549**, 523–527 (2017).
70. Zhao, N. et al. APOE epsilon2 is associated with increased tau pathology in primary tauopathy. *Nat. Commun.* **9**, 4388 (2018).
71. Kwon, M. J. et al. Deficiency of clusterin exacerbates high-fat diet-induced insulin resistance in male mice. *Endocrinology* **155**, 2089–2101 (2014).
72. DeMattos, R. B. et al. ApoE and clusterin cooperatively suppress Abeta levels and deposition: evidence that ApoE regulates extracellular Abeta metabolism in vivo. *Neuron* **41**, 193–202 (2004).
73. Stone, D. J., Rozovsky, I., Morgan, T. E., Anderson, C. P. & Finch, C. E. Increased synaptic sprouting in response to estrogen via an apolipoprotein E-dependent mechanism: implications for Alzheimer's disease. *J. Neurosci.* **18**, 3180–3185 (1998).
74. An, N. et al. Synergistic effects of APOE and CLU may increase the risk of Alzheimer's disease: acceleration of atrophy in the volumes and shapes of the hippocampus and amygdala. *J. Alzheimers Dis.* **80**, 1311–1327 (2021).
75. Lenzi, C. et al. The down-regulation of clusterin expression enhances the alphasynuclein aggregation process. *Int J Mol Sci* **21**, https://doi.org/10.3390/ijms21197181 (2020).
76. Pilippini, A. et al. Extracellular clusterin limits the uptake of alpha-synuclein fibrils by murine and human astrocytes. *Glia*, https://doi.org/10.1002/glia.23920 (2020).
77. Vranova, H. P. et al. CSF markers of neurodegeneration in Parkinson's disease. *J. Neural Transm.* **117**, 1177–1181 (2010).
78. Buchman, A. S. et al. Progressive parkinsonism in older adults is related to the burden of mixed brain pathologies. *Neurology* **92**, E1821–E1830 (2019).
79. Irwin, D. J., Lee, V. M. Y. & Trojanowski, J. Q. Parkinson's disease dementia: convergence of alpha-synuclein, tau and amyloid-beta pathologies. *Nat. Rev. Neurosci.* **14**, 626–636 (2013).
80. Goedhart, J. et al. Structure-guided evolution of cyan fluorescent proteins towards a quantum yield of 93%. *Nat. Commun.* **3**, 751 (2012).
81. Hoover, B. R. et al. Tau mislocalization to dendritic spines mediates synaptic dysfunction independently of neurodegeneration. *Neuron* **68**, 1067–1081 (2010).
82. Catanzariti, A. M., Soboleva, T. A., Jans, D. A., Board, P. G. & Baker, R. T. An efficient system for high-level expression and easy purification of authentic recombinant proteins. *Protein Sci.* **13**, 1331–1339 (2004).
83. Hedgepeth, C. M. et al. Activation of the Wnt signaling pathway: a molecular mechanism for lithium action. *Dev. Biol.* **185**, 82–91 (1997).
84. Rospigliosi, C. C. et al. E46K Parkinson's-linked mutation enhances C-terminal-to-N-terminal contacts in alpha-synuclein. *J. Mol. Biol.* **388**, 1022–1032 (2009).
85. Furlong, R. A., Narain, Y., Rankin, J., Wyttenbach, A. & Rubinsztein, D. C. Alpha-synuclein overexpression promotes aggregation of mutant huntingtin. *Biochem J.* **346**, 577–581 (2000).
86. Durocher, Y., Perret, S. & Kamen, A. High-level and high-throughput recombinant protein production by transient transfection of suspension-growing human 293-EBNA1 cells. *Nucleic Acids Res.* **30**, E9 (2002).
87. Li, Z., Michael, I. P., Zhou, D., Nagy, A. & Rini, J. M. Simple piggyBac transposon-based mammalian cell expression system for inducible protein production. *Proc. Natl Acad. Sci. USA* **110**, 5004–5009 (2013).
88. Trinkaus, V. A. et al. In situ architecture of neuronal alpha-Synuclein inclusions. *Nat. Commun.* **12**, 2110 (2021).
89. Volpicelli-Daley, L. A., Luk, K. C. & Lee, V. M. Addition of exogenous alpha-synuclein preformed fibrils to primary neuronal cultures to seed recruitment of endogenous alpha-synuclein to Lewy body and Lewy neurite-like aggregates. *Nat. Protoc.* **9**, 2135–2146 (2014).
90. Imamoglu, R., Balchin, D., Hayer-Hartl, M. & Hartl, F. U. Bacterial Hsp70 resolves misfolded states and accelerates productive folding of a multi-domain protein. *Nat. Commun.* **11**, 365 (2020).
91. Gupta, A. J., Haldar, S., Milicic, G., Hartl, F. U. & Hayer-Hartl, M. Active cage mechanism of chaperonin-assisted protein folding demonstrated at single-molecule level. *J. Mol. Biol.* **426**, 2739–2754 (2014).
92. Wilkins, D. K. et al. Hydrodynamic radii of native and denatured proteins measured by pulse field gradient NMR techniques. *Biochemistry* **38**, 16424–16431 (1999).
93. Banning, C. et al. A flow cytometry-based FRET assay to identify and analyse protein-protein interactions in living cells. *PLoS ONE* **5**, e9344 (2010).

Acknowledgements

We thank Marc Diamond for the N1-TauRD (P301L/V337M)-EYFP plasmid; Michael Gropp for the pHUE-TauRD (P301L/V337M) plasmid; Saurabh Gautam for FLTau protein; Itika Saha for sharing aggregate seeding protocols; Prof. Wolfgang Baumeister and his department for microscope support; Martin Spitaler, Markus Oster, and Giovanni Cardone from the Max Planck Institute of Biochemistry (MPIB) imaging facility for support with flow cytometry, imaging and image processing; Sabine Suppmann and Judith Scholz from the MPIB Biochemistry core facility for producing recombinant Clusterin; the MPIB cryo-EM facility for EM support; David Balchin for helpful discussion; Gopal Jayaraj for commenting on the manuscript and helpful discussion. The research leading to these results has received funding from the European Commission under Grant FP7 GA ERC- 2012-SyG_318987–ToPAG, the Deutsche Forschungsgemeinschaft (DFG, German Research Foundation) under Germany's Excellence Strategy within the framework of the Munich Cluster for Systems Neurology (EXC 2145 SyNergy—ID 390857198) and by the joint efforts of The Michael J. Fox Foundation for Parkinson's Research (MJFF) and the Aligning Science Across Parkinson's (ASAP) initiative. MJFF administers the grant ASAP-000282 on behalf of ASAP and itself. For the purpose of open access, the authors have applied a CC-BY public copyright license to the Author Accepted Manuscript version arising from this submission.

Author contributions

F.U.H. conceived the project. P.Y. designed, performed, and analyzed most of the research. V.T. conducted experiments with α-Syn. I.R. performed experiments with mouse primary neurons. R.I. conducted and analyzed dcFCCS experiments. T.S. optimized and purified recombinant Clusterin. H.W. performed Tau negative stain electron

microscopy. I.D. supervised experiments with primary neurons. M.S.H. initially co-supervised the project and commented on the manuscript. A.B. co-supervised the project and contributed to experimental design. P.Y., A.B., and F.U.H. wrote the manuscript with input from the other authors.

Funding
Open Access funding enabled and organized by Projekt DEAL.

Competing interests
The authors declare no competing interests.

Additional information
Supplementary information The online version contains supplementary material available at https://doi.org/10.1038/s41467-021-25060-1.

Correspondence and requests for materials should be addressed to F.U.H.

Peer review information *Nature Communications* thanks Lukasz Joachimiak and the other, anonymous, reviewer(s) for their contribution to the peer review of this work.

Supplementary Information

The extracellular chaperone Clusterin enhances Tau aggregate seeding in a cellular model

Patricia Yuste-Checa[1,2], Victoria A. Trinkaus[1,2,3], Irene Riera-Tur[4,5], Rahmi Imamoglu[1], Theresa F. Schaller[1,6], Huping Wang[1], Irina Dudanova[4,5], Mark S. Hipp[1,7,8], Andreas Bracher[1] and F. Ulrich Hartl[1,2,3,*]

[1]Department of Cellular Biochemistry, Max Planck Institute of Biochemistry, Am Klopferspitz 18, 82152 Martinsried, Germany.

[2]Aligning Science Across Parkinson's (ASAP) Collaborative Research Network, Chevy Chase, MD, USA.

[3]Munich Cluster for Systems Neurology (SyNergy), Munich, Germany.

[4]Department of Molecules - Signaling - Development, Max Planck Institute of Neurobiology, 82152, Martinsried, Germany.

[5]Molecular Neurodegeneration Group, Max Planck Institute of Neurobiology, 82152 Martinsried, Germany.

[6] Present address: Institute for Molecular Medicine, University Medical Center of the Johannes Gutenberg-University Mainz, Mainz, Germany.

[7]Present address: Department of Biomedical Sciences of Cells and Systems, University Medical Center Groningen, University of Groningen, Groningen, The Netherlands.

[8]Present address: School of Medicine and Health Sciences, Carl von Ossietzky University Oldenburg, Oldenburg, Germany.

[*]Correspondence to uhartl@biochem.mpg.de

Supplementary information includes 10 Supplementary Figures.

Supplementary Figures

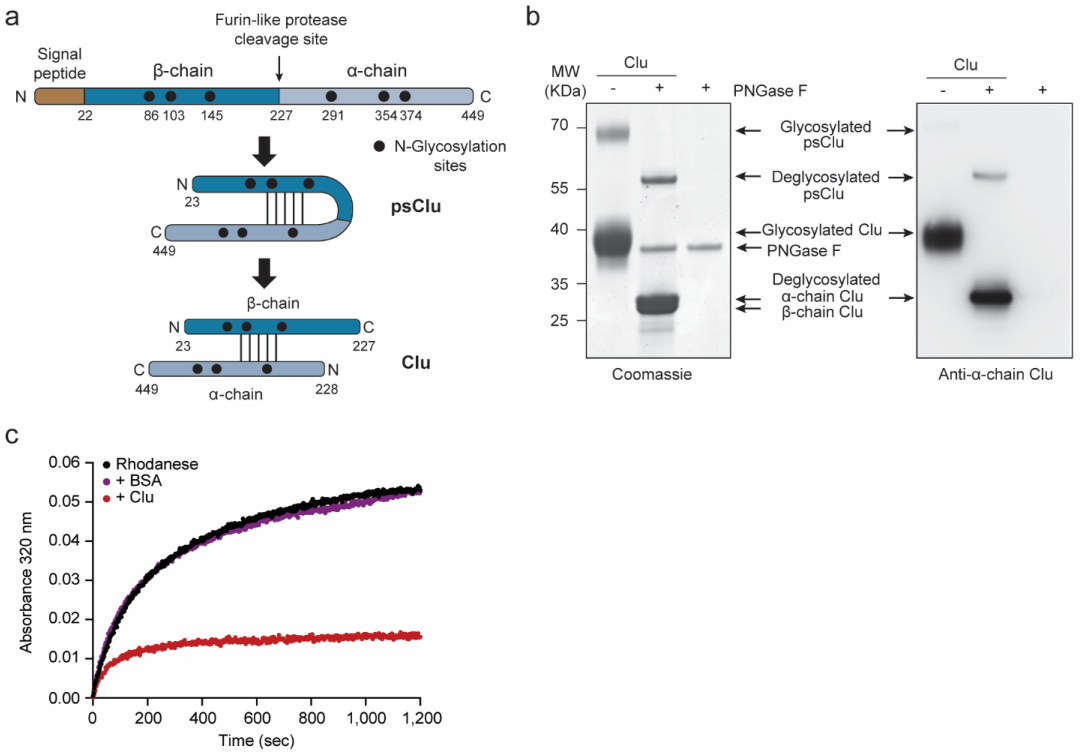

Supplementary Fig. 1: Characterization of recombinant human Clusterin. a, Biogenesis of Clu. The signal peptide (brown) is cleaved from the nascent chain during translocation into the ER, followed by N-glycosylation (black circles) and formation of five intramolecular disulfide bonds (black lines), resulting in pre-secretory Clu (psClu). During passage through the Golgi apparatus, psClu is processed into α- and β-chains (light and dark blue, respectively). Numbers represent amino acid position. **b,** Coomassie blue stain (left) and immunoblotting analysis (right) of SDS-PAGE gels showing recombinant human Clu before and after treatment with the glycosidase enzyme PNGase F. The SDS-PAGE samples were prepared under reducing conditions. The immunoblot shows staining with an antibody against an epitope in the α-chain of Clu. psClu: pre-secretory Clu. Molecular weight (MW) standards and protein bands are indicated. (n=3 independent experiments). **c,** Prevention of rhodanese aggregation by Clu. Bovine rhodanese denatured in 6M guanidine was 200-fold diluted (final concentration 0.5 μM) into buffer (20 mM MOPS-NaOH pH 7.2, 100 mM) containing either no protein (black), Clu (red) or bovine serum albumin (BSA, magenta) at 0.5 μM. Rhodanese aggregation at 25 °C was monitored by turbidity at 320 nm. Representative results are shown (n=3 independent experiments).

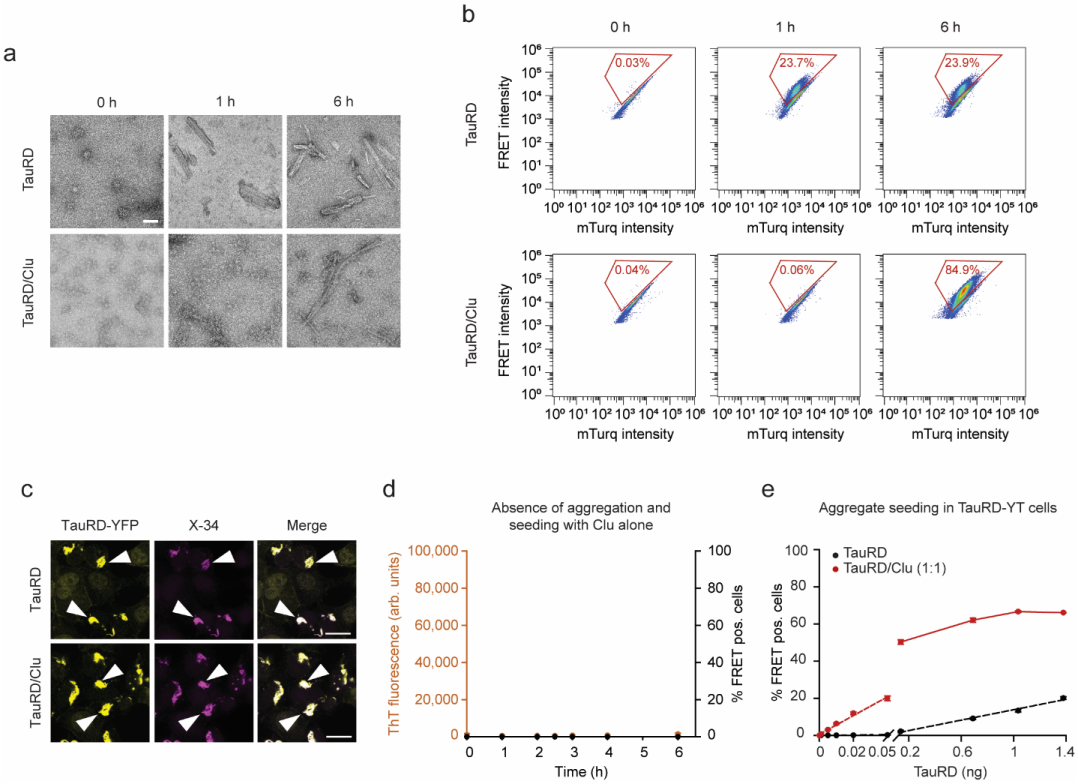

Supplementary Fig. 2: Clusterin potentiates Tau seeding competence. a, Negative-stain electron microscopy of TauRD aggregation reactions performed without or with equimolar Clu for the times indicated. Scale bar, 50 nm. (n=3 independent experiments). **b,** Flow cytometry analysis of TauRD-YT cells after seeding with TauRD or TauRD/Clu aggregation reactions. A double logarithmic pseudocolor dot plot representation of FRET intensity against mTurquoise2 (mTurq) intensity from individual cells is shown. Aggregation times are shown on top. The gate for "FRET-positive" cells is depicted in red and the % of FRET positive cells is indicated. **c,** Representative fluorescence microscopy images of seeded TauRD-YT cells stained with the amyloid dye X-34. Cells seeded with TauRD (top) and TauRD/Clu aggregation reactions (bottom). TauRD-YFP and X-34 staining signals are shown in yellow and magenta, respectively. Arrow heads indicate amyloid-positive TauRD-YFP aggregates. Scale bar, 20 µm. (n=3 independent experiments). **d,** Clu alone does not induce aggregate formation. Clu was incubated in the absence of TauRD and analyzed by ThT fluorescence (left y-axis; orange). After the times indicated, Clu samples were retrieved and used for seeding TauRD-YT cells (right y-axis; black). arb.units, arbitrary units. (n=3 independent experiments). **e,** Quantification of seeding potency of TauRD (black) and TauRD/Clu (red) aggregation reactions. The fraction of FRET-positive (pos.) cells after seeding is shown in dependence of the total amount of TauRD in the inoculum. Aliquots of aggregate reactions that had reached the plateau phase were used for seeding TauRD-YT cells (TauRD, 1 h reaction time; TauRD/Clu, 6 h reaction time, Fig. 1b).

Seeding efficiency depends linearly on TauRD amount at low concentrations of TauRD. Dashed lines represent linear fits to the data. Data represent the mean ± SEM (n=3 independent experiments).

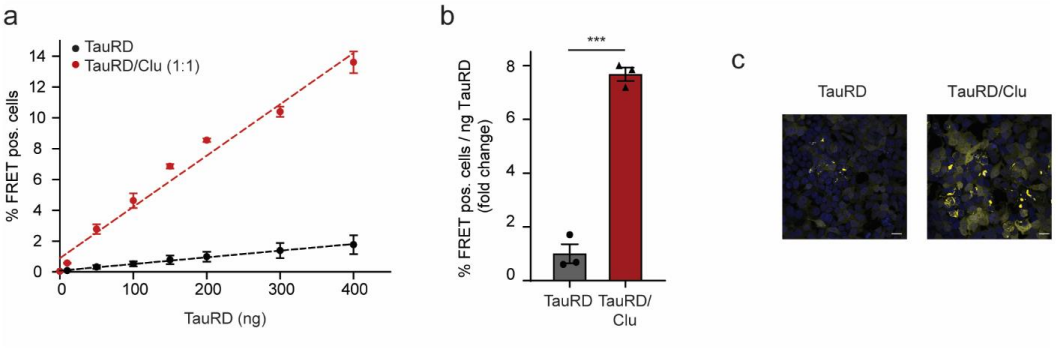

Supplementary Fig. 3: Effect of Clusterin on TauRD seeding in the absence of transfection reagent a, Quantification of seeding potency of TauRD (black) and TauRD/Clu (red) aggregation reactions in TauRD-YT cells in the absence of lipofectamine. Titration of seeding potency was performed as described in Supplementary Fig. 2e. Dashed lines represent linear fits to the data. Data represent the mean ± SEM (n=3 independent experiments). **b,** Fold change of seeding potency of TauRD aggregation reactions containing Clu (red) compared to control reactions without Clu (grey). Bar graphs represent the average slope ± SEM from the linear regression analyses described in (a). Data represent the mean ± SEM (n=3 independent experiments). ***p<0.001 ($p=1x10^{-4}$) by two-tailed Student's t-test. **c,** Fluorescence microscopy images of TauRD-YT cells seeded with 400 ng TauRD from aggregation reactions that had reached the plateau phase (TauRD, 1h reaction time; TauRD/Clu, 6 h reaction time; Fig. 1b). TauRD-YFP and DAPI nuclear staining signals are shown in yellow and blue, respectively. Scale bar, 20 µm. Experiments were performed in the absence of lipofectamine. (n=3 independent experiments).

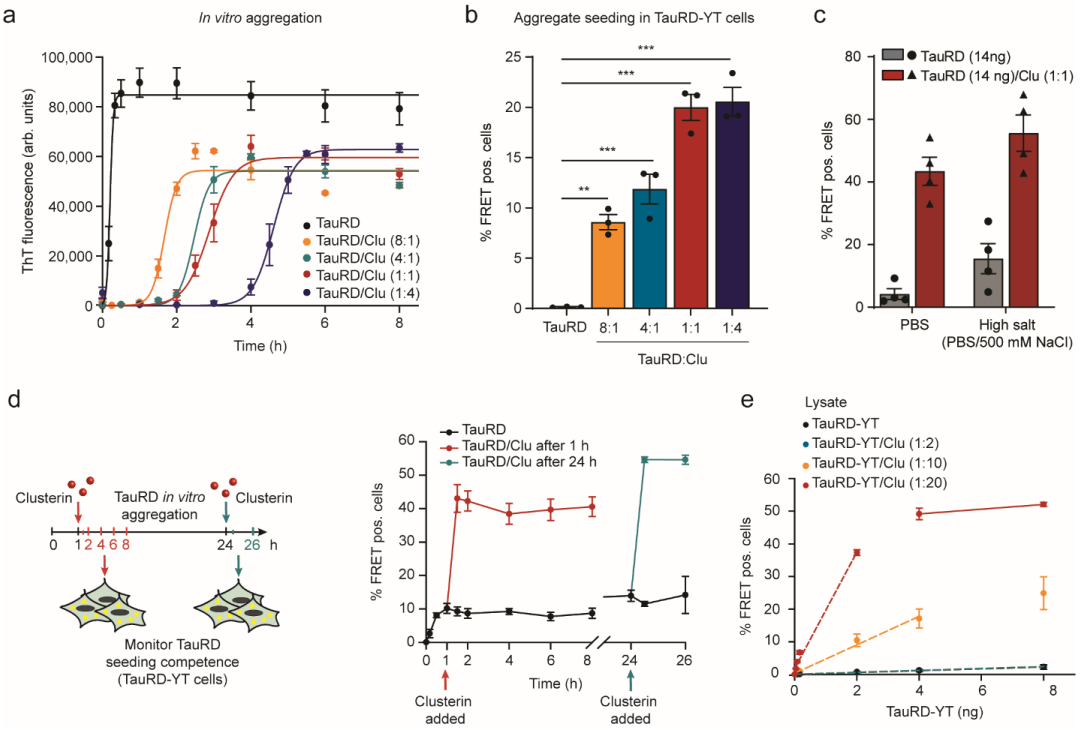

Supplementary Fig. 4: Concentration-dependent effect of Clusterin on TauRD seeding potency, on pre-formed TauRD aggregates, and effect of ionic strength on TauRD and TauRD/Clu aggregates a, Effect of Clu concentration on aggregation kinetics of TauRD as monitored by ThT fluorescence. Aggregation of TauRD (10 μM) without or with Clu (1.25 μM, 2.5 μM, 10 μM and 40 μM). Molar ratios of TauRD:Clu are indicated. Data represent the mean ± SEM (n=3 independent experiments). TauRD alone and TauRD:Clu equimolar ratio (n=10 independent experiments, Fig. 1b). arb.units, arbitrary units. **b,** Dependence of TauRD seeding capacity on Clu concentration in the aggregation reaction. Samples containing 0.05 ng TauRD from TauRD (10 μM) aggregation reactions with increasing concentrations of Clu (1.25 μM, 2.5 μM, 10 μM and 40 μM) were retrieved after reaching the plateau phase (1 h, 4 h, 6 h, 6 h and 8 h, respectively(a)) and used for seeding TauRD-YT cells. Molar ratios of TauRD:Clu are indicated. Lipofectamine was used as transfection reagent. Data represent the mean ± SEM (n=3 independent experiments). *** p<0.001; ** p<0.01 by one-way ANOVA with Bonferroni post hoc test. (TauRD vs. TauRD:Clu 8:1 p=0.0035; TauRD vs. TauRD:Clu 4:1 $p=2.5x10^{-4}$; TauRD vs. TauRD:Clu 1:1 $p=2.2x10^{-6}$; TauRD vs. TauRD:Clu 1:4 $p=1.7x10^{-6}$). **c,** Effect of ionic strength on TauRD and TauRD/Clu (14 ng TauRD, molar ratio TauRD:Clu 1:1) aggregate seeding. Aggregates (TauRD, 1h reaction time; TauRD/Clu, 6 h reaction time, Fig. 1b) were incubated for 1 h with PBS or high salt buffer (PBS/500 mM NaCl) prior to addition to TauRD-YT cells. Lipofectamine was used as transfection reagent. Data represent the mean ± SEM (n=4 independent experiments). **d,** Formation of seeds in TauRD (10 μM) aggregation reactions in the absence of Clu (black) or upon addition of Clu (10 μM) at 1 h (red) or 24 h (cyan) after starting aggregation.

The fraction of FRET-positive (pos.) cells was monitored after seeding (14 ng TauRD) with lipofectamine. Data represent the mean ± SEM (n=3 independent experiments). **e,** Titration experiment of the effect of Clu on seeding potency of TauRD-YT aggregates contained in TauRD-YT cell lysates. Whole cell lysates of FRET-positive (pos.) TauRD-YT cells were incubated with or without Clu (molar ratios TauRD-YT:Clu 1:2, 1:10 and 1:20, Fig. 1f). Titration of seeding potency was performed as described in Supplementary Fig. 2e. Dashed lines represent linear fits to the data. Data represent the mean ± SEM (n=3 independent experiments).

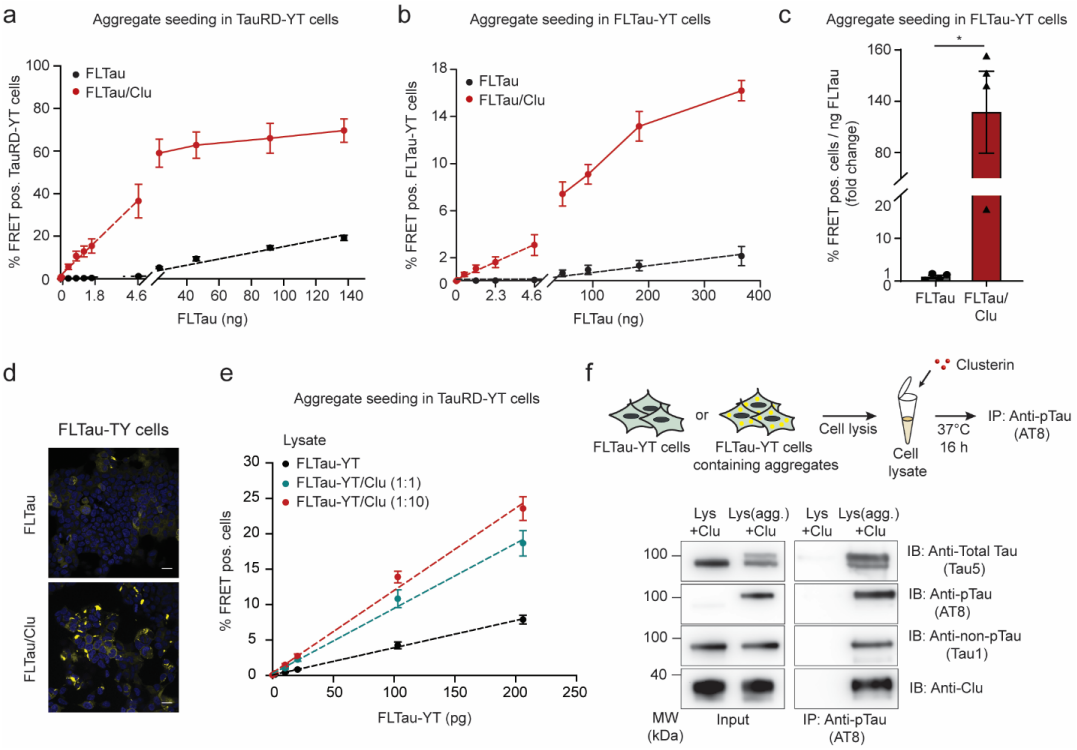

Supplementary Fig. 5: Clusterin potentiates FLTau seeding competence and binds to aggregates containing phosphorylated FLTau. **a,** Quantification of seeding potency of FLTau (black) and FLTau/Clu (red) aggregation reactions in TauRD-YT cells. Aggregate seeds were from the plateau phase of aggregation reactions (10 days, Fig. 2a). Titration of the samples was performed as described in Supplementary Fig. 2e. Dashed lines represent linear fits to the data. Data represent mean ± SEM (n=3 independent experiments). **b,** Quantification of seeding potency of FLTau (black) and FLTau/Clu (red) aggregation reactions in FLTau-YT cells. Aggregate seeds were from the plateau phase of aggregation reactions (12 days, Fig. 2a). Titration of the samples was performed as described in Supplementary Fig. 2e. Dashed lines represent linear fits to the data. Data represent mean ± SEM (n=4 independent experiments). **c,** Effect of Clu on seeding potency of FLTau aggregation reactions in FLTau-YT cells. Bar graphs represent the average slope ± SEM (n=4 independent experiments) from the linear regression analyses described in (b). *p<0.05 (p=0.0134) by two-tailed Student's t-test. **d,** Fluorescence microscopy images of FLTau-YT cells seeded with aggregation reactions (370 ng FLTau) with and without Clu. FLTau-YFP and DAPI nuclear staining signals are shown in yellow and blue, respectively. Scale bars, 20 µm. (n=3 independent experiments). **e,** Clu enhances the seeding potency of FLTau aggregates formed in FLTau-YT cells. Whole cell lysates of FRET-positive FLTau-YT cells were incubated without or with Clu (molar ratios FLTau-YT:Clu 1:1 and 1:10, Fig. 2g). Titration of the samples was performed as described in Supplementary Fig. 2e with TauRD-YT cells as recipient cells. Dashed lines represent linear fits to the data. Data represent the mean ± SEM

(n=3 independent experiments). **f,** Clu binds to Tau aggregates containing phospho-FLTau-YT. Whole cell lysates of FRET-positive FLTau-YT cells (Lys(agg.)) and naïve FLTau-YT cells (Lys) as control were incubated with Clu (molar ratio FLTau-YT:Clu 1:1) followed by p-Tau (AT8 antibody) immunoprecipitation (IP) and immunoblotting (IB) using anti-Tau5 (total Tau antibody), anti-Tau1 (non-pTau antibody), anti-AT8 (pTau antibody) and anti-Clu antibody (n=3 independent experiments). Molecular weight (MW) standards are indicated.

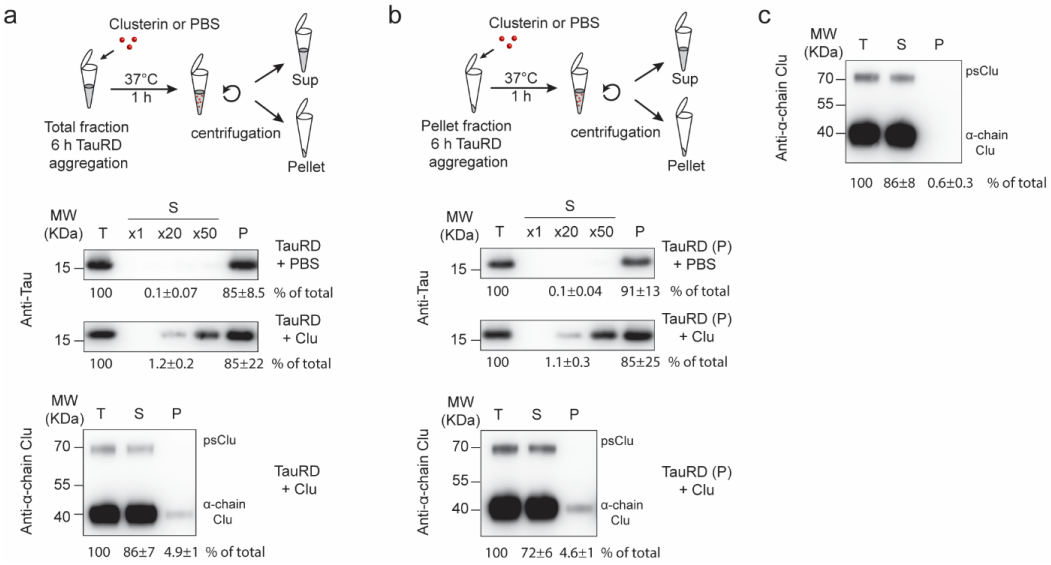

Supplementary Fig. 6: Clusterin mediates production of soluble TauRD from pre-formed TauRD aggregates. a, Effect of Clu on TauRD solubility when added to total aggregation reactions. TauRD aggregation reactions that had reached the plateau phase (6 h aggregation, Fig. 1b) were incubated either with PBS or Clu for 1 h at 37 °C. Reactions were fractionated by centrifugation. Total (T), supernatant (S) and pellet (P) fractions were analyzed by immunoblotting with antibodies against Tau (top panel) and α-chain Clu (bottom panel). psClu: pre-secretory Clu. TauRD and Clu were quantified by densitometry and amounts expressed as % of total. 20- (x20) and 50-fold (x50) amounts of supernatant were analyzed to quantify soluble TauRD. **b,** Effect of Clu on TauRD solubility when added to the insoluble fraction of aggregation reactions. Insoluble TauRD was isolated by centrifugation from an aggregation reaction that had reached the plateau phase (6 h aggregation, Fig. 1b). Insoluble TauRD was resuspended in PBS, followed by incubation with or without Clu for 1 h at 37 °C. Reactions were then fractionated and total (T), supernatant (S) and pellet (P) fractions analyzed as in (a). TauRD and Clu were quantified by densitometry and amounts expressed as % of total. **c,** Clu remains soluble in the absence of TauRD. Clu was incubated for 1 h at 37 °C as in (a) and (b) but in the absence of TauRD. The reaction was fractionated by centrifugation and analyzed by immunoblotting with anti-α-chain Clu antibody. Clu was quantified by densitometry and amounts expressed as % of total. Values represent mean ± SEM (n=3 independent experiments). Molecular weight (MW) standards are indicated.

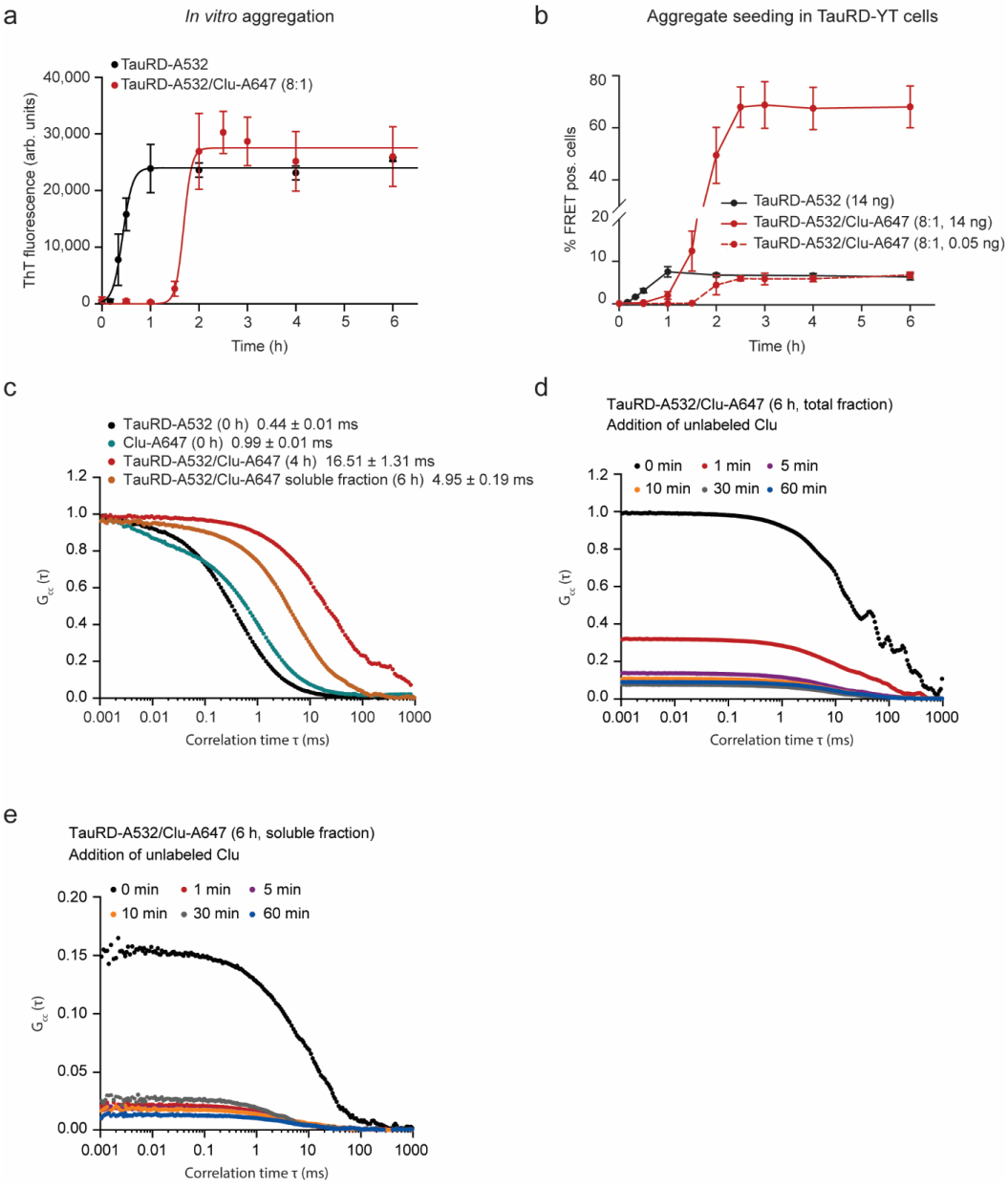

Supplementary Fig. 7: Aggregation and seeding properties of fluorescent labeled TauRD in the presence of fluorescent labeled Clu. a, Fluorescent labeled Clu delays aggregation of fluorescent labeled TauRD. Aggregation of TauRD-A532 (1 µM TauRD-A532 and 9 µM unlabeled TauRD) without (black) or with Clu-A647 (1.25 µM, red) was monitored by ThT fluorescence. Data represent the mean ± SEM (n=3 independent experiments). arb.units, arbitrary units. **b,** Fluorescent labeled Clu amplifies the seeding potency of fluorescent labeled TauRD aggregates.

Aggregation reactions as in (a) were used to seed TauRD-YT cells with lipofectamine as described in Fig. 1a. TauRD-YT cells were transfected with reactions containing 14 ng (solid lines) or 0.05 ng (dashed lines). Data represent the mean ± SEM (n=3 independent experiments). **c,** Diffusion times of TauRD/Clu complexes. Fluorescence correlation spectroscopy (FCS) of TauRD-A532 (black) and Clu-A647 (cyan) immediately upon initiation of aggregation (0 h). Dual-color fluorescence cross-correlation spectroscopy (dcFCCS) of the interaction of TauRD-A532 and Clu-A647 in the total aggregation reaction after 4 h of aggregation (a, red) and dcFCCS analysis of the interaction of TauRD-A532 and Clu-A647 in the soluble fraction after 6 h of aggregation (a, orange). Representative measurements are shown. Diffusion time ± SEM (n=4 independent experiments). **d, e,** Dynamic nature of TauRD/Clu complexes in total aggregation reactions (**d**) and in the soluble fraction of aggregation reactions (**e**). Analysis of the interaction of TauRD-A532 and Clu-A647 by dcFCCS after 6 h of aggregation either without or with addition of a 10-fold excess of unlabeled Clu and incubation for 1 min to 60 min as indicated. Representative measurements are shown (n=3 independent experiments).

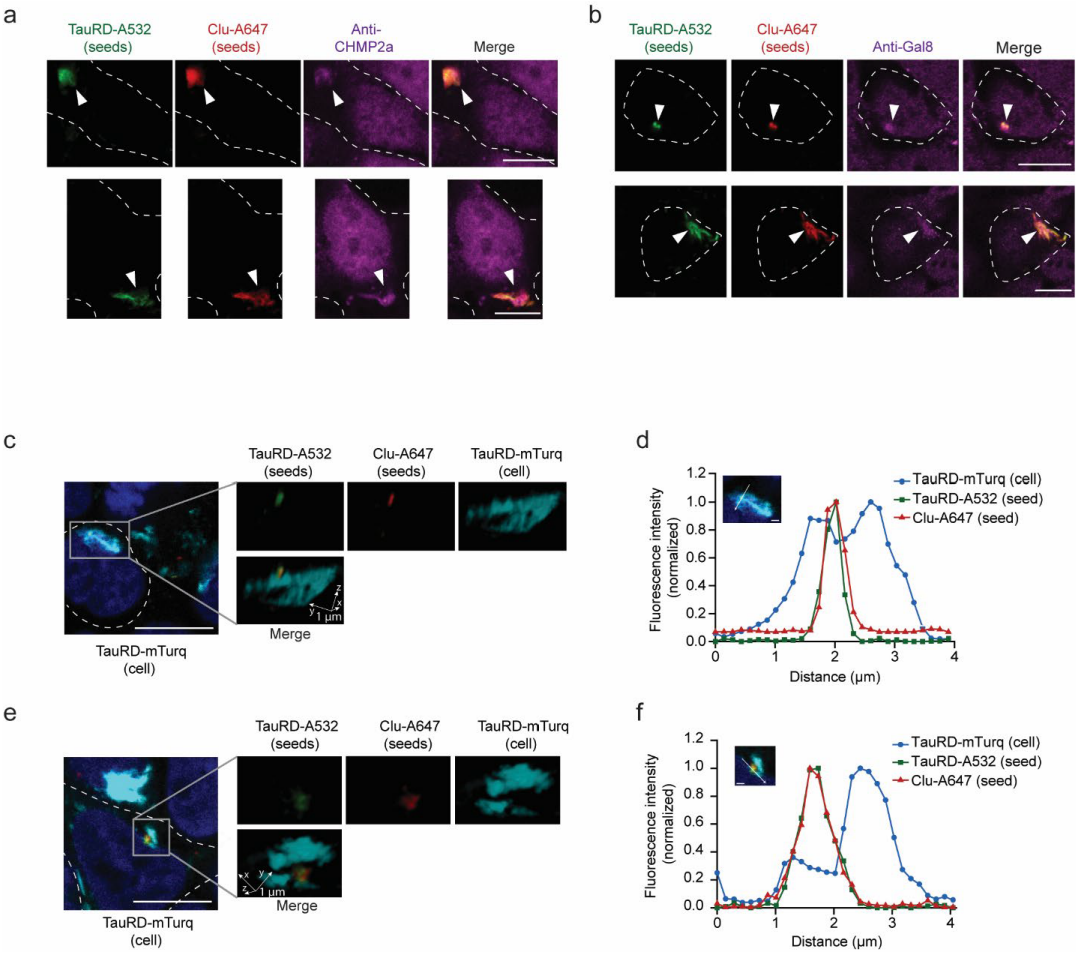

Supplementary Fig. 8: Uptake and seeding of Clusterin-associated Tau aggregates. a, b, Colocalization of TauRD/Clu seeds (TauRD-A532 in green, Clu-A647 in red) (arrow heads) with the endocytosis marker CHMP2a (magenta) **(a)** and the marker of ruptured endomembranes, galectin-8 (GAL-8; magenta) **(b)** in TauRD-T cells. Representative results of confocal imaging are shown. The cell outline is indicated by a white dashed line. Scale bar, 10 µm. (n=3 independent experiments). **c-f,** Colocalization of TauRD/Clu seeds with endogenous TauRD-mTurquoise2 (TauRD-mTurq) aggregates. **c, e,** Representative slices from a confocal stack are shown (scale bar, 10 µm) where cells are outlined with a white dashed line. One aggregate region, marked with a square in the slice, is represented by volume rendering (1 µm scale bars indicated by arrows). Channels are also displayed separately. TauRD-A532 seed in green, Clu-A647 in red, endogenous TauRD aggregate in turquoise. (n=3 independent experiments). **d, f,** Quantification of relative fluorescence intensity in the aggregate shown in the inset in (c) and (e), respectively. TauRD-mTurq (blue), TauRD-A532 (green) and Clu-A647 (red). The colocalization line profile on a midfocal plane (inset image) along the white arrow is shown. Scale bar, 1 µm.

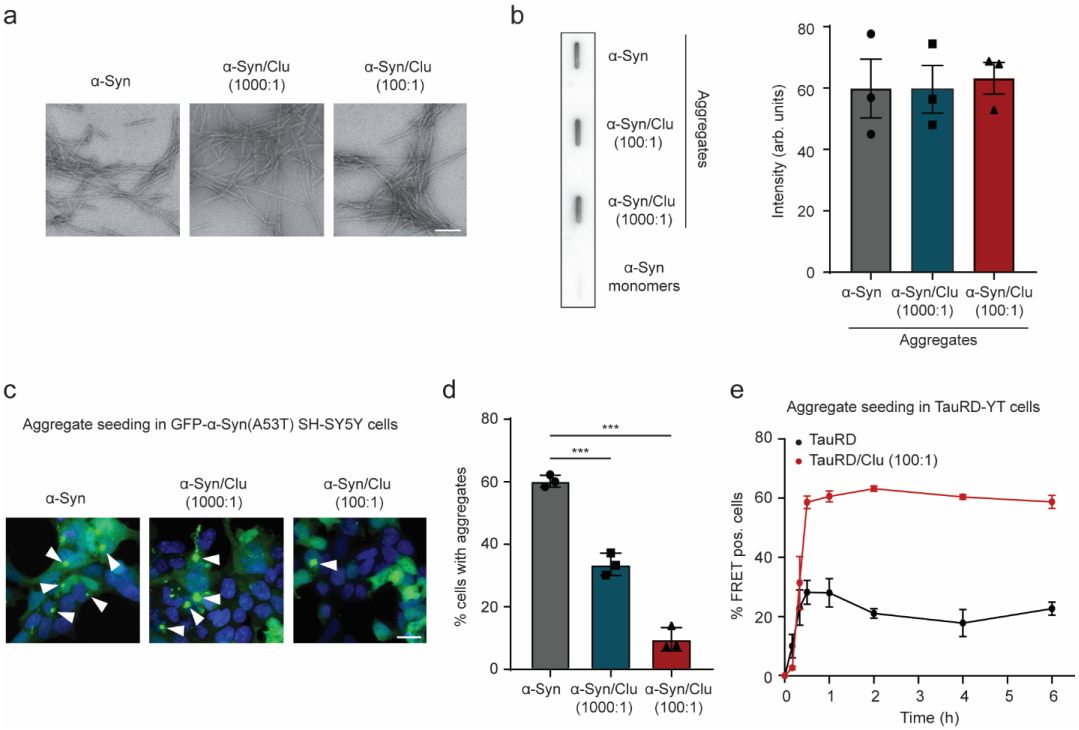

Supplementary Fig. 9: Effect of Clusterin on α-Synuclein aggregation and seeding in SH-SY5Y cells. a, Negative-stain electron microscopy of α-Syn aggregation reactions without or with Clu (molar ratio α-Syn:Clu 1000:1 and 100:1). Samples were analyzed after reaching the plateau phase of aggregation (72 h, (Fig. 5a)). Scale bar, 200 nm. (n=3 independent experiments). **b,** Filter retardation assay of α-Syn monomers and aggregation reactions without and with Clu (molar ratio α-Syn:Clu 1000:1 and 100:1) after reaching the plateau phase of aggregation (72 h, (Fig. 5a)). Bar graphs represent quantification by densitometry of the aggregation reactions. Average ± SEM (n=3 independent experiments). arb. units, arbitrary units. **c,** Representative images of the effect of Clu on seeding potency of α-Syn aggregation reactions as in Fig. 5a using SH-SY5Y as reporter cell line. SH-SY5Y GFP-α-Syn(A53T) cells were seeded (with lipofectamine) with aggregation reactions with or without Clu (10 µg α-Syn after 72 h aggregation, Fig. 5a) and cells with aggregates were analyzed after 24 h. Molar ratios of α-Syn:Clu are indicated. GFP-α-Syn(A53T) and DAPI nuclear staining are shown in green and blue, respectively. Arrow heads indicate aggregates. Scale bar, 20 µm. **d,** Bar graphs represent the quantification of the % of cells presenting aggregates after seeding as described in (c). Averages ± SEM (n=3 independent experiments). ***p<0.001 by one-way ANOVA with Bonferroni post hoc test. (α-Syn vs. α-Syn/Clu 1000:1 $p=1.5x10^{-4}$; α-Syn vs. α-Syn/Clu 100:1 $p=3.5x10^{-6}$) **e,** Substoichiometric amounts of Clu enhance seeding competence of TauRD aggregates. Seed formation was analyzed in aggregation reactions containing 10 µM TauRD without (black) or with 0.1 µM Clu (red) as judged by the fraction of FRET-positive (pos.) TauRD-YT cells. Reporter cells were transfected

with aggregation reactions containing 14 ng TauRD with lipofectamine. The molar ratio of TauRD:Clu was 100:1. Averages ± SEM (n=3 independent experiments).

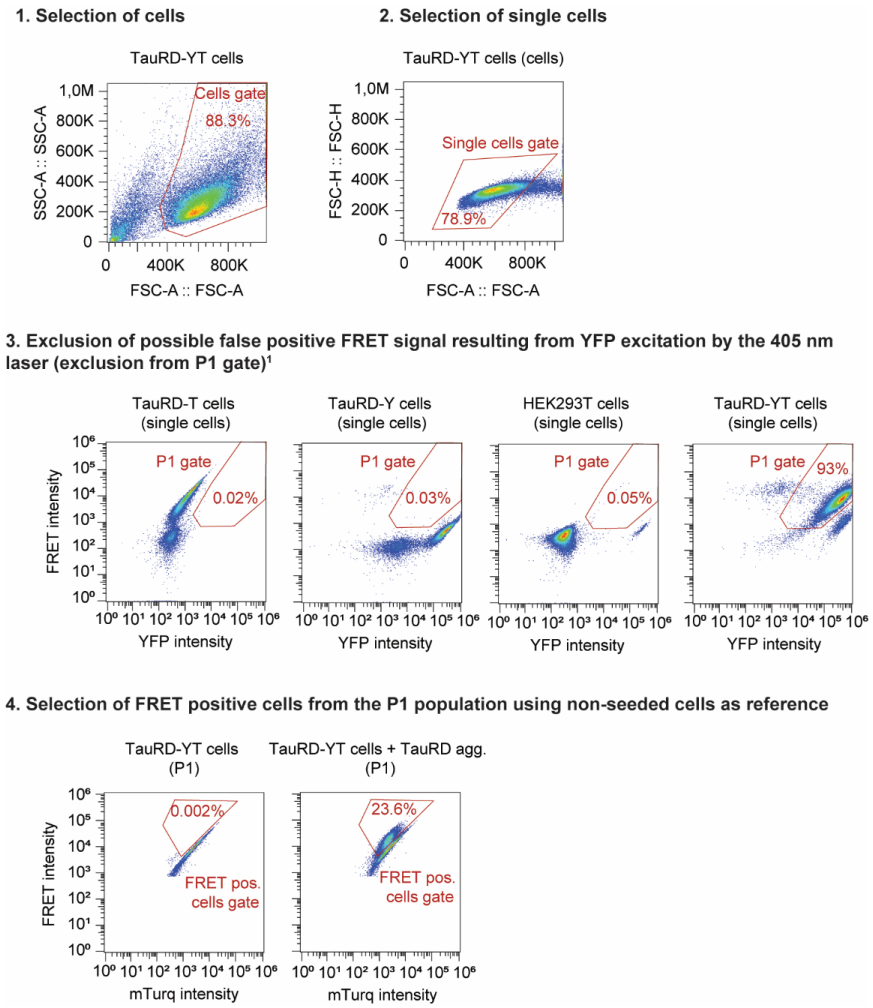

Supplementary Fig. 10: Flow cytometry strategy for quantification of FRET positive cells. To measure the mTurquoise2 and FRET fluorescence signals, cells were excited with 405 nm laser light and fluorescence was determined using 440/50 and 530/30 filters, respectively. To measure the YFP fluorescence signal, cells were excited at 488 nm and emission was recorded using a 530/30 filter. For each sample, 50,000 single cells were analyzed. First, cells were selected (1), followed by single cell selection (2). After gating single cells, an additional gate (P1) was introduced to exclude YFP-only cells that show a false-positive signal in the FRET channel due to excitation at 405 nm using as reference TauRD-T cells, TauRD-Y cells and HEK293T cells[1] (3). The FRET positive gate was set by plotting the FRET fluorescence signal versus the mTurquoise2 fluorescence signal using as reference non-seeded cells (4).

Supplementary References

1 Banning, C. *et al.* A flow cytometry-based FRET assay to identify and analyse protein-protein interactions in living cells. *PLoS One* **5**, e9344, doi:10.1371/journal.pone.0009344 (2010).

2.2 Publication 2: *In situ* architecture of neuronal α-Synuclein inclusions

Aim and key results of the study:

In this study, we employed cryo-electron tomography (cryo-ET) to analyze the ultrastructure and the cellular interactions of neuronal α-syn aggregates. To this end, we imaged α-syn aggregates in primary mouse neurons that were seeded with *in vitro* formed fibrils, as well as with aggregates purified from *post mortem* human brain tissue from an MSA patient.

We showed that endogenously expressed α-syn monomers form amyloid fibrils in LB-like neuronal α-syn aggregates. We found that these α-syn fibrils do not interact with membranes or organelles directly. Interestingly however, and contrary to other amyloid aggregates, many organelles, including mitochondria, ER and lysosomes, were present inside the fibrillar aggregate meshwork. To determine whether smaller α-syn aggregate species, such as oligomers, might interact with the membranes and cluster them, we measured the inter-membrane distances between the organelles and found that the organelles inside the aggregates had a similar amount of close-contacts as organelles found in control neurons – indicating that within α-syn aggregates, no membrane clustering occurs.

Lastly, we studied the seeding mechanism *in situ* by using gold-labeled α-syn fibrils as seeds. We found that only small fibrils are seeding competent and that α-syn fibrils grow unidirectionally from the internalized gold-labeled seeds.

Contribution:

V.A.T planned research and helped with manuscript preparation, conducted biochemical experiments, including protein purification and *in vitro* generation of α-syn fibrils, performed cell-biological experiments, including generation of stable cell lines and immunofluorescence stainings in human neuroblastoma cells and conducted all cryo-ET experiments, including sample preparation, data acquisition, post processing and helped with the data analysis.

nature COMMUNICATIONS

ARTICLE

https://doi.org/10.1038/s41467-021-22108-0 OPEN

In situ architecture of neuronal α-Synuclein inclusions

Victoria A. Trinkaus[1,2,3], Irene Riera-Tur[4,5], Antonio Martínez-Sánchez[6,7,8], Felix J. B. Bäuerlein[6,7,8], Qiang Guo[6,9,10,11], Thomas Arzberger[3,12,13], Wolfgang Baumeister[6], Irina Dudanova[4,5], Mark S. Hipp[1,3,14,15], F. Ulrich Hartl[1,3,16]✉ & Rubén Fernández-Busnadiego[6,7,8,16]✉

The molecular architecture of α-Synuclein (α-Syn) inclusions, pathognomonic of various neurodegenerative disorders, remains unclear. α-Syn inclusions were long thought to consist mainly of α-Syn fibrils, but recent reports pointed to intracellular membranes as the major inclusion component. Here, we use cryo-electron tomography (cryo-ET) to image neuronal α-Syn inclusions in situ at molecular resolution. We show that inclusions seeded by α-Syn aggregates produced recombinantly or purified from patient brain consist of α-Syn fibrils crisscrossing a variety of cellular organelles. Using gold-labeled seeds, we find that aggregate seeding is predominantly mediated by small α-Syn fibrils, from which cytoplasmic fibrils grow unidirectionally. Detailed analysis of membrane interactions revealed that α-Syn fibrils do not contact membranes directly, and that α-Syn does not drive membrane clustering. Altogether, we conclusively demonstrate that neuronal α-Syn inclusions consist of α-Syn fibrils intermixed with membranous organelles, and illuminate the mechanism of aggregate seeding and cellular interaction.

[1] Department of Cellular Biochemistry, Max Planck Institute of Biochemistry, Martinsried, Germany. [2] Graduate School of Quantitative Biosciences Munich, Munich, Germany. [3] Munich Cluster for Systems Neurology (SyNergy), Munich, Germany. [4] Molecular Neurodegeneration Group, Max Planck Institute of Neurobiology, Martinsried, Germany. [5] Department of Molecules - Signaling – Development, Max Planck Institute of Neurobiology, Martinsried, Germany. [6] Department of Molecular Structural Biology, Max Planck Institute of Biochemistry, Martinsried, Germany. [7] Institute of Neuropathology, University Medical Center Göttingen, Göttingen, Germany. [8] Cluster of Excellence "Multiscale Bioimaging: from Molecular Machines to Networks of Excitable Cells" (MBExC), University of Göttingen, Göttingen, Germany. [9] School of Life Sciences, Peking University, Beijing, China. [10] Peking-Tsinghua Center for Life Sciences, Peking University, Beijing, China. [11] State Key Laboratory of Protein and Plant Gene Research, Peking University, Beijing, China. [12] Center for Neuropathology and Prion Research, Ludwig-Maximilians-University Munich, Munich, Germany. [13] Department of Psychiatry and Psychotherapy, University Hospital, Ludwig-Maximilians-University Munich, Munich, Germany. [14] Department of Biomedical Sciences of Cells and Systems, University Medical Center Groningen, University of Groningen, Groningen, The Netherlands. [15] School of Medicine and Health Sciences, Carl von Ossietzky University Oldenburg, Oldenburg, Germany. [16] Aligning Science Across Parkinson's (ASAP) Collaborative Research Network, Chevy Chase, MD, USA. ✉email: uhartl@biochem.mpg.de; ruben.fernandezbusnadiego@med.uni-goettingen.de

α-Synuclein (α-Syn) aggregation is a hallmark of several devastating neurodegenerative disorders, including Parkinson's disease (PD) and multiple systems atrophy (MSA)[1,2]. α-Syn aggregates undergo spreading throughout the brain during disease progression[1–3], suggesting mechanisms of intercellular seeding. Similar to other disease-related protein aggregates, pathological α-Syn is thought to adopt the amyloid fold[4]. Formation of α-Syn amyloid fibrils is observed in vitro[5,6] and fibrillar α-Syn has been purified from patient brains[7,8]. Early electron microscopy (EM) studies suggested that Lewy bodies[9–12] and glial cytoplasmic inclusions[13,14], characteristic of PD and MSA, respectively, are fibrillar. However, conventional EM lacks the resolution to unequivocally determine the molecular identity of these fibrils in situ.

Intriguingly, X-ray diffraction measurements confirmed the presence of amyloid fibrils only in some Lewy bodies[15]. A recent study using correlative EM on chemically fixed PD brain tissue suggested that cellular membranes were the main component of Lewy bodies, alongside unidentified fibrillar material[16]. These findings resonated with reports[17] that native α-Syn binds lipids, such as synaptic vesicle membranes[18], observations that lipids can catalyze α-Syn aggregation in vitro[19], and that α-Syn expression in cells is associated with membrane abnormalities[20]. Thus, the disease relevance of fibrillar (amyloid-like) α-Syn aggregation has been questioned, leading to a model in which the main role of α-Syn in pathological inclusions is to cluster cellular membranes[20,21].

Cryo-electron tomography (cryo-ET) is ideally suited to test these new ideas, as it can reveal the molecular architecture of protein aggregates at high resolution within neurons pristinely preserved by vitrification[22–24]. Here, we apply cryo-ET to analyze the fine architecture and cellular interactions of neuronal α-Syn inclusions in situ. We show that α-Syn inclusions consist of α-Syn fibrils intermixed with cellular organelles. However, α-Syn does not link organelles to each other and fibrils do not interact with membranes directly. Furthermore, experiments with gold-labeled extracellular seeds demonstrate that small fibrils are the most seeding-competent species in our preparations.

Results and discussion

Neuronal α-Syn inclusions contain α-Syn fibrils. We performed cryo-ET on neuronal α-Syn aggregates using a well-established seeding paradigm that recapitulates interneuronal spreading and key neuropathological features of Lewy bodies, including the ability to bind amyloid dyes[1,25–27]. Primary mouse neurons were cultured on EM grids, transduced with GFP-α-Syn and incubated with recombinant α-Syn preformed fibrils (PFFs; Supplementary Fig. 1a, b). Unless otherwise stated, all experiments were carried out using the familial A53T α-Syn mutation due to its higher seeding potency[28]. As reported, seeding of neurons led to the formation of GFP-α-Syn inclusions that were positive for Lewy body markers, including phospho-α-Syn (Ser129) and p62 (Supplementary Fig. 1c, d). GFP-α-Syn inclusions in cell bodies or neurites were targeted for cryo-ET by correlative microscopy and cryo-focused ion beam (cryo-FIB) milling[22–24,29,30] (Supplementary Fig. 2). In all cases, this analysis revealed large fibrillar accumulations at sites of GFP-α-Syn fluorescence (Fig. 1a, d and Supplementary Movie 1). Interestingly, the fibrils appeared to be composed of a core decorated by globular GFP-like densities (Fig. 1b), reminiscent of GFP-labeled polyQ and *C9orf72* poly-GA aggregates[22,23]. The fibrils were clearly distinct from cytoskeletal elements (Fig. 1c). However, in contrast to polyQ and poly-GA inclusions, GFP-α-Syn inclusions were populated by numerous cellular organelles, including endoplasmic reticulum, mitochondria, autophagolysosomal structures, and small vesicles (Fig. 1a, d and Supplementary Movie 1). Thus, the α-Syn inclusions formed in our cellular system recapitulated key molecular and ultrastructural features of PD Lewy bodies and mature Lewy body-like inclusions in culture[12,16,31].

To further investigate the nature of the fibrils observed at sites of GFP-α-Syn fluorescence and avoid possible artifacts caused by GFP-α-Syn overexpression, we next imaged inclusions formed by endogenous α-Syn in neurons seeded by recombinant PFFs. Given the high p62 signal observed in Lewy bodies[1,32] and GFP-α-Syn inclusions (Supplementary Fig. 1d), we expressed p62-RFP as a surrogate marker[23] of endogenous α-Syn inclusions (Supplementary Fig. 1e) to guide correlative cryo-FIB/ET analysis. Although endogenous α-Syn inclusions were smaller than those formed by GFP-α-Syn (Supplementary Fig. 1c), cryo-ET imaging revealed a similar nanoscale organization, consisting of various organelles crisscrossed by abundant fibrils (Fig. 1e, h). Importantly, the fibrils appeared identical to those observed in GFP-α-Syn inclusions (Fig. 1b), except that they were not decorated by globular densities (Fig. 1f). The fibrils were ~10 nm in diameter, similar to recombinant and patient-derived α-Syn fibrils[33,34] and clearly distinct from neurofilaments (Fig. 1g). These data conclusively demonstrate that the fibrils observed in α-Syn inclusions are formed by α-Syn, and argue against a major effect of GFP-α-Syn overexpression on inclusion architecture. Nevertheless, GFP-α-Syn overexpression enhanced the rate of inclusion formation and neuronal toxicity (Supplementary Fig. 1f, g), implicating aggregated α-Syn in neuronal death[27].

Recent studies have demonstrated that amyloid fibrils, including those formed by α-Syn, may adopt different conformations when purified from patient brain in comparison to fibrils generated in vitro from recombinant proteins[33,35]. Therefore, to assess the disease relevance of our findings using recombinant PFFs, we seeded primary neurons expressing GFP-α-Syn with α-Syn aggregates purified from MSA patient brain (Supplementary Fig. 3). Similar to PFFs, MSA seeds triggered the formation of intracellular GFP-α-Syn inclusions positive for phospho-α-Syn (Ser129) and p62 (Supplementary Fig. 3e). Importantly, cryo-ET analysis showed that MSA-seeded neuronal aggregates also consisted of a dense meshwork of α-Syn fibrils interspersed by cellular organelles (Fig. 2a–c). Therefore, our results show that neuronal α-Syn aggregates seeded by MSA patient material are formed by accumulations of α-Syn fibrils intermixed with cellular membranes.

We further investigated possible morphological differences between fibrils seeded by PFFs and MSA aggregates, and in neurons expressing endogenous α-Syn or GFP-α-Syn. In all cases, mean fibril length was ~250 nm (Fig. 2d and Supplementary Table 1). However, fibril density within inclusions, defined as the fraction of cytosolic volume occupied by fibrils, was significantly higher in cells expressing GFP-α-Syn (Fig. 2e and Supplementary Table 1). This was likely due to the higher expression level of this construct, resulting in a higher aggregate load (Supplementary Fig. 1c, f). We next calculated the persistence length of the fibrils to investigate their mechanical properties. Interestingly, whereas PFF-seeded fibrils in neurons expressing GFP-α-Syn or endogenous α-Syn were almost identical in persistence length (Supplementary Fig. 4), MSA-seeded GFP-α-Syn fibrils displayed a considerably lower persistence length (Supplementary Fig. 4), reflecting higher structural flexibility. These values are in the range of those measured for α-Syn[36] and tau[37] fibrils in vitro, as well as for polyQ fibrils in situ[22]. Our measurements are also consistent with single-particle studies reporting a higher twist, indicative of higher flexibility[38], for MSA-derived fibrils[33] (~60 nm) than for most structures of recombinant fibrils[34] (90–120 nm). Thus, different types of exogenous α-Syn aggregates seed neuronal inclusions with different mechano-physical properties.

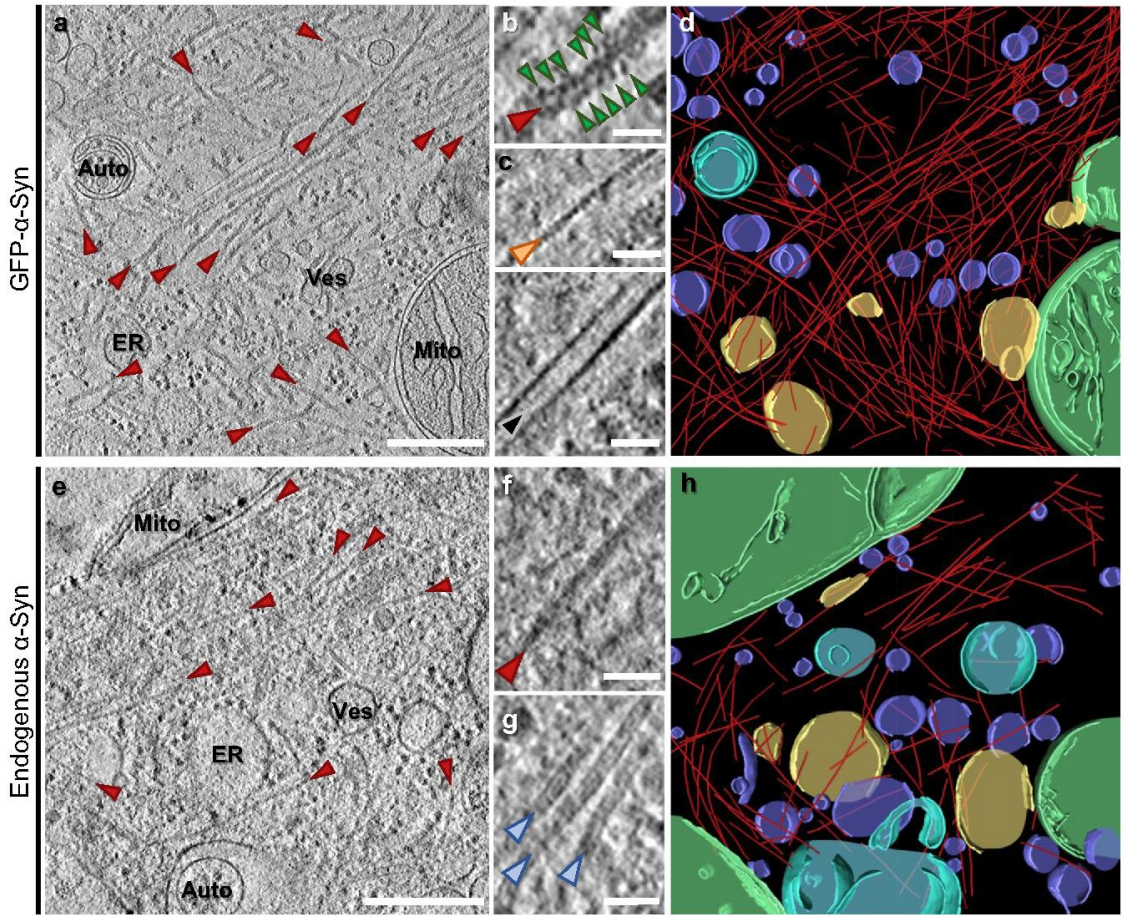

Fig. 1 Cryo-ET imaging of α-Syn aggregates seeded by PFFs in neurons. a A tomographic slice (thickness 1.8 nm) of an inclusion seeded by PFFs in a neuron expressing GFP-α-Syn. Auto; autophagosome, ER; endoplasmic reticulum, Mito; mitochondrion, Ves; vesicles. Fibrils are marked by red arrowheads. Scale bar: 350 nm. **b** Magnified view of a fibril with GFP-like densities (green arrowheads) decorating the fibril core. Scale bar: 30 nm. **c** Magnified views of an actin filament (orange arrowhead) and a microtubule (black arrowhead). Scale bars: 30 nm. **d** 3D rendering of the tomogram depicted in **a** showing α-Syn fibrils (red), an autophagosome (cyan), ER (yellow), mitochondria (green), and various vesicles (purple). **e** A tomographic slice (thickness 1.4 nm) of an inclusion seeded by PFFs in a neuron expressing p62-RFP. Scale bar: 350 nm. **f** Magnified view of a fibril. Note that fibrils in cells not expressing GFP-α-Syn are not decorated by GFP-like densities. Scale bar: 30 nm. **g** Magnified view of neurofilaments (blue arrowheads). Scale bar: 30 nm. **h** 3D rendering of the tomogram depicted in **e**. The number of tomograms and biologically independent cryo-ET experiments is listed in Supplementary Table 1. Representative images are shown.

Small fibrils drive seeding of neuronal α-Syn inclusions. The seeding of intracellular aggregation by extracellular aggregates may underlie the spreading of pathology across different brain regions during the progression of various neurodegenerative diseases, including synucleinopathies[1–3,39]. To gain a better mechanistic understanding of the seeding process, we tracked the fate of extracellular gold-labeled α-Syn seeds upon internalization into neurons expressing GFP-α-Syn. In this case, we used WT PFFs as they allowed higher labeling efficiency. Recombinant WT α-Syn fibrils were conjugated to 3-nm gold beads via NHS ester coupling, resulting in densely gold-labeled PFFs (Fig. 3a) that efficiently seeded the formation of neuronal GFP-α-Syn inclusions (Supplementary Fig. 5a). Some of these experiments were also carried out in a SH-SY5Y cell line stably expressing GFP-α-Syn as a simpler model system (Supplementary Fig. 6). Interestingly, cryo-ET analysis of inclusions seeded by gold-labeled PFFs showed GFP-α-Syn fibrils with one end decorated by three to ten gold particles (Fig. 3b, c), indicating that exogenous seeds triggered the fibrillation of cellular α-Syn in a polarized manner, consistent with the polar structures of recombinant α-Syn fibrils[34]. Although patient-derived α-Syn fibrils are polar as well[7,8,33,40], it remains to be established whether disease-related seeds also trigger unidirectional fibril growth in cells. Our data also show that, in our experimental conditions, small α-Syn fibrils are the most seeding-competent species, in agreement with previous results[41]. Therefore, despite the presence of abundant large fibrils in the exogenously added PFF material (Fig. 3a), these species are apparently not efficiently internalized. On the other hand, given the mechano-physical differences between neuronal fibrils growing from PFFs and MSA seeds (Supplementary Fig. 4), the seeding-competent species likely contain the necessary information to confer these structural features. Although α-Syn strains can be transmitted between cells in vitro and in vivo[3], the cellular environment may also modify the strain characteristics[42].

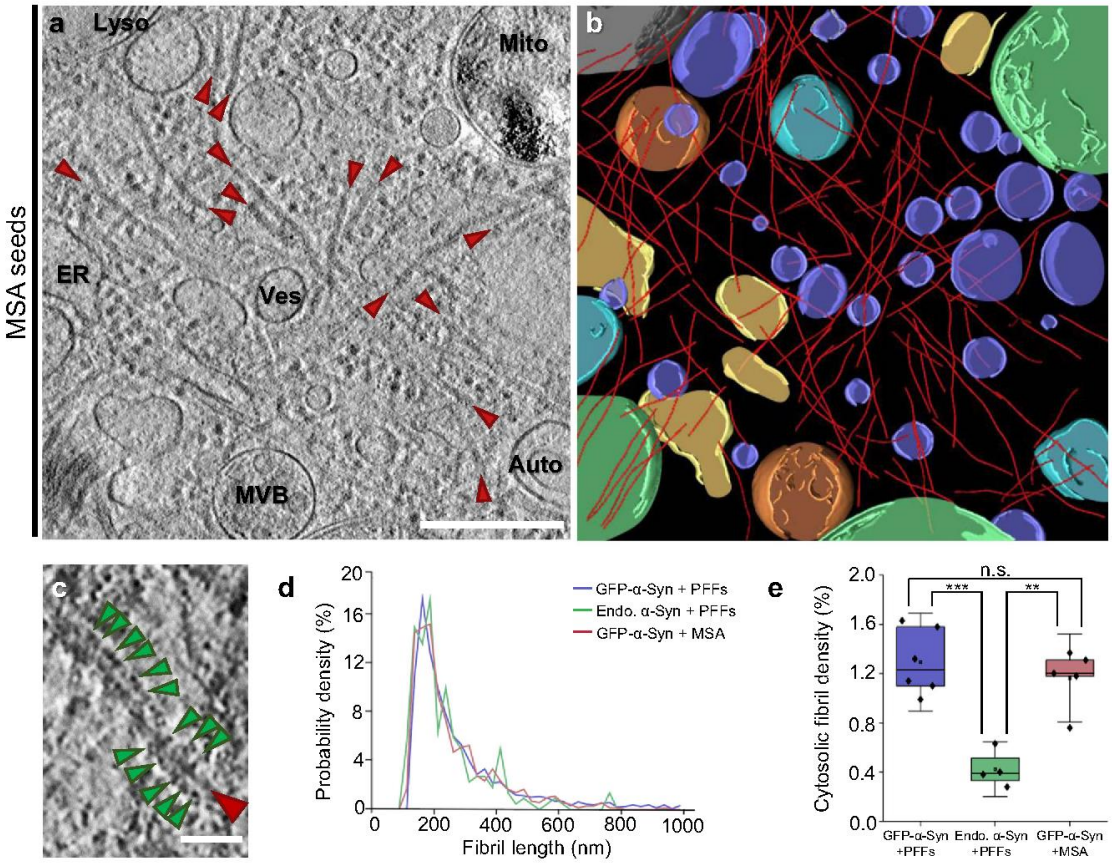

Fig. 2 Cryo-ET imaging of α-Syn aggregates seeded by MSA patient brain material in neurons. a A tomographic slice (thickness 1.4 nm) of an inclusion seeded by MSA patient brain material in a neuron expressing GFP-α-Syn. Auto; autophagosome, ER; endoplasmic reticulum, Lyso; lysosome, Mito; mitochondrion, MVB; multivesicular body, Ves; vesicles. Fibrils are marked by red arrowheads. Scale bar: 350 nm. **b** 3D rendering of the tomogram depicted in **a** showing α-Syn fibrils (red), autophagosomes (cyan), ER (yellow), a lysosome (gray), mitochondria (green), multivesicular bodies (orange), and various vesicles (purple). **c** Magnified view of a fibril with GFP-like densities (green arrowheads) decorating the fibril core. Scale bar: 30 nm. **d** Histogram of fibril length. $n = 1592$ (GFP-α-Syn + PFFs), 220 (endogenous α-Syn + PFFs), and 721 (GFP-α-Syn + MSA) fibrils analyzed over three biologically independent experiments for all conditions. **e** Box plots of cytosolic fibril density within inclusions, defined as the fraction of cytosolic volume occupied by fibrils. The horizontal lines of each box represent 75% (top), 50% (middle), and 25% (bottom) of the values, and a black square the average value. Whiskers represent 1.5× standard deviation and black diamonds the individual data points. $n = 6$ (GFP-α-Syn + PFFs), 4 (endogenous α-Syn + PFFs), and 5 (GFP-α-Syn + MSA) tomograms analyzed over three biologically independent experiments for all conditions; n.s., ** and *** indicate respectively $p = 0.4$, $p = 0.0010$, and $p = 4 \times 10^{-4}$ by one-way ANOVA. The number of fibrils, tomograms, and biologically independent cryo-ET experiments is listed in Supplementary Table 1. Representative images are shown in **a**–**c**. Source data for **d** and **e** are provided as a Source data file.

Thus, higher resolution data are needed to elucidate to what extent the structure of the seed is templated in the aggregates seeded within cells.

Gold-labeled α-Syn was also observed within the lumen of endolysosomal compartments (Fig. 3d and Supplementary Fig. 5b) and at their membrane (Fig. 3e and Supplementary Fig. 5b). Although the growth of α-Syn fibrils was occasionally observed directly at such membrane-bound gold-labeled structures (Fig. 3e, f), most gold-labeled fibrils were cytosolic (Fig. 3b). These data are in agreement with a model where small α-Syn fibrils entering the cell are targeted to endosomes, from which they escape and trigger intracellular growth of α-Syn fibrils[3,43].

α-Syn does not cluster cellular membranes within inclusions. The affinity of α-Syn for lipids[17] has led to the proposal that α-Syn drives the accumulation of cellular membranes in Lewy bodies[16,20,21], e.g., by fibril-membrane contacts as observed for polyQ fibrils[22]. Such contacts existed within α-Syn inclusions (Supplementary Fig. 7a, b), but they were extremely rare and did not seem to cause the kind of membrane deformations (Supplementary Fig. 7a) seen with polyQ[22]. Although we found a few examples of fibrils contacting membranes at areas of high curvature (Supplementary Fig. 7b), such areas also existed in the absence of fibril contacts (Supplementary Fig. 7c). Thus, apparent fibril-membrane contacts seemed to be mainly a consequence of the crowded cellular environment. To test this hypothesis, we computationally introduced random shifts and rotations to the experimentally determined positions of α-Syn fibrils within the tomograms. This analysis revealed that close fibril-membrane distances (<20 nm) were significantly more frequent in random simulations than in the experimental data (Fig. 4a, b, Supplementary Fig. 7d, and Supplementary Table 1). Together, these

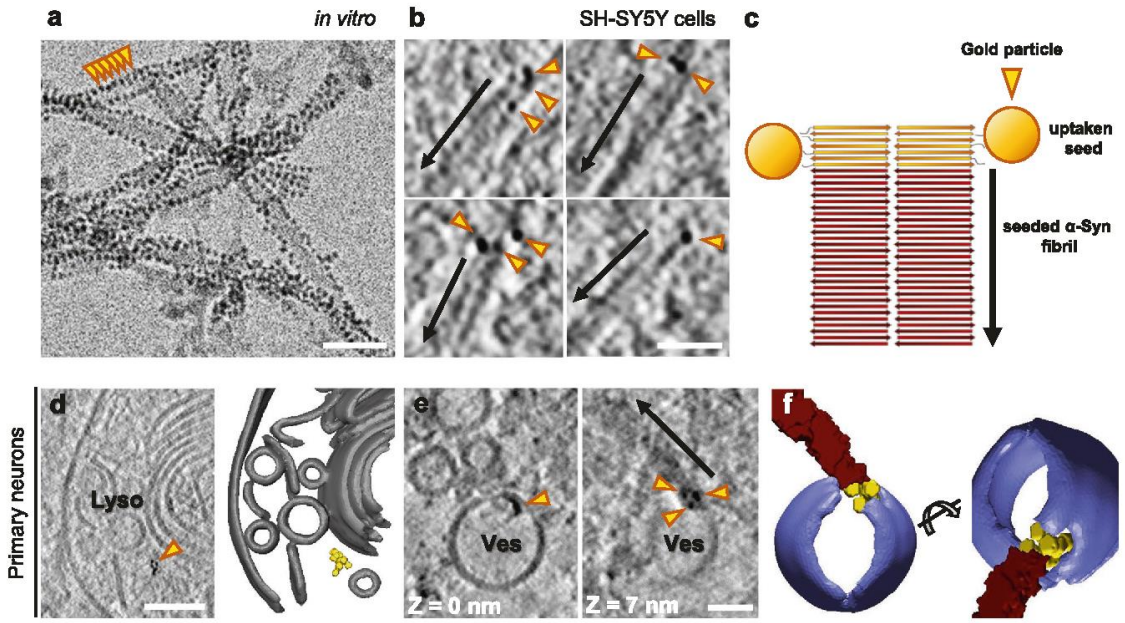

Fig. 3 Seeding of α-Syn aggregates by gold-labeled PFFs. a Cryo-electron microscopy image of PFFs labeled with 3-nm gold beads (orange arrowheads) via NHS esterification. Scale bar: 30 nm. Three biologically independent experiments were performed. The average distance between gold bead centers was 35 ± 4 Å (mean ± sd). Considering a typical distance between β strands of ~4.8 Å within α-Syn fibrils[33,34], this corresponds to labeling every seventh or eighth β-strand on the fibril. **b** Tomographic slices (thickness 1.8 nm) showing α-Syn fibrils seeded by gold-labeled PFFs within SH-SY5Y cells expressing GFP-α-Syn. Arrows mark the direction of fibril growth from the gold-labeled seed. Scale bar: 40 nm. Two biologically independent experiments were performed. **c** Schematic of the hypothetical molecular organization of α-Syn fibrils seeded by gold-labeled PFFs. **d** A tomographic slice (thickness 1.4 nm; left) and 3D rendering of the tomogram (right) showing gold-labeled PFFs within the lumen of a lysosome in a primary neuron expressing GFP-α-Syn. Lyso; lysosome. Lysosomal membranes (gray), gold particles labeling the PFF (yellow). Scale bar: 70 nm. **e** Tomographic slices (thickness 1.4 nm) at different *Z* heights showing gold-labeled PFFs found within the membrane of a vesicle (Ves) and seeding an α-Syn fibril (arrow) in a primary neuron expressing GFP-α-Syn. Scale bar: 30 nm. Two biologically independent experiments were performed. **f** 3D rendering of the tomogram depicted in **e** in two different orientations. Vesicle membrane (purple), α-Syn fibril (red), gold particles (yellow). Representative images are shown in **a**, **b**, **d**, **e**, and **f**.

results indicate that direct interactions between α-Syn fibrils and membranes are infrequent, and unlikely to induce substantial membrane clustering.

However, the previously suggested membrane clustering[20,21] could also be driven by α-Syn species smaller than fibrils, which cannot be readily detected by cryo-ET. For example, soluble α-Syn molecules can cluster vesicles at distances shorter than 15 nm in vitro[44]. To explore this possibility, we compared the shortest distances between all cellular membranes in tomograms of α-Syn inclusions and in untransduced, unseeded control neurons. This analysis revealed that close contacts (<20 nm) between membranes were similarly common within α-Syn inclusions as in control cells (Fig. 4c, Supplementary Fig. 7e, and Supplementary Table 1), arguing against α-Syn-mediated membrane clustering in inclusions.

Altogether, we show that neuronal α-Syn aggregates consist of both α-Syn fibrils and various cellular membranes. In agreement with a recent report[31], our findings suggest that the fibrils observed in pathological α-Syn inclusions[12–14,16] are indeed α-Syn fibrils. Intracellular α-Syn aggregation can be triggered by internalized small fibrils, suggesting that this mechanism is relevant to the spreading of aggregate pathology. However, α-Syn fibrils do not interact with membranes and do not seem to induce the type of membrane damage observed for other amyloids[22,45]. At the same time, α-Syn does not drive membrane clustering directly. Thus, it remains to be elucidated why membrane structures are enriched in α-Syn inclusions[12,16,31], in comparison with other neurotoxic protein aggregates[22–24]. An intriguing possibility is that the abundance of vesicular organelles in α-Syn inclusions is caused by the impairment of the autophagic and endolysosomal machineries by α-Syn aggregation[46].

Methods

Plasmids. Plasmids for the expression of recombinant α-Syn were: pT7-7 α-Syn (Addgene plasmid #36046 (ref. [47]); http://n2t.net/addgene:36046; RRID: Addgene_36046) and pT7-7 α-SynA53T (Addgene plasmid #105727 (ref. [48]); http://n2t.net/addgene:105727; RRID: Addgene_105727; gift from Hilal Lashuel).

Plasmid EGFP-α-SynA53T (Addgene plasmid #40823 (ref. [49]); http://n2t.net/addgene:40823; RRID: Addgene_40823) was used for expression in SH-SY5Y cells (gift from David Rubinsztein).

The following plasmids were used for viral transfections: pFhSynW2 (ref. [50]; GFP-SynA53T-Flag, Flag-GFP), PU3a (p62-tagRFP)[23], psPAX2 (a gift from Didier Trono; Addgene plasmid #12260; http://n2t.net/addgene:12260; RRID: Addgene_12260), and pVsVg[51]. pFhSynW2 and pVsVg were a gift of Dieter Edbauer.

pFhSynW2 GFP-synA53T-Flag was cloned by inserting the GFP-α-SynA53T sequence from plasmid EGFP-α-SynA53T between the XmaI and NheI restriction sites, using the primers described in Supplementary Table 2.

pFhSynW2 Flag-GFP was cloned by inserting the GFP sequence from the plasmid EGFP-α-SynA53T between the BamHI and EcoRI restriction sites, using the primers described in Supplementary Table 2.

Antibodies. The following primary antibodies were used: GFP (A10262, Thermo Fisher, 1:500; RRID: AB_2534023), K48-linked ubiquitin (05-1307, Millipore; 1:500; RRID: AB_1587578), MAP2 (NB300-213, Novus Biologicals; 1:500; RRID: AB_2138178), p62 (ab56416, Abcam; 1:200; RRID: AB_945626), phospho-α-Syn Ser129 (ab51253, Abcam; 1:500 for immunofluorescence, 1:2500 for western blot; RRID: AB_869973), α-Syn (610787, BD Biosciences; 1:1000; RRID: AB_398108), and p62 lck ligand (610832, BD Biosciences; 1:100; RRID: AB_398151).

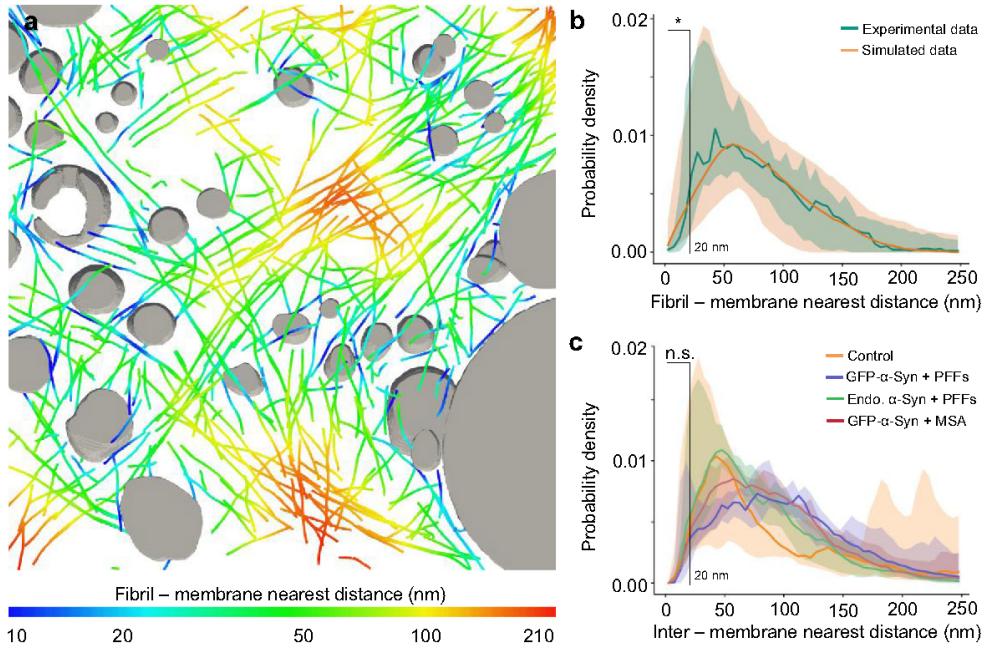

Fig. 4 Quantification of fibril-membrane and inter-membrane distances within α-Syn inclusions. a Visualization of fibril-membrane distances in the tomogram rendered in Fig. 1d. Organelles are shown in gray, and fibrils are color-coded according to their distance to the nearest organelle membrane. **b** Histogram of nearest distances between a fibril and a membrane in the pooled experimental data ($n = 15$ tomograms, including 6 of GFP-α-Syn + PFFs, 4 of endogenous α-Syn + PFFs, and 5 of GFP-α-Syn + MSA over three biologically independent experiments for all conditions), and in simulations shifting and rotating fibrils from their experimentally determined positions (200 simulations for each experimental tomogram). Solid lines represent the median of all tomograms. The shaded areas represent 5–95% confidence intervals. Fibril-membrane distances <20 nm are significantly more abundant in the simulated data ($p = 0.03$ by two-tailed Kolmogorov–Smirnov test). See also Supplementary Table 1. **c** Histogram of inter-membrane nearest distances for all organellar membranes in the tomograms. Inter-membrane distances <20 nm are not significantly different within α-Syn inclusions than in control untransduced and unseeded cells ($p = 0.4$ by two-tailed Kolmogorov–Smirnov test). Solid lines represent medians, shaded areas represent 5–95% confidence intervals. $n = 5$ (untransduced – PFFs), 6 (GFP-α-Syn + PFFs), 4 (endogenous α-Syn + PFFs), and 5 (GFP-α-Syn + MSA) tomograms analyzed over two (untransduced – PFFs) or three biologically independent experiments (GFP-α-Syn + PFFs, endogenous α-Syn + PFFs, and GFP-α-Syn + MSA). The number of tomograms and biologically independent cryo-ET experiments is listed in Supplementary Table 1. A representative image is shown in **a**. Source data for **b** and **c** are provided as a Source data file.

The following secondary antibodies were used: Alexa Fluor 488 AffiniPure Donkey anti-chicken (703-545-155, Jackson ImmunoResearch; 1:250), Alexa Fluor 647 AffiniPure Donkey anti-chicken (703-605-155, Jackson ImmunoResearch; 1:250), Cy3 AffiniPure Donkey anti-rabbit (711-165-152, Jackson ImmunoResearch; 1:250), Alexa Fluor 488 AffiniPure Donkey anti-mouse (715-545-150, Jackson ImmunoResearch; 1:250), Cy3-conjugated AffiniPure Goat anti-mouse IgG (115-165-003, Jackson ImmunoResearch; 1:1000), Cy3-conjugated AffiniPure Goat anti-rabbit (111-165-045, Dianova; 1:1000; RRID: AB_2338003), and HRP-conjugated goat anti-rabbit (A9169, Sigma; 1:5000; RRID: AB_258434).

Recombinant α-Syn purification and fibril assembly. Recombinant human WT and A53T α-Syn were purified as follows based on a published procedure[25] (see https://edmond.mpdl.mpg.de/imeji/collection/dBIbxxKvWaYMpyhI for a detailed protocol). BL21 (DE3) *Escherichia coli* (Agilent) were transformed with pT7-7 α-Syn or pT7-7 α-SynA53T. Protein expression was induced by 1 mM IPTG for 4 h. Bacteria were harvested and pellets were lysed in high salt (HS) buffer (750 mM NaCl, 50 mM Tris, pH 7.6, and 1 mM 2,2′,2″,2‴-(ethane-1,2-diyldinitrilo) tetraacetic acid (EDTA)). The lysate was sonicated for 5 min and boiled subsequently. The boiled suspension was centrifuged, the supernatant dialyzed in 50 mM NaCl, 10 mM Tris, and 1 mM EDTA, and purified by size-exclusion chromatography (Superdex 200). Fractions were collected and those containing α-Syn were combined. The combined fractions were applied onto an anion exchange column (MonoQ). α-Syn was purified by a gradient ranging from 50 mM to 1 M NaCl. Fractions containing α-Syn were combined and dialyzed in 150 mM KCl and 50 mM Tris, pH 7.6.

For fibril assembly, purified α-Syn monomers (5 mg/ml) were centrifuged at high speed (100,000 × *g*) for 1 h. The supernatant was transferred into a new reaction tube, incubated with constant agitation (1000 r.p.m.) at 37 °C for 24 h. The resulting fibrils were diluted 1:20 in PBS and sonicated for 60 s (0.5 s on, 0.5 s off) using a Branson sonifier. The presence of α-Syn fibrils was confirmed by negative stain EM. Except for gold labeling experiments, cells were seeded using A53T α-Syn PFFs.

Labeling of fibrils with 3 nm monovalent gold beads (Nanopartz) via NHS ester coupling was performed, as described in the manufacturer's protocol. In brief, WT α-Syn PFFs were dialyzed in PBS and subsequently added to the gold beads. The reaction was facilitated by sonication (as above) and constant agitation at 30 °C for 30 min. Labeled PFFs and free gold beads were separated by sequential centrifugation and washing with 0.1% Tween20 and 1% PBS. Labeling of PFFs with gold beads was confirmed by negative stain and cryo-EM.

Immunohistochemistry on MSA patient brain. MSA patient brain tissue was obtained from Neurobiobank Munich (Germany). All autopsy cases of the Neurobiobank Munich are collected on the basis of an informed consent according to the guidelines of the ethics commission of the Ludwig-Maximilians-University Munich, Germany. The experiments performed in this paper were approved by the Max Planck Society's Ethics Council. The sample was from a male patient who died at the age of 54, 6 years after being diagnosed with a cerebellar type of MSA. Postmortem delay was ~30 h. Brain regions with abundant α-Syn inclusions were identified by postmortem histological examination.

For immunohistochemistry (IHC), mouse monoclonal antibodies against α-Syn and p62 lck ligand were used. Paraffin sections of human brain tissue were deparaffinated and rehydrated. Pretreatment (cooking in cell conditioning solution 1, pH 8 for 30 min for α-Syn IHC or for 56 min in case of p62 IHC), IHC, and counterstaining of nuclei with hematoxylin (Roche) and Bluing reagent (Roche) were performed with the Ventana Bench-Mark XT automated staining system (Ventana), using the UltraView Universal DAB Detection Kit (Roche). For α-Syn, IHC slides were additionally pretreated in 80% formic acid for 15 min after cooking. Slides were coverslipped with Entellan (Merck) mounting medium.

Images were recorded with a BX50 microscope (Olympus) using a 40× objective and cellSens 2.1 software (Olympus).

Preparation of sarkosyl-insoluble fraction from MSA patient brain. The sarkosyl-insoluble fraction was prepared as follows based on a published procedure[42]. Frozen tissue from the basilar part of the pons (1 cm^3) was homogenized in HS buffer (50 mM Tris-HCl pH 7.5, 750 mM NaCl, 10 mM NaF, and 5 mM EDTA) with protease and phosphatase inhibitors (Roche), and incubated on ice for 20 min. The homogenate was centrifuged at 100,000 × *g* for 30 min. The resulting pellet was washed with HS buffer and then re-extracted sequentially with 1% Triton X-100 in HS buffer, 1% Triton X-100 in HS buffer and 30% sucrose, and 1% sarkosyl in HS buffer and finally PBS. The incubation with 1% sarkosyl in HS buffer was performed overnight at 4 °C. The final fraction was sonicated and the presence of α-Syn aggregates was confirmed by immunobloting against phospho-α-Syn (Ser129) upon SDS–PAGE. Uncropped SDS–PAGE and immunoblots are shown in the Source data file.

Cell culture. To create a stable cell line expressing EGFP-α-SynA53T, SH-SY5Y cells (ACC209, DSMZ; RRID: CVCL_0019) were transfected using Lipofectamine 2000 (Thermo Fisher). Cells were cultured in in Dulbecco's modified Eagle's medium (DMEM, Biochrom) supplemented with 10% fetal bovine serum (FBS, GIBCO), 2 mM L-glutamine (GIBCO), and 1000 µg/ml geneticin for selection. Polyclonal cell lines were generated by fluorescence-activated cell sorting (FACS) with a BD FACS Aria III using FACSDiva 6.1.3 software. Upon selection, cells were cultured in medium supplemented with 200 µg/ml geneticin (Thermo Fisher) and penicillin/streptomycin (Thermo Fisher).

Cells were seeded as described[25] using 300 nM (monomer) of α-SynA53T PFFs or gold-conjugated WT α-Syn PFFs. In brief, sonicated PFFs were diluted in a mixture of 50 µl of Optimem (Biochrom) and 3 µl of Lipofectamine 2000. Subsequently, the suspension was added to 1 ml of cell culture medium.

Lentivirus packaging. HEK293T cells (632180, Lenti-X 293T cell line, Takara; RRID: CVCL_0063) for lentiviral packaging were expanded to 70–85% confluency in DMEM Glutamax (+4.5 g/l D-glucose, -pyruvate) supplemented with 10% FBS (Sigma), 1% G418 (Gibco), 1% NEAA (Thermo Fisher), and 1% Hepes (Biomol). Only low passage cells were used. For lentiviral production, a three-layered 525 cm^2 flask (Falcon) was seeded and cells were henceforth cultured in medium without G418. On the following day, cells were transfected with the expression plasmid pFhSynW2 (GFP-SynA53T-Flag, Flag-GFP) or FU3a (p62-tagRFP), and the packaging plasmids psPAX2 and pVsVg using TransIT-Lenti transfection reagent (Mirus). The transfection mix was incubated for 20 min at room temperature (RT) and cell medium was exchanged. A total of 10 ml of transfection mix were added to the flask and incubated overnight. The medium was exchanged on the next day. After 48–52 h, culture medium containing the viral particles was collected and centrifuged for 10 min at 1200 × *g*. The supernatant was filtered through 0.45 µm pore size filters using 50 ml syringes, and Lenti-X concentrator (Takara) was added. After an overnight incubation at 4 °C, samples were centrifuged at 1500 × *g* for 45 min at 4 °C, the supernatant was removed, and the virus pellet was resuspended in 600 µl TBS-5 buffer (50 mM Tris-HCl, pH 7.8, 130 mM NaCl, 10 mM KCl, and 5 mM $MgCl_2$). After aliquoting, viruses were stored at −80 °C.

Primary neurons. Primary cortical neurons were prepared from E15.5 CD-1 wild-type mouse embryos of both sexes (breeding line MpiCrlIcr:CD-1). Mice were housed in a specific pathogen-free facility at 22 ± 1,5 °C, 55 ± 5% humidity, 14-h light/10-h dark cycle. All experiments involving mice were performed in accordance with the relevant guidelines and regulations of the Government of Upper Bavaria (Germany). Pregnant females were sacrificed by cervical dislocation, the uterus was removed from the abdominal cavity and placed into a 10 cm sterile Petri dish on ice containing dissection medium, consisting of Hank's balanced salt solution supplemented with 0.01 M HEPES, 0.01 M $MgSO_4$, and 1% penicillin/streptomycin. Embryos of both sexes were chosen randomly. Each embryo was isolated, heads were quickly cut, and brains were removed from the skull and immersed in ice-cold dissection medium. Cortical hemispheres were dissected and meninges were removed under a stereo-microscope. Cortical tissue from typically six to seven embryos was transferred to a 15 ml sterile tube, and digested with 0.25% trypsin containing 1 mM EDTA and 15 µl 0.1% DNAse I for 20 min at 37 °C. The enzymatic digestion was stopped by removing the supernatant and washing the tissue twice with Neurobasal medium (Invitrogen) containing 5% FBS. The tissue was resuspended in 2 ml medium and triturated to achieve a single-cell suspension. Cells were spun at 130 × *g*, the supernatant was removed, and the cell pellet was resuspended in Neurobasal medium with 2% B27 (Invitrogen), 1% L-glutamine (Invitrogen), and 1% penicillin/streptomycin (Invitrogen). For immunostaining, neurons were cultured in 24-well plates on 13 mm coverslips coated with 1 mg/ml poly-D-lysine (Sigma) and 1 µg/ml laminin (Thermo Fisher Scientific; 100,000 neurons per well). For thiazolyl blue tetrazolium bromide (MTT) assay, neurons were cultured in 96-well plates coated in the same way (19,000 neurons per well). For Cryo-ET, EM grids were placed in 24-well plates and coated as above (120,000 neurons per well). For lentiviral transduction at DIV 10, viruses were thawed and immediately added to freshly prepared neuronal culture medium.

Neurons in 24-well plates received 1 µl of virus/well, while neurons in 96-well plates received 0.15 µl of virus/well. A fifth of the medium from cultured neurons was removed and the equivalent volume of virus-containing medium was added. Three days after transduction, 2 µg/ml of seeds (α-SynA53T PFFs, gold-conjugated WT α-Syn PFFs, or MSA-derived aggregates) were added to the neuronal culture medium.

MTT viability assay. Viability of transduced neurons was determined using MTT (Sigma-Aldrich). Cell medium was exchanged for 100 µl of fresh medium, followed by addition of 20 µl of 5 mg/ml MTT in PBS and incubation for 2–4 h at 37 °C, 5% CO_2. Subsequently, 100 µl solubilizer solution (10% SDS and 45% dimethylformamide in water, pH 4.5) was added, and on the following day absorbance was measured at 570 nm. Three biologically independent experiments were performed for each condition, and absorbance values were averaged for each experiment. Viability values of neurons seeded with α-Syn aggregates were normalized to those of neurons that received PBS only.

Immunofluorescence. Immunofluorescence stainings on SH-SY5Y cells were performed 24 h after seeding. Cells were fixed for 10 min with 4% paraformaldehyde (PFA) in PBS and subsequently incubated for 5 min in permeabilization solution (0.1% Triton X-100 in PBS) at RT. After blocking with 5% milk in permeabilization solution, primary antibodies were diluted in blocking solution and incubated with the cells overnight at 4 °C. Secondary antibodies were incubated with the cells in blocking solution for 3 h at RT. The coverslips were subsequently incubated with 500 nM DAPI for 10 min and then mounted on glass slides. Images were taken using a CorrSight microscope (Thermo Fisher) in spinning disc mode with a 63× oil immersion objective.

Primary neurons were fixed with 4% PFA in PBS for 20 min; remaining free groups of PFA were blocked with 50 mM ammonium chloride in PBS for 10 min at RT. Cells were rinsed once with PBS and permeabilized with 0.25% Triton X-100 in PBS for 5 min. After washing with PBS, blocking solution consisting of 2% BSA (Roth) and 4% donkey serum (Jackson ImmunoResearch) in PBS was added for 30 min at RT. Coverslips were transferred to a light protected humid chamber and incubated with primary antibodies diluted in blocking solution for 1 h. Cells were washed with PBS and incubated with secondary antibodies diluted 1:250 in blocking solution, with 0.5 µg/ml DAPI added to stain the nuclei. Coverslips were mounted on Menzer glass slides using Prolong Glass fluorescence mounting medium. Confocal images were obtained at a SP8 confocal microscope (Leica) using 40× or 63× oil immersion objectives and Las X 3.5.7.23225 software (Leica). Neurons containing aggregates in the soma were manually quantified using the Cell Counter plugin of ImageJ 2.0.0 (ref. [52]; RRID: SCR_003070).

Negative stain EM. For negative stain analysis, continuous carbon Quantifoil grids (Cu 200 mesh, QuantifoilMicro Tools) were glow discharged using a plasma cleaner (PDC-3XG, Harrick) for 30 s. Grids were incubated for 1 min with PFFs, blotted and subsequently washed two times with water for 10 s. The blotted grids were stained with 0.5% uranyl acetate solution, dried, and imaged in a Polara cryo-electron microscope (Thermo Fisher) operated at 300 kV, using a pixel size of 2.35 or 3.44 Å.

Cryo-ET sample preparation. Quantifoil grids (R1/4 or 1.2/20, Au mesh grid with SiO_2 film, QuantifoilMicro Tools) were glow discharged using a plasma cleaner (PDC-3XG, Harrick) for 30 s. Cells were plated on the grids as described above. SH-SY5Y cells were seeded with α-Syn aggregates 24 h after plating and plunge frozen after another 24 h. Neurons were transduced on DIV 10, seeded with α-Syn aggregates on DIV 13, and plunge frozen on DIV 20. Plunge freezing was performed on a Vitrobot (Thermo Fisher) with the following settings: temperature, 37 °C; humidity, 80%; blot force, 10; and blot time, 10 s. The grids were blotted from the back and the front using Whatman filter paper and plunged into a liquid ethane/propane mixture. Subsequently the vitrified samples were transferred into cryo-EM boxes and stored in liquid nitrogen.

Correlative cryo-light microscopy and cryo-FIB milling. Grids were mounted onto autogrid sample carriers (Thermo Fisher) that contain cutout regions to facilitate shallow-angle FIB milling. Subsequently, grids were transferred into the stage of a CorrSight cryo-light microscope (Thermo Fisher) cooled at liquid nitrogen temperature. Overview images of the grids were acquired using a 20× lens (air, N.A., 0.8). Cells containing fluorescence signal of interest (GFP-α-Syn or p62-RFP) were mapped using MAPS 2.1 software (Thermo Fisher; RRID: SCR_018738).

The samples were transferred into a Scios or Quanta dual beam cryo-FIB/scanning electron microscopes (SEM; Thermo Fisher). To avoid charging of the samples, a layer of inorganic platinum was deposited on the grids. That was followed by the deposition of organometallic platinum using an in situ gas injection system (working distance—10 mm, heating—27 °C, time—8 s) to avoid damaging the cells by out-of-focus gallium ions. Subsequently, 2D correlation was performed using MAPS and the three-point alignment method between the fluorescence and the SEM image, as described[23].

For PIB milling, the grid was tilted to 18° and gallium ions at 30 kV were used to remove excess material from above and below the region of interest. Rough milling was conducted at a current of 0.5 nA and fine milling at a current of 50 pA, resulting in 100–200 nm thick lamellas (see https://edmond.mpdl.mpg.de/imeji/collection/dBIbxxKvWaYMpyhI for a detailed protocol of these procedures).

Cryo-ET data collection and reconstruction. The lamellas were transferred into a Titan Krios cryo-electron microscope (Thermo Fisher) operated at 300 kV, and subsequently loaded onto a compustage cooled to liquid nitrogen temperatures. Lamellas were oriented perpendicular to the tilt axis. Images were collected using a 4 k × 4 k K2 Summit or K3 (Gatan) direct detector cameras operated in dose fractionation mode (0.2 s, 0.15 e /Å^2). A BioQuantum (Gatan) post column energy filter was used with a slit width of 20 eV. Tilt series were recorded using SerialEM 3.7.0 (ref. [53]; RRID: SCR_017293) at pixel size of 3.38, 3.52, or 4.39 Å. Tilt series were recorded dose symmetrically[54] from −50° to +60° with an angular increment of 2°, resulting in a total dose of 100–130 e /Å^2 per tilt series. Frames were aligned using Motioncor2 1.2.1 (ref. [55]). Final tilt series were aligned using fiducial-less patch tracking, and tomograms were reconstructed by using back projection in IMOD 4.9.0 (ref. [56]; RRID: SCR_003297). Contrast was enhanced by filtering the tomograms using tom_deconv (https://github.com/dtegunov/tom_deconv) within MATLAB 2017a (MathWorks).

Tomogram segmentation. The membranes of the tomograms were segmented using the automatic membrane tracing package TomoSegMemTV[57]. The results were refined manually in Amira 6.2 (FEI Visualization Science Group; RRID: SCR_014305). The lumen of organelles was filled manually based on the membrane segmentations. For tracing of α-Syn fibrils, the XTracing module[58] of Amira was used. For that the tomograms were first denoised with a nonlocal means filter, and subsequently searched with a cylindrical template of 10 nm diameter and 80 nm length. Based on the cross-correlation fields, thresholds producing an optimal balance of true positives and negatives were applied. Filaments were subsequently traced with a search cone of 50 nm length and an angle of 37°. The direction coefficient was 0.3 and the minimum filament length was set to 100 nm. Selected filaments were inspected visually. Supplementary Movie 1 was created using Amira.

Fibril diameter and density of gold labeling. The diameter of endogenous α-Syn fibrils was measured using IMOD. 40 different positions were measured along different fibrils in three tomograms. For gold-labeled PFFs, the distance between the centers of gold particles was also measured with IMOD at 20 different positions. To estimate the labeling density, the average distance between gold particles was divided by 4.8 Å, approximately corresponding to the spacing between β-strands measured in α-Syn fibrils[33,34].

Cytosolic fibril density. The density of fibrils within the inclusion was calculated as the fraction of cytosolic volume occupied by fibrils. Cellular volume was calculated multiplying the X and Y dimensions of the tomogram by the thickness of the lamella along the Z direction. To calculate cytoplasmic volume, the lumina of organelles were subtracted from the tomogram volume. Fibril volume was calculated approximating fibrils by cylinders with radius of 5 nm and the length calculated by filament tracing. Calculations were performed in Origin 2019b (RRID: SCR_014212).

Fibril persistence length. The persistence length (L_p) measures the stiffness of polymers as the average distance for which a fibril is not bent. It was calculated using an in-house script, as previously described[22] executed in MATLAB. Briefly, L_p is calculated as the expectation value of cos θ, where θ is defined as the angle between two tangents to the fibril at positions 0 and l (ref. [59]):

$$\langle \cos(\theta_0 - \theta_l) \rangle = e^{-(l/L_p)} \quad (1)$$

The Young's modulus (E) can be calculated from L_p as:

$$E = \frac{L_p k_B T}{I} \quad (2)$$

where k_B is the Boltzmann constant (1.38×10^{-23} m^2 kg s^{-2} K^{-1}), T is the absolute temperature (here 295 K), and I is the momentum of inertia. Approximating the fibril by a solid rod, I can be calculated from its radius r as:

$$I = \frac{\pi r^4}{4} \quad (3)$$

Here, we used $r = 5$ nm.

Confidence intervals were calculated by fitting the data points to a linear polynomial using linear least squares in the MATLAB function "fit".

Fibril-membrane distance. Fibril-membrane nearest distance was defined for each point on the fibril as the minimum Euclidean distance to another point on a membrane. The algorithm computing fibril-membrane nearest distances is described in the Supplementary Methods.

Inter-membrane distance. Each segmented lumen was labeled differently to identify different organelles. The inter-membrane nearest distance for a point on a membrane was defined as the minimum Euclidean distance to another point on a membrane associated to a different lumen. The algorithm for computing inter-membrane nearest distances is described in the Supplementary Methods.

Statistical analysis. For the quantification of the percentage of neurons with aggregates using light microscopy (Supplementary Fig. 1f), $n = 4$ (GFP-α-Syn + PFFs) and 3 (endogenous α-Syn + PFFs) biologically independent experiments were performed, and a total of 100–500 neurons per condition and per experiment were counted. Statistical analysis was carried out by two-tailed unpaired t test with Welch's correction in Prism 6 (GraphPad; RRID: SCR_002798).

For the quantification of neuronal viability using the MTT assay (Supplementary Fig. 1g), $n = 3$ biologically independent experiments were performed for all conditions. Untransduced and unseeded control cells were used as reference. Statistical analysis was carried out by two-way ANOVA and Dunnett's multiple comparison test in Prism 6.

The number of tomograms and fibrils, as well as the total membrane area analyzed for each condition are shown in Supplementary Table 1.

Statistical analysis of cytosolic fibril density (Fig. 2e) was carried out by one-way ANOVA in Origin (RRID:SCR_014212). Confidence intervals for fibril-membrane (Fig. 4b) and inter-membrane (Fig. 4c) distances were calculated as the 5–95 percentiles from the curves of each individual tomogram. The differences between the curves within 20 nm were statistically analyzed by Kolmogorov–Smirnov test.

Additional information on statistical analyses can be found in the Source data file.

Reporting summary. Further information on research design is available in the Nature Research Reporting Summary linked to this article.

Data availability

The data supporting the findings of this manuscript are available from the corresponding authors upon reasonable request. A reporting summary for this Article is available as a Supplementary Information file. The individual values for the average graphs shown in Figs. 2d and 4b, c, and Supplementary Fig. 4 are available at the Edmond repository: https://edmond.mpdl.mpg.de/imeji/collection/rnVkI2lwG8loNXOi. The tomograms shown in Figs. 1 and 2 are available in EMPIAR through accession codes EMD-11401 (Fig. 1a), EMD-11417 (Fig. 1e), and EMD-11416 (Fig. 2a). Source data are provided with this paper. Protocols for recombinant α-Syn purification and cryo-correlative microscopy are available at the Edmond repository: https://edmond.mpdl.mpg.de/imeji/collection/dBIbxxKvWaYMpyhI. All other data are available from the corresponding authors upon reasonable request.

Code availability

The tomogram deconvolution filter is available at: https://github.com/dtegunov/tom_deconv. The script[60] for the calculation of L_p is available at: https://github.com/FJBauerlein/Huntington. The scripts[61] for fibril-membrane and inter-membrane distance calculations were performed within the PySeg software[62] and are available at: https://github.com/anmartinezs/pyseg_system/tree/master/code/pyorg/scripts/filaments.

Received: 13 August 2020; Accepted: 27 January 2021;
Published online: 14 April 2021

References

1. Henderson, M. X., Trojanowski, J. Q. & Lee, V. M. alpha-Synuclein pathology in Parkinson's disease and related alpha-synucleinopathies. *Neurosci. Lett.* **709**, 134316 (2019).
2. Goedert, M., Spillantini, M. G., Del Tredici, K. & Braak, H. 100 years of Lewy pathology. *Nat. Rev. Neurol.* **9**, 13–24 (2013).
3. Peelaerts, W., Bousset, L., Baekelandt, V. & Melki, R. a-Synuclein strains and seeding in Parkinson's disease, incidental Lewy body disease, dementia with Lewy bodies and multiple system atrophy: similarities and differences. *Cell Tissue Res.* **373**, 195–212 (2018).
4. Ke, P. C. et al. Half a century of amyloids: past, present and future. *Chem. Soc. Rev.* **49**, 5473–5509 (2020).
5. Conway, K. A., Harper, J. D. & Lansbury, P. T. Accelerated in vitro fibril formation by a mutant alpha-synuclein linked to early-onset Parkinson disease. *Nat. Med.* **4**, 1318–1320 (1998).
6. Giasson, B. I., Uryu, K., Trojanowski, J. Q. & Lee, V. M. Mutant and wild type human alpha-synucleins assemble into elongated filaments with distinct morphologies in vitro. *J. Biol. Chem.* **274**, 7619–7622 (1999).
7. Spillantini, M. G. et al. Filamentous alpha-synuclein inclusions link multiple system atrophy with Parkinson's disease and dementia with Lewy bodies. *Neurosci. Lett.* **251**, 205–208 (1998).

8. Spillantini, M. G., Crowther, R. A., Jakes, R., Hasegawa, M. & Goedert, M. alpha-Synuclein in filamentous inclusions of Lewy bodies from Parkinson's disease and dementia with lewy bodies. *Proc. Natl Acad. Sci. USA* **95**, 6469–6473 (1998).
9. Porno, L. S. Neuropathology of Parkinson's disease. *J. Neuropathol. Exp. Neurol.* **55**, 259–272 (1996).
10. Roy, S. & Wolman, L. Ultrastructural observations in Parkinsonism. *J. Pathol.* **99**, 39–44 (1969).
11. Duffy, P. E. & Tennyson, V. M. Phase and electron microscopic observations of lewy bodies and melanin granules in the substantia nigra and locus caeruleus in Parkinson's disease. *J. Neuropathol. Exp. Neurol.* **24**, 398–414 (1965).
12. Lashuel, H. A. Do Lewy bodies contain alpha-synuclein fibrils? and Does it matter? A brief history and critical analysis of recent reports. *Neurobiol. Dis.* **141**, 104876 (2020).
13. Gai, W. P. et al. alpha-Synuclein fibrils constitute the central core of oligodendroglial inclusion filaments in multiple system atrophy. *Exp. Neurol.* **181**, 68–78 (2003).
14. Tu, P. H. et al. Glial cytoplasmic inclusions in white matter oligodendrocytes of multiple system atrophy brains contain insoluble alpha-synuclein. *Ann. Neurol.* **44**, 415–422 (1998).
15. Araki, K. et al. Parkinson's disease is a type of amyloidosis featuring accumulation of amyloid fibrils of alpha-synuclein. *Proc. Natl Acad. Sci. USA* **116**, 17963–17969 (2019).
16. Shahmoradian, S. H. et al. Lewy pathology in Parkinson's disease consists of crowded organelles and lipid membranes. *Nat. Neurosci.* **22**, 1099–1109 (2019).
17. Galvagnion, C. The role of lipids interacting with alpha-synuclein in the pathogenesis of Parkinson's disease. *J. Parkinsons Dis.* **7**, 433–450 (2017).
18. Fusco, G., Sanz-Hernandez, M. & De Simone, A. Order and disorder in the physiological membrane binding of alpha-synuclein. *Curr. Opin. Struct. Biol.* **48**, 49–57 (2018).
19. Galvagnion, C. et al. Chemical properties of lipids strongly affect the kinetics of the membrane-induced aggregation of alpha-synuclein. *Proc. Natl Acad. Sci. USA* **113**, 7065–7070 (2016).
20. Panning, S., Selkoe, D. & Dettmer, U. Parkinson's disease: proteinopathy or lipidopathy? *NPJ Parkinsons Dis.* **6**, 3 (2020).
21. Bartels, T. A traffic jam leads to Lewy bodies. *Nat. Neurosci.* **22**, 1043–1045 (2019).
22. Bauerlein, F. J. B. et al. In situ architecture and cellular interactions of PolyQ inclusions. *Cell* **171**, 179–187 e110 (2017).
23. Guo, Q. et al. In situ structure of neuronal C9orf72 poly-GA aggregates reveals proteasome recruitment. *Cell* **172**, 696–705 e612 (2018).
24. Schaefer, T. et al. Amyloid-like aggregates cause lysosomal defects in neurons via gain-of-function toxicity. Preprint at *bioRxiv* https://doi.org/10.1101/2019.12.16.877431 (2019).
25. Volpicelli-Daley, L. A., Luk, K. C. & Lee, V. M. Addition of exogenous alpha-synuclein preformed fibrils to primary neuronal cultures to seed recruitment of endogenous alpha-synuclein to Lewy body and Lewy neurite-like aggregates. *Nat. Protoc.* **9**, 2135–2146 (2014).
26. Luk, K. C. et al. Exogenous alpha-synuclein fibrils seed the formation of Lewy body-like intracellular inclusions in cultured cells. *Proc. Natl Acad. Sci. USA* **106**, 20051–20056 (2009).
27. Volpicelli-Daley, L. A. et al. Exogenous alpha-synuclein fibrils induce Lewy body pathology leading to synaptic dysfunction and neuron death. *Neuron* **72**, 57–71 (2011).
28. Luk, K. C. et al. Molecular and biological compatibility with host alpha-synuclein influences fibril pathogenicity. *Cell Rep.* **16**, 3373–3387 (2016).
29. Rigort, A. et al. Focused ion beam micromachining of eukaryotic cells for cryoelectron tomography. *Proc. Natl Acad. Sci. USA* **109**, 4449–4454 (2012).
30. Marko, M., Hsieh, C., Schalek, R., Frank, J. & Mannella, C. Focused-ion-beam thinning of frozen-hydrated biological specimens for cryo-electron microscopy. *Nat. Methods* **4**, 215–217 (2007).
31. Mahul-Mellier, A. L. et al. The process of Lewy body formation, rather than simply alpha-synuclein fibrillization, is one of the major drivers of neurodegeneration. *Proc. Natl Acad. Sci. USA* **117**, 4971–4982 (2020).
32. Kuusisto, E., Salminen, A. & Alafuzoff, I. Ubiquitin-binding protein p62 is present in neuronal and glial inclusions in human tauopathies and synucleinopathies. *Neuroreport* **12**, 2085–2090 (2001).
33. Schweighauser, M. et al. Structures of alpha-synuclein filaments from multiple system atrophy. *Nature* **585**, 464–469 (2020).
34. Guerrero-Ferreira, R., Kovacik, L., Ni, D. & Stahlberg, H. New insights on the structure of alpha-synuclein fibrils using cryo-electron microscopy. *Curr. Opin. Neurobiol.* **61**, 89–95 (2020).
35. Zhang, W. et al. Heparin-induced tau filaments are polymorphic and differ from those in Alzheimer's and Pick's diseases. *Elife* **8**, e43584 (2019).
36. Makky, A., Bousset, L., Polesel-Maris, J. & Melki, R. Nanomechanical properties of distinct fibrillar polymorphs of the protein alpha-synuclein. *Sci. Rep.* **6**, 37970 (2016).
37. Wegmann, S. et al. Human Tau isoforms assemble into ribbon-like fibrils that display polymorphic structure and stability. *J. Biol. Chem.* **285**, 27302–27313 (2010).
38. Lu, L., Deng, Y., Li, X., Li, H. & Karniadakis, G. E. Understanding the twisted structure of amyloid fibrils via molecular simulations. *J. Phys. Chem. B* **122**, 11302–11310 (2018).
39. Jucker, M. & Walker, L. C. Self-propagation of pathogenic protein aggregates in neurodegenerative diseases. *Nature* **501**, 45–51 (2013).
40. Crowther, R. A., Daniel, S. E. & Goedert, M. Characterisation of isolated alpha-synuclein filaments from substantia nigra of Parkinson's disease brain. *Neurosci. Lett.* **292**, 128–130 (2000).
41. Pieri, L., Madiona, K. & Melki, R. Structural and functional properties of prefibrillar alpha-synuclein oligomers. *Sci. Rep.* **6**, 24526 (2016).
42. Peng, C. et al. Cellular milieu imparts distinct pathological alpha-synuclein strains in alpha-synucleinopathies. *Nature* **557**, 558–563 (2018).
43. Karpowicz, R. J. Jr. et al. Selective imaging of internalized proteopathic alpha-synuclein seeds in primary neurons reveals mechanistic insight into transmission of synucleinopathies. *J. Biol. Chem.* **292**, 13482–13497 (2017).
44. Fusco, G. et al. Structural basis of synaptic vesicle assembly promoted by alpha-synuclein. *Nat. Commun.* **7**, 12563 (2016).
45. Milanesi, L. et al. Direct three-dimensional visualization of membrane disruption by amyloid fibrils. *Proc. Natl Acad. Sci. USA* **109**, 20455–20460 (2012).
46. Arotcarena, M. L., Teil, M. & Dehay, B. Autophagy in synucleinopathy: the overwhelmed and defective machinery. *Cells* **8**, 565 (2019).
47. Paleologou, K. E. et al. Phosphorylation at Ser-129 but not the phosphomimics S129E/D inhibits the fibrillation of alpha-synuclein. *J. Biol. Chem.* **283**, 16895–16905 (2008).
48. Rospigliosi, C. C. et al. E46K Parkinson's-linked mutation enhances C-terminal-to-N-terminal contacts in alpha-synuclein. *J. Mol. Biol.* **388**, 1022–1032 (2009).
49. Furlong, R. A., Narain, Y., Rankin, J., Wyttenbach, A. & Rubinsztein, D. C. Alpha-synuclein overexpression promotes aggregation of mutant huntingtin. *Biochem. J.* **346**, 577–581 (2000).
50. May, S. et al. C9orf72 FTLD/ALS-associated Gly-Ala dipeptide repeat proteins cause neuronal toxicity and Unc119 sequestration. *Acta Neuropathol.* **128**, 485–503 (2014).
51. Kuhn, P. H. et al. ADAM10 is the physiologically relevant, constitutive alpha-secretase of the amyloid precursor protein in primary neurons. *EMBO J.* **29**, 3020–3032 (2010).
52. Schneider, C. A., Rasband, W. S. & Eliceiri, K. W. NIH Image to ImageJ: 25 years of image analysis. *Nat. Methods* **9**, 671–675 (2012).
53. Mastronarde, D. N. Automated electron microscope tomography using robust prediction of specimen movements. *J. Struct. Biol.* **152**, 36–51 (2005).
54. Hagen, W. J. H., Wan, W. & Briggs, J. A. G. Implementation of a cryo-electron tomography tilt-scheme optimized for high resolution subtomogram averaging. *J. Struct. Biol.* **197**, 191–198 (2017).
55. Zheng, S. Q. et al. MotionCor2: anisotropic correction of beam-induced motion for improved cryo-electron microscopy. *Nat. Methods* **14**, 331–332 (2017).
56. Kremer, J. R., Mastronarde, D. N. & McIntosh, J. R. Computer visualization of three-dimensional image data using IMOD. *J. Struct. Biol.* **116**, 71–76 (1996).
57. Martinez-Sanchez, A., Garcia, I., Asano, S., Lucic, V. & Fernandez, J. J. Robust membrane detection based on tensor voting for electron tomography. *J. Struct. Biol.* **186**, 49–61 (2014).
58. Rigort, A. et al. Automated segmentation of electron tomograms for a quantitative description of actin filament networks. *J. Struct. Biol.* **177**, 135–144 (2012).
59. Nagashima, H. & Asakura, S. Dark-field light microscopic study of the flexibility of F-actin complexes. *J. Mol. Biol.* **136**, 169–182 (1980).
60. Bäuerlein, F. J. B. FJBauerlein/Huntington: v1.0 (Version v1.0). Zenodo https://doi.org/10.5281/zenodo.4428865 (2017).
61. Martinez-Sanchez, A. Anmartinezs/pyseg-filaments: first release (Version v1.0.0). Zenodo https://doi.org/10.5281/zenodo.4429140 (2020).
62. Martinez-Sanchez, A. et al. Template-free detection and classification of membrane-bound complexes in cryo-electron tomograms. *Nat. Methods* **17**, 209–216 (2020).

Acknowledgements

We thank Philipp Erdmann, Günter Pfeifer, Jürgen Plitzko, and Miroslava Schaffer for electron microscopy support, and Ana Jungclaus and Nadine Wischnewski for wet lab support. We thank Dieter Edbauer, Hilal Lashuel, David Rubinsztein, and Didier Trono for sharing plasmids. We thank Konstanze Winklhofer and Joerg Tazelt for sharing the SH-SY5Y cell line and helpful discussions. We are also grateful to Sophie Keeling for help in plasmid cloning, Javier Collado for help with sample preparation, Jonathan Schneider and William Wan for help with image processing, Patrick Auer for help in aggregate

quantification, as well as Itika Saha, Eri Sakata, and Patricia Yuste-Checa for helpful discussions. Finally, we thank the anonymous MSA patient and his family for the donation of brain tissue to the Neurobiobank Munich. Fluorescence-activated cell sorting was carried out at the Imaging Facility of the Max Planck Institute of Biochemistry. V.A.T. was supported by the Graduate School of Quantitative Biosciences Munich. V.A.T., I.R.-T., A.M.-S., F.J.B., Q.G., W.B., I.D., M.S.H., F.U.H., and R.F.-B. have received funding from the European Commission (FP7 GA ERC-2012-SyG_318987-ToPAG). I.D. acknowledges financial support from the Horst Kübler-Stiftung. V.A.T., T.A., M.S.H., F.U.H., and R.F.-B. acknowledge funding from the Deutsche Forschungsgemeinschaft (DFG, German Research Foundation) through Germany's Excellence Strategy—EXC 2067/1—390729940 (R.F.-B.) and EXC 2145 – 390857198 (V.A.T., T.A., M.S.H. and F.U.H). F.U.H. and R.F.-B. were funded by the joint efforts of The Michael J. Fox Foundation for Parkinson's Research (MJFF) and the Aligning Science Across Parkinson's (ASAP) initiative. MJFF administers the grant ASAP-000282 on behalf of ASAP and itself. For the purpose of open access, the authors have applied a CC-BY public copyright license to the Author Accepted Manuscript version arising from this submission.

Author contributions

V.A.T. performed biochemical and electron microscopy experiments, immunofluorescence imaging of SH-SY5Y cells, and contributed to computational data analysis. I.R.-T. produced lentivirus and neuronal cultures, and performed viability assays and immunofluorescence imaging of neurons. A.M.S. developed software procedures for data analysis. F.B. and Q.G. contributed to data analysis. T.A. collected the autopsy case, characterized it neuropathologically, and performed immunohistochemistry. V.A.T., I.R.-T., W.B., I.D., M.S.H., F.U.H., and R.F.-B. planned research. I.D. supervised neuronal culture experiments. M.S.H. and F.U.H. supervised biochemical experiments. R.F.-B. supervised electron microscopy experiments and data analysis. R.F.-B. wrote the manuscript with contributions from all authors.

Funding

Open Access funding enabled and organized by Projekt DEAL.

Competing interests

The authors declare no competing interests.

Additional information

Supplementary information The online version contains supplementary material available at https://doi.org/10.1038/s41467-021-22108-0.

Correspondence and requests for materials should be addressed to F.U.H. or R.F.-B.

Peer review information *Nature Communications* thanks Tanmay Bharat, Michel Goedert and the other, anonymous, reviewer(s) for their contribution to the peer review of this work. Peer reviewer reports are available.

Reprints and permission information is available at http://www.nature.com/reprints

Publisher's note Springer Nature remains neutral with regard to jurisdictional claims in published maps and institutional affiliations.

In situ architecture of neuronal α-Synuclein inclusions

V.A. Trinkaus et al.

Supplementary Files

Contents

Supplementary Table 1 | Statistics of cryo-ET experiments on mouse neurons.

Condition	Experiments	Analyzed tomograms	Analyzed filaments	Analyzed membrane area (µm²)
GFP-α-syn + PFFs	3	6	1592	4.11
Endogenous α-syn + PFFs	3	4	220	2.87
GFP-α-syn + MSA	3	5	721	3.70
Untransduced - PFFs	2	5	-	3.67

Neurons were either transduced with GFP-α-syn and seeded with PFFs ("GFP-α-syn + PFFs"), transduced with p62-RFP and seeded with PFFs ("Endogenous α-syn + PFFs"), transduced with GFP-α-syn and seeded with aggregates derived from a MSA patient brain ("GFP-α-syn + MSA"), or untransduced and unseeded as control ("Untransduced - PFFs"). The column "Experiments" lists biologically independent replicates. "Analyzed filaments" includes all filaments analyzed in Fig. 2d, e, Fig. 4 and Supplementary Fig. 7d. "Analyzed membrane area" includes all membranes analyzed in Fig. 4 and Supplementary Fig. 7e.

Supplementary Table 2 | List of primers.

Primer name	Sequence
Forward primer pFhSynW2 GFP-synA53T-Flag	GCA GTC GAG AGG ATC CCG GGC CCA CCA TGG TGA GCA AGG GCG AG
Reverse primer pFhSynW2 GFP-synA53T-Flag	CCG CTC TAG AGC TAG CTT ATT TAT CGT CGT CAT CCT TGT AAT CGG CTT CAG GTT CGT AGT CTT GAT AC
Forward primer pFhSynW2 Flag-GFP	GAG CGC AGT CGA GAG GAT CCC CCA CCA TGG ATT ACA AGG ATG ACG ACG ATA AGC CCG GGA TGG TGA GCA AGG GCG AG
Reverse primer pFhSynW2 Flag-GFP	GCT TGA TAT CGA ATT CTT ACT TGT ACA GCT CGT CCA TGC

Primers used for cloning the pFhSynW2 GFP-synA53T-Flag and pFhSynW2 Flag-GFP constructs.

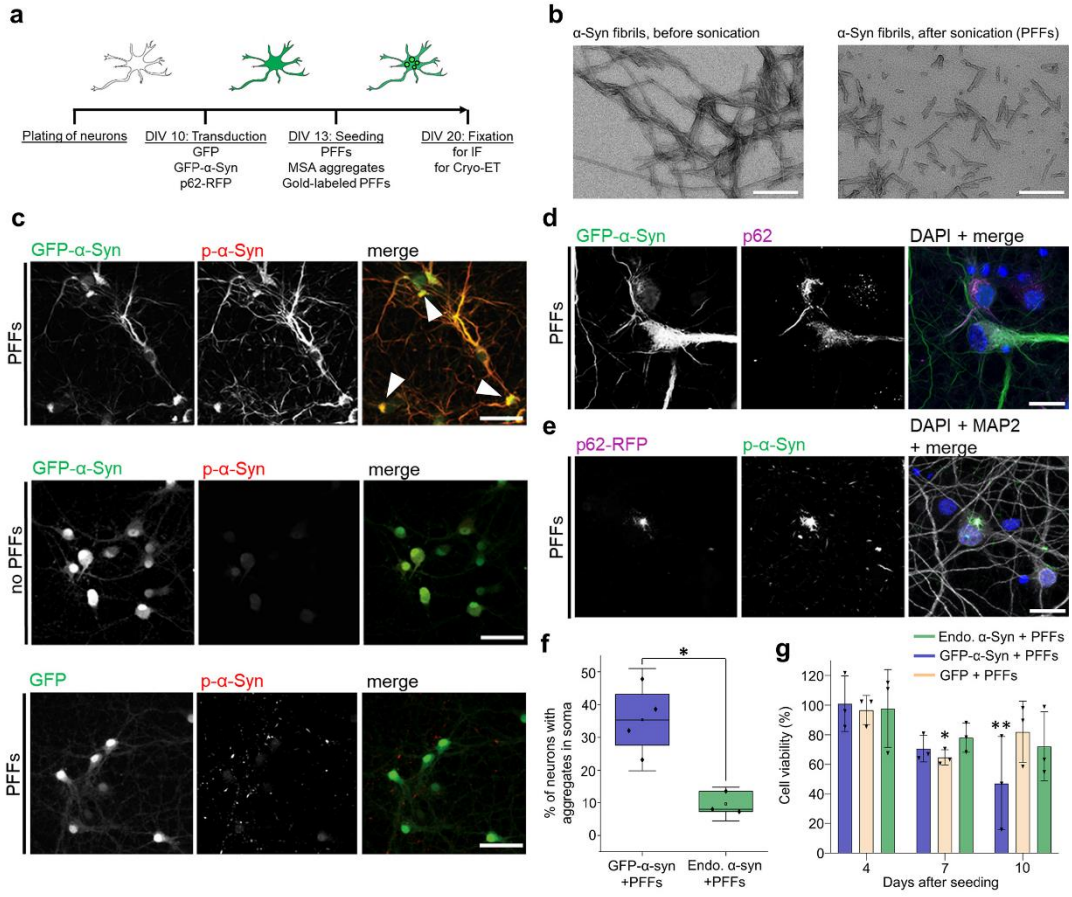

Supplementary Fig. 1 | Seeding of α-Syn aggregates in neurons. a, Schematic of the seeding of α-Syn aggregates in primary neurons. Primary mouse neurons were transduced at day *in vitro* (DIV) 10 with GFP, GFP-α-Syn or p62-RFP. Seeds (PFFs or MSA brain-derived) were applied at DIV 13, and α-Syn inclusions were studied at DIV 20 by light microscopy or cryo-ET upon chemical or cryo-fixation, respectively. For light microscopy imaging, GFP signal was enhanced by staining with an antibody against GFP. **b**, Negative stain images of α-Syn fibrils before (left) and after (right) sonication. Sonicated seeds were used for all seeding experiments. Scale bars: 250 nm. Two biologically independent experiments were performed. **c**, Immunofluorescence imaging of α-Syn aggregates, as detected by an antibody against phosphorylated α-Syn Ser129 (p-α-Syn). Top: aggregate formation (arrowheads) upon seeding cells expressing GFP-α-Syn with exogenous PFFs. Middle: no aggregate formation in cells expressing GFP-α-Syn in the

absence of PFFs. Bottom: PFFs seed smaller aggregates in cells with endogenous α-Syn levels that express GFP only as control (see Supplementary Fig. 1f for quantification). Scale bars: 50 μm. Two biologically independent experiments were performed. **d**, Immunofluorescence imaging of GFP-α-Syn aggregates detected by an antibody against p62. The merged image shows a superposition of the GFP-α-Syn (green), p62 (magenta) and DAPI (blue) channels. An arrowhead indicates the colocalization of GFP-α-Syn and p62. Scale bar: 20 μm. Two biologically independent experiments were performed. **e**, Immunofluorescence imaging of endogenous α-Syn aggregates positive for p-α-Syn colocalizing with p62-RFP. The merged image shows a superposition of the p62-RFP (magenta), phospho-α-Syn (green), the neuronal marker MAP2 (gray) and DAPI (blue) channels. Scale bar: 20 μm. Two biologically independent experiments were performed. **f**, Quantification of the percentage of neurons with aggregates in the soma upon treatment with PFFs of cells transduced with GFP-α-Syn (blue) or untransduced (green; endogenous α-Syn). The horizontal lines of each box represent 75% (top), 50% (middle) and 25% (bottom) of the values, and a black square the average value. Whiskers represent 1.5x standard deviation and black diamonds the individual data points. * indicates $p = 0.011$ by two-tailed unpaired t-test with Welch's correction, $n = 4$ (GFP-α-Syn + PFFs) and 3 (endogenous α-Syn + PFFs) biologically independent experiments. **g**, Quantification of neuronal viability upon seeding with PFFs for cells expressing endogenous α-Syn (Endo. α-Syn + PFFs), or transduced with GFP-α-Syn (GFP-α-Syn + PFFs) or with GFP only (GFP + PFFs) relative to untransduced and unseeded control cells. Bars represent average values, the error bars the standard deviation and black triangles the individual data points. *and ** respectively indicate $p = 0.04$ and $p = 0.002$ by two-way ANOVA and Dunnett's multiple comparison test, $n = 3$ biologically independent experiments for all conditions. Representative images are shown in **b**, **c**, **d**. Source data for **f**, **g** are provided as a Source Data file.

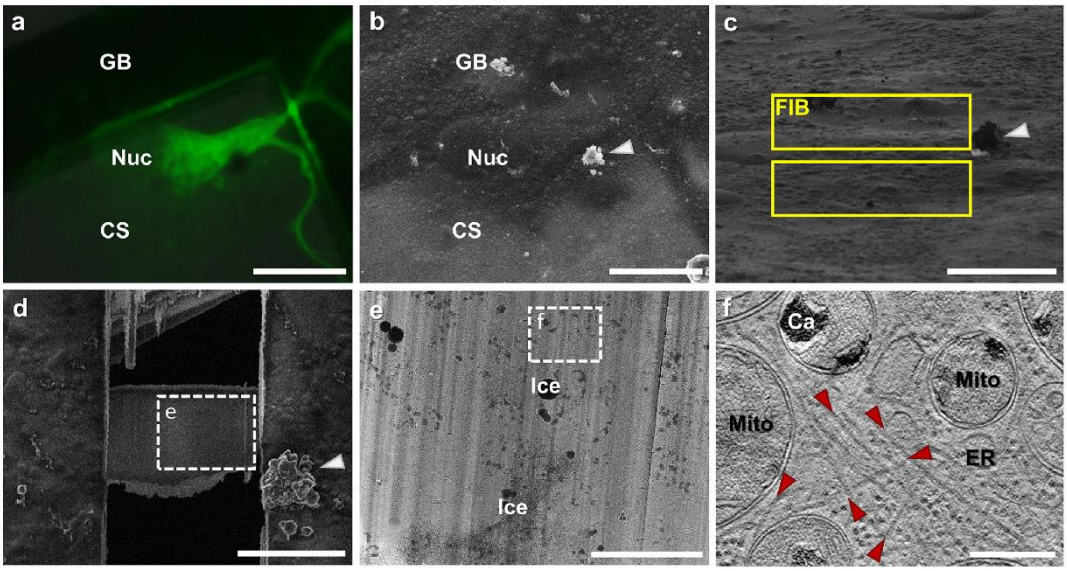

Supplementary Fig. 2 | Cryo-ET workflow. a, Cryo-light microscopy imaging of GFP fluorescence in a primary neuron grown on the carbon support (CS) of an EM grid. The cell was transduced with GFP-α-Syn at DIV 10 and aggregate formation was seeded at DIV 13. The grid was vitrified at DIV 20. GB: grid bar, Nuc: nucleus. Scale bar: 25 µm. **b**, Correlative scanning electron microscopy imaging of the same cell within the cryo-FIB instrument upon coordinate transformation. A white arrowhead marks a piece of ice crystal contamination that can also be found in panels **c** and **d** as visual reference. Scale bar: 25 µm. **c**, FIB-induced secondary electron image of the same cell. Yellow boxes indicate the regions to be milled away by the FIB during lamella preparation. Scale bar: 15 µm. **d**, Scanning electron microscopy imaging of the same cell upon preparation of a 150 nm-thick electron transparent lamella. The white rectangle marks the region of the lamella shown in **e**. Scale bar: 10 µm. **e**, Low magnification transmission electron microscopy image of the area of the lamella marked in **d**. Ice: ice crystal contamination on the lamella surface. The white rectangle marks the region shown in **f**. Scale bar: 3 µm. **f**, A tomographic slice (thickness 1.4 nm) recorded in the area indicated in **e**. Ca: mitochondrial calcium stores, ER: endoplasmic reticulum, Mito: mitochondrion. Red arrowheads indicate α-Syn fibrils. Scale bar: 300 nm. The number of tomograms and biologically independent cryo-ET experiments is listed in Supplementary Table 1. Representative images are shown for all panels.

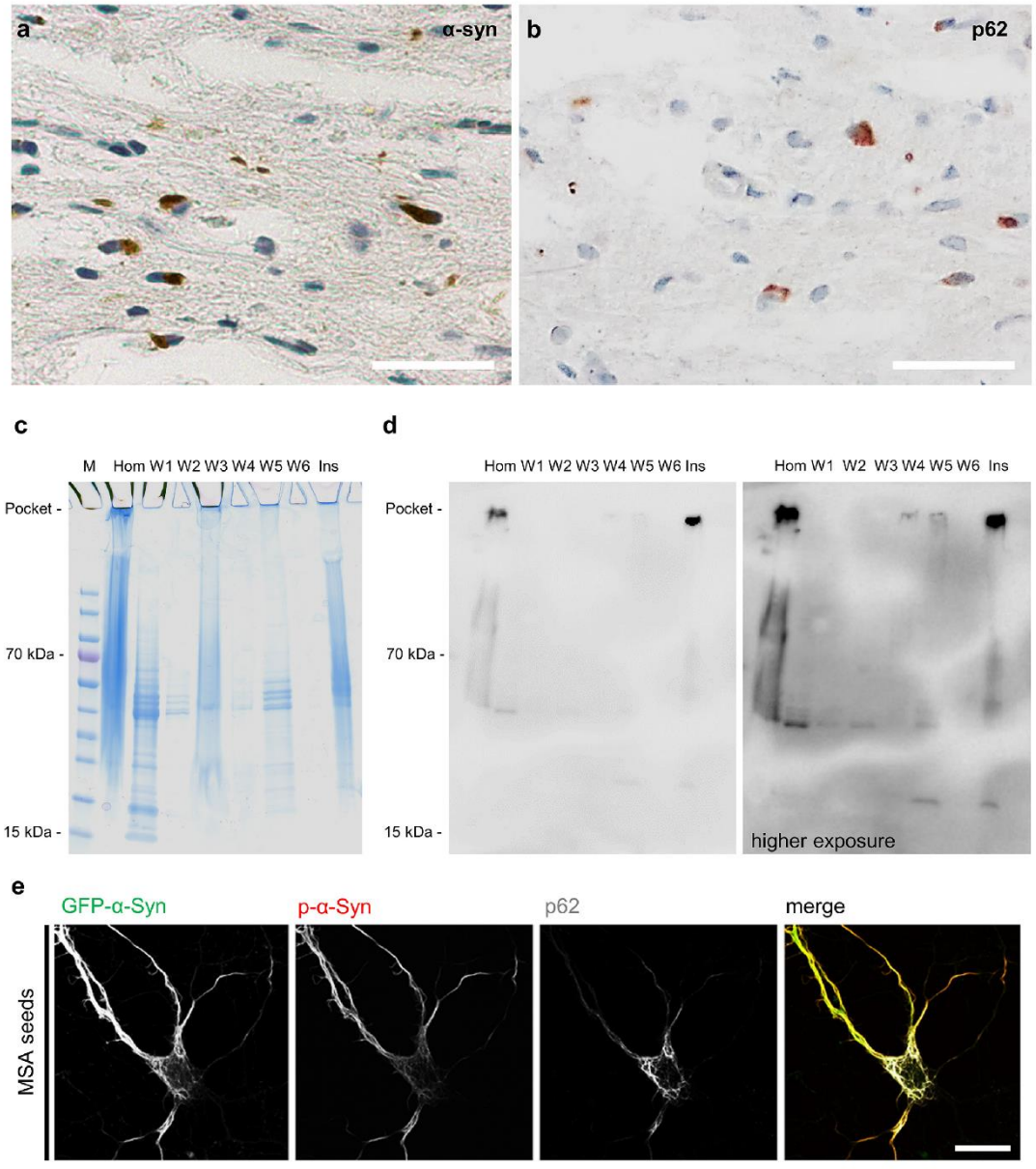

Supplementary Fig. 3 | Purification of α-Syn aggregates from MSA patient brain.

a, **b,** Immunohistochemistry staining showing cytoplasmic inclusions (brown) positive for α-Syn (**a**) and p62 (**b**) in the basilar part of the pons of the brain of an MSA patient. Nuclei are stained in blue. Aggregates for seeding neurons for cryo-ET imaging were purified from the same region

(**c**, **d**). Scale bars: 50 μm. Experiment was performed once. **c**, **d**, Purification of α-Syn aggregates from the MSA patient brain shown in **a**, **b**. Coomassie staining (**c**) and anti-phospho-α-Syn western blot (**d**) of SDS PAGE gels loaded with brain homogenate (Hom), washing fractions (W1-6) and the final sarkosyl-insoluble fraction (Ins) at low (left) and high (right) exposure levels. M: molecular weight marker. Note the aggregated material in the stacking gel. For gel source images, see Supplementary Fig. 2. Experiment was performed once. **e**, Immunofluorescence images of a GFP-α-Syn-expressing neuron seeded with the sarkosyl-insoluble fraction from MSA patient brain, showing aggregates positive for phospho-α-Syn and p62. GFP signal was enhanced by staining with an antibody against GFP. The merged image shows a superposition of the GFP-α-Syn (green), phospho-α-Syn (red) and p62 (gray) channels. Scale bar: 20 μm. Two biologically independent experiments were performed. Representative images are shown for all panels. Source data for **c**, **d** are provided as a Source Data file.

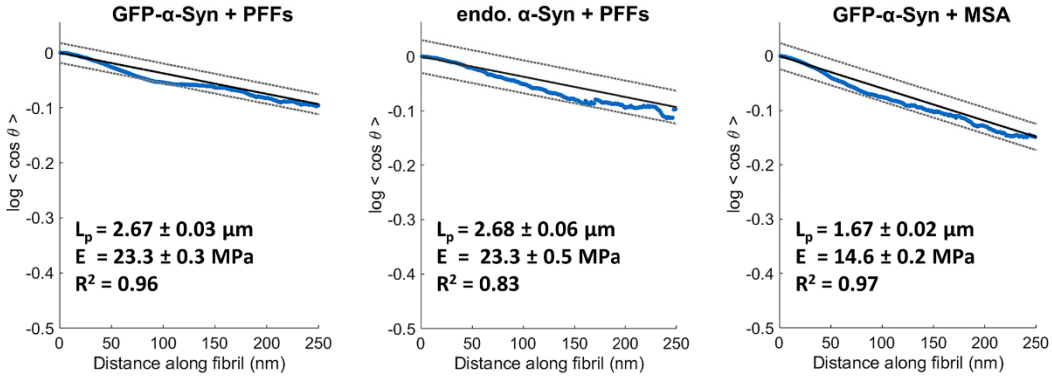

Supplementary Fig. 4 | Persistence length of α-Syn fibrils. Linear fit of the total persistence length for all fibrils analyzed. n = 1295 (GFP-α-Syn + PFFs), 220 (endogenous α-Syn + PFFs) and 721 (GFP-α-Syn + MSA) fibrils in total over two (GFP-α-Syn + PFFs) or three (endogenous α-Syn + PFFs and GFP-α-Syn + MSA) biologically independent experiments. The blue curves represent the original data. 95% confidence interval (dotted lines) and the values of the persistence length (L_p), Young's modulus (E) and coefficients of determination (R^2) are indicated. Note that the values are almost identical for GFP-α-Syn and endogenous α-Syn seeded with PFFs, but lower for GFP-α-Syn seeded with MSA patient aggregates. Source data are provided as a Source Data file.

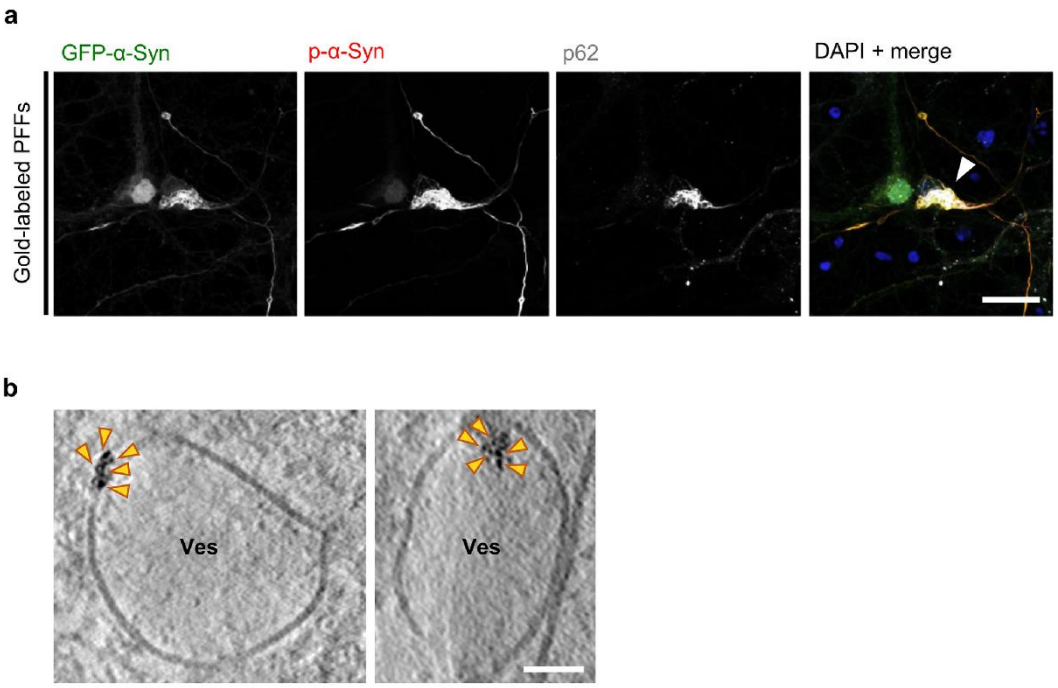

Supplementary Fig. 5 | Seeding of α-Syn aggregates in neurons by gold-labeled PFFs. a, Immunofluorescence images of a GFP-α-Syn-expressing neuron seeded with gold-labeled PFFs. The cells develop α-Syn aggregates, as detected by antibodies against phosphorylated α-Syn Ser129 and p62. GFP signal was enhanced by staining with an antibody against GFP. The merged image shows a superposition of the GFP-α-Syn (green), phospho-α-Syn (red), p62 (gray) and DAPI (blue) channels. An arrowhead indicates the GFP-α-Syn aggregates. Scale bar: 20 µm. **b**, Tomographic slices (thickness 1.4 nm) showing accumulations of gold particles (orange arrowheads) at the membrane (left) or in the lumen (right) of intracellular vesicles. Ves: vesicles. Scale bar: 50 nm. Two biologically independent experiments were performed in all cases. Representative images are shown for all panels.

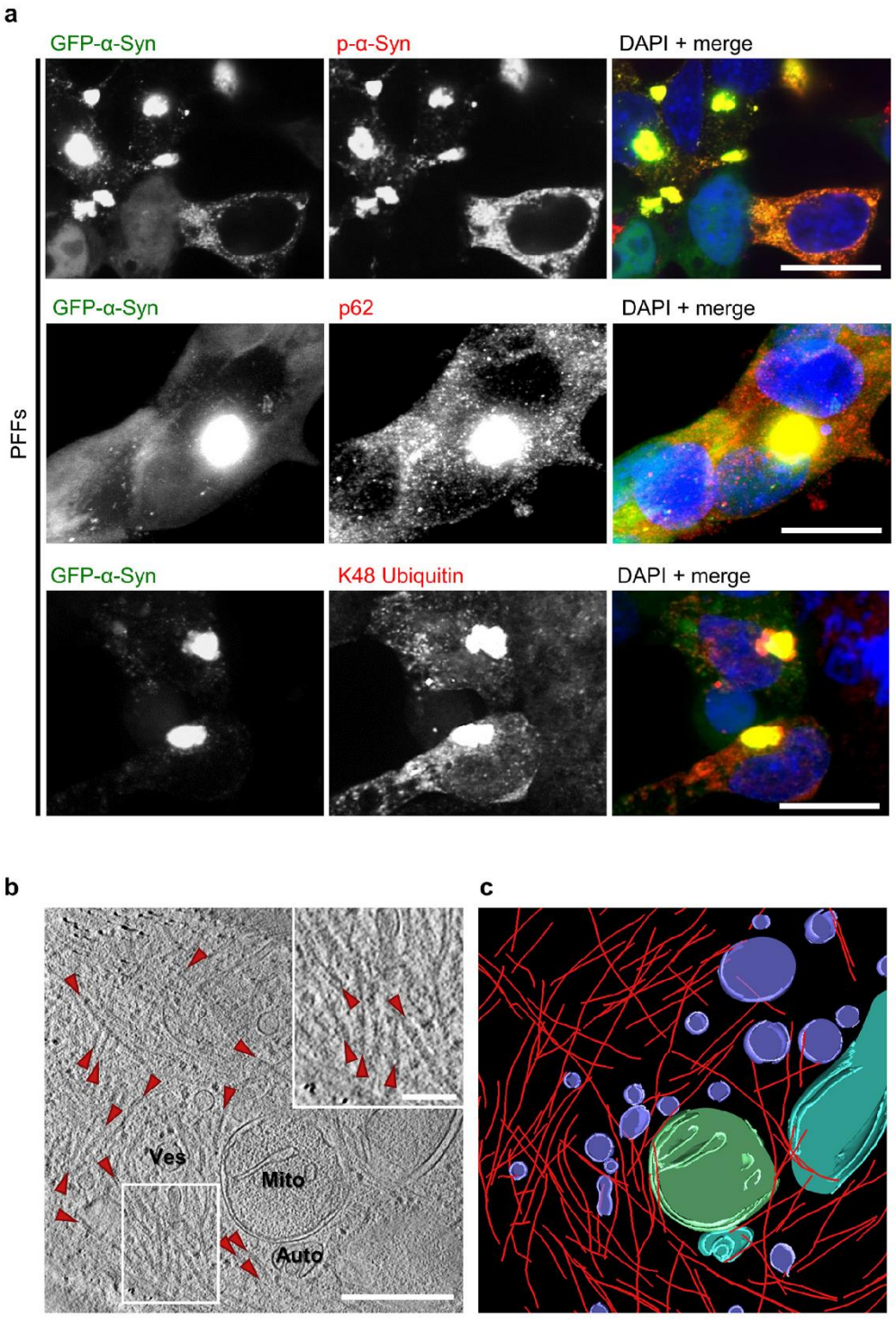
a
GFP-α-Syn
p-α-Syn
DAPI + merge
GFP-α-Syn
p62
DAPI + merge
PFFs
GFP-α-Syn
K48 Ubiquitin
DAPI + merge
b
c
Ves
Mito
Auto

Supplementary Fig. 6 | α-Syn aggregates in SH-SY5Y cells. a, Immunofluorescence images of SH-SY5Y cells stably expressing GFP-α-Syn and seeded with PFFs. The cells develop α-Syn inclusions, as detected by antibodies against phosphorylated α-Syn Ser129 (top), p62 (middle) and K48-linked ubiquitin (bottom). The merged images show a superposition of the respective green and red channels plus DAPI (blue). Scale bars: 15 µm. **b**, A tomographic slice (thickness 1.8 nm) of an inclusion seeded by PFFs in a SH-SY5Y cell expressing GFP-α-Syn. Auto: autophagosome; Mito: mitochondrion; Ves: vesicles. Fibrils are marked by red arrowheads. Scale bars: 350 nm (main panel) and 100 nm (inset). **c**, 3D rendering of the tomogram depicted in **b** showing α-Syn fibrils (red), autophagosomes (cyan), mitochondria (green) and various vesicles (purple). Three biologically independent experiments were performed in all cases. Representative images are shown for all panels. Source data are provided as a Source Data file.

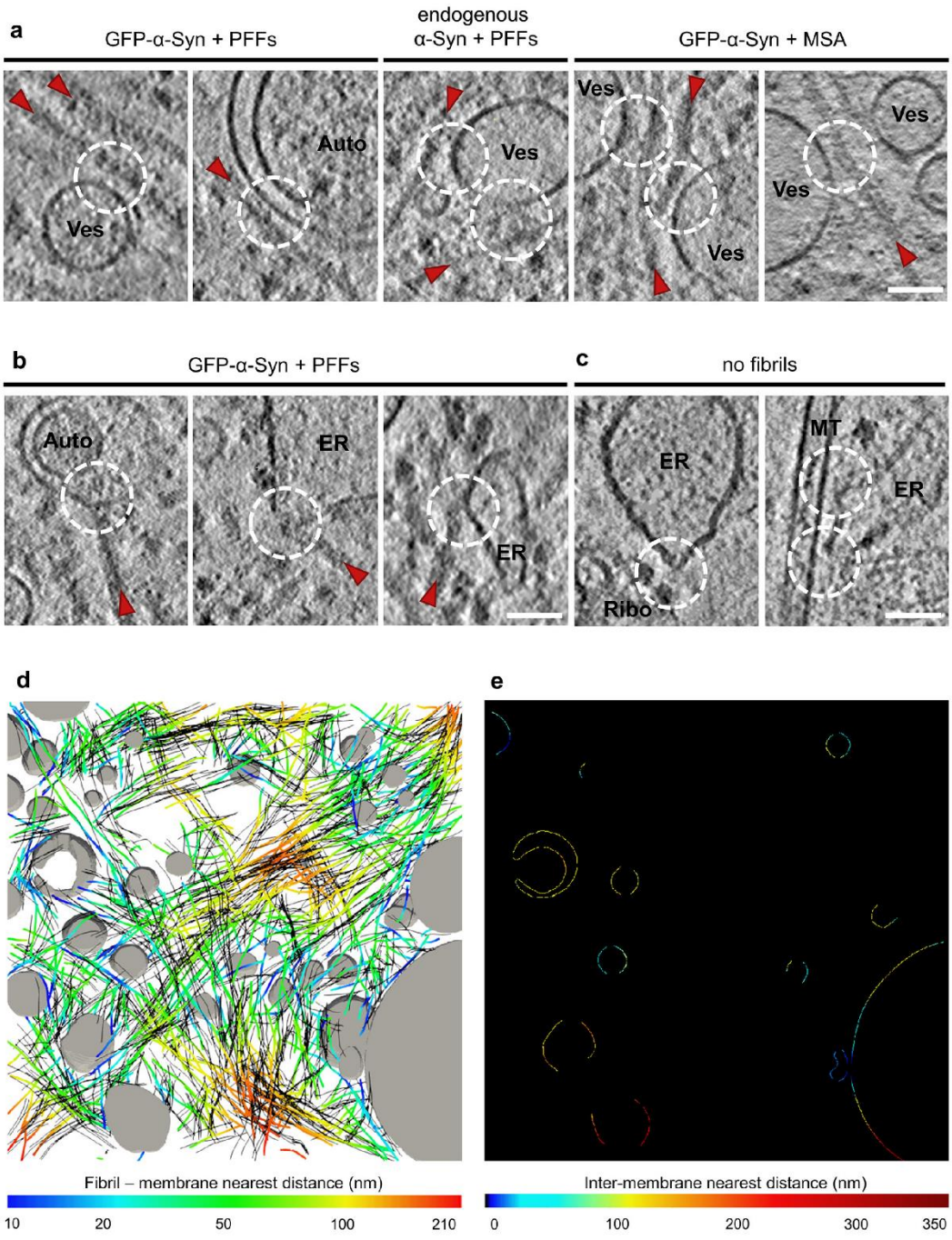
a
GFP-α-Syn + PFFs
endogenous
α-Syn + PFFs
GFP-α-Syn + MSA
Ves
Auto
Ves
Ves
Ves
Ves
Ves
b
GFP-α-Syn + PFFs
c
no fibrils
Auto
ER
ER
ER
MT
ER
Ribo
d
e
Fibril – membrane nearest distance (nm)
10
20
50
100
210
Inter-membrane nearest distance (nm)
0
100
200
300
350

Supplementary Fig. 7 | Proximity of α-Syn fibrils and cellular membranes. a, Gallery of tomographic slices showing close proximity events (dashed white circles) between α-Syn fibrils (red arrowheads) and different cellular membranes with no apparent interactions. Auto: autophagosome, Ves: vesicles. Tomographic slices are 1.8 nm (GFP-α-Syn + PFFs) or 1.4 nm (endogenous α-Syn + PFFs and GFP-α-Syn + MSA) thick. Scale bar: 50 nm. **b,** Gallery of tomographic slices (thickness 1.8 nm) showing apparent contacts between α-Syn fibrils and different cellular membranes at sites of high membrane curvature (dashed white circles), within inclusions seeded by PFFs in neurons expressing GFP-α-Syn. ER: endoplasmic reticulum. Scale bar: 50 nm. **c,** Tomographic slices showing sites of high membrane curvature (dashed white circles) in the absence of α-Syn fibrils in neurons expressing p62-RFP and seeded with PFFs. MT: microtubule; Ribo: ribosome. Tomographic slices are 1.4 nm thick. Scale bar: 60 nm. **d**, 3D rendering shown in Fig. 1d and Fig. 4a with α-Syn fibrils color-coded according to their distance to the nearest cellular membrane (gray). To elucidate whether the events of close proximity between fibrils and membranes were caused by chance or mediated by molecular interactions, random shifts (by 10 – 20 nm) and rotations (between 0 and 10°) were performed to the experimentally determined location of the fibrils. Black lines show 5 simulations for 50 randomly chosen fibrils. **e**, Measurements of inter-membrane distances for a 2D slice of the tomogram shown in **d**. The number of tomograms and biologically independent cryo-ET experiments is listed in Supplementary Table 1. Representative images are shown.

Supplementary Methods | Fibril-membrane and inter-membrane distance calculation.

Fibril-membrane distance

The algorithm computing fibril-membrane nearest distances can be summarized as follows:

For each tomogram:

1. Use the segmentation of organelle lumina to compute the distance transform tomogram[1], which calculates the Euclidean distance from each background voxel to the nearest segmented one.
2. For each fibril:

2.1. The curve defined by Amira's Xtracing module during segmentation is sampled uniformly each 5 nm (i.e. similar to the fibril radius).

2.2. For each point in the fibril:

2.2.1. To achieve subvoxel precision, get the interpolated value of the distance transform tomogram at the coordinates of that point.

2.2.2. Add this value to a list of fibril-membrane nearest distances.

The probability density was computed as the normalized histogram of the list of fibril-membrane nearest distances.

To test whether these fibril-membrane nearest distances resulted from random or specific interactions, we compared the experimentally determined distances with those of simulated fibrils. These simulated fibrils were created by randomly shifting and rotating the experimentally measured fibrils as follows:

For each tomogram, generate 200 synthetic tomograms:

1. Take randomly an input experimental fibril as reference.
2. Shift the reference fibril in respect to its center at a random distance in a range of [10, 20] nm.
3. Rotate the fibril randomly with respect to the fibril center with Euler angles selected randomly in the range of [0, 10] degrees.
4. Try to insert the resulting fibril in the synthetic tomogram. The insertion fails in the following cases:

4.1. The fibril intersects with another one, considering that fibrils have a cross-section radius of 5 nm.

4.2. The fibril intersects with a segmented membrane.

4.3. Part of the fibril is out of the tomogram boundaries.

5. Iterate until 50 fibrils are inserted or 5000 tries are reached.

Inter-membrane distance

The algorithm for computing inter-membrane nearest distances can be summarized as follows:

For each tomogram:

1. Assign labels for the lumen of each organelle.
2. Associate segmented membranes and lumina by a proximity criterion. For each voxel in a membrane segmentation, the label of the nearest lumen voxel is determined. The lumen is then associated to the membrane segmentation most frequently found.
3. For each lumen:

3.1. Compute the distance transform tomogram[1] from all lumina.

3.2. Erase the current lumen.

3.3. For each pixel on the membrane segmentation associated to the current lumen:

3.3.1. Get the interpolated value of the distance transform tomogram at the coordinates of that point.

3.3.2. Add this value to a list of inter-membrane nearest distances.

Probability densities were computed as described for fibril-membrane nearest distances.

References

1 van der Walt, S., Colbert, S. C. & Varoquaux, G. The NumPy Array: A Structure for Efficient Numerical Computation. *Comput Sci Eng* **13**, 22-30, doi:10.1109/mcse.2011.37 (2011).

2.3 Publication 3: The Hsc70 disaggregation machinery removes monomer units directly from α-synuclein fibril ends

Aim and key results of the study:

Previous studies showed that the Hsp70 chaperone system is capable of disaggregating α-syn amyloid fibrils *in vitro*. The exact mechanism, however, has not been understood. To elucidate the mode of action, we conducted microfluidic measurements of α-syn species formed during the disaggregation reaction. We showed that Hsc70 together with its co-chaperones DnajB1 and Apg2 removes α-syn monomers from the amyloid fibril ends and that fibril fragmentation has only a small effect on the kinetics of the disaggregation reaction. Together with previous reports, we were able to describe a detailed mechanism of Hsc70-mediated disaggregation of α-syn amyloid fibrils.

Contribution:

V.A.T. conducted negative stain electron microscopy experiments of α-syn fibrils at different time points during the disaggregation reaction and helped with *in vitro* disaggregation assays using ThT fluorescence measurements.

nature COMMUNICATIONS

ARTICLE

https://doi.org/10.1038/s41467-021-25966-w OPEN

The Hsc70 disaggregation machinery removes monomer units directly from α-synuclein fibril ends

Matthias M. Schneider[1,6], Saurabh Gautam[2,5,6], Therese W. Herling[1,6], Ewa Andrzejewska[1,6], Georg Krainer[1,6], Alyssa M. Miller[1], Victoria A. Trinkaus[2,3], Quentin A. E. Peter[1], Francesco Simone Ruggeri[1], Michele Vendruscolo[1], Andreas Bracher[2], Christopher M. Dobson[1,8], F. Ulrich Hartl[2,3,7✉] & Tuomas P. J. Knowles[1,4,7✉]

Molecular chaperones contribute to the maintenance of cellular protein homoeostasis through assisting de novo protein folding and preventing amyloid formation. Chaperones of the Hsp70 family can further disaggregate otherwise irreversible aggregate species such as α-synuclein fibrils, which accumulate in Parkinson's disease. However, the mechanisms and kinetics of this key functionality are only partially understood. Here, we combine microfluidic measurements with chemical kinetics to study α-synuclein disaggregation. We show that Hsc70 together with its co-chaperones DnaJB1 and Apg2 can completely reverse α-synuclein aggregation back to its soluble monomeric state. This reaction proceeds through first-order kinetics where monomer units are removed directly from the fibril ends with little contribution from intermediate fibril fragmentation steps. These findings extend our mechanistic understanding of the role of chaperones in the suppression of amyloid proliferation and in aggregate clearance, and inform on possibilities and limitations of this strategy in the development of therapeutics against synucleinopathies.

[1] Yusuf Hamied Department of Chemistry, Centre for Misfolding Diseases, University of Cambridge, Lensfield Road, Cambridge CB2 1EW, UK. [2] Department of Cellular Biochemistry, Max-Planck Institute of Biochemistry, Am Klopferspitz 18, 82152 Martinsried, Germany. [3] Munich Cluster for Systems Neurology (SyNergy), Munich, Germany. [4] Department of Physics, Cavendish Laboratory, University of Cambridge, JJ Thomson Road, Cambridge CB3 0HE, UK. [5] Present address: ViraTherapeutics GmbH, 6063 Rum, Austria. [6] These authors contributed equally: Matthias M. Schneider, Saurabh Gautam, Therese W. Herling, Ewa Andrzejewska, Georg Krainer. [7] These authors jointly supervised this work: F. Ulrich Hartl, Tuomas P. J. Knowles. [8] Deceased: Christopher M. Dobson. ✉email: uhartl@biochem.mpg.de; tpjk2@cam.ac.uk

Misfolding and aggregation of proteins and peptides into amyloidogenic fibrils are hallmarks of a wide range of neurodegenerative disorders[1–3], including α-synuclein (αS) in Parkinson's disease, the Aβ-peptide in Alzheimer's disease, and Huntingtin (HTT) in Huntington's disease[4]. The accumulation of such fibrillar deposits in the central nervous system occurs in an age-dependent manner; earlier in life, this process is counteracted by efficient cellular protein quality control machinery that inhibits the amyloid formation and thus disease[5–7].

Molecular chaperones are critical components of this quality control system[7]. Initially identified as part of the heat stress response[8–10], chaperones have been shown to assist protein folding and rescue misfolded states[6,8]. Particularly variants of the 70 kDa heat shock protein family (Hsp70s) populate some of the most critical nodes in the proteostasis network and are involved in assisting protein folding and in exerting holdase activity. They are also actively engaged in preventing protein aggregation and in degrading misfolded proteins, as well as in mediating the assembly and disassembly of oligomeric protein species[7,11,12]. In fact, Hsp70s, along with various other chaperones, have been shown to modulate essentially all microscopic steps in amyloid formation, including elongation[13,14], primary nucleation[15], as well as secondary nucleation[16].

In recent years, mounting evidence has indicated that Hsp70 chaperones are also involved in the disassembly of aggregates and are capable of disaggregating even persistent amyloidogenic aggregate structures such as αS, HTT and Tau fibrils[17–27]. In particular, the constitutively expressed chaperone heat shock cognate Hsc70 (HSPA8) together with the Hsp40 class B J-protein DnaJB1 and the Hsp110 family nucleotide exchange factors (NEFs) Apg2 or Hsp105α have been demonstrated to constitute a powerful ATP-driven disaggregase system that disassembles amyloids within minutes, promoting their fragmentation and depolymerisation into monomers or smaller oligomeric structures[17,18,20].

Several studies have provided substantial insights into the basic working principles of the Hsc70–DnaJB1–Hsp110 triad chaperone system (Fig. 1)[7,18,19,28]. Structurally, Hsc70, as other Hsp70 chaperones, contains an N-terminal nucleotide-binding domain (NBD) of 40-kDa, which is linked via a flexible, hydrophobic linker to a 15-kDa substrate-binding domain (SBD) and a 10-kDa α-helical lid[7,11,12]. The SBD recognises hydrophobic peptide segments that are exposed in non-native substrate proteins[29–31], which are delivered to Hsp70 by J-protein chaperones such as DnaJB1. Upon ATP hydrolysis to ADP induced by the J-protein, the lid closes to form a stable substrate–Hsp70 complex and the J-protein dissociates from Hsp70[7,11,12]. NEFs, in particular members of the Hsp110 family (e.g., Apg2 or Hsp105α)[32–36], replace the bound ADP with ATP, facilitating lid-opening and substrate release. Since assembly of the chaperone machinery on a protein aggregate leads to a significant entropy loss due to excluded volume effects, the chaperone is thought to act on its substrate by entropic pulling, that is, by exerting a force of up to 15–20 pN to the region it is bound to, leading to the fibril disaggregation[37–39].

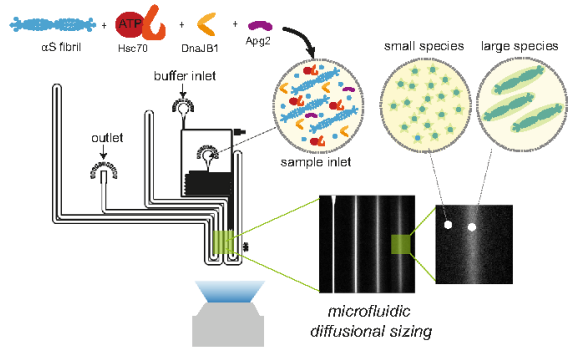

Fig. 1 Hsc70-mediated αS fibril disaggregation monitored by direct size measurements through microfluidic diffusional sizing. αS fibrils are incubated with the Hsc70–DnaJB1–Apg2 chaperone triad. At different time points, the reaction mixture is analysed using microfluidic diffusional sizing which probes the sizes and hence molecular weights of the species present in the solution. From the recorded diffusion profiles, the size decay of fibrils with time is monitored, allowing kinetic and mechanistic analysis of the disaggregation reaction.

While basic aspects of the functional cooperation of the Hsc70–DnaJB1–Apg2 chaperone system in protein disaggregation have been established,[7,18,19] key mechanistic questions remain unanswered. Specifically, it is unclear if the disaggregase machinery acts predominantly on the fibril ends or along the fibril surface, and if the monomer is removed from the fibril substrate, or whether smaller fragments are produced. Moreover, fundamental functional and biophysical parameters such as binding stoichiometry and binding affinities describing the interaction between the participating components are yet to be resolved. Insights into these aspects are of fundamental importance, not least because of the therapeutic potential of Hsp70-mediated disaggregation in neurodegeneration.

Here, we dissect the molecular mechanisms by which the Hsc70–DnaJB1–Apg2 chaperone system disaggregates αS fibrils. We employ microfluidic diffusional sizing in conjunction with chemical kinetics analysis to quantify and characterise the molecular species formed during disaggregation (Fig. 1). A key finding of this study is that the chaperones disassemble αS fibrils into monomers. This ATP-dependent process requires all three components of the Hsp70 system and follows pseudo-first-order kinetics, which suggests that monomer units are removed directly from the fibril ends. Indeed, single-round disaggregation experiments clearly show that αS monomer is produced after a single disaggregation cycle in a step mediated by the action of Apg2 on fibril-bound Hsc70. Lastly, we assess the binding properties between the different chaperones and co-chaperones as well as between the chaperones and the fibrils. Based on these results, we establish a full kinetic and thermodynamic profile of the Hsc70-mediated disaggregation reaction and, consistent with recent findings[19], propose a model of αS disaggregation suggesting that Hsc70 chaperones form a cluster in order to exhibit disaggregase functionality on αS fibrils.

Results

Kinetics of αS fibril disaggregation by the Hsc70 chaperone machinery. To gain insights into the mechanism of αS fibril disaggregation, we sought to obtain quantitative data on the time evolution of this process directly in solution. To this effect, we applied a microfluidic diffusional sizing approach[40–42] to investigate the time evolution of αS fibril disaggregation by the Hsc70 chaperone machinery. Such heterogeneous multi-component systems can be challenging to study using conventional surface-based analysis approaches, but the absence of convective mixing on microfluidic scales allows these interactions to be investigated directly in solution without the requirement for any of the binding partners to be immobilised onto a surface. Alternative methods such as dynamic light scatting (DLS) have been used to analyse heterogeneous aggregation reactions[43–46], but can be challenging to apply to multi-component systems like the one studied here where the specific signal originating from the

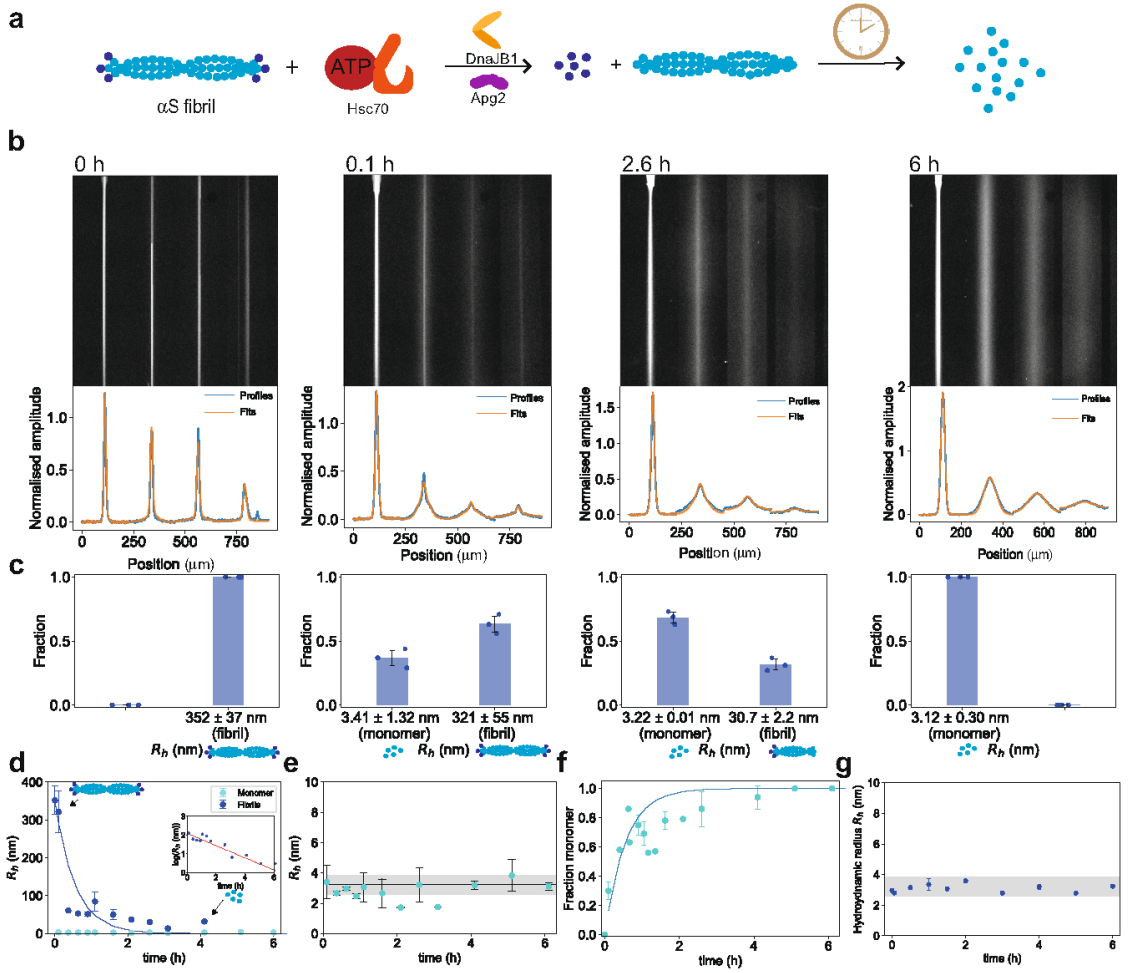

Fig. 2 Diffusional sizing and kinetic analysis of αS fibril disaggregation by the Hsc70 chaperone machinery. a Schematic of the disaggregation reaction and the experimental assay. **b** Representative images of microfluidic diffusional sizing experiments at different time points and diffusion profiles obtained from image analysis during the disaggregation time course. The four different channels represent four different diffusion times; the less diffusive spreading there is in these four channels, the larger the molecule is. It can be seen that diffusion profiles broaden over time, indicating that a smaller species is created during the disaggregation reaction. At 0.1 h and 2.6 h, the profiles show an overlay of two species, one with high diffusivity, one with little diffusivity, indicating a heterogeneous population of a small, broadly diffused-out species and a larger, little diffusing species was observed, while the population was homogeneous at 0 h and 6 h. Extracted R_h values for the small and large species from diffusion profile fitting at these time points are reported in panel **b**. The experimentally obtained diffusional profiles are shown in blue and the obtained fits in orange. **c** Histograms showing the size distribution of the two species from image analysis. At 0 h and 6 h, R_h values of single-component fits are reported. The individual data points are overlayed on the bar plot. **d** Evolution of R_h for small (cyan) and large species (blue) over time. The size of the larger species decayed monotonically, consistent with a single exponential fit (blue line). The size of the smaller species remained constant over time. Inset: logarithmic representation of $R_{h,large}$ over time. From these fits, a rate constant of $k = 1.8 \pm 0.3 \times 10^{-4}$ s^{-1} was determined ($R^2 = 0.89$). **e** R_h of the small species compared to R_h of pure monomer (black line and grey region indicate the expected size and size range from pure monomer). This analysis shows that monomer is produced throughout the reaction and no other intermediate is generated. **f** Fraction of monomer over time (cyan), showing that the fraction of monomer increases over time, whereby less monomer is generated at later time points, consistent with Fig. 2d. ($R^2 = 0.89$). **g** Time course experiment. 100 nM αS monomers labelled with Alexa Fluor 488 are added to a disaggregation mixture with 2 μM unlabelled αS fibrils, and the size of the fluorescent species is measured over time. The size remains largely constant over the time course of the 6 h experiment, showing the inhibition of elongation through the disaggregation machinery. Data in **c**–**g** are represented as mean ± standard deviation of $n = 3$ independent experiments.

chaperone proteins would obscure the signal of αS disaggregation products. The diffusional sizing approach overcomes this problem by measuring the diffusivity of fluorescently labelled molecular species in solution and monitoring changes as they undergo binding events. In practice, we capture the diffusion process in both space and time by acquiring the longitudinal diffusion profiles of protein molecules, here αS species, flowing in a microfluidic channel (Fig. 2a). The diffusion profiles are then analysed by considering advection–diffusion processes to extract the distribution of diffusion coefficients (not shape-dependent) and the corresponding hydrodynamic radii (R_h) of the individual species present in solution[40,42]. The diffusion coefficient is,

according to the Stokes–Einstein relationship, inversely proportional to the hydrodynamic radius[40]. Therefore, increased broadening of the diffusion profile is expected for smaller proteins in comparison to larger proteins. Crucially, this method also allows for the detection of protein–protein interactions by monitoring the increase in size of diffusing species associated with binding[16,47]. Thus, microfluidic diffusional sizing allows distinguishing different species in αS fibril disaggregation based on their hydrodynamic radii.

In the first series of experiments, we monitored the kinetics of αS fibril disaggregation by the Hsc70 disaggregation machinery. To this end, we incubated the chaperone system consisting of Hsc70, DnaJB1, and Apg2 in presence of an ATP-regenerating system (see the "Methods" section and Fig. 2a) with preformed αS fibrils labelled with AlexaFluor488 (amine labelling of αS monomers). These fibrils were produced by mixing 10% labelled and 90% unlabelled monomers. Such labelled fibrils were structurally comparable to unlabelled fibrils, as shown by atomic force microscopy (AFM) (Supplementary Fig. 1) and were disaggregated with similar kinetics as unlabelled fibrils in bulk assays followed by thioflavin T (ThT) fluorescence (Supplementary Fig. 2). The sample was introduced at the centre of the microfluidic channel and the extent of diffusion towards the edges of the channel was monitored as a function of channel position. A solution of pure fibrils in the absence of the disaggregation machinery consisted of a high molecular weight species with the only little broadening of the sample stream along the microfluidic channel (Fig. 2b, 0 h), in agreement with the expected large size of αS fibrils (~200–300 nm, Supplementary Fig. 3). By contrast, a clear signature of fibril disintegration became apparent in the presence of the disaggregase system as diffusion profiles broadened over the time course of the reaction.

At early time points (Fig. 2b, 0.1 h), fibrils were still predominant; however, a second protein species with a high degree of diffusive broadening became apparent, showing that the initiation of the disaggregation reaction is fast (i.e., within a few minutes) and that a smaller molecular weight species is being produced. At intermediate time points (Fig. 2b, 2.6 h), the fluorescence intensity arising from the smaller diffused-out species increased relative to the larger species, while fibrils were still present. At late time points (Fig. 2b, 6 h), the diffusion profiles broadened significantly and yielded a monodisperse population of the smaller molecular weight species. Full disaggregation was observed after ~3 h. Crucially, disaggregation required the presence of all three chaperone components and ATP. Specifically, Hsc70 alone with ATP was unable to mediate fibril disaggregation (Supplementary Fig. 4).

Quantitative analysis of the diffusion profiles as a function of time revealed that the profiles are best described by two diffusing species (Fig. 2c and Supplementary Fig. 5). The fraction of the larger species with an initial R_h of ~350 nm, corresponding to the size of fibrils (Fig. 2d), decayed monotonically over time, while simultaneously the fraction of a smaller, diffused-out species with an R_h of ~3 nm gradually increased (Fig. 2e, f). The smaller species, that built up in time, corresponds in size to pure monomer (Fig. 2e), demonstrating that the reconstituted Hsc70 machinery disaggregates αS fibrils into monomer units. As shown in Supplementary Fig. 6, we are able to distinguish fluorescently labelled monomers from fibrils, oligomers from fibrils, and monomers from oligomers and to quantify the ratio of the present species accurately. In contrast, as shown in Supplementary Fig. 7, in DLS measurements it is challenging to obtain this level of resolution in a heterogeneous mixture and the method largely reports on the larger species present in solution under these conditions.

The observation that monomer was already abundant at very early time points not only highlights the fact that the fibril-to-monomer conversion reaction is very fast (i.e., on the minutes timescale) but also strongly indicates that monomer units are removed from the fibril ends directly, as opposed to scenarios that involve intermediate fragmentation steps, in which case other species than fibrils and monomer would have been observed. No monomer is observed in the fibril-only sample (Fig. 2b, 0 min).

Further quantification revealed that the size decay of the large fibrillar species was best described with a single exponential kinetic model, yielding a rate constant of $k = 1.8 \pm 0.3 \times 10^{-4}\ s^{-1}$. Crucially, the apparent size of the species converged to that of the smaller species (i.e., monomer) after ~3 h, indicating that the disaggregation reaction had gone to completion. The single exponential behaviour was observed independent of whether the experiments were performed with full-length fibrils (see above) or sonicated fibrils (Supplementary Fig. 8). However, the reaction rate per synuclein concentration for the complete conversion of fibrils to monomer was accelerated by ~20% for the sonicated fibrils, which are ~20% smaller (270 vs. 350 nm), indicating that the abundance of more fibril ends allows a faster decline, as the Hsc70 is present in excess under the disaggregation reaction conditions (Supplementary Fig. 9). This finding supports the conclusion that the removal of monomer, simultaneously from both the fibril ends, depends on the number of fibril ends. A single exponential behaviour is consistent with a pseudo-first-order kinetic model (Fig. 2d) and thus supportive of a one-step disaggregation reaction mechanism, without previous fragmentation of the fibril.

Lastly, we investigated whether the disaggregation machinery also has the capacity to inhibit the forward aggregation reaction. To this effect, we performed an experiment where we added labelled monomer to unlabelled fibrils in the presence of the chaperone system, without detecting an increase in size (Fig. 2g), as opposed to the absence of chaperone (Supplementary Fig. 10). This suggests that the presence of chaperones in the aggregation mixture prevents monomer re-binding and, thus, fibril elongation. This mechanism is complementary to the active dissociation capacity of the chaperone machinery and means that freshly dissociated monomer units are protected against immediately being reincorporated into aggregates, thus enhancing the overall efficiency of the disaggregation process.

To further explore the dissociation mechanism, we monitored the outcome of the disaggregation reaction using diffusional sizing combined with confocal microscopy[48–50] (Fig. 3a, b). In this approach, the molecular diffusivity of sample components is probed by moving the confocal observation volume across the microfluidic device at the mid-height of the channel perpendicular to the flow direction, as shown in Fig. 3b (left panel). By measuring the fluorescence signal of molecules passing the confocal volume along the scan trajectory, the number of molecular species of different diffusion coefficients and hence different sizes can be measured directly.

We first performed experiments on pure fibrils and pure monomers in the absence of the disaggregation machinery to establish the signature of the two species present in disaggregation reactions (Fig. 3b, right panel). For fibrils, large fluorescent bursts located at the centre of the channel, corresponding to the detection of single aggregates, were observed. Fibrils contain a large number of fluorophores since 10% of the monomers within the fibril are fluorescently labelled. This results in the detection of burst events of high fluorescence intensity that are narrowly distributed around the centre of the channels and indicate a low diffusion coefficient and correspondingly large size. For the monomer sample, which was probed at nanomolar concentrations, the sizing profiles exhibited a broader spread, due to the larger diffusivity of the monomeric units as compared to fibrils. The signal is continuous because nanomolar concentrations are

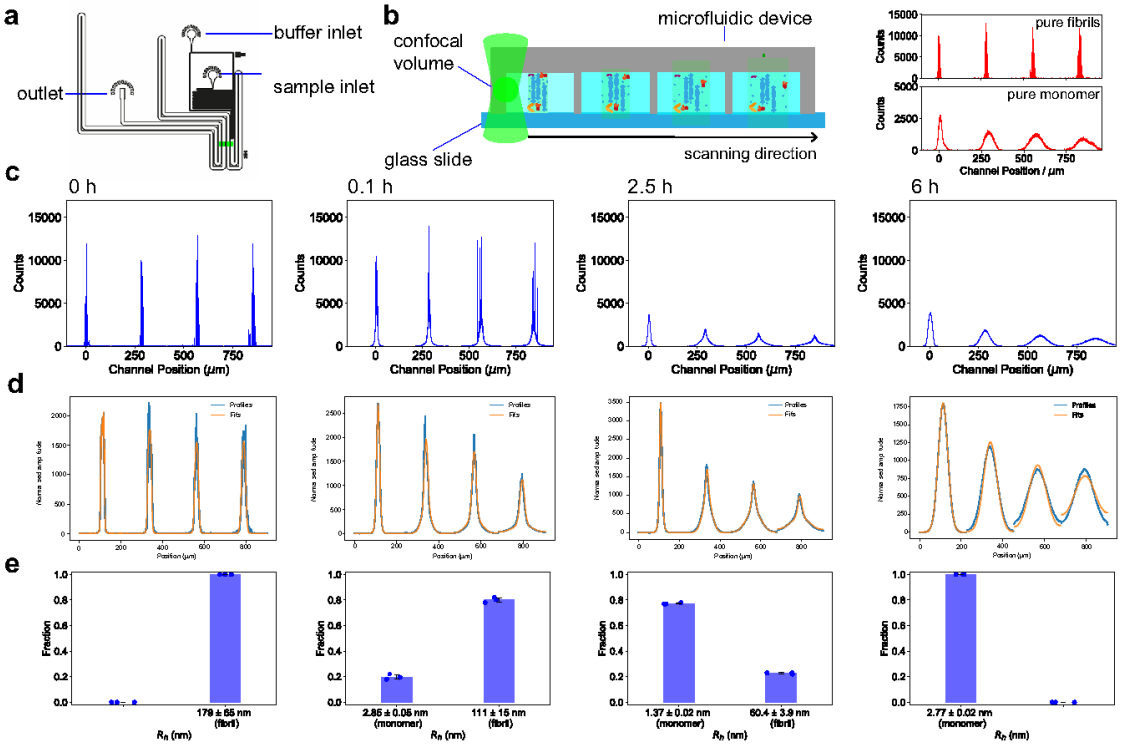

Fig. 3 Analysis of αS fibril disaggregation by the Hsc70 chaperone machinery using confocal microfluidic diffusional sizing. a Design of the microfluidic device for confocal microfluidic diffusional sizing. The chip design is the same as for the epifluorescence microscopy experiments (see Fig. 1). **b** The confocal volume scans across the four innermost channels of the microfluidic chip made of polydimethylsiloxane (PDMS) (highlighted in panel **a**), thereby capturing the diffusive broadening of the reaction mixture with increased diffusion time. (Right) Typical diffusion profiles for pure fibrils and monomers. Pure fibrils show large fluorescence bursts due to the high number of fluorophores detected per fibril, as well as little broadening due to the large size of the fibrils. Profiles for pure monomer samples exhibit no bursts, due to the bulk concentrations employed and because each detected monomer only carries one label. Monomer profiles are broadened significantly in comparison to fibrils due to the small hydrodynamic radius of the monomeric protein. **c** Diffusion profiles for confocal scanning across the microfluidic channel for αS fibrils at different time points during the disaggregation reaction. Consistent with Fig. 2, the width of the profile base broadens significantly. Furthermore, the bursts, indicating the presence of numerous fluorophores as found in a fibrillar state, vanish at later time points, consistent with the disappearance of fibrils as a result of Hsc70-mediated disaggregation. **d** Fitting generated for profiles in panel (**c**). Normalised experimentally obtained diffusional profiles are shown in blue and the obtained fits in orange. **e** Histograms showing the size and fractional distribution of the two species from diffusion profile analysis. At 0 and 360 min, R_h values of single-component fits are reported. The individual data points are overlaid on the bar plot. Data in **e** are represented as mean ± standard deviation of $n = 3$ independent experiments.

used, and therefore multiple monomeric units traverse the confocal detection volume at the same time, resulting in a bulk fluorescence signal rather than individual single-molecule events, in contrast to the aggregate sample.

After having established the properties of fibrillar and monomeric samples, we monitored the kinetics of Hsc70-mediated αS fibril disaggregation using confocal microfluidic diffusional sizing. At time point zero (Fig. 3c, d, 0 h), again narrowly distributed profiles with large bursts were recorded, consistent with fibrillar species. Shortly after starting the disaggregation reaction (Fig. 3c, 0.1 h), profiles started to broaden at the profile base, with bursts still being detectable. This indicates the emergence of a second, small protein species with a high degree of diffusive broadening. At intermediate time points (Fig. 3c, 2.5 h), the fluorescence intensity arising from the smaller diffused-out species increased relative to the larger burst species. At late time points (Fig. 3c, 6 h), the diffusion profiles broadened significantly and yielded a monodisperse population of the smaller molecular weight species. No large burst signals that would stem from fibrils were detected at this late time point. Diffused out species of the diffusion profiles of the disaggregation reaction were identical to the profiles obtained from the pure monomer sample. Quantitative analysis of the diffusion profiles of all time points during the disaggregation reaction using a two-species fitting procedure (Fig. 3d, e) yielded sizes and fractional distributions consistent with fibrils and monomer, in line with the results obtained from widefield diffusional sizing measurements (cf., Fig. 2). The analysis was performed with the same two species fitting as mentioned before for the widefield diffusional sizing measurements and as detailed in the "Methods" section.

Single round disaggregation experiments. To further substantiate the above findings, the outcome of a single round of chaperone-mediated disaggregation was measured and the products characterised. For this purpose, αS fibrils were incubated with DnaJB1, Hsc70, and the ATP regeneration system for 5 min to ensure chaperone binding to the fibrils. A single round of the disaggregation reaction was then triggered by the addition of Apg2 and a 200-fold molar excess of the Hsc70-binding peptide GSGNRLLLTG[29–31] was added to the primed Hsc70–fibril

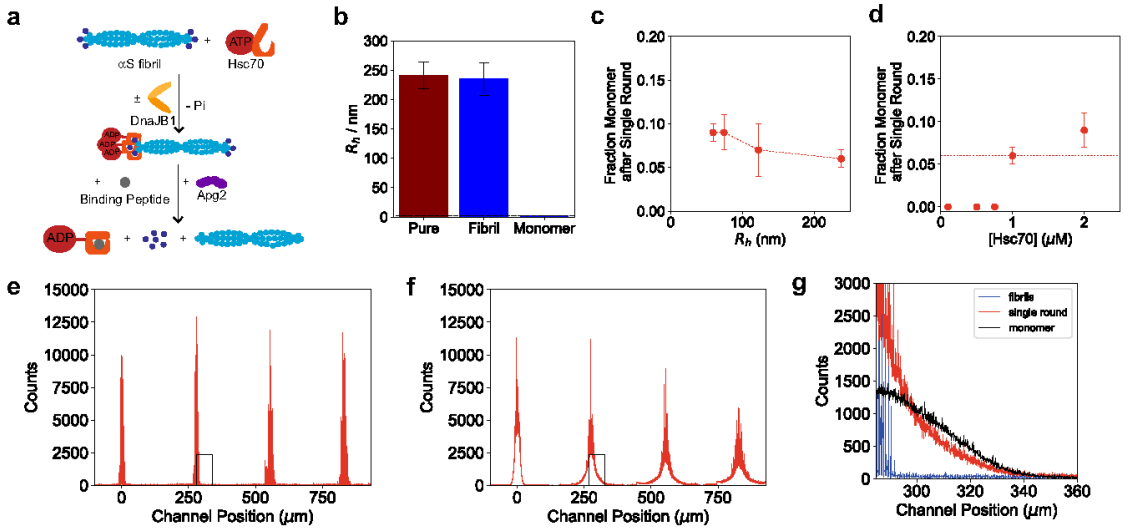

Fig. 4 Single round disaggregation experiments. a To measure the outcome of a single disaggregation round, αS fibrils (2 μM monomer equivalent) were incubated with Hsc70 and DnaJB1. Subsequently, a 200-fold molar excess of Hsc70-binding peptide GSGNRLLLTG was added, to block Hsc70 re-binding to fibrils. **b** Outcome of a single disaggregation round, as measured by epifluorescence detection. Two species were detectable, the larger of which had a similar size to the initial fibril, the second of which had the size of monomer. Red represents pure fibrils, blue the outcome after a single disaggregation round. **c** Fraction of monomer generated as a function of fibril length at constant αS concentration, corresponding to an increased number of fibril ends. Shorter fibrils lead to more monomer release per single disaggregation round than longer fibrils, whereby this effect plateaus for fibrils longer than 100 nm. **d** Fraction of monomer measured at different Hsc70 concentrations. No disaggregation took place for Hsc70 concentrations below 1 μM, suggesting that there is a critical Hsc70 concentration required for efficient disaggregation. Data in **b**–**d** are represented as mean ± standard deviation of $n = 3$ independent experiments. **e** Diffusion profile for confocal scanning across the microfluidic channel for pure αS fibrils. The profile does hardly broaden, as expected for a large amyloid fibril. **f** Diffusion profile for confocal scanning across the microfluidic channel after a single disaggregation round. This leads to significant broadening, whilst the burst height remains similar, indicating that fibrils of similar length and a small species are generated. **g** Comparison of the signal of pure fibrils (blue), single round disaggregation (red) and pure monomer (black). The red signal after a single disaggregation round is the overlay between the two sets.

complex (Fig. 4a). Due to the presence of Hsc70-binding peptide, Hsc70 is unable to re-bind to αS fibrils. Note that no disaggregation occurs until Apg2 is added, which results in the release of Hsc70 from fibrils[19] (see Fig. 4a). This assay thus allowed us to monitor the outcome of only a single round of disaggregation per Hsc70 molecule bound to the fibrils. As shown in Fig. 4b, two αS species were observed: a smaller species with a radius of $R_h = 2.05 \pm 0.44$ nm, corresponding to monomer, and a larger species with a radius of $R_h = 71.2 \pm 3.7$ nm, corresponding to the fibril size (cf. $R_h = 74.4 \pm 1.0$ nm) prior to disaggregation. Due to the conserved fibril length, these data further support the notion that monomer is taken off the fibril ends. In the case of a fragmentation mechanism, in contrast, fibrillar species of smaller length would be observed. As expected, the addition of the Hsc70-binding peptide to an ongoing disaggregation stopped the disaggregation reaction immediately (Supplementary Fig. 11a), and no disaggregation was observed upon addition of peptide before adding Hsc70 to fibrils (Supplementary Fig. 11b). The same behaviour was found when the reaction was carried out with equimolar concentrations of ATP relative to Hsc70 and an excess of the slowly hydrolysable ATP analogue ATP-γ-S (Supplementary Fig. 11c).

Interestingly, the fraction of monomers generated during a single round of disaggregation increased with shorter fibril lengths under constant Hsc70 concentrations (Fig. 4c). As the total αS and Hsc70 concentrations were both 2 μM, there is an excess of chaperone relative to the number of fibrils ends (Supplementary Fig. 11). We investigated, therefore, the extent to which the number of fibril ends governs the rate of disaggregation. In this experiment, the fibril length was decreased by a factor of two to three by sonication, but the total mass concentration of αS was kept constant, resulting in an increased concentration of fibril ends for removal of monomer units. Noteworthily, the fibril population is very heterogeneous (see above, Supplementary Fig. 1c) and we report here on the mean size. The fraction of αS released in a single disaggregation round decreased with the concentration of fibril ends, this effect levelled off for fibril lengths above 100 nm (Fig. 4c), indicative of a critical ratio between Hsc70 concentration and the number of fibril ends for effective disaggregation. To validate this hypothesis, single round experiments were performed with fibrils of identical length distributions but with varying concentrations of the Hsc70 chaperone (Fig. 4d). This experiment revealed that, at an Hsc70 concentration below 1 μM, no disaggregation is observable. This result is interesting, as it suggests a cooperative action or clustering of multiple Hsc70 molecules at individual fibril ends, consistent with a recent report[19]. In contrast, there was no significant difference in the monomer fraction released from fibrils at higher Hsc70 concentrations, suggesting that the number of Hsc70 molecules that can bind to fibril ends is limited (Fig. 4d).

Next, we monitored the outcome of a single round of disaggregation using confocal-based diffusional sizing[48,49]. We first performed experiments on pure fibrils (i.e., in the absence of the disaggregation machinery) (Fig. 4e). As described above, diffusion profiles showed large bursts located at the centre of the channel and profile shapes that do hardly broaden along the channel, as expected for large amyloid fibrils containing numerous labelled monomer units. Fitting of the profile from

the confocal measurements yielded a hydrodynamic radius of $R_h = 156.82 \pm 3.57$ nm consistent with the diffusional sizing experiments in epifluorescence mode and the expected size of fibrils. Strikingly, after a single round of disaggregation, a diffused-out monomeric population with a hydrodynamic radius $R_h = 2.96 \pm 0.01$ nm appeared in addition to the fibril bursts located at the centre of the channel; the hydrodynamic radius of $R_h = 155.28 \pm 1.5$ nm of the fibril bursts was conserved compared to the fibril-only experiment. Comparing the diffusion profile of the monomer population obtained in the single round disaggregation experiment with a concentration series performed on labelled αS monomer (Supplementary Fig. 12) revealed that ~100 nM of monomeric protein is present after the single disaggregation round. This suggests that ~5% of the αS population is monomeric after a single round of disaggregation. Importantly, no intermediate species between monomer and fibrils were observed. Together, these findings support the conclusion that the monomer is taken directly off the fibril ends. Assuming an average length fibril consists of 500 monomer units, ~12 monomers would be released per fibril end per disaggregation round.

Interactions between chaperones and their binding to fibrils. We next focused on the interactions between chaperones as well as between chaperones and fibrils in order to gain further mechanistic insights into the disaggregation reaction. Upon binding of a labelled chaperone to an unlabelled chaperone or fibril, a decrease in its molecular diffusivity concomitant with an increase in its effective molecular weight and size upon binding is expected, thereby allowing us to determine the binding affinity of the respective interactions[16].

First, we performed experiments involving Hsc70 in the presence of ATP, ADP, and the non-hydrolysable ATP analogue ATP-γ-S. Note that Hsc70 labelled with Alexa Fluor 647 shows normal disaggregation activity (Supplementary Fig. 2). As shown in Fig. 5a, Hsc70 did undergo a conformational change upon binding of ATP or ATP-γ-S, as reflected in a decrease in its hydrodynamic radius. Conversely, Hsc70 in the ADP bound state has a conformation similar to apo-Hsc70. These observations are consistent with structural analyses of Hsp70 showing that in the ATP state the hydrophobic interdomain linker and the α-helical lid of the SBD are associated with the NBD, and the SBD is in an open conformation, whereas the SBD and NBD are loosely associated in the ADP state[51–55].

Next, we performed sizing experiments of Hsc70 in the presence of DnaJB1 or Apg2 (Fig. 5b). Hsc70 bound to DnaJB1 in the absence of ATP ($K_d = 46.0 \pm 13.5$ nM) (Supplementary Fig. 13a), but not in the presence of ATP or ADP; however, binding was detectable in presence of ATP-γ-S. DnaJB1 is known to strongly accelerate the hydrolysis of ATP by Hsc70 and is likely to dissociate from ADP-bound Hsc70[12]. This is consistent with the results obtained here. Evidently, the ATP-state of Hsc70 is short-lived in the presence of DnaJB1, precluding detection of binding in the fluidics system. However, a significant size increase of Hsc70 due to DnaJB1 binding was observed in the presence of the non-hydrolysable ATP analogue ATP-γ-S, which prolongs the ATP-state of Hsc70. Similarly, Hsc70 showed only weak binding to Apg2, consistent with a transient interaction during nucleotide exchange. The size of Apg2 was large ($R_h = 4.46 \pm 0.20$ nm) (Supplementary Fig. 13b), which may contribute to its effectiveness in the disaggregation reaction in an entropic pulling mechanism[37–39].

We next investigated the binding between Hsc70 and fibrils. As shown in Fig. 5c in presence of hydrolysable ATP, a binding affinity of $K_d = 139.0 \pm 27.6$ nM is observed, which is increased to $K_d = 47.5 \pm 16.0$ nM in the presence of DnaJB1, consistent with DnaJB1 accelerating the hydrolysis of ATP to ADP. Furthermore, stoichiometry analysis of Hsc70 binding to fibrils yielded one Hsc70 molecule per 5.3 ± 0.6 αS monomer units. Notably, as this stoichiometric ratio represents an average value, it is also consistent with the clustering of Hsc70 at fewer binding sites on the fibrils. Indeed, given that we observed no disaggregation at decreased Hsc70 concentrations (see above), our results support the view that clustering of Hsc70 at fibril ends is a critical feature of the disaggregation mechanism. This proposed mechanism is consistent with findings by Wentink et al.[19], who showed that Hsc70 clustered on αS fibrils when recruited by DnaJB1. Such clustering may also prevent the re-attachment of monomeric units to fibrils, as discussed above (Fig. 2g).

While no binding of Apg2 alone to the fibrils was detectable, DnaJB1 bound the fibrils with an affinity of $K_d = 246.1 \pm 28.1$ nM (Fig. 5d), consistent with the role of DnaJB1 in recruiting Hsc70.

Discussion

Hsc70 cooperates with its co-chaperones DnaJB1 and Apg2 (Hsp110) in disaggregating αS fibrils[18]. By bringing together microfluidic measurements with chemical kinetics and thermodynamic analysis, we have investigated this process here in a quantitative manner. We have found that, during the disaggregation reaction, only two species are significantly populated, namely larger, fibrillar species and αS monomer units released from the fibrils. The time-dependent size decrease of the larger species is consistent with pseudo-first-order kinetics, under conditions where Hsc70 is in excess and the concentration of fibrils is limiting. Thus, αS monomers are taken off the fibrils directly. Indeed, the pure monomer is abundant almost immediately after the addition of the chaperones, and the monomer fraction increases linearly. An advantage of microfluidic diffusional sizing is that the end product of the disaggregation reaction, monomeric αS, can be detected, which is not ThT active and thus not observable in traditional disaggregation assays. Interestingly, our results indicate that each disaggregation event is independent of the initial fibril lengths, while the rate is slightly accelerated for shorter fibrils as shown with a change in the rate constant with respect to the total concentration of synuclein. As a single round of chaperone action produces only monomer and fibrils, this further suggests that the monomer is taken off the fibril ends. Dissociation of monomers from within the fibrils would have resulted in a substantial decrease in fibril length due to induced fragmentation. Future directions will include investigating the effect of different fibril polymorphs and αS variants on the disaggregation kinetics.

Our analysis of the disaggregation kinetics and the interactions between the chaperone components and their interactions with αS fibrils, together with the previous reports[7,19], leads to a picture of chaperone function as shown in Fig. 6 and suggests that the disaggregation reaction can be divided into the following six steps: DnaJB1 binds first to the fibrils (step 1) and recruits Hsc70 in the ATP state. ATP hydrolysis on Hsc70, accelerated by DnaJB1, results in tight binding of Hsc70 to fibrils (step 2), subsequent hydrolysis of ATP to ADP (step 3), and clustering of Hsc70 on the fibril ends (step 4, see below). Disaggregation resulting in αS monomer production then occurs upon addition of Apg2 (step 5/6). As Apg2 alone does not detectably interact with the fibrils, it may act solely as a NEF, although interaction with the fibril substrate in the presence of Hsc70 cannot be ruled out. The large size of Apg2 may facilitate disaggregation according to the model of entropic pulling[37–39], consistent with recent findings that the larger size of Apg2 relative to other NEFs of Hsc70 plays a role[19]. Our data suggest further that disaggregation requires clustering of Hsc70 molecules, with repulsive forces between αS-bound Hsc70 molecules inducing monomer

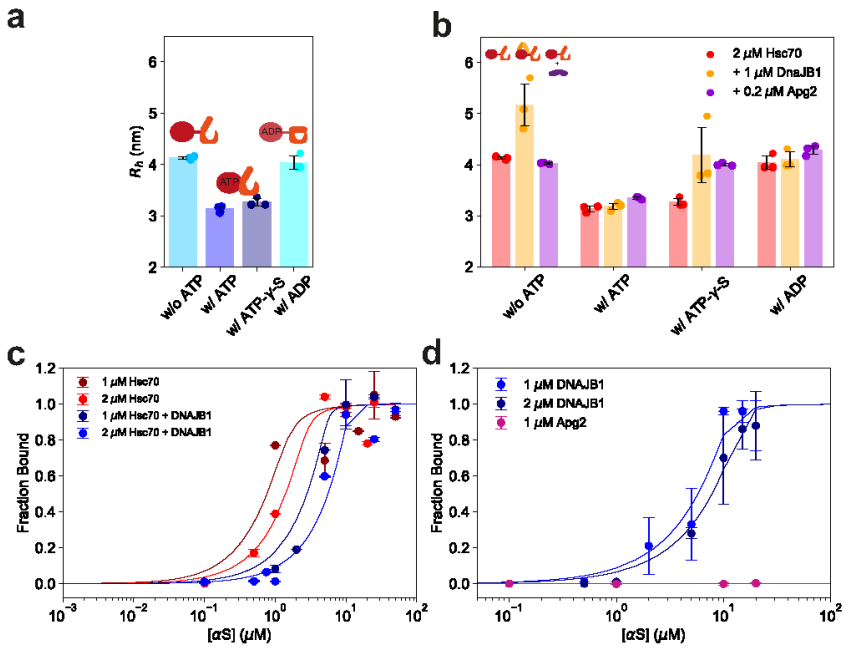

Fig. 5 Characterisation of the binding interaction between chaperones and αS fibrils. a Conformational compaction of fluorescently labelled Hsc70 upon binding of ATP and ATPγS, as shown by the change in hydrodynamic radius. Binding to ADP preserves the more expanded state. **b** Binding interaction between fluorescently labelled Hsc70 and its co-chaperones. Binding was observed between Hsc70 and DnaJB1, leading to an increase in hydrodynamic radius. DnaJB1 can bind in absence of ATP and in presence of ATP-γ-S but dissociates from Hsc70 in the presence of ATP due to the fast hydrolysis of ATP. **c** Binding of Hsc70 to αS fibrils. Hsc70 shows a binding affinity of $K_d = 139.0 \pm 27.6$ nM in the presence of ATP ($R^2 = 0.98$) and a tighter affinity $K_d = 47.5 \pm 16.0$ nM in the presence of DnaJB1 ($R^2 = 0.96$), which triggers hydrolysis of ATP to ADP, thereby leading to lid closure and stronger binding. **d** Binding of DnaJB1 and Apg2 to αS fibrils. Apg2 did not bind to αS fibrils. DnaJB1 bound to αS fibrils with an affinity of $K_d = 246.1 \pm 28.1$ nM ($R^2 = 0.98$). The concentrations of αS are given with respect to monomer equivalents. Data in **b**–**d** are represented as mean ± standard deviation of $n = 3$ independent experiments.

dissociation from fibril ends (step 5). This could be mechanistically similar to the observed conformational expansion of non-native proteins by the binding of multiple Hsp70 to sites within the same polypeptide chain[31,56]. Alternatively, since αS monomer dissociation from the fibril critically depends on Apg2, we speculate that binding of Apg2 to clustered Hsc70 molecules induces the steric repulsion that drives disaggregation (Fig. 6). Moreover, clustering likely functions to prevent re-attachment of monomeric units to fibrils. However, given the stoichiometry of approximately one Hsc70 bound per 6 αS monomers, it is likely that Hsc70 binds along the fibril surface as well, and that only binding to the fibril ends is productive. Binding along the fibril surface may be involved in reducing secondary nucleation of aggregation by αS monomers[1,57]. This unproductive binding and the necessity for having clustered chaperones explains why, despite nanomolar affinity, no disaggregation occurs below a Hsc70 concentration of 1 μM, as shown in Fig. 4d. Further directions to extend on our studies should include investigation of these phenomena with various other substrates, including the amyloid-β peptide or Tau protein, key players in the onset and progression of Alzheimer's disease.

In conclusion, we present here a comprehensive kinetic and thermodynamic description of a complex protein quality control mechanism allowing the clearance of amyloidogenic deposits of the protein αS. We found that, in the disaggregation reaction of αS fibrils, the monomer is taken directly from the fibril ends, apparently mediated by the Hsc70 chaperone system assembling in clusters at the fibril ends. This process follows single exponential kinetics and is highly effective, such that it leads to complete disaggregation of amyloid fibrils, thereby likely contributing to the prevention of Parkinson's disease.

Methods

Materials. All chemicals were purchased in the highest purity available. Hydroxyethyl piperazineethanesulfonic acid (HEPES), potassium hydroxide (KOH), potassium chloride (KCl), dithiothreitol (DTT), and Tween20 were purchased from Sigma Aldrich (St. Louis, MO, USA) and were of analytical grade. Pyruvate kinase (10109045001) from rabbit muscle was purchased from Roche (Basel, Switzerland). Poly-(dimethylsiloxane) (PDMS) and curing agent were purchased from Momentive (Techsil, Bidford-on-Avon, UK) and carbon nanoparticles (Plasmachem, Berlin, Germany) were added as previously described[41]. For all microfluidic experiments, the buffer used contained 50 mM HEPES–KOH (pH 7.5), 50 mM KCl, 5 mM $MgCl_2$, 2 mM DTT; co-flow buffer was additionally supplied with 0.01% Tween20.

Expression and purification of molecular chaperones and αS monomer. Recombinant human wildtype αS was purified as described previously[58]. In brief, *Escherichia coli* BL21(DE3) cells were transformed with pT7-7 αS and cultured in a lysogenic broth (LB) medium. Protein expression was induced by 1 mM isopropyl β-D-1-thiogalactopyranoside (IPTG) for 4 h at 37 °C. Bacteria were harvested, and pellets were lysed in 10 mM Tris–HCl (pH 8.0), 1 mM EDTA, 1 mM phenylmethylsulfonyl fluoride (PMSF). The lysate was sonicated for 5 min and boiled subsequently for 15 min, followed by centrifugation. The supernatant was subjected to streptomycin sulfate and ammonium sulfate precipitation steps as described. The ammonium sulfate pellet formed after centrifugation at 5200×*g* for 30 min was dissolved in 50 mM Tris–HCl (pH 7.5), 150 mM KCl and subjected to size exclusion chromatography (SEC) on a Superdex 200 column (GE Healthcare, Chalfont St Giles, UK). αS fibrils were generated by shaking a mixture containing 10% labelled and 90% unlabelled monomer at 37 °C and 200 rpm for 4 days. Fibrils were sonicated (cycle 0.3, power 10%, 90 s) using a Sonopuls ultrasonic homogeniser (Bandelin, Nänikon, Switzerland).

Human Hsc70, DnaJB1, and Apg2 were expressed in *E. coli* BL21(DE3) as fusion proteins with protease-cleavable His_6- or His_6-Smt3 tags and purified by

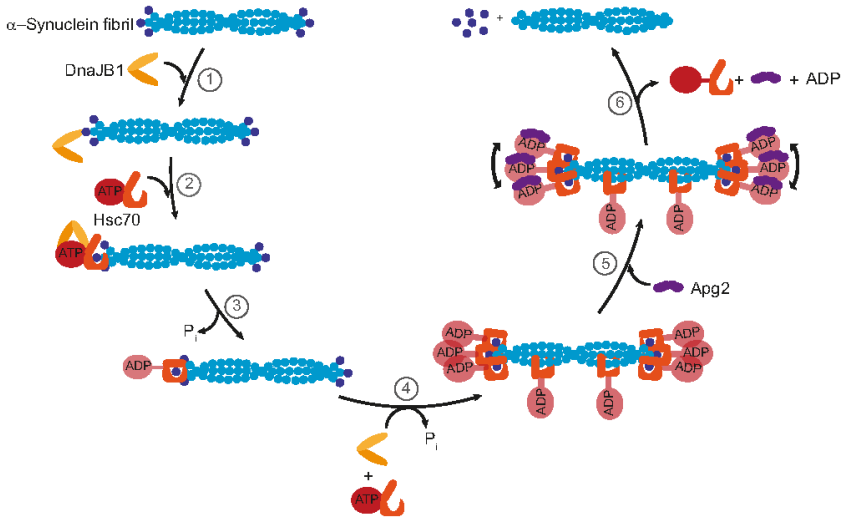

Fig. 6 Emerging principles of Hsc70 disaggregase activity. Model for Hsc70-mediated protein disaggregation of αS fibrils. This disaggregation mechanism comprises six steps: step 1, DnaJB1 binding to αS fibrils; step 2, Hsc70 loading onto fibrils mediated by DnaJB1; step 3, hydrolysis of Hsc70-bound ATP to ADP and dissociation of DNAJB1; step 4: further Hsc70 loading resulting in clustering of Hsc70 at fibril ends; step 5, Apg2 binding to Hsc70; step 6, dissociation of αS monomer coupled to ADP dissociation from Hsc70 and disassembly of the chaperone machinery.

tandem Ni-affinity chromatography with intermittent protease cleavage similar as described previously[59].

Hsc70 was expressed from the plasmid pProEx-HtA Hsc70. Cells were grown in LB medium at 37 °C to an OD_{600} ~0.5 and induced with 0.5 mM IPTG for 18 h at 21 °C. Cells were lysed by ultrasonication in 50 mM HEPES–KOH (pH 8.0), 10 mM KCl, 5 mM $MgCl_2$ (buffer A) containing 0.8 mg/mL lysozyme at 4 °C. The supernatant after centrifugation at 125,000×*g* for 45 min was applied to a Ni-NTA column (GE Healthcare, Chalfont St Giles, UK) equilibrated in buffer A. The column was washed with a step gradient of buffer A containing increasing amounts of imidazole (20/250/1000 mM). The bound protein was eluted with buffer A containing 250 mM imidazole. This was followed by cleavage of the His_6-moiety at 4 °C with His_6-tobacco etch virus (TEV) protease for 45 h. After transfer into buffer A using a desalting column, the material was passed over the Ni-NTA column and the flow-through was collected. Next, Hsc70 was purified by anion exchange chromatography on MonoQ (GE Healthcare, UK) in the same buffer system using a linear salt gradient (0–700 mM KCl) in 50 mM HEPES–KOH (pH 8.0), 5 mM $MgCl_2$. Pinally, the Hsc70-containing fractions were subjected to SEC on Superdex 200 column (GE Healthcare, Chalfont St Giles, UK) in 50 mM HEPES–KOH (pH 8.0), 150 mM KCl, 5 mM $MgCl_2$ and 5% glycerol.

DnaJB1 and Apg2 were expressed from the plasmids pCA528-DnaJB1 and pCA528-HspA4, respectively[17]. Cells were grown in LB medium at 37 °C to an OD_{600} ~0.5 and induced with 0.5 mM IPTG for 5.5 h at 30 °C. Cells were lysed with an Emulsiflex (Avestin, Ottawa, Canada) cell disruptor in 50 mM HEPES–KOH (pH 7.4), 10 mM KCl, 5 mM $MgCl_2$ (buffer B) containing 2 mM PMSF and Complete protease inhibitor cocktail (Roche). After centrifugation, the supernatant was applied to a Ni-NTA column equilibrated in buffer B. After washing with buffer B, the bound protein was eluted with buffer B containing 250 mM imidazole. The His_6-Smt3 moiety was cleaved with PEN2 protease (MPIB Core facility) at 4 °C in the presence of 1 mM dithiothreitol (DTT). After buffer exchange, the mixture was passed over the Ni-NTA column and the flow-through was collected. SEC on Sephacryl S-200 (GE Healthcare, UK) in 50 mM Tris–HCl (pH 8.0), 5 mM $MgCl_2$ and 150 mM KCl (buffer C) was the final purification step for Apg2. DnaJB1 was further purified by SEC on Sephacryl S-100 in buffer C containing 5% glycerol, and by cation exchange chromatography on Source 30S (GE Healthcare), wherein the elution was carried out with a linear salt gradient (0–400 mM NaCl) in 50 mM Tris–HCl (pH 7.5).

Hsc70, DnaJB1, and Apg2 were buffer exchanged to 0.1 M $NaHCO_3$ and incubated with 3 molar equivalents of Alexa Fluor 647 overnight at 4 °C. Free dye was removed by size exclusion chromatography on a Superdex 200 increase column with 50 mM HEPES–KOH, pH 7.5, as elution buffer, yielding labelled chaperones with 1.7 labels per molecule.

Microfluidic diffusional sizing. A scheme of the chip design is shown in Fig. 1. Fabrication and operation of the microfluidic devices for microfluidic diffusional sizing have been described previously[40,60]. Briefly, the microfluidic devices were fabricated in PDMS by standard soft-lithography techniques and bonded onto a glass coverslip after activation with oxygen plasma. Sample loading from reservoirs connected to the respective inlets and control of flow rate was achieved by applying negative pressure at the outlet using a glass syringe (Hamilton, Bonaduz, Switzerland) and a syringe pump (neMESYS, Cetoni GmbH, Korbussen, Germany). A custom-built inverted epifluorescence microscope equipped with a charge-coupled-device camera (Prime 95B, Photometrics, Tucson, AZ, USA) and brightfield LED light sources (Thorlabs, Newton, NJ, USA) was used to record the images, using the Cy5-4040C-000 Filter set from Semrock (Laser 2000, Huntingdon, UK) for detection of Alexa647-labelld chaperones and a fluorescent filter set with an excitation filter at 475 ± 35 nm, emission filter at 525 ± 30 nm and dichroic mirror for 506 nm (Laser 2000, Huntingdon, UK) for detection of Alexa-488 labelled αS. Images were taken using Micro Manager (Version 1.4.23 20170327), typically at flow rates 20, 60, and 100 μL/h, and lateral diffusion profiles were recorded at four different positions along the microfluidic channels.

Diffusional sizing experiments involving confocal microscopy were done on a custom-built laser confocal microscopy setup. Briefly, the microscope is equipped with a 488-nm laser line (Cobolt 06-MLD, Hübner Photonics, Derby, UK) and a single-photon counting avalanche photodiode (SPCM-14, PerkinElmer, Seer Green, UK) for subsequent detection of emitted fluorescence photons. Further details of the optical unit have been described previously[48,49]. Diffusion profile recording was done by continuously moving the confocal observation volume through the centre four channels of the microfluidic device. Profiles were typically taken at a flow rate of 100 μL/h, and lateral diffusion profiles were recorded at four different positions along the microfluidic channels.

Diffusion profiles extracted from fluorescence images and confocal recordings were fitted using a custom-written analysis software by numerical model simulations solving the diffusion–advection equations for mass transport under flow[42]. For evaluation of the disaggregation time courses, we assumed two species representing the fibrils and the dissociated monomers. For the thermodynamic evaluation and sizing of pure species, we fitted the diffusion profiles with one species only to determine the average size of the bound and unbound chaperone.

Kinetic measurements. The reaction mixture for disaggregation measurements contained 2 μM αS fibrils, 2 μM Hsc70, 1 μM DnaJB1, 0.2 μM Apg2, 5 mM 2-phosphoenolpyruvate, 0.05 mg/mL pyruvate kinase, and 5 mM ATP in 50 mM HEPES–KOH (pH 7.5), 50 mM KCl, 5 mM $MgCl_2$, 2 mM DTT. This mixture was incubated at 300 rpm and 30 °C. At different time points, 8 μL aliquots were taken out, injected into the microfluidic chip and images were acquired as described above. The rate of monomer release is proportional to the number of ends in the system. As shorter fibrils are consumed, the number of ends decreases. We thus approximate the time evolution of the mass concentration, *M*, of fibrils as:

$$\frac{dM}{dt} = -k \cdot M(t) \tag{1a}$$

$$M(t) = M(t_0)e^{-kt} \tag{1b}$$

Therefore, the hydrodynamic radius of the fibril population at time t is described by:

$$R_h(t) = R_h(t_0)e^{-kt} \quad (2)$$

Likewise, the concentration of monomer, m, increases as

$$\frac{dM}{dt} = -\frac{dm}{dt} \quad (3)$$

or, in its integrated and normalised form, the fraction of monomer, f_m, becomes

$$f_m(t) = (1 - e^{-kt}) \quad (4)$$

Single round disaggregation experiments. The reaction mixture for disaggregation measurements contained 2 μM αS fibrils, 2 μM Hsc70, 1 μM DnaJB1, 5 mM 2-phosphoenolpyruvate, 0.05 mg/mL pyruvate kinase, and 5 mM ATP in 50 mM HEPES–KOH (pH 7.5), 50 mM KCl, 5 mM $MgCl_2$, 2 mM DTT. This mixture was incubated at 300 rpm and 30 °C for 5 min. Subsequently, 0.2 μM Apg2 and 400 μM Hsc70-binding peptide GSGNRLLLTG[29–31] were added. This peptide can bind to Hsc70, thereby preventing substrate rebinding and, thus, terminating the disaggregation.

Thermodynamic characterisation. For binding experiments, samples were prepared in typically 30 μL total volume, using the same working concentrations of the interacting partners considered as in the disaggregation time course described above under the same buffer conditions. The protocol for the equilibrium binding curves was adapted from the previous reports[16]. The concentration of one of the interacting molecules was varied between 0.1 and 10 μM accordingly, while the labelled component was held at a constant concentration equal to the working concentration discussed previously. The samples were typically incubated for 30 min and then measured in triplicates in three independent channels at three flow rates.

Atomic force microscopy. AFM was performed on positively functionalized mica substrates.10 μL of 0.5% (v/v) 3-aminopropyl-triethoxysilane (APTES, Sigma) in Milli-Q water was deposited onto freshly cleaved mica and incubated for 1 min. The substrate was rinsed three times with 1 mL of Milli-Q water and dried by a gentle stream of nitrogen gas. Finally, for each sample, an aliquot of 10 μL of the solution was deposited on the positively functionalized surface. The droplet was incubated for 5 min, then rinsed with 1 mL of Milli-Q water and dried under nitrogen gas. The preparation was carried out at room temperature. AFM maps were acquired using an NX10 AFM (Park Systems) operating in non-contact mode and equipped with a silicon tip (PPP-NCHR, 42 N/m) with a nominal radius <10 nm. Image flattening was performed by SPIP (Image Metrology) software.

Reporting summary. Further information on experimental design is available in the Nature Research Reporting Summary linked to this paper.

Data availability

The raw data and analysis code underlying this study will be made available upon reasonable request. Source data are provided with this paper. All data generated in this study and included in this manuscript have been deposited in the Figshare database under https://doi.org/10.6084/m9.figshare.15173088. Source data are provided with this paper.

Code availability

Code available under https://zenodo.org/record/3881940#.YRGzCSV4UlQ.

Received: 1 November 2020; Accepted: 25 August 2021;
Published online: 14 October 2021

References

1. Knowles, T. P. J., Vendruscolo, M. & Dobson, C. M. The amyloid state and its association with protein misfolding diseases. *Nat. Rev. Mol. Cell Biol.* **15**, 384–396 (2014).
2. Cohen, S. I. A., Vendruscolo, M., Dobson, C. M. & Knowles, T. P. J. From macroscopic measurements to microscopic mechanisms of protein aggregation. *J. Mol. Biol.* **421**, 160–171 (2012).
3. Hartl, F. U. Protein misfolding diseases. *Annu. Rev. Biochem.* **86**, 21–26 (2017).
4. Chiti, F. & Dobson, C. M. Protein misfolding, functional amyloid, and human disease. *Annu. Rev. Biochem.* **75**, 333–366 (2006).
5. Morimoto, R. I. Regulation of the heat shock transcriptional response: cross talk between a family of heat shock factors, molecular chaperones, and negative regulators. *Genes Dev.* **12**, 3788–3796 (1998).
6. Dobson, C. M. Protein folding and misfolding. *Nature* **426**, 884–890 (2003).
7. Hartl, F. U., Bracher, A. & Hayer-Hartl, M. Molecular chaperones in protein folding and proteostasis. *Nature* **475**, 324–332 (2011).
8. Hartl, F. U. Molecular chaperones in cellular protein folding. *Nature* **381**, 571–580 (1996).
9. Pelham, H. R. B. Speculations on the functions of the major heat shock and glucose-regulated proteins. *Cell* **46**, 959–961 (1986).
10. Finley, D., Ciechanover, A. & Varshavsky, A. Thermolability of ubiquitin-activating enzyme from the mammalian cell cycle mutant ts85. *Cell* **37**, 43–55 (1984).
11. Balchin, D., Hayer-Hartl, M. & Hartl, F. U. In vivo aspects of protein folding and quality control. *Science.* **353**, aac4354 (2016).
12. Mayer, M. P. & Gierasch, L. M. Recent advances in the structural and mechanistic aspects of Hsp70 molecular chaperones. *J. Biol. Chem.* **294**, 2085–2097 (2019).
13. Knowles, T. P. J. et al. An analytical solution to the kinetics of breakable filament assembly. *Science.* **326**, 1533–1537 (2009).
14. Wright, M. A. et al. Cooperative assembly of Hsp70 subdomain clusters. *Biochemistry* **57**, 3641–3649 (2018).
15. Arosio, P. et al. Kinetic analysis reveals the diversity of microscopic mechanisms through which molecular chaperones suppress amyloid formation. *Nat. Commun.* **7**, 10948 (2016).
16. Scheidt, T. et al. Secondary nucleation and elongation occur at different sites on Alzheimer's amyloid-β aggregates. *Sci. Adv.* **5**, eaau3112 (2019).
17. Rampelt, H. et al. Metazoan Hsp70 machines use Hsp110 to power protein disaggregation. *EMBO J.* **31**, 4221–4235 (2012).
18. Gao, X. et al. Human Hsp70 disaggregase reverses Parkinson's-linked α-synuclein amyloid fibrils. *Mol. Cell* **59**, 781–793 (2015).
19. Wentink, A. S. et al. Molecular dissection of amyloid disaggregation by human HSP70. *Nature* **587**, 483–488 (2020).
20. Nachman, E. et al. Disassembly of Tau fibrils by the human Hsp70 disaggregation machinery generates small seeding-competent species. *J. Biol. Chem.* **295**, 9676–9690 (2020).
21. De Mattos, E. P. et al. Protein quality control pathways at the crossroad of synucleinopathies. *J. Parkinsons. Dis.* **10**, 369–382 (2020).
22. Duennwald, M. L., Echeverria, A. & Shorter, J. Small heat shock proteins potentiate amyloid dissolution by protein disaggregases from yeast and humans. *PLoS Biol.* **10**, e1001346 (2012).
23. Nillegoda, N. B. & Bukau, B. Metazoan Hsp70-based protein disaggregases: emergence and mechanisms. *Front. Mol. Biosci.* **2**, 57 (2015).
24. Nillegoda, N. B. et al. Crucial HSP70 co-chaperone complex unlocks metazoan protein disaggregation. *Nature* **524**, 247–251 (2015).
25. Scior, A. et al. Complete suppression of Htt fibrilization and disaggregation of Htt fibrils by a trimeric chaperone complex. *EMBO J.* **37**, 282–299 (2018).
26. Shorter, J. The mammalian disaggregase machinery: Hsp110 synergizes with Hsp70 and Hsp40 to catalyze protein disaggregation and reactivation in a cell-free system. *PLoS ONE* **6**, e26319 (2011).
27. Tittelmeier, J. et al. The HSP110/HSP70 disaggregation system generates spreading-competent toxic α-synuclein species. *EMBO J.* **39**, e103954 (2020).
28. Kityk, R., Kopp, J. & Mayer, M. P. Molecular mechanism of J-domain-triggered ATP hydrolysis by Hsp70 chaperones. *Mol. Cell* **69**, 227–237e4 (2018).
29. Zhu, X. et al. Structural analysis of substrate binding by the molecular chaperone DnaK. *Science.* **272**, 1606–1614 (1996).
30. Mayer, M. P., Rüdiger, S. & Bukau, B. Molecular basis for interactions of the DnaK chaperone with substrates. *Biol. Chem.* **381**, 877–885 (2005).
31. Imamoglu, R., Balchin, D., Hayer-Hartl, M. & Hartl, F. U. Bacterial Hsp70 resolves misfolded states and accelerates productive folding of a multi-domain protein. *Nat. Commun.* **11**, 365 (2020).
32. Dragovic, Z., Broadley, S. A., Shomura, Y., Bracher, A. & Hartl, F. U. Molecular chaperones of the Hsp110 family act as nucleotide exchange factors of Hsp70s. *EMBO J.* **25**, 2519–2528 (2006).
33. Raviol, H., Sadlish, H., Rodriguez, F., Mayer, M. P. & Bukau, B. Chaperone network in the yeast cytosol: Hsp110 is revealed as an Hsp70 nucleotide exchange factor. *EMBO J.* **25**, 2510–2518 (2006).
34. Bracher, A. & Verghese, J. The nucleotide exchange factors of Hsp70 molecular chaperones. *Front. Mol. Biosci.* **2**, 10 (2015).
35. Polier, S., Dragovic, Z., Hartl, F. U. & Bracher, A. Structural basis for the cooperation of Hsp70 and Hsp110 chaperones in protein folding. *Cell* **133**, 1068–1079 (2008).
36. Steel, G. J., Fullerton, D. M., Tyson, J. R. & Stirling, C. J. Coordinated activation of Hsp70 chaperones. *Science.* **303**, 98–101 (2004).
37. De Los Rios, P. & Barducci, A. Hsp70 chaperones are non-equilibrium machines that achieve ultra-affinity by energy consumption. *Elife* **3**, e02218 (2014).
38. De Los Rios, P., Ben-Zvi, A., Slutsky, O., Azem, A. & Goloubinoff, P. Hsp70 chaperones accelerate protein translocation and the unfolding of stable protein aggregates by entropic pulling. *Proc. Natl. Acad. Sci. USA* **103**, 6166–6171 (2006).
39. Sousa, R. et al. Clathrin-coat disassembly illuminates the mechanisms of Hsp70 force generation. *Nat. Struct. Mol. Biol.* **23**, 821–829 (2016).

40. Arosio, P. et al. Microfluidic diffusion analysis of the sizes and interactions of proteins under native solution conditions. *ACS Nano* **10**, 333–341 (2016).
41. Herling, T. W. et al. A microfluidic platform for real-time detection and quantification of protein–ligand interactions. *Biophys. J.* **110**, 1957–1966 (2016).
42. Müller, T. et al. Particle-based Monte-Carlo simulations of steady-state mass transport at intermediate Péclet numbers. *Int. J. Nonlinear Sci. Numer. Simul.* **17**, 175–183 (2015).
43. Bolisetty, S., Adamcik, J. & Mezzenga, R. Snapshots of fibrillation and aggregation kinetics in multistranded amyloid β-lactoglobulin fibrils. *Soft Matter* **7**, 493–499 (2011).
44. Streets, A. M., Sourigues, Y., Kopito, R. R., Melki, R. & Quake, S. R. Simultaneous measurement of amyloid fibril formation by dynamic light scattering and fluorescence reveals complex aggregation kinetics. *PLoS ONE* **8**, e54541 (2013).
45. Gladytz, A. et al. Intermediates caught in the act: tracing insulin amyloid fibril formation in time by combined optical spectroscopy, light scattering, mass spectrometry and microscopy. *Phys. Chem. Chem. Phys.* **17**, 918–927 (2015).
46. Ruesink, H. et al. Stabilization of α-synuclein oligomers using formaldehyde. *PLoS ONE* **14**, e0216764 (2019).
47. Arter, W. E., Levin, A., Krainer, G. & Knowles, T. P. J. Microfluidic approaches for the analysis of protein–protein interactions in solution. *Biophys. Rev.* **12**, 575–585 (2020).
48. Krainer, G. et al. Direct digital sensing of proteins in solution through single-molecule optofluidics. Preprint at *bioRxiv* https://doi.org/10.1101/2020.05.24.113498 (2020).
49. Arter, W. E. et al. Rapid structural, kinetic, and immunochemical analysis of alpha-synuclein oligomers in solution. *Nano Lett* **20**, 8163–8169 (2020).
50. Krainer, G., Keller, S. & Schlierf, M. Structural dynamics of membrane-protein folding from single-molecule FRET. *Curr. Opin. Struct. Biol.* **58**, 124–137 (2019).
51. Kityk, R., Kopp, J., Sinning, I. & Mayer, M. P. Structure and dynamics of the ATP-bound open conformation of Hsp70 chaperones. *Mol. Cell* **48**, 863–874 (2012).
52. Qi, R. et al. Allosteric opening of the polypeptide-binding site when an Hsp70 binds ATP. *Nat. Struct. Mol. Biol.* **20**, 900–907 (2013).
53. Zhuravleva, A. & Gierasch, L. M. Substrate-binding domain conformational dynamics mediate Hsp70 allostery. *Proc. Natl. Acad. Sci. USA* **112**, E2865–E2873 (2015).
54. Sikor, M., Mapa, K., von Voithenberg, L. V., Mokranjac, D. & Lamb, D. C. Real-time observation of the conformational dynamics of mitochondrial Hsp70 by spFRET. *EMBO J.* **32**, 1639–1649 (2013).
55. Mayer, M. P. Hsp70 chaperone dynamics and molecular mechanism. *Trends Biochem. Sci.* **38**, 507–514 (2013).
56. Kellner, R. et al. Single-molecule spectroscopy reveals chaperone-mediated expansion of substrate protein. *Proc. Natl. Acad. Sci. USA* **111**, 13355–13360 (2014).
57. Linse, S. Mechanism of amyloid protein aggregation and the role of inhibitors. *Pure Appl. Chem.* **91**, 211–229 (2019).
58. Hoyer, W. et al. Dependence of α-synuclein aggregate morphology on solution conditions. *J. Mol. Biol.* **322**, 383–393 (2002).
59. Malakhov, M. P. et al. SUMO fusions and SUMO-specific protease for efficient expression and purification of proteins. *J. Struct. Funct. Genom.* **5**, 75–86 (2004).
60. Qin, D., Xia, Y. & Whitesides, G. M. Soft lithography for micro- and nanoscale patterning. *Nat. Protoc.* **5**, 491–502 (2010).

Acknowledgements

The research presented in this manuscript has received funding from the European Research Council (ERC) under the European Union's Seventh Framework Programme (FP7/2007–2013) through the ERC grant PhysProt (agreement no. 337969) and under European Union's Horizon 2020 research and innovation programme (ETN grant 674979-NANO-TRANS) (M.M.S., T.W.H., E.A., Q.A.E.P., T.P.J.K.), the Marie Skłodowska-Curie grant (agreement no. 749370) (S.G.) and Marie Skłodowska-Curie grant MicroSPARK (agreement no. 841466) (G.K.). This research has been supported by the Centre for Misfolding Diseases (C.M.D., T.P.J.K.), the Frances and Augustus Newman Foundation (T.W.H., T.P.J.K.), the Welcome Trust (MBAG/301 RG84912) (C.M.D., T.P.J.K.), the Engineering and Physical Sciences Research Council (EPSRC) (T.P.J.K.), St John's College Cambridge, UK (M.M.S., C.M.D., T.P.J.K.), the Oppenheimer Early Career Research Fellowship (T.W.H.), the Herchel Smith Funds of the University of Cambridge (G.K.), and the Wolfson College Junior Research Fellowship (G.K.). F.U.H. acknowledges funding from the Michael J. Fox Foundation and the Aligning Science Across Parkinson's initiative (ASAP-000282). We are grateful to Romy Lange and Nadine Wischnewski for their assistance with protein expression. Plasmids pCA528-HspA4 and pCA528-DnaJB1 were kind gifts from Bernd Bukau, University of Heidelberg. We are thankful for assistance with the diffusion analysis code by Raphaël Jacquat, University of Cambridge.

Author contributions

F.U.H., T.P.J.K., C.M.D., A.B., M.V., S.G., G.K., T.W.H. and M.M.S. designed the study. M.M.S., T.W.H., S.G., E.A., G.K., A.M.M., V.T., A.B. and F.S.R. performed the experiments. T.W.H., S.G., G.K., A.B., C.M.D., F.U.H. and T.P.J.K. provided materials and methods. M.M.S., T.W.H., E.A., G.K., Q.A.E.P., F.U.H. and T.P.J.K. analysed the data. M.M.S., T.W.H., G.K., A.B., F.U.H., T.P.J.K. wrote the paper. All authors discussed the results and commented on the manuscript.

Competing interests

The authors declare no competing interests.

Additional information

Supplementary information The online version contains supplementary material available at https://doi.org/10.1038/s41467-021-25966-w.

Correspondence and requests for materials should be addressed to F. Ulrich Hartl or Tuomas P. J. Knowles.

Peer review information *Nature Communications* thanks the anonymous reviewer(s) for their contribution to the peer review of this work.

Reprints and permission information is available at http://www.nature.com/reprints

Publisher's note Springer Nature remains neutral with regard to jurisdictional claims in published maps and institutional affiliations.

The Hsc70 Disaggregation Machinery Removes Monomer Units Directly from α-Synuclein Fibril Ends

Supplementary Information

Matthias M. Schneider[1,+], Saurabh Gautam[2,3,+], Therese W. Herling[1,+], Ewa Andrzejewska[1,+], Georg Krainer[1,+], Alyssa Miller[1], Victoria Trinkaus[2], Quentin A. E. Peter[1], Simone Francesco Ruggeri[1], Michele Vendruscolo[1], Andreas Bracher[2], Christopher M. Dobson[1,†], F. Ulrich Hartl[2,*], Tuomas P. J. Knowles[1,4,*]

[1] Centre for Misfolding Diseases, Yusuf Hamied Department of Chemistry, University of Cambridge, Lensfield Road, Cambridge CB2 1EW, United Kingdom

[2] Department of Cellular Biochemistry, Max-Planck Institute of Biochemistry, Am Klopferspitz 18, 82152 Martinsried, Germany

[3] Present affiliation: ViraTherapeutics GmbH, 6063 Rum, Austria

[4] Cavendish Laboratory, Department of Physics, University of Cambridge, JJ Thomson Road, Cambridge CB3 0HE, United Kingdom

[+] These authors contributed equally

[†] Deceased (September 2019)

[*] To whom correspondence should be addressed: uhartl@biochem.mpg.de (FUH), tpjk2@cam.ac.uk (TPJK)

Supplementary Figures

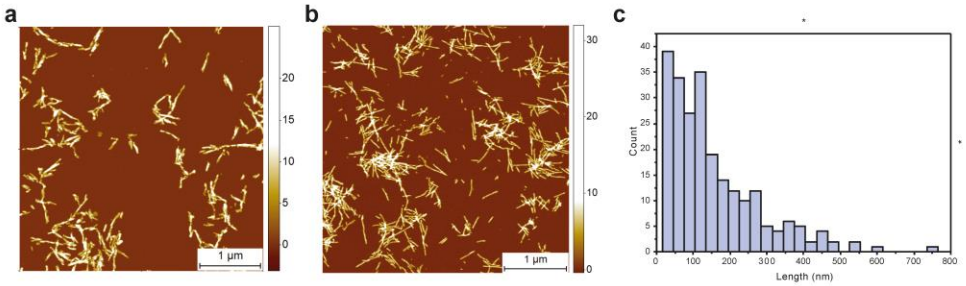

Supplementary Figure 1 : AFM imaging to compare labelled and unlabelled αS fibrils. (**a**) unlabelled and (**b**) labelled fibrils were imaged by atomic force microscopy (AFM). (**c**) A length analysis of labelled fibrils is consistent with diffusional sizing assays. For a-c, 20 scans were taken per sample. The location of imaging was chosen systematically, with the same pre-determined areas of the mica being imaged to ensure comparability between the samples.

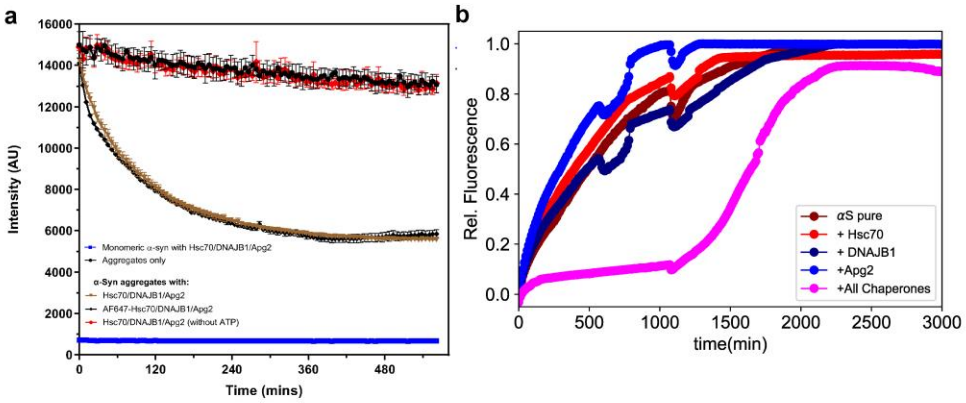

Supplementary Figure 2 : Kinetics of αS aggregation and disaggregation by the Hsc70-DnaJB1-Apg2 system in the presence of ATP. (**a**) Disaggregation was followed by ThT fluorescence. Protein concentrations were: Hsc70 2 μM, DnaJB1 1 μM; Apg2 0.2 μM, ATP 5 mM. ThT fluorescence is decreasing over time when all chaperones are present. Consistent results when Alexa Fluor 647 labelled Hsc70 was used. (**b**) Aggregation of αS in HEPES-KOH, pH 7.5, under heavily seeded conditions (300 muM at 30 muM αS conditions, i.e. 1% of the mass concentration are seeds to follow elongation kinetics.

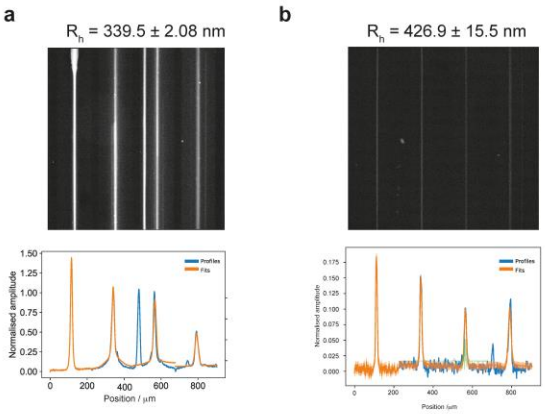

Supplementary Figure 3 : Diffusional Sizing of pure fibrils at different lengths. (**a**) 340 ± 2 nm and (**b**) 427 ± 16 nm.

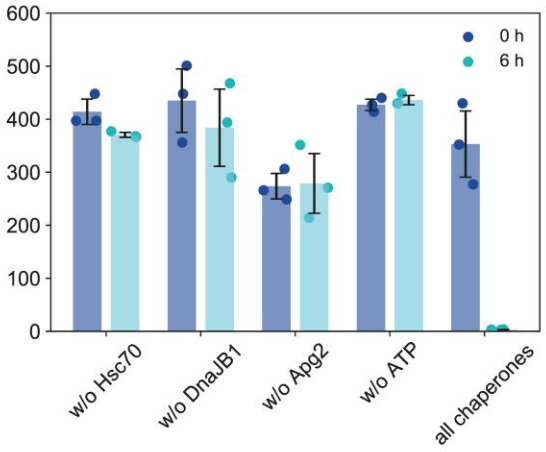

Supplementary Figure 4 : Negative Controls. Disaggregation by MDS in absence of the chaperone Hsc70 as well as the co-chaperones DnaJB1 and Apg2, or in the absence of ATP at 0 h (blue) and 6 h (cyan). No decrease in hydrodynamic radius, R_h, is observable after 6 hours, while a size decrease is observable in presence of all chaperones. Error bars represent the standard deviation (n = 3 independent measurements).

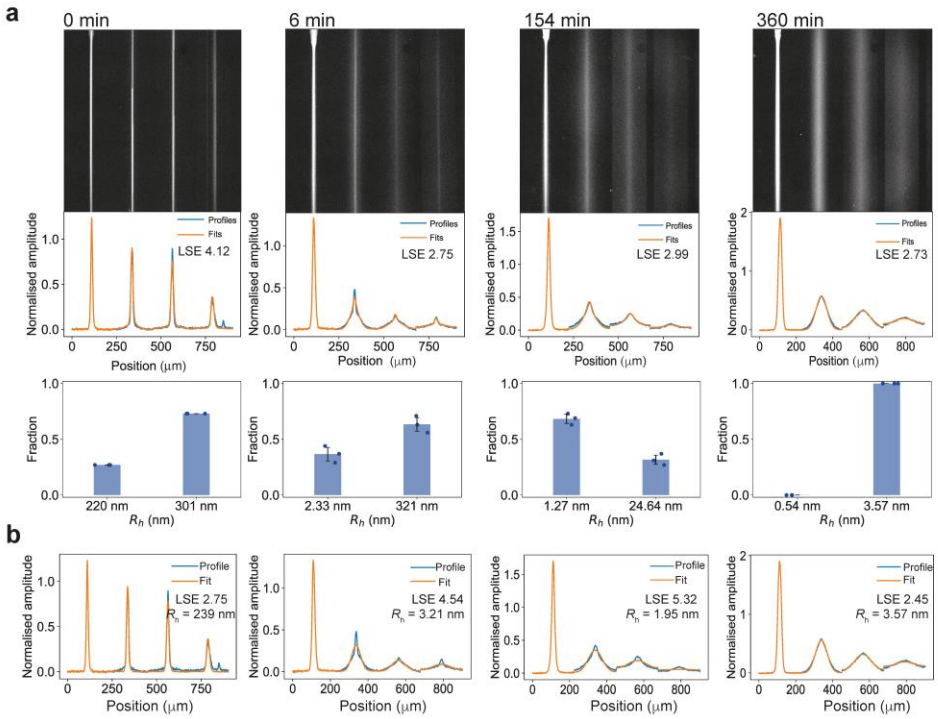

Supplementary Figure 5 : Statistical comparison of one and two species fit in microfluidic image analysis. (**a**) 2 species and (**b**) 1 species of the images shown in Figure 2. The distributions at time points t = 6 min and t = 154 min fit better to two species than to one species, as the reduced least squares estimation (LSE) is significantly lower for 2 species than 1 species. In contrast, the time points t = 0 min and t = 360 min are better represented by 1 species than 2 species, as it would be assumed given that only one species is present. Data in a are represented as mean ± standard deviation of n = 3 independent experiments.The individual data points are overlaid.

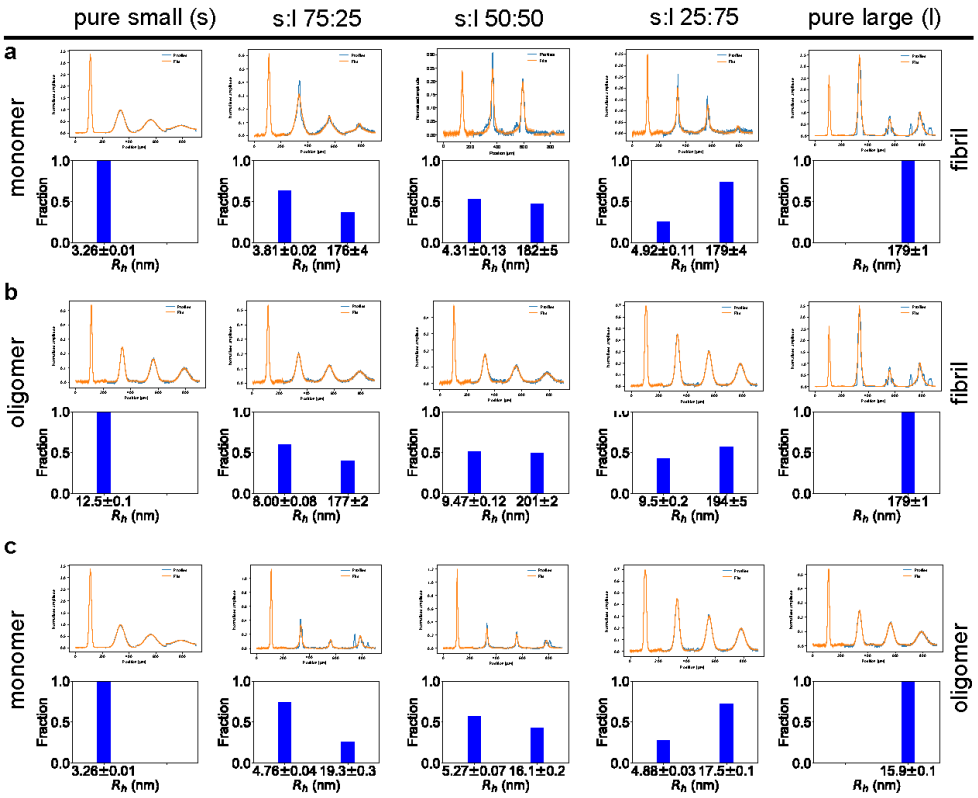

Supplementary Figure 6 : Control experiment demonstrating the ability of microfluidic diffusional sizing (MDS) to distinguish αS fibrils, oligomers and monomers in heterogeneous mixtures. (a) Monomer and fibril, (b) oligomer and fibril and (c) monomer and oligomer at identical mass concentration were mixed in different ratios. The fits are displayed for each mixture in the top row, the bottom row shows the aspect ratio and the radii for both species fitted.

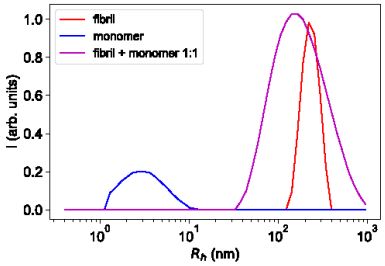

Supplementary Figure 7 : Challenges of dynamic light scattering (DLS) to detect monomers in the presence of fibrils. DLS of monomer, fibrils, and 1:1 mixture of monomer and fibrils, with a total mass concentration of 20 μM αS, revealing a hydrodynamic radius of 269 ± 49 nm for pure fibrils, 250 ± 80 nm for the 1:1 mixture, and 3.3 ± 1.9 nm for pure monomer. Data in a and b are represented as mean ± standard deviation of n = 3 independent experiments.

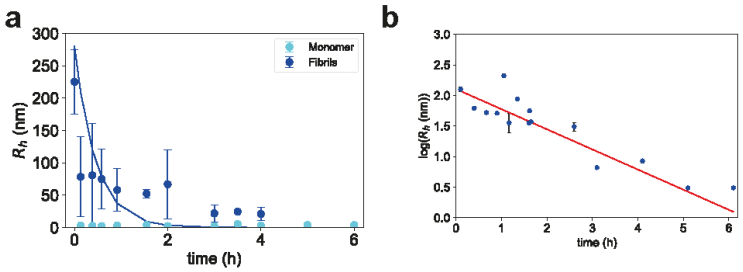

Supplementary Figure 8 : Disaggregation of sonicated αS fibrils. (a) Size population of monomers and fibrils over time, starting from 280 nm initial size. The size of the larger species decays with single exponential kinetics (solid line). The size of the smaller species appearing is conserved (Fig. 2e). Error bars represent the standard deviation (n = 3 independent measurements). (b) Kinetic fits of $\log(R_h)$ vs. time, according to the kinetic model described in equation 1 in materials and methods. From these fits, a rate constant $k = 2.2 \cdot 10^{-4} \pm 0.2 \cdot 10^{-4}$ s^{-1} was determined. $R^2 = 0.87$. Data in a, b and c are represented as mean $\pm$ standard deviation of n = 3 independent experiments.

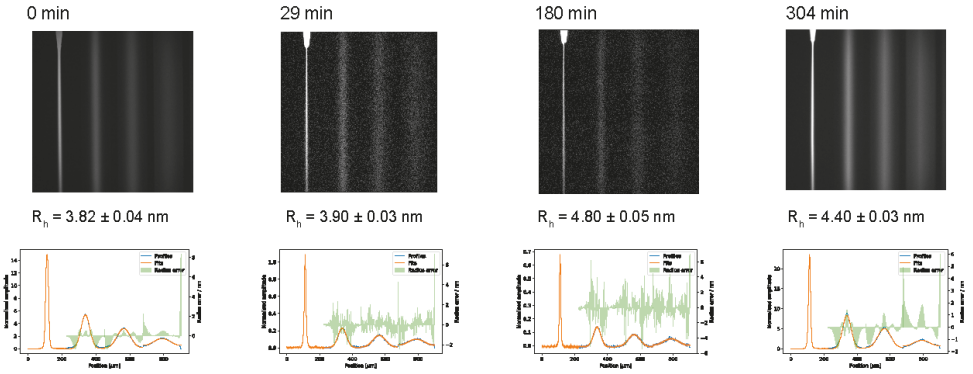

Supplementary Figure 9 : Hydrodynamic radius of Hsc70 at different times during disaggregation. The small size ($R_h \approx 3.9$ nm) indicates that the majority of the Hsc70 remains in an unbound state with only little Hsc70 in the bound state, indicating an excess of Hsc70 chaperone over aS fibrils. Time point at t=0 is pure Hsc70 before mixing with αS fibrils.

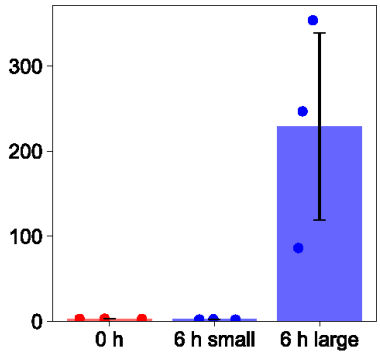

Supplementary Figure 10 : Negative Controls. Addition of labelled monomer to unlabelled fibrils. After 6 h, a large species of $229 \pm 53nm$ is observed as dominant species (90%) along with the monomer, indicating incorporation of monomer in unlabelled fibrils. Data in c, d, e, f and g are represented as mean $\pm$ standard deviation of n = 3 independent experiments.The individual data points are overlaid.

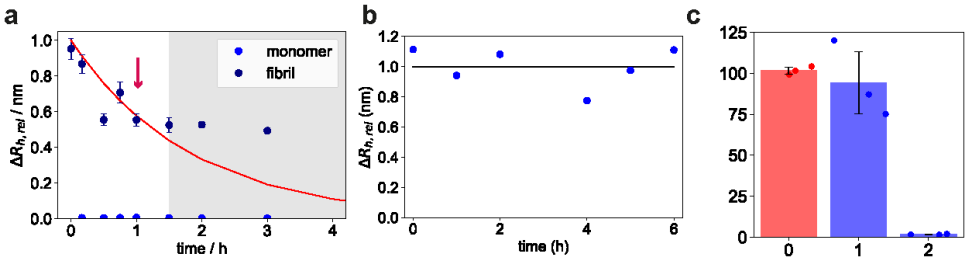

Supplementary Figure 11 : Inhibition/quenching of αS disaggregation by Hsc70 binding peptide and slowly hydrolysable ATP analogue. (**a**) Disaggregation time course was observed for 60 minutes, followed by addition of Hsc70 binding peptide (arrow) and monitoring disaggregation for another 120 minutes. The red line shows the progression of disaggregation in the absence of peptide. The behaviour of aS monomer is also shown. Error bars represent the standard deviation (n = 3 independent measurements). (**b**) Disaggregation time course with addition of Hsc70 binding peptide before Hsc70. The hydrodynamic radius of aS fibrils is conserved over 6 hours, showing that the disaggregation does not proceed in presence of the Hsc70 binding peptide. (**c**) Single Round experiment with the slowly hydrolysable ATP analogue ATP-γ-S, which cannot be dissociated by Apg2 and, therefore, stops the disaggregation after a single round. This shows that a single disaggregation round of fibrils of initial length 101.68 $\pm$ 2.51 nm results in the occurrence of two species, a fibrillar species of 94.17 $\pm$ 3.96 nm and a monomeric species of 2.11 $\pm$ 0.05 nm. Error bars represent the standard deviation (n = 3 independent measurements). The individual data points are overlaid in c.

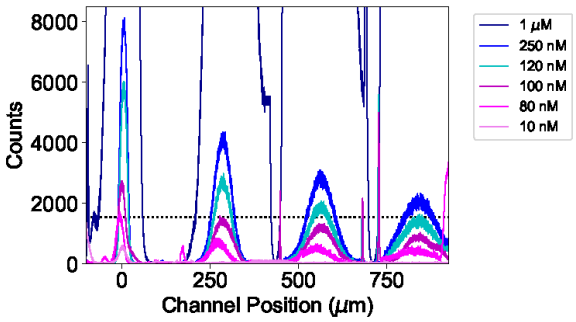

Supplementary Figure 12 : Fluorescence intensity of αS monomer at different concentrations. This data is used as calibration for the data in Fig. 4g.

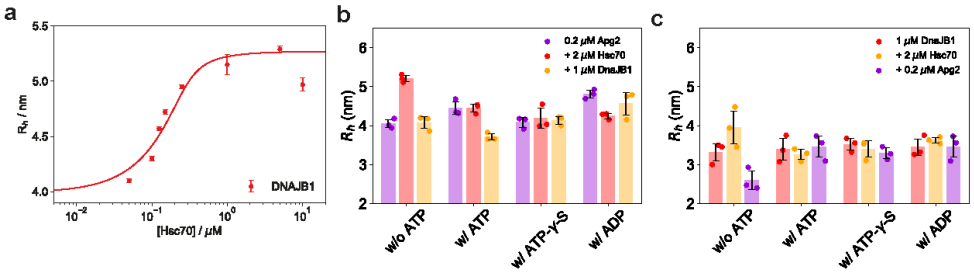

Supplementary Figure 13 : Binding of co-chaperones. (a) Binding curve for the interaction between Hsc70 and DnaJB1 ($K_d = 46.0 \pm 13.5$ nM) Error bars represent the standard deviation (n = 3 independent measurements). . Binding of (b) labelled Apg2 and (c) labelled DnaJB1 to Hsc70 with different ATP/ADP conditions, co-chaperone, yielding results consistent with Fig. 5a-b for labelled Hsc70. Data in a, b and c are represented as mean ± standard deviation of n = 3 independent experiments. The individual data points are overlaid.

2.4. Publication 4: The AAA+ chaperone VCP disaggregates Tau fibrils and generates aggregate seeds

Aim and key results of the study:

In this study, we aimed to elucidate how metazoan cells disaggregate amyloid protein aggregates. To this end, we conducted a mass spectrometric analysis of tau aggregates purified from human embryonic kidney cells. We found that the AAA+ ATPase VCP together with its co-factors Npl4 and Ufd1 are associated with the tau aggregates. Subsequent biochemical and cell-biological experiments revealed that VCP binds to ubiquitinated tau aggregates directly and disaggregates them. During this process, low molecular weight species, most likely tau monomers, are formed that can be degraded by the proteasome or be refolded by the Hsp70 chaperone system. Interestingly, as a byproduct, larger tau species also emerge, which are seeding competent and can propagate the amyloid tau aggregates during cell division.

Contribution:

V.A.T. conducted the cryo-ET experiments of Tau-YFP (Yellow Fluorescent Protein) aggregates in primary mouse neurons. This included cryo-ET sample preparation, data acquisition, post-processing as well as data analysis.

The AAA+ chaperone VCP disaggregates Tau fibrils and generates aggregate seeds

Itika Saha[1,2], Patricia Yuste-Checa[1,2], Miguel Da Silva Padilha[3,4], Qiang Guo[5,#], Roman Körner[1], Hauke Holthusen[1], Victoria A. Trinkaus[1,5,6], Irina Dudanova[3,4], Rubén Fernández-Busnadiego[2,5,7,8], Wolfgang Baumeister[5], David W. Sanders[9,†], Saurabh Gautam[1,§], Marc I. Diamond[9], F. Ulrich Hartl[1,2,6,*] and Mark S. Hipp[1,6,10,11*]

[1]Department of Cellular Biochemistry, Max Planck Institute of Biochemistry, Am Klopferspitz 18, 82152 Martinsried, Germany.

[2]Aligning Science Across Parkinson's (ASAP) Collaborative Research Network, Chevy Chase, MD, USA.

[3]Molecular Neurodegeneration Group, Max Planck Institute of Neurobiology, 82152 Martinsried, Germany.

[4]Department of Molecules – Signaling – Development, Max Planck Institute of Neurobiology, Am Klopferspitz 18, 82152 Martinsried, Germany.

[5]Department of Structural Molecular Biology, Max Planck Institute of Biochemistry, Am Klopferspitz 18, 82152 Martinsried, Germany.

[6]Munich Cluster for Systems Neurology (SyNergy), Munich, Germany.

[7]Institute of Neuropathology, University Medical Center Göttingen, 37099 Göttingen, Germany.

[8]Cluster of Excellence "Multiscale Bioimaging: from Molecular Machines to Networks of Excitable Cells" (MBExC), University of Göttingen, Germany.

[9]Center for Alzheimer's and Neurodegenerative Diseases, Peter O'Donnell Jr. Brain Institute, University of Texas Southwestern Medical Center, Dallas, 75390 Texas, USA.

[10]School of Medicine and Health Sciences, Carl von Ossietzky University Oldenburg, Oldenburg, Germany.

[11]Department of Biomedical Sciences of Cells and Systems, University Medical Center Groningen, University of Groningen, Antonius Deusinglaan, 1, 9713 AV Groningen, The Netherlands.

Present address: State Key Laboratory of Protein and Plant Gene Research, School of Life Sciences and Peking-Tsinghua Center for Life Sciences, Peking University, Beijing 100871, China.

‡ Present address: Department of Chemical and Biological Engineering, Princeton University, Princeton, NJ 08544, USA

§ Present address: Boehringer Ingelheim International GmbH, 55216 Ingelheim, Germany and ViraTherapeutics GmbH, 6063 Rum, Austria.

* To whom correspondence should be addressed:

uhartl@biochem.mpg.de (FUH); m.s.hipp@umcg.nl (MSH)

Abstract

Amyloid-like aggregates of the microtubule-associated protein Tau are associated with several neurodegenerative disorders including Alzheimer's disease. The existence of cellular machinery for the removal of such aggregates has remained unclear, as specialized disaggregase chaperones are thought to be absent in mammalian cells. Here we show in cell culture and in neurons that the AAA+ chaperone VCP is recruited to ubiquitylated Tau fibrils, resulting in their efficient disaggregation. Aggregate clearance depends on the functional cooperation of VCP with Hsp70 and the ubiquitin-proteasome machinery. Inhibition of VCP activity stabilizes large Tau aggregates, and is accompanied by a reduction in the amount of Tau species competent of prion-like aggregate seeding in recipient cells. Thus, disaggregation by VCP generates seeding-active Tau as byproduct. These findings identify VCP as a core component of the machinery for the removal of neurodegenerative disease aggregates and suggest that its activity can be associated with enhanced aggregate spreading in tauopathies.

Introduction

Deposition of amyloid-like Tau aggregates is a hallmark of devastating neurodegenerative disorders such as Alzheimer's disease and frontotemporal dementia[1]. In healthy neurons, Tau functions in microtubule (MT) assembly and stabilization by associating with MTs via its repeat domain (RD) consisting of three or four 31-32 residue imperfect repeats. Two hexapeptide motifs within the RD are critical for Tau aggregation, and the RD forms the structural core of disease-associated aggregates[1], with several RD mutations underlying familial tauopathies[2]. Expression of human Tau mutants in mouse models recapitulates essential features of

63 tauopathies including the formation of amyloid-like Tau deposits and neuronal loss[3,4], indicating
64 that Tau aggregation is central to neurodegeneration. Pathogenic Tau aggregates often exhibit the
65 ability to induce aggregation in naïve cells through a mechanism of transcellular propagation that
66 allows aggregate pathology to spread across brain regions[5,6]. Notably, pathological Tau
67 aggregates and spreading are resolved upon lowering Tau levels, which is accompanied by
68 improved neuronal health and extended lifespan[7,8]. However, the cellular mechanisms involved
69 in the reversal, clearance and spread of Tau aggregates remain poorly understood.

70 While specialized chaperones of the AAA+ family in bacteria, yeast and plants have the
71 ability to resolve amyloid-like aggregates[9,10], direct homologues of these hexameric
72 disaggregases have not been identified in mammalian cells. Instead, disaggregation in higher
73 eukaryotes is mainly attributed to the Hsp70 chaperone machinery[11-14]. The human Hsp70-
74 Hsp40-Hsp110 chaperone system efficiently dissociates Tau and α-synuclein fibrils in vitro[15-17]
75 independent of AAA+ disaggregases that cooperate with the Hsp70 system in yeast and bacteria
76 to achieve disaggregation[9]. The eukaryotic AAA+ ATPase valosin-containing protein (VCP)
77 exerts ATP-dependent protein unfolding activity[18,19] and has been proposed to resolve protein
78 aggregates[20,21] and certain condensates such as stress granules[22,23]. VCP facilitates protein
79 turnover via the ubiquitin-proteasome system[24,25], in addition to sustaining functional
80 autophagy[26]. Indeed, VCP mutations have been associated with aggregate deposition disorders
81 such as vacuolar tauopathy and inclusion body myopathy associated with Paget disease of bone
82 and frontotemporal dementia (IBMPFD)[20,27-29]. Accumulation of Tau aggregates in vacuolar
83 tauopathy was proposed to be a consequence of diminished ATPase activity of mutant VCP
84 (D395G)[20]. IBMPFD-associated VCP mutants exhibit increased basal ATP hydrolysis and
85 unfolding activity[30,31], altered interactions with cofactors[32,33] and perturbed autophagic

function[34]. Whether any of these mutations influence the clearance of pre-formed fibrillar Tau aggregates in cells is not known.

Here we provide direct evidence in a cell culture model and in primary murine neurons that VCP disaggregates amyloid-like Tau fibrils in a ubiquitin and proteasome-dependent manner, with the Hsp70 chaperone system contributing to aggregate clearance. This function of VCP is not detectably perturbed by pathogenic VCP mutations. Although disaggregation by VCP is coupled to proteasomal degradation, intermediates of the disaggregation process escape proteolysis and are a source of seeding-competent Tau species.

Results

To investigate the ability of cells to clear Tau aggregates, we used HEK293 cells stably expressing TauRD-Y (P301L/V337M), a mutant of the amyloid-forming repeat domain of Tau[35,36] fused to YFP via a flexible linker[37] (Fig. 1a). TauRD-Y is soluble and diffusely distributed in TauRD-Y cells, but the extracellular addition of Tau aggregates isolated from tauopathy brain tissue or generated in vitro induces its aggregation via template-based seeding, leading to formation of aggregates that are stably propagated for weeks[37,38] (Fig. 1b). Using TauRD-Y aggregate seeds[37], we generated a cell line (TauRD-Y*) in which phosphorylated TauRD-Y accumulated in cytosolic inclusions 0.5-5 μm^2 in size that stained with the amyloid-specific dye Amylo-Glo[39] (Fig. 1c, Supplementary Fig. 1a-c). Analysis of the inclusions in intact TauRD-Y* cells by cryo-electron tomography revealed TauRD-Y fibrils of ~18 nm diameter, which were distinguishable from cytoskeletal structures (Fig. 1d) and consistent with the structures of fibrillar Tau in tauopathy patient brain[40-44]. Thus, TauRD forms amyloid-like

fibrillar aggregates in TauRD-Y* cells. TauRD-Y aggregates were also able to induce aggregates of full-length Tau fused to YFP (FLTau-Y). These aggregates reacted with the AT-8 antibody specific for phosphorylation at serine 202 and threonine 205 (epitopes not present in TauRD) (Fig. 1a, Supplementary Fig. 1d,e), which has been used previously to detect paired helical filaments[45,46].

Proteasomal clearance of Tau aggregates

Soluble TauRD-Y was efficiently degraded in TauRD-Y cells upon inhibition of protein synthesis with cycloheximide (CHX) (Supplementary Fig. 1f). CHX treatment also led to partial clearance of TauRD inclusions in TauRD-Y* cells (Fig. 1e, Supplementary Fig. 1f,g). To avoid global inhibition of protein synthesis, we employed cells in which the expression of TauRD-Y is controlled with a Tet-regulated promoter (Tet-TauRD-Y and Tet-TauRD-Y* cells)[37] (Supplementary Fig. 2a). Addition of doxycycline resulted in clearance of TauRD-Y inclusions and insoluble TauRD-Y protein ($t_{1/2}$ ~12 h) (Supplementary Fig. 2a-d). The amount of insoluble TauRD-Y decreased faster than the level of soluble TauRD-Y (Supplementary Fig. 2d), consistent with aggregate material being solubilized prior to degradation. Moreover, inhibition of TauRD-Y synthesis resulted in a time dependent reduction of inclusion size and number per cell (Fig. 1f). Thus, the cells are able to efficiently dissociate and degrade amyloid-like TauRD-Y aggregates.

Addition of the selective proteasome inhibitor Epoxomicin or siRNA-mediated downregulation of the proteasome component PSMD11 stabilized aggregated TauRD-Y upon doxycycline shut-off and prevented aggregate clearance (Supplementary Fig. 3a-e). Proteasome inhibition also stabilized soluble TauRD-Y in Tet-TauRD-Y cells[47] (Supplementary Fig. 3a), but

did not lead to de novo Tau aggregation[48] (Supplementary Fig. 4h). Hence, the persistence of TauRD-Y aggregates upon proteasome inhibition is due to stabilization of pre-existing aggregates. In contrast, inhibition of lysosomal degradation with Bafilomycin A1 (confirmed by increased levels of LC3-II) or of autophagy with 3-methyladenine was without effect on the levels of total or aggregated TauRD-Y protein in the cellular model used (Supplementary Fig. 3a-c). Downregulation of autophagy components ATG5/7 supported this conclusion (Supplementary Fig. 3d,e). Thus, TauRD-Y aggregates are degraded in a proteasome-dependent, autophagy-independent manner.

Tau disaggregation requires VCP

Proteins must generally be unfolded to access the catalytic center of the 20S proteasome. Thus, prior to degradation, aggregated proteins need to undergo disaggregation[49]. To identify the cellular machinery involved in TauRD-Y disaggregation, we performed an interactome analysis of aggregated TauRD-Y by quantitative mass spectrometry. We identified the AAA+ ATPase VCP as one of the most highly enriched interactors of aggregated TauRD-Y, along with the ubiquitin-binding VCP cofactors UFD1L, NPLOC4 and NSFL1C, and multiple subunits of the 26S proteasome (Fig. 2a, Supplementary Table 1). Hsp70 was detected in the proteomic analysis but was not enriched on aggregated TauRD-Y. Co-localization of VCP and its cofactors with TauRD-Y aggregates was confirmed by fluorescence microscopy (Fig. 2b, Supplementary Fig. 4a-c).

VCP utilizes the energy from ATP hydrolysis to structurally remodel and unfold proteins in different cellular contexts[18,50]. To assess whether VCP is involved in TauRD-Y disaggregation, we inhibited VCP in cells using NMS-873, a small molecule allosteric inhibitor

of the VCP ATPase[51]. Similar to proteasome inhibition, NMS-873 blocked the clearance of TauRD-Y aggregates when TauRD-Y synthesis was stopped with doxycycline (Fig. 2c,d). Likewise, the aggregates were stabilized when VCP was inhibited using CB-5083 (Supplementary Fig. 4d), a competitive inhibitor of ATP binding in the D2 ATPase domain of VCP[52], or down-regulated with siRNA (Supplementary Fig. 4e,f). VCP inhibition during ongoing TauRD-Y synthesis resulted in a significant increase in inclusion size (Supplementary Fig. 4g), suggesting that the inclusions exist at a dynamic equilibrium between formation and disaggregation. No aggregation of soluble TauRD-Y was detected after treating cells with NMS-873 or VCP siRNA (Supplementary Fig. 4 h,i). VCP down-regulation caused a marginal increase in the level of soluble TauRD-Y in Tet-TauRD-Y cells, but did not result in a significant stabilization after doxycycline addition (Supplementary Fig. 4j). In contrast, aggregate-containing Tet-TauRD-Y* cells treated with VCP siRNA accumulated significantly higher amounts of TauRD-Y both in the absence or presence of doxycycline, indicating an aggregate-specific role of VCP (Supplementary Fig. 4j).

Importantly, VCP also co-localized with aggregates of full-length Tau (FLTau-Y) in FLTau-Y* cells (Supplementary Fig. 4k), and VCP or proteasome inhibition prevented the clearance of FLTau-Y aggregates (Supplementary Fig. 4l,m), recapitulating the behavior of TauRD. To exclude a possible role of the YFP tag on Tau in VCP-mediated disaggregation, we generated HEK293T cells stably expressing non-tagged full-length Tau (FLTau) and myc-tagged Tau repeat domain (TauRD) under a Tet-regulated promoter (Tet-FLTau, Tet-FLTau* and Tet-TauRD, Tet-TauRD* cells). Similar to FLTau-Y aggregates in FLTau-Y* cells, FLTau aggregates in Tet-FLTau* cells were phosphorylated at serine 202 and threonine 205 and colocalized with VCP (Fig. 2e, Supplementary Fig. 4n). FLTau and TauRD aggregates were

177 resolved in a VCP and proteasome-dependent manner when Tau synthesis was halted by adding
178 doxycycline (Fig. 2f, Supplementary Fig. 4o).

179 We next tested whether VCP also modulates Tau aggregation in neurons. Mouse primary
180 neurons were transduced to express soluble TauRD-Y (Fig. 3a,b). Upon seeding with TauRD
181 aggregates[37], we observed the formation of multiple inclusions of intracellular TauRD-Y
182 (Fig. 3b). Cryo-electron tomography of TauRD-Y inclusions in aggregate-containing neurons
183 revealed fibrillar aggregates similar to the aggregates in TauRD-Y* cells (Fig. 3c). The lower
184 cytosolic density of neurons allowed the observation that the TauRD-Y fibrils were coated with
185 globular domains consistent with the presence of YFP on TauRD (Supplementary Fig. 4p), as
186 previously observed for other amyloidogenic proteins fused to fluorescent protein[53,54]. Aggregate
187 seeding in neurons was accompanied by a ~40% decrease in cell viability (Fig. 3d). Most of the
188 neuronal TauRD-Y inclusions stained positive for VCP (Fig. 3b). Treatment with the VCP
189 inhibitor NMS-873 for 4 h caused a massive accumulation of TauRD aggregates in seeded
190 neurons, in some cases occupying most of the cell body area (Fig. 3e). No inclusions were
191 observed in unseeded cells upon VCP inhibition (Fig. 3e). These results demonstrate that VCP
192 functions in TauRD-Y disaggregation in neurons.

193

194 **Disaggregation depends on substrate ubiquitylation**

195 Ubiquitylation of VCP substrates, particularly the formation of lysine 48 (K48) linked
196 polyubiquitin chains, is required for VCP recruitment[18,19,30,50]. We therefore analyzed
197 immunoprecipitates of TauRD-Y for the presence of ubiquitin. Only in TauRD-Y* cells
198 containing aggregated TauRD-Y was the protein detectably modified by the addition of 1 to 4
199 ubiquitin molecules (Fig. 4a). Analysis with a K48-specific antibody verified the presence of

K48-linked ubiquitin (Fig. 4a). Immunofluorescence imaging also showed that the TauRD-Y aggregates stained positive for K48-linked ubiquitin chains (Fig. 4b, Supplementary Fig. 5a), while K63-linked ubiquitin was not detectable (Supplementary Fig. 5a). Likewise, the TauRD-Y inclusions in primary neurons colocalized with poly-ubiquitin chains (Supplementary Fig. 5b). K48-linked ubiquitin signal was also observed on the aggregates of untagged FLTau and TauRD (Supplementary Fig. 5c).

Inhibition of the ubiquitin-activating enzyme E1 with the specific inhibitor MLN7243[55] efficiently blocked ubiquitin conjugation (Supplementary Fig. 6a). TauRD-Y inclusions were still present but were no longer ubiquitin K48-reactive (Fig. 4b, Supplementary Fig. 6b). VCP was not recruited to these aggregates (Fig. 4c, Supplementary Fig. 6c), and both disaggregation and degradation of TauRD-Y in Tet-TauRD-Y* cells were blocked (Fig. 4d, Supplementary Fig. 6d). MLN7243 treatment also prevented the degradation of soluble TauRD-Y to a degree similar to proteasome inhibition (Supplementary Fig. 6e). Together these data show that VCP recruitment requires ubiquitylation of aggregated Tau, followed by disaggregation and remodeling to species that are accessible for proteasomal degradation.

Functions of VCP and Hsp70 in disaggregation

Disaggregation of both heat stress-induced and amyloid-like aggregates in mammalian cells has been assigned to the Hsp70 chaperone system[11-13,16]. Our findings raised the possibility of a functional cooperation between VCP and Hsp70 in these processes. To determine whether VCP participates in dissolving heat-induced aggregates, we expressed the metastable protein firefly luciferase (Fluc) fused to GFP in HEK293 cells. Heat stress at 43 ºC for 2 h combined with proteasome inhibition resulted in the formation of large (~2-3 µm) Fluc-GFP inclusions[56]

(Supplementary Fig. 7a). Unlike the TauRD-Y inclusions, the Fluc-GFP aggregates did not stain with an amyloid-specific dye (Supplementary Fig. 7a), suggesting that they were amorphous in structure. The Fluc-GFP aggregates were ubiquitin-negative and did not co-localize with VCP (Supplementary Fig. 7b-c). Accordingly, VCP inhibition with NMS-873 did not interfere with disaggregation (Supplementary Fig. 7d), arguing against a role of VCP in this process. However, inhibition of the ATPase activity of Hsp70 with the inhibitor VER-155008[57] prevented Fluc-GFP disaggregation (Supplementary Fig. 7d), confirming the role of the Hsp70 system in disaggregation.

To investigate whether Hsp70 participates in TauRD-Y disaggregation, we treated Tet-TauRD-Y* cells with VER-155008 or with NMS-873 and stopped TauRD-Y synthesis with doxycycline. VCP inhibition stabilized both large (>1.5 μm^2) and small (<1.5 μm^2) TauRD-Y inclusions (Supplementary Fig. 8a-b). In contrast, Hsp70 inhibition stabilized large aggregates only partially and resulted in a marked accumulation of small inclusions, consistent with VCP acting before Hsp70 in the disaggregation process (Supplementary Fig. 8a-b). These findings suggested that Hsp70 cooperates with VCP in disaggregation, either by dissociating fragments generated by VCP and/or by preventing re-aggregation of TauRD liberated from inclusions by VCP. Since Hsp70 was not enriched on TauRD-Y aggregates in the proteomic analysis (Supplementary Table 1), its interaction with TauRD may be transient.

Effects of VCP mutants on Tau disaggregation

Point mutations in VCP are associated with dominantly inherited disorders such as Inclusion body myopathy with Paget disease of bone and frontotemporal dementia (IBMPFD)[26] and vacuolar tauopathy[20]. These mutations lead to a dominant negative loss or alteration of VCP

246 function, presumably due to the oligomeric nature of VCP[58,59]. The mutation D395G (DG),
247 associated with vacuolar tauopathy is located in the D1 ATPase domain of VCP (Fig. 5a). It has
248 been reported to have a mildly reduced capacity to disaggregate Tau fibrils in an in vitro system,
249 due to a ~30% reduced ATPase activity[20]. The IBMPFD mutations, A232E (AE) and R155H
250 (RH), are located in the D1 ATPase domain and in the N-domain, respectively, and are
251 associated with enhanced ATPase activity compared to wild type (WT) VCP[31] (Fig. 5a). We
252 tested whether these mutations impair Tau disaggregation in our cellular model using the
253 ATPase defective VCP double-mutant E305Q/E578Q (EQ/EQ)[60] (Fig. 5a) as a control. The
254 mutant proteins, carrying a C-terminal myc-tag, were transiently overexpressed in Tet-TauRD-
255 Y* cells for 24 h and then TauRD-Y synthesis was stopped with doxycycline to observe
256 disaggregation. Note that mutant VCP was expressed in cells containing pre-formed aggregates
257 to exclude a potential role of VCP in aggregate seeding[61]. The myc-tagged mutant proteins were
258 present in hexamers that migrated on native PAGE like WT VCP (Supplementary Fig. 9a) and
259 colocalized with TauRD-Y aggregates (Fig. 5b).

260 As expected, expression of the ATPase defective VCP (EQ/EQ) effectively prevented
261 TauRD-Y aggregate clearance, even though the expression levels of this mutant were relatively
262 low when compared with the other constructs (Fig. 5c,d). Moreover, the TauRD-Y aggregates
263 increased in size upon VCP (EQ/EQ) expression as observed previously for inhibition of VCP
264 activity by NMS-873 (Supplementary Fig. 4g), presumably reflecting a shift of soluble TauRD to
265 the aggregates (Supplementary Fig. 2a). However, none of the disease-related VCP mutants,
266 including the vacuolar tauopathy mutant DG, when expressed at the indicated levels, detectably
267 stabilized TauRD-Y aggregates (Fig. 5b-d). Similar results were obtained when the presence of
268 aggregates was specifically analyzed in cells expressing the mutant VCP proteins by

immunofluorescence (Supplementary Fig. 9b). In conclusion, the effect of the VCP disease mutations on disaggregation, if any, is only mild, suggesting that inhibition of aggregate clearance may not be the primary mechanism by which these mutations cause disease.

VCP generates Tau species capable of seeding aggregation

Progression of tauopathies and other neurodegenerative diseases is thought to be mediated by aggregate spreading across brain regions through a prion-like seeding mechanism[5,6]. We speculated that the disaggregation activity of VCP could modulate the levels of aggregate species that are able to induce the aggregation of soluble Tau in recipient cells. To address this possibility, we measured the presence of seeding-competent TauRD species by FRET in cells expressing TauRD-mTurquoise2 and TauRD-Y (TauRD-TY cells)[62] (Fig. 6a). Addition of aggregate-containing total lysates from control TauRD-Y* cells induced TauRD aggregation in reporter cells (Supplementary Fig. 10a-b). Strikingly, treatment of TauRD-Y* cells with the VCP inhibitor NMS-873 reduced the seeding capacity of lysates by more than 50%, when equivalent amounts of TauRD-Y were compared (Fig. 6b). In contrast, such a reduction in seeding was not observed when cells were treated with proteasome inhibitor (Epoxomicin) or Hsp70 inhibitor (VER-155008) (Fig. 6b). However, treatment with the E1 enzyme inhibitor MLN7243, which prevented VCP recruitment to the aggregates (Fig. 4c), also caused a ~50% reduction of FRET positive TauRD-TY reporter cells. Similar effects were observed when lysates from TauRD-Y* cells transiently expressing VCP EQ/EQ were used. In contrast, expression of VCP DG did not reduce seeding (Fig. 6c, Supplementary Fig. 10c). Thus, VCP-mediated disaggregation generates seeding-active TauRD-Y species.

To characterize the seeding competent material in the presence and absence of VCP function, we fractionated lysates from TauRD-Y* cells by size-exclusion chromatography. Inclusions >0.2 µm were removed by filtration. The majority of the remaining TauRD-Y (~70%) fractionated at a high molecular weight (HMW) of ≥40 MDa in the void volume of the column. The remainder fractionated at a low molecular weight (LMW), equivalent to the position of soluble TauRD-Y from TauRD-Y cells (Fig. 6d). Both fractions isolated from TauRD-Y* cells were seeding competent, but the specific seeding activity of HMW TauRD-Y (% FRET positive cells per ng TauRD-Y) was ~10-fold higher than that of the LMW fraction (Supplementary Fig. 10d). Treatment with VCP inhibitor NMS-873 strongly reduced the total amount of TauRD-Y species <0.2 µm, consistent with the reduced seeding activity after VCP inhibition. Moreover, the ratio between HMW and LMW peaks was reversed as the former was decreased by ~80% and the latter by only ~25% (Fig. 6d). However, the specific seeding activity of TauRD in both fractions remained unchanged (Supplementary Fig. 10d), suggesting that VCP inhibition reduces the amount of seeds but not their intrinsic seeding potency. Together these results demonstrate that the disaggregation activity of VCP increases the available pool of seeding competent TauRD species.

Discussion

Metazoa do not possess a homologue of the AAA+ ATPase Hsp104 responsible for protein disaggregation in bacteria, fungi and plants[10,63]. Instead, dissociation of large protein aggregates, including amyloid fibrils, in animal cells is generally ascribed to the Hsp70/Hsp110/Hsp40 chaperone system[10,12-14,16]. Here we provide evidence that the AAA+ ATPase VCP functions in disaggregating amyloid fibrils of Tau in human cells and primary mouse neurons (Fig. 7). VCP

is distinct from Hsp104 in that it requires the target aggregate to be ubiquitylated, a critical element of control to ensure specificity and avoid dissolution of functional protein assemblies[64]. Consistent with such a control function, ubiquitylation likely occurs after aggregate formation as an essential prerequisite for disaggregation (Fig. 7). The E3 ubiquitin ligases involved in this process remain to be identified. Moreover, aggregate ubiquitylation ensures that disaggregation by VCP is coupled to degradation by the 26S proteasome. Additionally, the proteasomal 19S ATPase may contribute to disaggregation, consistent with its ability to fragment fibrils in vitro[65]. The Hsp70 chaperone system is required for the overall efficiency of the reaction, either by further dissociating aggregate fragments produced by VCP action or by preventing re-aggregation of Tau molecules that have been liberated from the fibrils (Fig. 7). As the smaller TauRD aggregates that accumulated upon Hsp70 inhibition were no longer VCP positive, disaggregation by VCP may allow Hsp70 to access aggregates of non-ubiquitylated Tau. This possibility is consistent with the reported ability of the Hsp70 system to disaggregate Tau aggregates in vitro[15].

Support for the physiological relevance of VCP in antagonizing amyloid aggregation is provided by mutations in VCP that are associated with the deposition of ubiquitylated aggregates in neurodegenerative diseases such as vacuolar tauopathy and IBMPFD[20,28,58]. However, the vacuolar tauopathy-associated VCP mutation D395G[20] and the IBMPFD mutations A232E and R155H[26] did not detectably impair VCP-mediated Tau disaggregation in our cellular model. Although even a small inhibitory effect on disaggregation may contribute to aggregate pathology in neurons over decades, the disease mutations may alternatively affect other steps during aggregate formation, including aggregate seeding and Tau degradation in cooperation with the proteasome. Indeed, an increase in intracellular aggregation is observed when VCP is inhibited

337 in recipient cells at the time of seeding[61] or when VCP D395G is expressed in the recipient
338 cells[20]. Note that we introduced the mutant VCP proteins in cells containing preexistent Tau
339 aggregates to exclude a potential role of VCP in the process of aggregate seeding.

340 Our finding that clearance of Tau aggregates by VCP generates smaller seeding
341 competent species as a byproduct (Fig. 7) provides a plausible explanation for how VCP can
342 exert both neuroprotective and neurotoxic effects. Indeed, overexpression of a VCP homologue
343 in a *Drosophila* model of polyglutamine protein aggregation hastened the degenerative
344 phenotype[66]. Transcellular aggregate spreading has been recognized as a major driver of
345 neurodegenerative disease progression[5,6,67], and generation of seeding competent species may be
346 an inevitable consequence of amyloid clearance mechanisms via disaggregation, not only by
347 VCP but also by the Hsp70 system[15]. We note, however, that in contrast to inhibition of VCP,
348 neither Hsp70 nor proteasome inhibition had a significant effect on the generation of seeding
349 competent Tau species in our model, suggesting that their function is not directly coupled to seed
350 production.

351 VCP-mediated aggregate disassembly followed by proteasomal degradation provides an
352 important alternative to autophagy as a mechanism for the elimination of terminally aggregated
353 proteins. Based on our results, both activation and inhibition of this pathway may have beneficial
354 effects dependent on the specific disease context. Non-human AAA+ ATPases with augmented
355 disaggregase activity are currently being developed with the aim to reverse pathogenic protein
356 aggregation[68,69]. Boosting cellular aggregate clearance, perhaps in combination with proteasome
357 activation[70], may offer a potential therapeutic strategy as long as the production of seeding
358 competent species can be controlled.
359

360 **Main Figures**

361

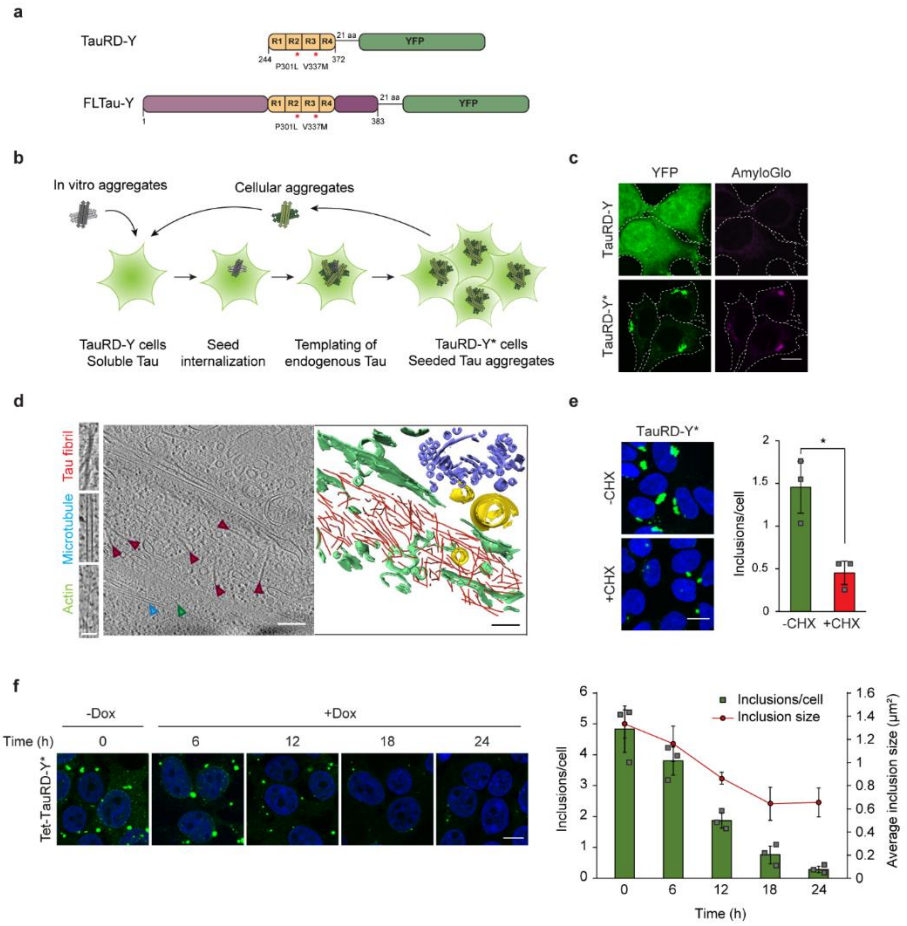

362

363 **Fig. 1 TauRD-Y forms amyloid-like aggregates that are cleared from cells. a** Schematic

364 representation of Tau constructs used in this study. TauRD-Y, the repeat domain, and FLTau-Y,

365 the 0N4R Tau isoform of full-length (FL) Tau with two frontotemporal dementia-associated

mutations, P301L and V337M, fused to YFP via 21 amino acid (aa) linkers. **b** Schematic representation of aggregate seeding. Extracellular addition of preformed Tau aggregates induces templating of intracellular Tau into aggregates that propagate with cell division. Aggregate seeds may be generated in vitro or be contained in cell lysate. TauRD-Y, naïve cells containing soluble TauRD-Y; TauRD-Y*, cells containing TauRD-Y aggregates. **c** Staining of TauRD-Y and TauRD-Y* cells with the amyloid-specific dye Amylo-Glo (magenta). White dashed lines indicate cell boundaries. Scale bar, 10 µm. **d** TauRD-Y aggregates are fibrillar in structure. Left, a 1.7 nm thick tomographic slice of a TauRD inclusion from TauRD-Y* cells is shown. Red, blue and green arrowheads indicate representative TauRD-Y fibril, microtubule and actin, respectively. Right, 3D rendering of corresponding tomogram showing TauRD-Y fibrils (red), Golgi (purple), mitochondria (yellow) and ER (green). Scale bars, 200 nm, inset 40nm. **e** Aggregate clearance. Left, TauRD-Y* cells treated for 24 h with cycloheximide (CHX; 50 µg/mL) where indicated. Nuclei were counterstained with DAPI (blue). Scale bar, 10 µm. Right, quantification of TauRD-Y foci. Mean ± s.d.; n=3; 500-600 cells analyzed per experiment; *$p<0.05$ ($p=0.0151$) from two-tailed Student's paired t-test. **f** Left, representative images of Tet-TauRD-Y* cells treated with Dox for the indicated times. Right, quantification of inclusions per cell and average inclusion size (μm^2). Mean ± s.d.; n=3. Scale bar, 10 µm.

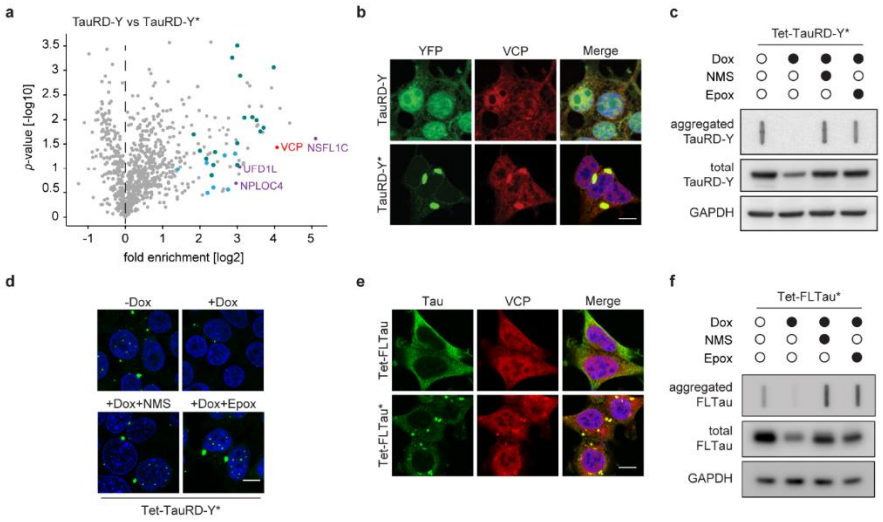

383 **Fig. 2 Disaggregation of Tau aggregates is dependent on VCP activity. a** Volcano plot of
384 TauRD-Y interactome from TauRD-Y and TauRD-Y* cells. Unlabeled green and blue symbols
385 represent proteasome subunits of 19S and 20S, respectively. VCP and its cofactors are
386 highlighted. **b** Association of VCP with TauRD-Y inclusions. Immunofluorescence staining of
387 VCP (red) and YFP fluorescence of TauRD-Y (green) in TauRD-Y and TauRD-Y* cells. Scale
388 bar, 10 µm. **c** Filter trap analysis of lysates from Tet-TauRD-Y* cells treated for 24 h with
389 doxycycline (Dox; 50 ng/mL) alone or in combination with NMS-873 (NMS; 2.5 µM) or
390 Epoxomicin (Epox; 50 nM). Aggregated and total TauRD-Y levels were determined by
391 immunoblotting against GFP. GAPDH served as loading control. **d** Representative images of
392 Tet-TauRD-Y* cells treated as in (c). Scale bar, 10 µm. **e** Association of VCP with FLTau
393 inclusions. Immunofluorescence staining of VCP (red) and Tau with Tau-5 antibody (green) in
394 FLTau and FLTau* cells. Scale bar, 10 µm. **f** Filter trap analysis of lysates from Tet-FLTau*
395 cells treated for 24 h with doxycycline (Dox; 50 ng/mL) alone or in combination with NMS-873
396 (NMS; 2.5 µM) or Epoxomicin (Epox; 50 nM). Aggregated and total FLTau levels were
397 determined by immunoblotting using AT8 and Tau-5 antibodies, respectively. GAPDH served as
398 loading control.
399

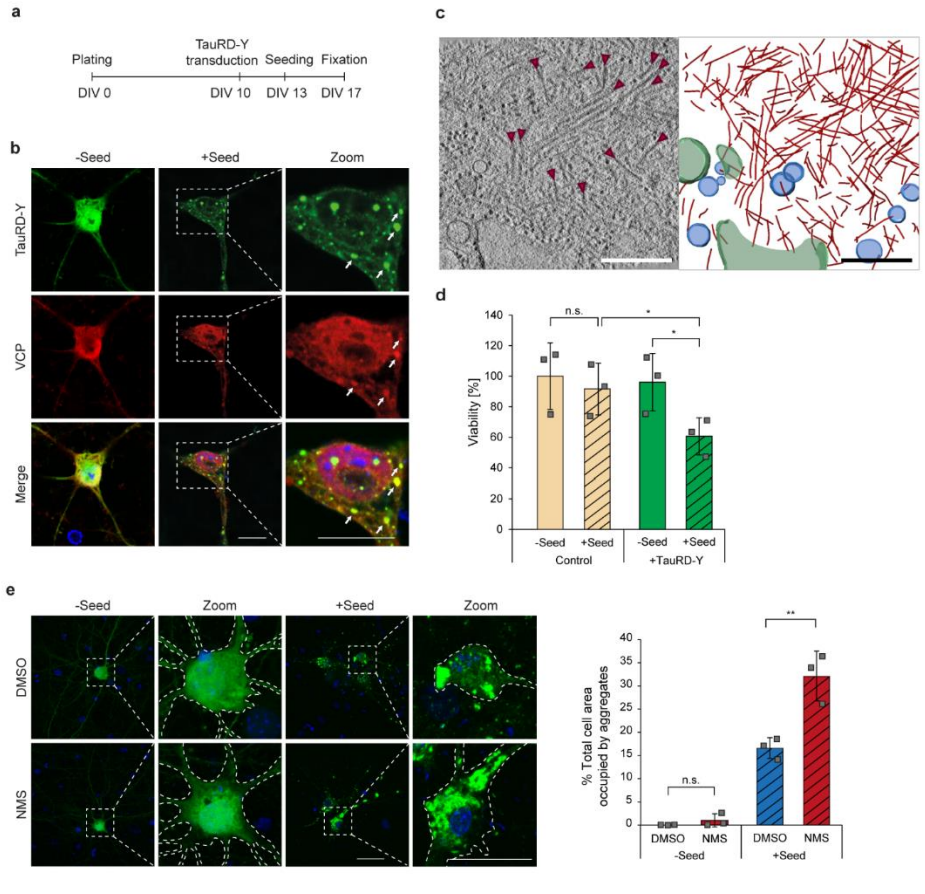

Fig. 3 Disaggregation of TauRD-Y aggregates in primary neurons is dependent on VCP activity. a Schematic representation of experimental timeline in primary neurons. DIV, days in vitro. **b** Association of VCP with TauRD-Y inclusions in primary neurons. Immunofluorescence staining of VCP (red) and YFP fluorescence of TauRD-Y (green). Arrows point to TauRD-Y inclusions containing VCP. Scale bars, 10 µm. **c** Fibrillar TauRD-Y aggregates in primary neurons. Left, a 1.4 nm thick tomographic slice of a TauRD inclusion from neurons is shown.

Red arrows indicate TauRD-Y fibrils. Right, 3D rendering of corresponding tomogram showing TauRD-Y fibrils (red), vesicles (blue) and ER (green). Scale bar, 350 nm. **d** Toxicity of TauRD-Y aggregation in primary neurons. Untransduced neurons or neurons transduced with TauRD-Y were treated with cell lysates containing TauRD-Y aggregates for 4 days where indicated. Viability was measured using an MTT assay. Mean ± s.d.; n=3; *p<0.05 (Control + Seed vs TauRD-Y + Seed, p=0.0184; TauRD-Y - Seed vs TauRD-Y + Seed, p=0.142); n.s. non-significant (Control - Seed vs Control + Seed, p=0.2074) from two-way ANOVA with Tukey post hoc test. **e** Left, representative images of primary neurons expressing TauRD-Y, exposed to cell lysates containing TauRD-Y aggregates and treated for 4 h with NMS-873 (NMS; 0.5 µM) where indicated. Scale bars, 20 µm. Right, quantification of area occupied by TauRD-Y aggregates as a percentage of total area of cells. Mean ± s.d.; n=3; **p<0.01 (+ Seed + DMSO vs + Seed + NMS, p=0.0098); n.s. non-significant (- Seed + DMSO vs - Seed + NMS, p=0.2998) from unpaired t test.

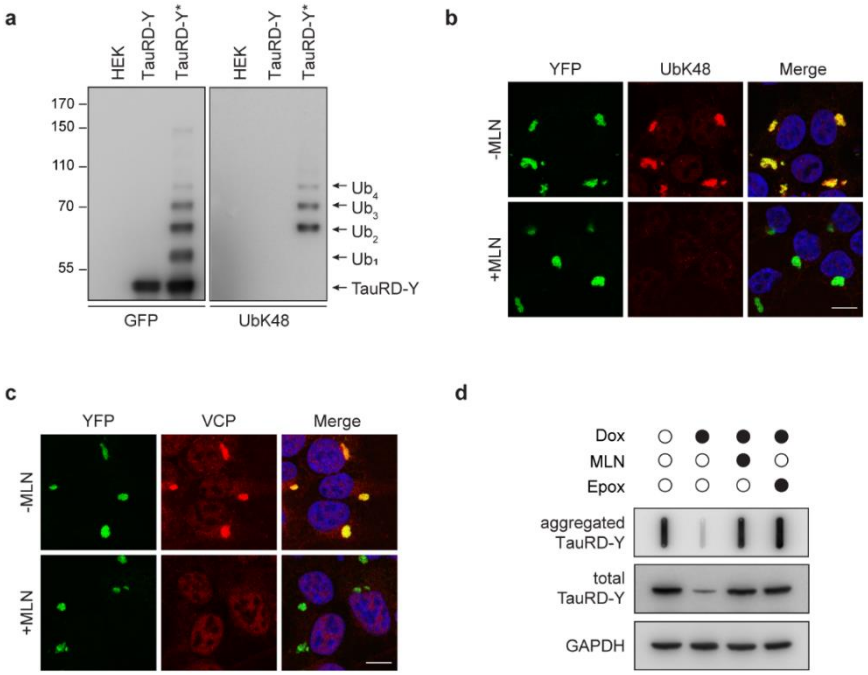

Fig. 4 Ubiquitination is necessary for VCP recruitment and disaggregation.

a Immunoprecipitation of TauRD-Y from lysates of control HEK cells, TauRD-Y and TauRD-Y* cells in the presence of 0.1% SDS using anti-GFP beads. Eluates were analyzed by immunoblotting with antibodies against GFP and K48-linked ubiquitin chains (UbK48). The TauRD-Y band shows the unmodified protein and arrowheads point at increments in ubiquitin conjugation (Ub_1-Ub_4). **b** Inhibition of ubiquitylation of TauRD inclusions. TauRD-Y* cells were treated for 12 h with MLN7243 (MLN; 0.5 µM) followed by immunofluorescence analysis with a UbK48 antibody (red). **c** Inhibition of TauRD ubiquitylation prevents VCP association. TauRD-Y* cells were treated as in (b). VCP (red) was visualized by immunofluorescence. Scale bars: 10 µm. **d** Filter trap analysis of lysates from Tet-TauRD-Y* cells treated for 24 h with 50

435 ng/mL doxycycline alone or in combination with 0.2 µM MLN7243 or 50 nM Epoxomicin.

436 Aggregated and total TauRD-Y levels were determined by immunoblotting against GFP.

437 GAPDH served as loading control.

438

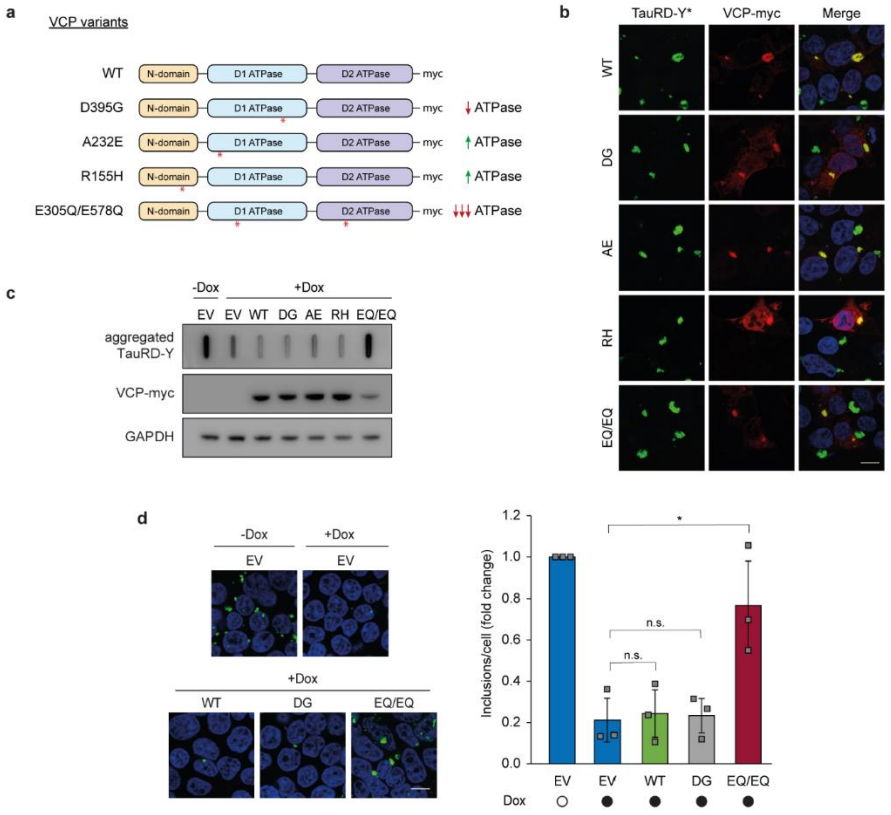

439 **Fig. 5 Effects of VCP mutants on Tau disaggregation.** **a** Schematic representation of VCP
440 variants used in this study. Wild type (WT), D395G (DG), A232E (AE), R155H (RH) and
441 E305Q/E578Q (EQ/EQ) VCP were tagged with a C-terminal myc-tag. Red asterisks indicate
442 relative positions of the mutations. **b** Association of transiently expressed VCP variants with
443 TauRD-Y inclusions. Immunofluorescence staining of myc (red) and YFP fluorescence of
444 TauRD-Y (green) in TauRD-Y* cells. Scale bar, 10 µm. **c** Filter trap analysis of lysates from

445 Tet-TauRD-Y* cells transiently transfected with empty vector (EV) or indicated VCP variants
446 for 24 h, and treated for another 24 h with doxycycline (Dox; 50 ng/mL). Aggregated TauRD-Y
447 and overexpressed VCP levels were determined by immunoblotting against GFP and myc,
448 respectively. GAPDH served as loading control. **d** Left, representative images of Tet-TauRD-Y*
449 cells treated as in (c). Scale bar, 10 µm. Right, quantification of aggregate foci in (d). Mean ±
450 s.d.; n=3; > 400 cells analyzed per experiment; *p<0.05 (EV + Dox vs EQ/EQ + Dox, p=
451 0.0209); n.s. non-significant (EV + Dox vs WT + Dox, p= 0.5017; EV + Dox vs DG + Dox, p=
452 0.7172) from two-tailed Student's paired t-test.

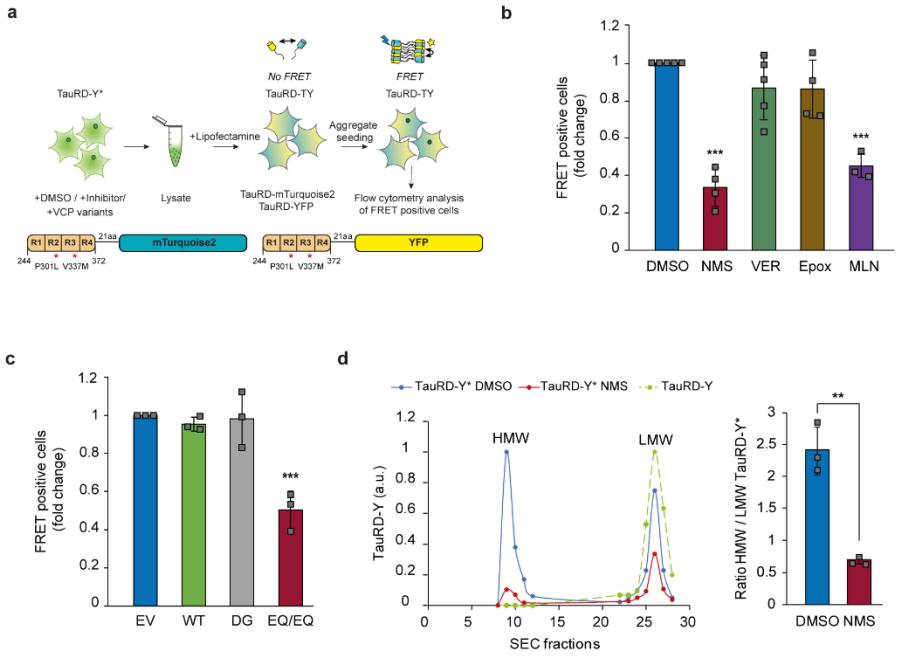

453 **Fig. 6 VCP-mediated disaggregation generates seeding-competent TauRD-Y species.**

454 **a** Experimental scheme to assess the effects of inhibitors of VCP, Hsp70, proteasome and
455 ubiquitylation on the level of TauRD-Y aggregate seeds in TauRD-Y* cells. **b** Flow cytometry
456 analysis of aggregate seeding in TauRD-TY reporter cells after addition of lysates from TauRD-
457 Y* cells treated with NMS (VCP inhibitor), VER (Hsp70 inhibitor), Epox (proteasome inhibitor)
458 and MLN (ubiquitylation inhibitor). Fold changes with respect to DMSO treated cells are shown.
459 Mean ± s.d.; NMS and Epox n=4, VER n=5, MLN n=3; ***p<0.001 (DMSO vs NMS, p=8.69 x
460 10^{-7}; DMSO vs MLN, p=4.2 x 10^{-5}) from one-way ANOVA with Tukey post hoc test. **c** Flow
461 cytometry analysis of aggregate seeding in TauRD-TY reporter cells after addition of lysates
462 from TauRD-Y* cells transfected with empty vector (EV), wild-type (WT), D395G (DG) and

463 ATPase deficient E305Q/E578Q (EQ/EQ) VCP constructs. Fold changes with respect to EV
464 transfected cells are shown. Mean ± s.d. n=3; ***p<0.001 (EV vs EQ/EQ, p= 0.0007) from one-
465 way ANOVA with Tukey post hoc test. **d** Left, fractionation of TauRD-Y from DMSO and
466 NMS-873 treated lysates of TauRD-Y* cells by size exclusion chromatography (SEC). Equal
467 amounts of total lysate protein were analyzed. Y-axis represents the relative amount of TauRD-Y
468 in the high molecular weight (HMW) and the low molecular weight (LMW) fractions quantified
469 by immunoblotting. Right, ratio of TauRD-Y in HMW/LMW fractions. Mean ± s.d.; n=3.
470 **p<0.01 (p= 0.002) from two-tailed Student's paired t-test.

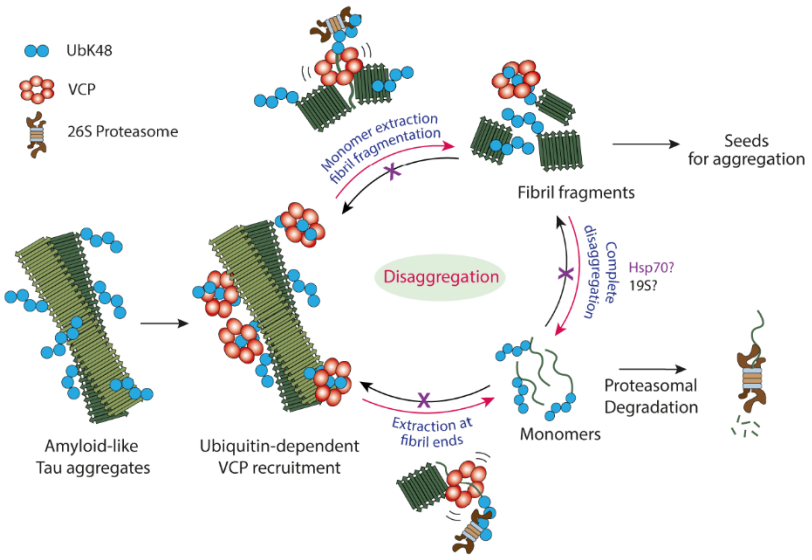

Fig. 7 Model of VCP-mediated disaggregation of amyloid-like Tau aggregates. Modification of aggregates with K48-linked ubiquitin chains allows recruitment of VCP. VCP may extract ubiquitylated Tau monomer from fibril ends or from within fibrils. Monomers are directly targeted for proteasomal degradation. Extraction from internal sites results in fibril fragmentation and generation of oligomers that act as seeds for aggregation. Completion of oligomer disaggregation may be accomplished by the 19S proteasome, perhaps with participation of the Hsp70 system (purple). Hsp70 may also contribute to aggregate clearance by preventing re-aggregation of disaggregation products.

Methods

Plasmids

The N1-TauRD (P301L/V337M)-EYFP and N1-FLTau (0N4R, P301L/V337M)-EYFP constructs were previously described[37,62]. To generate TauRD (P301L/V337M) and FLTau (0N4R, P301L/V337M) without fluorescent tag, a stop codon was introduced in the N1-TauRD (P301L/V337M)-EYFP and N1-FLTau (0N4R, P301L/V337M)-EYFP plasmids after the Tau sequence using the Q5 site directed mutagenesis (SDM) kit (New England Biolabs). Tau fragments were subcloned into pcDNA3.1 by restriction digestion and further into pCW57.1-MAT2A all-in-one tet-off lentiviral backbone (a gift from David Sabatini (Addgene plasmid # 100521))[71] by Gibson assembly. TauRD (P301L/V337M) construct contains a C-terminal myc-tag separated from TauRD by a 4 aa (GGSG) linker.

Wild type (WT) VCP (Addgene #23971), A232E VCP (Addgene #23973), R155H VCP (Addgene #23972) and E305Q/E578Q VCP (Addgene #23974) sequences were derived from plasmids described previously[34]. A C-terminal myc tag and stop codon was introduced using SDM followed by subcloning the VCP-myc fragments into pcDNA3.1. The D395G VCP construct was generated by introducing the D395G mutation in WT-VCP plasmid by SDM. All mutations were verified by sequencing. The plasmid expressing wild type firefly luciferase fused to EGFP (Fluc-GFP) was previously described[56].

Lentiviral packaging plasmid pVsVg was a gift from Dieter Edbauer. psPAX2 (Addgene #12260) and pMD2.G (Addgene #12259) also used for lentiviral production were gifts from Didier Trono. pFhSynW2 TauRD (P301L/V337M)-EYFP used for TauRD-EYFP expression in mouse primary neurons was previously described[62].

Cell lines and cell culture

Cells expressing constitutive and tet-regulated TauRD-Y (TauRD-Y and Tet-TauRD-Y cell lines, respectively), FRET biosensor TauRD-TY, and FLTau-Y cells were previously described[37,62]. Tet-FLTau and Tet-TauRD cell lines were generated by transducing HEK293T cells with 200 µL concentrated lentivirus in presence of 0.8 µg/mL Polybrene (Sigma). Transduced cells were selected with 10 µg/mL Blasticidin (Thermo) and thereafter sorted in 96 well-plates with a BD FACS Aria III (BD Biosciences) (Imaging Facility, MPI Biochemistry). Monoclonal cell lines stably expressing FLTau and TauRD were screened by immunofluorescence staining and immunoblotting followed by amplification.

All cell lines were cultured in Dulbecco's Modified Eagle Medium (Biochrom) supplemented with 10% FBS (Gibco), 2 mM L-glutamine (Gibco), 100 units/mL penicillin and 100 µg/mL streptomycin (Gibco), and non-essential amino acid cocktail (NEAA) (Gibco) and grown at 37 °C at 5% CO_2. TauRD-TY and FLTau-Y cells were maintained in presence of 200 µg/mL G418 (Gibco). HEK293 cells stably expressing Fluc-GFP were maintained in presence of 50 µg/mL hygromycin (Thermo).

Generation of cell lines propagating Tau aggregates

Tau aggregation was induced by addition of TauRD aggregates as described previously[37]. Briefly, HEK293 cells expressing TauRD-Y were initially treated with fibrillar aggregates generated in vitro from purified TauRD and clones that displayed the ability to maintain TauRD-Y aggregates for multiple passages were selected. Aggregate-containing TauRD-Y* cells were lysed in Triton buffer (0.05% Triton X-100/PBS (Gibco) supplemented with protease inhibitor cocktail (Roche, EDTA-free) and benzonase (prepared in-house)) and kept on ice for 20 min.

Cell lysate was centrifuged at 1,000 x g for 5 min and the supernatant was collected. Protein concentration in cell lysates was determined using Bradford assay (Bio-Rad). 30 µg of freshly prepared lysate was diluted in 100 µL Opti-MEM Reduced Serum Medium (Gibco). In a separate tube 4 µL Lipofectamine 2000 was diluted in 100 µL Opti-MEM and incubated at room temperature (RT) for 5 min. Contents of the tubes were gently mixed and incubated at RT for 20 min. The lysate-lipofectamine mixture was applied to naïve cells expressing soluble TauRD-Y, plated at 150,000 cells/well in a 12-well plate. 24 h later, cells were transferred to a 6-well plate and 3 days later to 10 cm dishes (<200 cells per dish) for 8 days, until clearly visible colonies were observed. Colonies were screened for the presence of YFP positive aggregates with an Axio Observer fluorescent microscope (Zeiss). Monoclonal cells displaying aggregate morphology similar to parental cells were amplified and frozen until use. TauRD, FLTau and FLTau-Y expressing cells were similarly seeded with cellular TauRD aggregates[37] and cultured for several days before experiments were performed with a polyclonal cell population.

Lentivirus production

For primary neuron transduction: HEK293T cells (LentiX 293T cell line, Takara) for lentiviral packaging were expanded to 70-85% confluency in DMEM Glutamax (+4.5 g/L D-glucose, -pyruvate) supplemented with 10% FBS (Sigma), 1% G418 (Gibco), 1% NEAA (Thermo Fisher) and 1% HEPES (Biomol). Only low passage cells were used. For lentiviral production, a three-layered 525 cm^2 flask (Falcon) was seeded and cells were henceforth cultured in medium without G418. On the following day, cells were transfected with the expression plasmid pFhSynW2 (TauRD-Y), the packaging plasmid psPAX2 and the envelope plasmid pVsVg using TransIT-Lenti transfection reagent (Mirus). The transfection mix was incubated for 20 min at RT. The

cell medium was exchanged in the meantime. 10 mL of transfection mix was added to the flask, followed by incubation overnight. The medium was exchanged on the following day. After 48-52 h, culture medium containing the viral particles was collected and centrifuged for 10 min at 1,200 x g. The supernatant was filtered through 0.45 µm pore size filters using 50 mL syringes, and Lenti-X concentrator (Takara) was added. After an overnight incubation at 4 °C, samples were centrifuged at 1,500 x g for 45 min at 4 °C, the supernatant was removed and the lentivirus pellet was resuspended in 150 µL TBS-5 buffer (50 mM Tris-HCl pH 7.8, 130 mM NaCl, 10 mM KCl, 5 mM $MgCl_2$). After aliquoting, lentivirus was stored at -80 °C.

For HEK293T transduction: HEK293T cells (LentiX 293T cell line, Takara) were transfected in 10 cm dishes with packaging plasmid psPAX2, envelope plasmid pMD2.G and expression plasmids (pCW Tet-off FLTau and TauRD) using Lipofectamine 3000. 48 h later virus-containing media was harvested and centrifuged for 5 min at 1,000 x g. Lenti-X concentrator was added to supernatant, incubated overnight at 4 °C and the following day centrifuged for 45 min at 1,500 x g at 4 °C. The lentiviral pellet was resuspended in 1 mL PBS, aliquoted and stored at -80 °C.

Primary neuronal cultures

Primary cortical neurons were prepared from E15.5 CD-1 wild type mouse embryos. All experiments involving mice were performed in accordance with the relevant guidelines and regulations. Pregnant female mice were sacrificed by cervical dislocation. The uterus was removed from the abdominal cavity and placed into a 10 cm sterile Petri dish on ice containing dissection medium, consisting of Hanks' balanced salt solution (HBSS) supplemented with 0.01 M HEPES, 0.01 M $MgSO_4$ and 1% penicillin/streptomycin. Each embryo was isolated,

573 heads were quickly cut, and brains were removed from the skull and immersed in ice-cold
574 dissection medium. Cortical hemispheres were dissected, and meninges were removed. The
575 cortices were collected in a 15 mL sterile tube and digested with 0.25% trypsin containing 1 mM
576 ethylenediaminetetraacetic acid (EDTA) and 15 µL 0.1% DNAse I for 20 min at 37 °C. The
577 digestion was stopped by removing the supernatant and washing the tissue twice with
578 Neurobasal medium (Invitrogen) containing 5% FBS. The tissue was resuspended in 2 mL
579 Neurobasal medium and triturated to achieve a single cell suspension. Cells were spun at 130 x
580 g, the supernatant was removed, and the cell pellet was resuspended in Neurobasal medium with
581 2% B-27 supplement (Invitrogen), 1% L-glutamine (Invitrogen) and 1% penicillin/streptomycin
582 (Invitrogen). For immunofluorescence microscopy, neurons were cultured in 24-well plates on
583 13 mm coverslips coated with 1 mg/mL poly-D-lysine (Sigma) and 1 µg/mL laminin (Thermo
584 Fisher Scientific) (100,000 neurons per well). For biochemical assays, neurons were cultured in
585 12-well plates coated in the same way (200,000 neurons per well). For viability measurements,
586 neurons were cultured in 96-well plates coated in the same way (18,000 neurons per well).
587 Lentiviral transduction was performed at 10 days in vitro (DIV 10). Virus preparation was
588 thawed and immediately added to freshly prepared neuronal culture medium. Neurons in 24-well
589 plates received 1 µL of virus per well. Neurons in 12-well plates received 1.5 µL of virus per
590 well. Neurons in 96-well plates received 0.15 µL of virus per well. A fifth of the medium from
591 cultured neurons was removed and the equivalent volume of virus-containing medium was
592 added. Three days after transduction (DIV 13), 2, 6 or 12 µg of HEK293 cell lysate containing
593 TauRD-Y aggregates, mixed with fresh medium (one tenth of medium volume in the well), were
594 added to the neuronal cultures in 96, 24 or 12-well plates, respectively. HEK293 cell lysate for

595 neurons was prepared by brief sonication of aggregate-containing cells in PBS. Six days after
596 transduction (DIV 16), neurons were treated with inhibitor or DMSO as control.
597
598 Neuronal viability assay
599 Viability of transduced neurons was determined using Thiazolyl Blue Tetrazolium Bromide
600 (MTT; Sigma-Aldrich). Seven days after transduction (DIV 17), cell medium was exchanged for
601 100 µL of fresh medium, followed by addition of 20 µL of 5 mg/ml MTT/PBS and incubation
602 for 4 h at 37 °C, 5% CO_2. Subsequently, 100 µL solubilizer solution (10% SDS, 45%
603 dimethylformamide in water, pH 4.5) was added, and on the following day absorbance was
604 measured at 570 nm. Each condition was measured in triplicates per experiment and absorbance
605 values were averaged for each experiment. The individual values for the 'Control-Seed'
606 condition obtained for each of the three experiments were normalized by the mean of these
607 values. The values of all other conditions were normalized by the new value of the 'Control-
608 Seed' condition of the corresponding independent experiment.
609
610 Plasmid and siRNA transfection
611 Plasmids were transfected with Lipofectamine 2000 (Thermo) after manufacturer's instructions
612 in 12- or 6-well plates using 2 or 4 µg DNA. All siRNAs were obtained from Dharmacon as ON-
613 TARGETplus SMART pools: VCP (L-008727-00-0005), Atg5 (M-004374-04-0005), Atg7 (L-
614 020112-00-0005), PSMD11 (L-011367-01-0005), non-targeting control (D-001810-03-20). Cells
615 were plated in 24-well plates in 500 µL antibiotic free DMEM. 2 µL of Dharmafect transfection
616 reagent and 50-100 nM of siRNA were diluted each in 50 µL Opti-MEM and incubated at RT for
617 5 min. Contents of the tubes were mixed gently by pipetting and incubated further at RT for 15

min. Subsequently, the transfection mixture was added to the cells drop-wise. 24 h later cells were split and plated in 12- or 6-well plates and allowed to grow for up to 96 h before immunoblotting or immunofluorescent staining.

Antibodies and chemicals

The following primary antibodies were used for immunoblotting or immunofluorescent staining: anti-VCP (AbCam #ab11433), anti-VCP (Novus Biologicals #NB100-1558) (Fig. 2e and Supplementary Fig. 9a), anti-GFP (Roche #11814460001), anti-ubiquitin Lys48-specific (Millipore #05-1307), anti-ubiquitin Lys63-specific (AbCam #ab179434), anti-ubiquitin (P4D1) (SantaCruz #sc-8017), anti-Tau (pS356) (GeneTex #GTX50165), anti-phospho-Tau (S202, T205) (Thermo #MN1020), anti-NPLOC4 (Sigma #HPA021560), anti-UFD1L (AbCam #ab96648), anti-ubiquitin FK2 (Millipore #04-263), anti-Tau (Tau-5) (Thermo #MA5-12808), anti-human Tau/Repeat Domain (2B11) (IBL #JP10237), anti-LC3B (Sigma #L7543), anti-Atg5 (Cell Signalling #2630S), anti-Atg7 (Cell Signalling #8558), anti-PSMD11 (Proteintech #14786-1-AP), anti-myc (in house, 9E10), anti-GAPDH (Millipore #MAB374), anti-Tubulin (Sigma #T6199).

The following secondary antibodies were used: Cy5-conjugated anti-mouse (Thermo #A10524), Cy-5 conjugated anti-rabbit (Thermo #A10523), Alexa Fluor 647 AffiniPure anti-mouse (Jackson ImmunoResearch #715-605-151), DyLight 488 anti-mouse (Thermo #SA5-10166), anti-mouse IgG peroxidase conjugate (Sigma #A4416) or anti-rabbit peroxidase conjugate (Sigma #A9169), IRDye 680RD anti-mouse (LI-COR #926-68070), IRDye 800CW anti-rabbit (LI-COR #926-32211).

The following chemicals were used: Cycloheximide (Sigma), doxycycline (Sigma), 3-methyladenine (Invivogen), bafilomycin A1 (Invivogen), epoxomicin (Cayman Chemical), NMS-873 (Sigma), CB-5083 (Cayman Chemical), VER-155008 (Sigma), MLN7243 (Chemietek). Solutions in DMSO were stored at -20 °C. 3-Methyadenine was dissolved in H_2O after manufacturer's instructions and applied immediately to cells.

Immunofluorescence staining

HEK293 cells were grown on poly-L-lysine (NeuVitro) coated glass coverslips for 24-48 h in 12-well plates before any treatment. At the end of the experiment, media was aspirated and cells were directly fixed in 4% formaldehyde (w/v) (Thermo, Methanol-free) in PBS for 10 min at RT, washed once with PBS and permeabilized in 0.1% Triton X-100/PBS for 5 min. Samples were blocked using 5% low-fat dry milk dissolved in 0.1% Triton X-100/PBS for 1 h at RT, followed by incubation with primary antibodies in blocking solution and fluorescently labelled secondary antibodies in PBS. Nuclei were counterstained with DAPI. For amyloid staining, after fixation and permeabilization, cells were incubated with Amylo-Glo (Biosensis TR-300-AG) at a dilution of 1:200/PBS with gentle shaking followed by washing twice with PBS. Cells were not counterstained with DAPI. Coverslips were mounted in fluorescent mounting medium (Dako) on glass slides and stored at 4 °C until imaging.

Primary neurons: Primary neurons were fixed at DIV 17 with 4% paraformaldehyde (Santa Cruz) (PFA)/PBS for 15 min; remaining free aldehyde groups of PFA were blocked with 50 mM ammonium chloride/PBS for 10 min at RT. Cells were rinsed once with PBS and permeabilized with 0.25% Triton X-100/PBS for 5 min. After washing with PBS, blocking solution consisting of 2% BSA (w/v) (Roth) and 4% donkey serum (v/v) (Jackson

663 ImmunoResearch Laboratories) in PBS was added for 30 min at RT. Coverslips were transferred
664 to a light protected humid chamber and incubated with primary antibodies diluted in blocking
665 solution for 1 h. Cells were washed with PBS and incubated with secondary antibody diluted in
666 blocking solution for 30 min and counterstained with DAPI. Coverslips were mounted using
667 Prolong Glass fluorescence mounting medium (Invitrogen).
668
669 Image acquisition (Microscopy)
670 Images were acquired with a Zeiss LSM 780, Leica SP8 FALCON (Imaging Facility, MPI
671 Biochemistry) or a Leica TCS SP8 Laser-scanning confocal microscope (Imaging Facility, MPI
672 Neurobiology) and analyzed using FIJI/ImageJ software. For multifluorescent imaging, samples
673 stained with individual fluorophores were used to correct emission bandwidths and exposure
674 settings to minimize spectral crossover.
675
676 Quantification of aggregates/cell and average size
677 Confocal z-stacks were used to create a maximum intensity projection (MIP) using the image
678 acquisition software ZEN (Zeiss). MIPs were further segmented to define aggregate foci by
679 thresholding. Aggregate number and size were computed by the Analyze Particle function (Size:
680 0-infinity). Cell numbers were determined by counting DAPI stained nuclei with the Cell
681 Counter plugin. Experiments were performed at least 3 times in biologically independent repeats.
682 For neuronal aggregates, neuronal cytoplasm area was calculated by manually selecting a region
683 of interest (ROI) around the soma of the neuron and utilizing the Analyze feature. Aggregate foci
684 were identified by thresholding the MIP images and aggregate size (area), within the previously
685 selected ROI, was calculated by the Analyze Particle function. The percentage of total neuron

686 area occupied by aggregate was the quotient of the division between aggregate area and neuronal
687 cytoplasmic area: (Aggregate area)/(Cytoplasm area) x 100. 60 individual neurons were imaged
688 per condition, in 3 biologically independent replicates.
689
690 mRNA quantification
691 Total RNA was isolated using the RNeasy Mini Kit (Qiagen) and reverse transcribed with
692 iScript™ cDNA Synthesis Kit (Biorad) according to manufacturers' instructions. Quantitative
693 real-time PCR was performed with PowerUp™ SYBR™ Green Master Mix (Applied
694 Biosystems) with a StepOnePlus Real-Time PCR System (Applied Biosystems). CT values were
695 measured and fold changes calculated by the ΔΔC(T) method[72] using the RPS18 gene as
696 reference. The following primers were used: RPS18 forward 5'-
697 TGTGGTGTTGAGGAAAGCA-3' and reverse 5'- CTTCAGTCGCTCCAGGTCTT-3'; Tau
698 forward: 5'-AGCAACGTCCAGTCCAAGTG-3' and reverse: 5'-
699 CCTTGCTCAGGTCAACTGGT-3'.
700
701 Correlative light and electron microscopy (CLEM), cryo-focused ion beam (FIB) and cryo-
702 Electron Tomography
703 2 x 10^4 TauRD-Y* cells or 1 x 10^5 neurons were seeded on EM grids (R2/1, Au 200 mesh grid,
704 Quantifoil Micro Tools) in a 35 mm dish or 24-well plate and cultured for 24 h or transduced
705 with lentivirus and treated with aggregate-containing cell lysate as described earlier in section
706 'Primary neuronal cultures'. The grids were blotted for 10 s using filter paper and vitrified by
707 plunge freezing into a liquid ethane/propane mixture with a manual plunger. CLEM, cryo-FIB
708 and tomographic data collection were performed as described in detail before[73]. In brief, EM

grids were mounted onto modified Autogrid sample carriers[74] and then transferred onto the cryo-stage of a CorrSight microscope (FEI) for cryo-light microscopy. Images of the samples and TauRD-Y signal were acquired with MAPS software (FEI) in transmitted light and confocal mode using a 5x and 20x lens, respectively. The samples were then transferred into a dual-beam (FIB/SEM) microscope (Quanta 3D FEG, FEI) using a cryo-transfer system (PP3000T, Quorum). Cryo-light microscope and SEM images were correlated with MAPS software. Lamellas (final thickness, 100-200 nm) were prepared using a Ga^{2+} ion beam at 30 kV in the regions of the TauRD-Y fluorescence signal. In case of TauRD-Y* cells, an additional layer of platinum was sputter-coated (10 mA, 5 s) on the grids to improve conductivity of the lamellas.

The grids were then transferred to a Titan Krios transmission electron microscope (FEI) for tomographic data collection. For the whole procedure, samples were kept at a constant temperature of -180 °C. Tomographic tilt series were recorded with a Gatan K2 Summit direct detector in counting mode. A GIF-quantum energy filter was used with a slit width of 20 eV to remove inelastically scattered electrons. Tilt series were collected from -50° to +70° with an increment of 2° and total dose of 110 $e^-/Å^2$ using SerialEM software[75] at a nominal magnification of 33,000x, resulting in a pixel size of 4.21 Å for TauRD-Y* cells and at a nominal magnification of 42,000x, resulting in a pixel size of 3.52 Å for the primary neurons. In case of TauRD-Y* cells, a Volta phase plate was used together with a defocus of -0.5 µm for contrast improvement[76].

For image processing of TauRD-Y* cell tomograms, frames were aligned during data collection using in-house software K2align based on previous work[77] or in case of the primary neuron tomograms by using the software Morioncor2 and Tomoman (https://github.com/williamnwan/TOMOMAN). The IMOD software package[78] was used for

732 tomogram reconstruction. The tilt series were first aligned using fiducial-less patch tracking, and
733 tomograms were then reconstructed by weighted back projection of the resulting aligned images.
734 For segmentation, tomograms were rescaled with a binning factor of four and in case of
735 the primary neurons tomograms filtered with a deconvolution filter
736 (https://github.com/dtegunov/tom_deconv). Tau filaments were traced with XTracing Module in
737 Amira using a short cylinder as a template[79]. The membranes were first segmented automatically
738 with TomoSegMemTV[80] using tensor voting, and then manually optimized in Amira.
739
740 Immunoblotting
741 Cells were lysed in RIPA lysis and extraction buffer (Thermo) supplemented with protease
742 inhibitor cocktail and benzonase for 30 min on ice with intermittent vortexing. Protein
743 concentration in total cell lysates was determined using Bradford assay (Bio-Rad) and
744 normalized in all samples before adding 2x SDS sample buffer. Samples were denatured by
745 boiling at 95 °C for 5 min. Proteins were resolved on NuPAGE 4-12% gradient gels (Thermo)
746 with MES or MOPS (Thermo) running buffer at 200 V for 45 min. Proteins were transferred to
747 nitrocellulose or PVDF membranes (Roche) in tris-glycine buffer at 110 V for 1 h. Membranes
748 were washed once in TBS-T and blocked in 5% low-fat dry milk dissolved in TBS-T for 1 h at
749 RT. Subsequently, blots were washed 3 times with TBS-T and probed with primary and
750 secondary antibodies. Chemiluminescence was developed using HRP substrate (Luminata
751 Classico, Merk) and detected on a LAS 4000 (Fuji) or ImageQuant800 (Amersham) imager.
752 AIDA image software (Elysia Raytest) was used to quantify intensity of protein bands.
753

Interactome analysis by mass spectrometry

SILAC labelling of cells and TauRD-Y immunoprecipitation: Interactome analyses were performed using a stable isotope labelling by amino acids in cell culture (SILAC)-based quantitative proteomics approach[81]. Frozen TauRD-Y and TauRD-Y* cells were thawed in arginine lysine deficient SILAC media (PAA) containing light (L) (Arg_0, Lys_0, Sigma) and heavy (H) (Arg_{10}, Lys_8, Silantes) amino acid isotopes, respectively, and supplemented with 10% dialyzed FCS (PAA), 2 mM L-glutamine (Gibco), 100 units/mL penicillin and 100 µg/mL streptomycin (Gibco), and non-essential amino acid cocktail (Gibco). A third cell line, not part of this study but included in the PRIDE entry PXD023400, was simultaneously expanded in SILAC medium supplemented with medium (M) (Arg_6, Lys_4, Silantes) amino acid isotopes, and was processed and analyzed together with TauRD-Y and TauRD-Y* samples. Cells were passaged for a minimum of two weeks to allow efficient incorporation of amino acid isotopes into the cellular proteome. Cells from a 10 cm dish were washed in PBS, lysed by gentle pipetting in 400 µL ice cold lysis buffer (1% Triton X-100/PBS supplemented with protease inhibitor cocktail and benzonase). Lysates were sonicated briefly and centrifuged at 2,000 x g for 5 min at 4 °C. 300 µL of the supernatant was removed and protein concentration was determined using Bradford assay (Bio-Rad). 50 µL anti-GFP beads (µMACS GFP Isolation kit, Miltenyi Biotech) were added to 500 µg total protein diluted in a total volume of 800 µL lysis buffer. Lysates were incubated for 1 h at 4 °C with end over end rotation at 10 rpm. µ-Columns (Miltenyi Biotech) were placed in the magnetic field of a µMACS Separator (Miltenyi Biotech) and equilibrated with 250 µL lysis buffer before lysates were applied. Columns were washed 4 times with 1 mL cold Triton buffer and 2 times with 1 mL PBS followed by elution in 70 µL preheated 1x SDS sample buffer without bromophenol blue.

MS sample processing: 20 µL sample from each of the H, M and L eluates was mixed and processed by the filter-aided sample preparation (FASP) method as previously described[82]. Samples were loaded in a 30 kDa centrifugation device and washed 3 times with 200 µL freshly prepared urea buffer (UB) (8 M urea, 0.1 M Tris pH 8.5). Reduction and alkylation was performed sequentially using 10 mM DTT and 50 mM iodoacetamide in UB, respectively. Samples were washed 2 times with 200 µL 50 mM ammonium bicarbonate (NH_4HCO_3) to remove urea before an over-night trypsin treatment. Peptides were recovered in 40 µL NH_4HCO_3, acidified with 12 µL of a 25% TFA solution and dried in a vacuum concentrator. The peptides were further fractionated using home-made SAX columns in 200 µL microtips by stacking 2 punch-outs of Empore High Performance Extraction Disk (Anion-SR) material. Peptides were sequentially eluted with 6 different Britton & Robinson buffers (BURB) of decreasing pH (pH 11, 8, 6, 5, 4, 3) and acidified to 1% TFA. The last elution step was with MeOH/water (1:1)/1% formic acid. The fractionated peptides were desalted with home-made micro-columns containing C18 Empore disks and eluted with 70% ACN 1% formic acid followed by drying in a vacuum concentrator. The samples were stored at -20 °C until analysis.

LC-MS: The desalted peptides were dissolved in 5 µL of 5% formic acid, sonicated in an ultrasonic bath, centrifuged and transferred to MS autosampler vials. Samples were analyzed on an Easy nLC-1000 nanoHPLC system (Thermo) coupled to a Q-Exactive Orbitrap mass spectrometer (Thermo). Peptides were separated on home-made spray-columns (ID 75 µm, 20 cm long, 8 µm tip opening, NewObjective) packed with 1.9 µm C18 particles (Reprosil-Pur C18-AQ, Dr Maisch GmbH) using a stepwise 115 min gradient between buffer A (0.2% formic acid in water) and buffer B (0.2% formic acid in acetonitrile). Samples were loaded on the column by the nanoHPLC autosampler at a flow rate of 0.5 µL per min. No trap column was used. The

HPLC flow rate was set to 0.25 µL per min during analysis. MS/MS analysis was performed with standard settings using cycles of 1 high resolution (70000 FWHM setting) MS scan followed by MS/MS scans (resolution 17500 FWHM setting) of the 10 most intense ions with charge states of 2 or higher.

MS data analysis: Protein identification and SILAC based quantitation was performed using MaxQuant (version 1.5.4.1) using default settings. The human sequences of UNIPROT (version 2019-03-12) were used as database for protein identification. MaxQuant used a decoy version of the specified UNIPROT database to adjust the false discovery rates for proteins and peptides below 1%. We used normalized MaxQuant ratios for enrichment analyses to correct for uneven total protein amounts in the SILAC-labeling states. Proteins quantified in at least 2 experiments with normalized H/L ratios ≥2 were considered as interactors of TauRD-Y in TauRD-Y* cells. Volcano plot was generated using Perseus1.6.2.3.

Biochemical detection of aggregated Tau

Cells were lysed for 30 min on ice in lysis buffer followed by brief sonication or 1 h in RIPA buffer. Lysates were centrifuged at 2,000 or 1,000 x g for 5 min. The supernatant was carefully removed and protein concentration was normalized across all samples. Lysates were then used for solubility or filter trap assays. Lysates were centrifuged at 186,000 x g for 1 h at 4 °C. Supernatant was removed and the pellet was washed with 200 µL PBS and centrifuged again for 30 min. Pellets were disintegrated in PBS by pipetting and boiled in 1x SDS sample buffer. Filter trap assays were performed with 200 µg total protein diluted in 200 µL lysis buffer. A cellulose acetate membrane (0.2 µm pore size, GE Healthcare) was pre-equilibrated in 0.1% SDS and affixed to the filter trap apparatus (PR648 Slot Blot Blotting Manifold, Hoefer). Samples were

loaded and allowed to completely pass through the filter under vacuum. Wells were washed 3 times with 200 µL 0.1% SDS/H_2O followed by standard immunoblotting of the membrane.

Detection of Tau ubiquitylation

Cells were lysed as described in section Immunoblotting, with the addition of 20 mM N-ethylmalemide followed by brief sonication and centrifugation at 2,000 x g for 5 min. Protein concentration was determined using Bradford assay (Bio-Rad). 50 µL anti-GFP beads were added to 1 mg total protein diluted in a total volume of 600 µL RIPA buffer. Lysates were incubated for 1 h at 4 °C with end over end rotation. Cell lysates were applied to µ-columns equilibrated with 250 µL RIPA buffer. Columns were washed 4 times with 1 mL 0.1% SDS/PBS. Bound proteins were eluted by applying 50 µL pre-heated (95 °C) 1x SDS sample buffer. Input and eluates were resolved on NuPAGE 4-12% gradient gels in MOPS running buffer and transferred to nitrocellulose membranes. Membranes were probed with antibodies against GFP or ubiquitin-K48.

Native-PAGE analysis

Tet-TauRD-Y* cells were plated in 12-well plates and transfected with VCP variants using Lipofectamine 2000 for 2 days. Cells were then lysed in 50 µL 0.5% TritonX-100/PBS supplemented with protease inhibitor cocktail and benzonase for 1 h on ice. Lysates were centrifuged at 10,000 x g for 2 min and supernatant was collected. Protein concentration in the supernatant was determined using Bradford assay and normalized in all samples before adding 2x native sample buffer (40 % glycerol, 240 mM Tris pH 6.8, 0.04 % bromophenol blue). Samples were analyzed on Novex Value 4 to 12% Tris-glycine gels (Thermo) using 20 mM Tris

200 mM Glycine buffer at pH 8.4. Proteins were transferred to nitrocellulose membrane in Tris-glycine buffer, blocked in 5% low-fat dry milk and co-incubated with primary followed by fluorescent secondary antibodies. Fluorescent signal was detected on an Odyssey Fc imager (LI-COR).

TauRD-Y seeding assay

TauRD-Y* cells were treated with 2 µM NMS, 10 µM VER or 50 nM epoxomicin for 24 h or 0.5 µM MLN for 12 h, or with DMSO as control and lysed on ice in Triton buffer supplemented with protease inhibitor cocktail and benzonase for 20 min. The amount of TauRD-Y across the samples was normalized by quantifying TauRD-Y by immunoblotting using anti-GFP antibody and anti-GAPDH antibody as loading control. Lysates containing equal amounts of TauRD-Y were combined with Opti-MEM and Lipofectamine 3000, incubated for 20 min at RT and added to FRET biosensor cells. 24 h later, cells were harvested with trypsin, washed with PBS and analyzed on an Attune NxT flow cytometer (Imaging Facility, MPI Biochemistry). mTurquoise2 and FRET fluorescence signals were measured by exciting cells with a 405 nm laser and collecting fluorescent signal with 440/50 and 530/30 filters, respectively. To measure the YFP fluorescence signal, cells were excited with a 488 nm laser and emission was collected with a 530/30 filter. For each sample 50,000 single cells were evaluated. Data was processed using FlowJo v10.7.1 software (FlowJo LLC). After gating single cells, an additional gate was introduced to exclude cells that generate a false-positive signal in the FRET channel due to excitation at 405 nm[83]. A FRET positive gate was drawn by plotting the FRET fluorescence signal versus the mTurquoise2 fluorescence signal using unseeded cells as reference.

Size exclusion chromatography of cell lysates

TauRD-Y* cells that had been treated for 24 h with DMSO or 2 µM NMS were analyzed. Untreated TauRD-Y cells were analyzed as control. Cells were lysed as described in the section Seeding assay. Lysates were clarified by centrifugation at 1,000 x g for 5 min at 4 °C and filtered with a PVDF 0.22 µm filter (Millex). The total protein amount of the lysates was determined by Bradford assay (Bio-Rad). 3 mg total protein was loaded on a Superose 6 HR10/30 (GE Healthcare) column equilibrated with PBS. The individual fractions separated by size exclusion chromatography were analyzed and quantified by immunoblotting using anti-GFP antibody. TauRD-Y species were detected in the void volume (HMW) and low molecular weight (LMW) fractions. Corresponding fractions were pooled and analyzed by immunoblotting using anti-GFP antibody. Seeding experiments were performed as described above, using 0.5 ng TauRD-Y from HMW and LMW fractions.

Statistical analysis

Statistical analysis was performed in Excel, Origin 2019b or GraphPad Prism 7 on data acquired from at least three independent experiments. Matched samples were compared using two-tailed Student's paired t-test. For multiple comparisons, one-way ANOVA followed by a Tukey post hoc test was used.

Data availability

All data supporting the findings of this study are included in the manuscript and the Supplemental Information, additional data that support the findings of this study are available from the corresponding author upon reasonable request. The mass spectrometry proteomics data associated to Fig. 2a have been deposited to the ProteomeXchange Consortium via the PRIDE[84]

891 partner repository (https://www.ebi.ac.uk/pride/archive/) with the dataset identifier PXD023400.

892 This PRIDE entry additionally contains analyses that are not a part of this study.

References

1 Goedert, M., Eisenberg, D. S. & Crowther, R. A. Propagation of Tau aggregates and neurodegeneration. *Annu Rev Neurosci* **40**, 189-210 (2017).

2 Strang, K. H., Golde, T. E. & Giasson, B. I. MAPT mutations, tauopathy, and mechanisms of neurodegeneration. *Laboratory Investigation* **99**, 912-928 (2019).

3 Lewis, J. *et al.* Neurofibrillary tangles, amyotrophy and progressive motor disturbance in mice expressing mutant (P301L) Tau protein. *Nat Genet* **25**, 402-405 (2000).

4 Allen, B. *et al.* Abundant Tau filaments and nonapoptotic neurodegeneration in transgenic mice expressing human P301S Tau protein. *J Neurosci* **22**, 9340-9351 (2002).

5 Jucker, M. & Walker, L. C. Propagation and spread of pathogenic protein assemblies in neurodegenerative diseases. *Nat Neurosci* **21**, 1341-1349 (2018).

6 Vaquer-Alicea, J. & Diamond, M. I. Propagation of protein aggregation in neurodegenerative diseases. *Annual review of biochemistry* **88**, 785-810 (2019).

7 DeVos, S. L. *et al.* Tau reduction prevents neuronal loss and reverses pathological Tau deposition and seeding in mice with tauopathy. *Sci Transl Med* **9**, 374 (2017).

8 Polydoro, M. *et al.* Reversal of neurofibrillary tangles and Tau-associated phenotype in the rTgTauEC model of early Alzheimer's disease. *J Neurosci* **33**, 13300-13311 (2013).

9 Doyle, S. M., Genest, O. & Wickner, S. Protein rescue from aggregates by powerful molecular chaperone machines. *Nat Rev Mol Cell Biol* **14**, 617-629 (2013).

10 Mogk, A., Bukau, B. & Kampinga, H. H. Cellular handling of protein aggregates by disaggregation machines. *Mol Cell* **69**, 214-226 (2018).

11 Nillegoda, N. B., Wentink, A. S. & Bukau, B. Protein disaggregation in multicellular organisms. *Trends Biochem Sci* **43**, 285-300 (2018).

12 Faust, O. *et al.* HSP40 proteins use class-specific regulation to drive HSP70 functional diversity. *Nature* **587**, 489-494 (2020).

13 Wentink, A. S. *et al.* Molecular dissection of amyloid disaggregation by human HSP70. *Nature* **587**, 483-488 (2020).

14 Shorter, J. The mammalian disaggregase machinery: Hsp110 synergizes with Hsp70 and Hsp40 to catalyze protein disaggregation and reactivation in a cell-free system. *PLoS One* **6**, e26319, (2011).

15 Nachman, E. *et al.* Disassembly of Tau fibrils by the human Hsp70 disaggregation machinery generates small seeding-competent species. *J Biol Chem* **295**, 9676-9690 (2020).

16 Schneider, M. M. *et al.* The Hsc70 disaggregation machinery removes monomer units directly from α-synuclein fibril ends. *Nature Communications* **12**, 5999 (2021).

17 Gao, X. *et al.* Human Hsp70 disaggregase reverses Parkinson's-linked alpha-Synuclein amyloid fibrils. *Mol Cell* **59**, 781-793 (2015).

18 Bodnar, N. O. & Rapoport, T. A. Molecular mechanism of substrate processing by the Cdc48 ATPase complex. *Cell* **169**, 722-735 (2017).

19 Ji, Z. *et al.* Translocation of polyubiquitinated protein substrates by the hexameric Cdc48 ATPase. *Mol Cell*, **82**(3), 570-584 (2021).

20 Darwich, N. F. *et al.* Autosomal dominant VCP hypomorph mutation impairs disaggregation of PHF-tau. *Science*, eaay8826 (2020).

21 Kobayashi, T., Manno, A. & Kakizuka, A. Involvement of valosin-containing protein (VCP)/p97 in the formation and clearance of abnormal protein aggregates. *Genes Cells* **12**, 889-901 (2007).

22 Gwon, Y. *et al.* Ubiquitination of G3BP1 mediates stress granule disassembly in a context-specific manner. *Science* **372**, eabf6548 (2021).

23 Buchan, J. R., Kolaitis, R.-M., Taylor, J. P. & Parker, R. Eukaryotic stress granules are cleared by autophagy and Cdc48/VCP function. *Cell* **153**, 1461-1474 (2013).

24 van den Boom, J. & Meyer, H. VCP/p97-mediated unfolding as a principle in protein homeostasis and signaling. *Mol Cell* **69**, 182-194 (2018).

25 Olszewski, M. M., Williams, C., Dong, K. C. & Martin, A. The Cdc48 unfoldase prepares well-folded protein substrates for degradation by the 26S proteasome. *Communications Biology* **2**, 29 (2019).

26 Meyer, H. & Weihl, C. C. The VCP/p97 system at a glance: connecting cellular function to disease pathogenesis. *Journal of Cell Science* **127**, 3877 (2014).

27 Johnson, J. O. *et al.* Exome sequencing reveals VCP mutations as a cause of familial ALS. *Neuron* **68**, 857-864 (2010).

28 Schroder, R. *et al.* Mutant valosin-containing protein causes a novel type of frontotemporal dementia. *Annals of neurology* **57**, 457-461 (2005).

29 Watts, G. D. *et al.* Inclusion body myopathy associated with Paget disease of bone and frontotemporal dementia is caused by mutant valosin-containing protein. *Nat Genet* **36**, 377-381 (2004).

30 Blythe, E. E., Olson, K. C., Chau, V. & Deshaies, R. J. Ubiquitin- and ATP-dependent unfoldase activity of P97/VCP*NPLOC4*UFD1L is enhanced by a mutation that causes multisystem proteinopathy. *Proc Natl Acad Sci U S A* **114**, E4380-E4388 (2017).

31 Manno, A., Noguchi, M., Fukushi, J., Motohashi, Y. & Kakizuka, A. Enhanced ATPase activities as a primary defect of mutant valosin-containing proteins that cause inclusion body myopathy associated with Paget disease of bone and frontotemporal dementia. *Genes Cells* **15**, 911-922 (2010).

32 Blythe, E. E., Gates, S. N., Deshaies, R. J. & Martin, A. Multisystem Proteinopathy mutations in VCP/p97 increase NPLOC4·UFD1L binding and substrate processing. *Structure* **27**, 1820-1829 (2019).

33 Ritz, D. *et al.* Endolysosomal sorting of ubiquitylated caveolin-1 is regulated by VCP and UBXD1 and impaired by VCP disease mutations. *Nature Cell Biology* **13**, 1116-1123 (2011).

34 Tresse, E. *et al.* VCP/p97 is essential for maturation of ubiquitin-containing autophagosomes and this function is impaired by mutations that cause IBMPFD. *Autophagy* **6**, 217-227 (2010).

35 Barghorn, S., Davies, P. & Mandelkow, E. Tau paired helical filaments from Alzheimer's disease brain and assembled in vitro are based on beta-structure in the core domain. *Biochemistry* **43**, 1694-1703 (2004).

36 Crowther, T., Goedert, M. & Wischik, C. M. The repeat region of microtubule-associated protein Tau forms part of the core of the paired helical filament of Alzheimer's disease. *Ann Med* **21**, 127-132 (1989).

37 Sanders, D. W. *et al.* Distinct Tau prion strains propagate in cells and mice and define different tauopathies. *Neuron* **82**, 1271-1288 (2014).

38 Frost, B., Ollesch, J., Wille, H. & Diamond, M. I. Conformational diversity of wild-type Tau fibrils specified by templated conformation change. *J Biol Chem* **284**, 3546-3551 (2009).

39 Schmued, L. *et al.* Introducing Amylo-Glo, a novel fluorescent amyloid specific histochemical tracer especially suited for multiple labeling and large scale quantification studies. *Journal of Neuroscience Methods* **209**, 120-126 (2012).

40 Falcon, B. *et al.* Structures of filaments from Pick's disease reveal a novel Tau protein fold. *Nature* **561**, 137-140 (2018).

41 Falcon, B. *et al.* Novel Tau filament fold in chronic traumatic encephalopathy encloses hydrophobic molecules. *Nature* **568**, 420-423 (2019).

42 Fitzpatrick, A. W. P. *et al.* Cryo-EM structures of Tau filaments from Alzheimer's disease. *Nature* **547**, 185-190 (2017).

43 Spillantini, M. G. *et al.* Familial multiple system tauopathy with presenile dementia: a disease with abundant neuronal and glial Tau filaments. *Proc Natl Acad Sci U S A* **94**, 4113-4118 (1997).

44 Zhang, W. *et al.* Novel Tau filament fold in corticobasal degeneration. *Nature* **580**, 283-287 (2020).

45 Braak, H., Thal, D. R., Ghebremedhin, E. & Del Tredici, K. Stages of the pathologic process in Alzheimer disease: age categories from 1 to 100 years. *J Neuropathol Exp Neurol* **70**, 960-969 (2011).

46 Goedert, M., Jakes, R. & Vanmechelen, E. Monoclonal antibody AT8 recognises Tau protein phosphorylated at both serine 202 and threonine 205. *Neurosci Lett* **189**, 167-169 (1995).

47 Petrucelli, L. *et al.* CHIP and Hsp70 regulate Tau ubiquitination, degradation and aggregation. *Human Molecular Genetics* **13**, 703-714 (2004).

48 Hyun, D. H., Lee, M., Halliwell, B. & Jenner, P. Proteasomal inhibition causes the formation of protein aggregates containing a wide range of proteins, including nitrated proteins. *Journal of neurochemistry* **86**, 363-373 (2003).

49 Hjerpe, R. *et al.* UBQLN2 mediates autophagy-independent protein aggregate clearance by the proteasome. *Cell* **166**, 935-949 (2016).

50 Twomey, E. C. *et al.* Substrate processing by the Cdc48 ATPase complex is initiated by ubiquitin unfolding. *Science* **365**, eaax1033 (2019).

51 Magnaghi, P. *et al.* Covalent and allosteric inhibitors of the ATPase VCP/p97 induce cancer cell death. *Nat Chem Biol* **9**, 548-556 (2013).

52 Zhou, H.-J. *et al.* Discovery of a first-in-class, potent, selective, and orally bioavailable inhibitor of the p97 AAA ATPase (CB-5083). *Journal of Medicinal Chemistry* **58**, 9480-9497 (2015).

53 Bäuerlein, F. J. B. *et al.* In situ architecture and cellular interactions of polyQ inclusions. *Cell* **171**, 179-187 (2017).

54 Trinkaus, V. A. *et al.* In situ architecture of neuronal α-Synuclein inclusions. *Nat Commun* **12**, 2110 (2021).

55 Hyer, M. L. *et al.* A small-molecule inhibitor of the ubiquitin activating enzyme for cancer treatment. *Nat Med* **24**, 186-193 (2018).

56 Gupta, R. *et al.* Firefly luciferase mutants as sensors of proteome stress. *Nat Methods* **8**, 879-884 (2011).

57 Schlecht, R. *et al.* Functional analysis of Hsp70 inhibitors. *PLoS One* **8**, e78443-e78443 (2013).

58 Forman, M. S. *et al.* Novel ubiquitin neuropathology in frontotemporal dementia with valosin-containing protein gene mutations. *J Neuropathol Exp Neurol* **65**, 571-581 (2006).

59 Weihl, C. C., Dalal, S., Pestronk, A. & Hanson, P. I. Inclusion body myopathy-associated mutations in p97/VCP impair endoplasmic reticulum-associated degradation. *Human Molecular Genetics* **15**, 189-199 (2005).

60 Dalal, S., Rosser, M. F., Cyr, D. M. & Hanson, P. I. Distinct roles for the AAA ATPases NSF and p97 in the secretory pathway. *Mol Biol Cell* **15**, 637-648 (2004).

61 Zhu, J. *et al.* VCP protects neurons from proteopathic seeding. *BioRxiv*, doi.org/10.1101/2021.07.12.452081 (2021).

62 Yuste-Checa, P. *et al.* The extracellular chaperone Clusterin enhances Tau aggregate seeding in a cellular model. *Nature Communications* **12**, 4863 (2021).

63 Erives, A. J. & Fassler, J. S. Metabolic and chaperone gene loss marks the origin of animals: evidence for Hsp104 and Hsp78 chaperones sharing mitochondrial enzymes as clients. *PLoS One* **10**, e0117192-e0117192 (2015).

64 Sontag, E. M., Samant, R. S. & Frydman, J. Mechanisms and functions of spatial protein quality control. *Annual review of biochemistry* **86**, 97-122 (2017).

65 Cliffe, R. *et al.* Filamentous aggregates are fragmented by the proteasome holoenzyme. *Cell Rep* **26**, 2140-2149 (2019).

66 Higashiyama, H. *et al.* Identification of ter94, Drosophila VCP, as a modulator of polyglutamine-induced neurodegeneration. *Cell Death Differ* **9**, 264-273 (2002).

67 Khosravi, B. *et al.* Cell-to-cell transmission of C9orf72 poly-(Gly-Ala) triggers key features of ALS/FTD. *EMBO J* **39**, e102811 (2020).

68 Jackrel, M. E. *et al.* Potentiated Hsp104 variants antagonize diverse proteotoxic misfolding events. *Cell* **156**, 170-182 (2014).

69 Shorter, J. Engineering therapeutic protein disaggregases. *Mol Biol Cell* **27**, 1556-1560 (2016).

70 VerPlank, J. J. S., Tyrkalska, S. D., Fleming, A., Rubinsztein, D. C. & Goldberg, A. L. cGMP via PKG activates 26S proteasomes and enhances degradation of proteins, including ones that cause neurodegenerative diseases. *Proc Natl Acad Sci U S A* **117**, 14220-14230 (2020).

71 Gu, X. *et al.* SAMTOR is an S-adenosylmethionine sensor for the mTORC1 pathway. *Science* **358**, 813-818 (2017).

72 Schmittgen, T. D. & Livak, K. J. Analyzing real-time PCR data by the comparative C(T) method. *Nat Protoc* **3**, 1101-1108 (2008).

73 Guo, Q. *et al.* In situ structure of neuronal C9orf72 poly-GA aggregates reveals proteasome recruitment. *Cell* **172**, 696-705 (2018).

74 Rigort, A. *et al.* Focused ion beam micromachining of eukaryotic cells for cryoelectron tomography. *Proc Natl Acad Sci U S A* **109**, 4449-4454 (2012).

75 Mastronarde, D. N. Automated electron microscope tomography using robust prediction of specimen movements. *J Struct Biol* **152**, 36-51 (2005).

76 Fukuda, Y., Laugks, U., Lučić, V., Baumeister, W. & Danev, R. Electron cryotomography of vitrified cells with a Volta phase plate. *J Struct Biol* **190**, 143-154 (2015).

77 Li, X. *et al.* Electron counting and beam-induced motion correction enable near-atomic-resolution single-particle cryo-EM. *Nat Methods* **10**, 584-590 (2013).

78 Kremer, J. R., Mastronarde, D. N. & McIntosh, J. R. Computer visualization of three-dimensional image data using IMOD. *J Struct Biol* **116**, 71-76 (1996).

79 Rigort, A. *et al.* Automated segmentation of electron tomograms for a quantitative description of actin filament networks. *J Struct Biol* **177**, 135-144 (2012).

80 Martinez-Sanchez, A., Garcia, I., Asano, S., Lucic, V. & Fernandez, J. J. Robust membrane detection based on tensor voting for electron tomography. *J Struct Biol* **186**, 49-61 (2014).

81 Ong, S. E. *et al.* Stable isotope labeling by amino acids in cell culture, SILAC, as a simple and accurate approach to expression proteomics. *Mol Cell Proteomics* **1**, 376-386 (2002).

82 Wiśniewski, J. R., Zielinska, D. F. & Mann, M. Comparison of ultrafiltration units for proteomic and N-glycoproteomic analysis by the filter-aided sample preparation method. *Anal Biochem* **410**, 307-309 (2011).

83 Banning, C. *et al.* A flow cytometry-based FRET assay to identify and analyse protein-protein interactions in living cells. *PLoS One* **5**, e9344 (2010).

84 Perez-Riverol, Y. *et al.* The PRIDE database and related tools and resources in 2019: improving support for quantification data. *Nucleic Acids Res* **47**, D442-d450 (2019).

Acknowledgements

We thank Ralf Zenke, Markus Oster, Giovanni Cardone and Martin Spitaler from the MPIB Imaging Facility for assistance with confocal microscopy, image analysis and flow cytometry, and Albert Ries for assistance with mass spectrometry. We acknowledge Gopal Jayaraj for generation of the Fluc-GFP cell line and Alonso Izzat Carvajal Alvarez for help with native PAGE analysis. The research leading to these results has received funding from the European Commission under Grant FP7 GA ERC- 2012-SyG_318987–ToPAG (I.S., R.K., P.Y.-C., I.D., R.F.-B., F.U.H. and M.S.H.), Marie Skłodowska-Curie grant (agreement no. 749370) (S.G.), the Deutsche Forschungsgemeinschaft (DFG, German Research Foundation) under Germany's Excellence Strategy within the framework of the Munich Cluster for Systems Neurology (EXC 2145 SyNergy – ID 390857198) (V.A.T., F.U.H. and M.S.H.) and MBExC (EXC 2067/1 — ID 390729940) (R.F.-B.), as well as by the joint efforts of The Michael J. Fox Foundation for Parkinson's Research (MJFF) and the Aligning Science Across Parkinson's (ASAP) initiative. MJFF administers the grant ASAP-000282 on behalf of ASAP and itself. M.S.H. acknowledges the funding from Alzheimer Nederland (Grant Number WE.03-2020-12).

Author contributions

I.S. designed and performed most experiments. P.Y. performed seeding experiments. M.D.P. performed neuronal cultures. Q.G. and V.A.T. carried out cryo-electron tomography of Tau aggregates in TauRD-Y* cells and primary neurons, respectively. R.K. performed mass spectrometry analysis. S.G. helped with initial experiments and quantified inclusion size. H.H. performed mRNA analysis. I.D. supervised experiments with neuronal cultures. R.F.B. and W.B. supervised cryo-electron tomography experiments. D.W.S. and M.I.D. provided cell lines,

protocols and contributed to the interactome analysis. F.U.H. and M.S.H. initiated and supervised the project and wrote the manuscript with input from I.S. and the other authors.

Competing interests

Authors declare no competing interests.

Supplementary Information

The AAA+ chaperone VCP disaggregates Tau fibrils and generates aggregate seeds

Itika Saha[1,2], Patricia Yuste-Checa[1,2], Miguel Da Silva Padilha[3,4], Qiang Guo[5,#], Roman Körner[1], Hauke Holthusen[1], Victoria A. Trinkaus[1,5,6], Irina Dudanova[3,4], Rubén Fernández-Busnadiego[2,5,7,8], Wolfgang Baumeister[5], David W. Sanders[9,‡], Saurabh Gautam[1,§], Marc I. Diamond[9], F. Ulrich Hartl[1,2,6,*] and Mark S. Hipp[1,6,10,11*]

[1]Department of Cellular Biochemistry, Max Planck Institute of Biochemistry, Am Klopferspitz 18, 82152 Martinsried, Germany.

[2]Aligning Science Across Parkinson's (ASAP) Collaborative Research Network, Chevy Chase, MD, USA.

[3]Molecular Neurodegeneration Group, Max Planck Institute of Neurobiology, 82152 Martinsried, Germany.

[4]Department of Molecules – Signaling – Development, Max Planck Institute of Neurobiology, Am Klopferspitz 18, 82152 Martinsried, Germany.

[5]Department of Structural Molecular Biology, Max Planck Institute of Biochemistry, Am Klopferspitz 18, 82152 Martinsried, Germany.

[6]Munich Cluster for Systems Neurology (SyNergy), Munich, Germany.

[7]Institute of Neuropathology, University Medical Center Göttingen, 37099 Göttingen, Germany.

[8]Cluster of Excellence "Multiscale Bioimaging: from Molecular Machines to Networks of Excitable Cells" (MBExC), University of Göttingen, Germany.

[9]Center for Alzheimer's and Neurodegenerative Diseases, Peter O'Donnell Jr. Brain Institute, University of Texas Southwestern Medical Center, Dallas, 75390 Texas, USA.

[10]School of Medicine and Health Sciences, Carl von Ossietzky University Oldenburg, Oldenburg, Germany.

[11]Department of Biomedical Sciences of Cells and Systems, University Medical Center Groningen, University of Groningen, Antonius Deusinglaan, 1, 9713 AV Groningen, The Netherlands.

Present address: State Key Laboratory of Protein and Plant Gene Research, School of Life Sciences and Peking-Tsinghua Center for Life Sciences, Peking University, Beijing 100871, China.

34 ‡ Present address: Department of Chemical and Biological Engineering, Princeton University,
35 Princeton, NJ 08544, USA

36 § Present address: Boehringer Ingelheim International GmbH, 55216 Ingelheim, Germany and
37 ViraTherapeutics GmbH, 6063 Rum, Austria.

38

39 *Correspondence to uhartl@biochem.mpg.de and m.s.hipp@umcg.nl

40

41 Supplementary information includes 10 Supplementary Figures and 1 Table
42

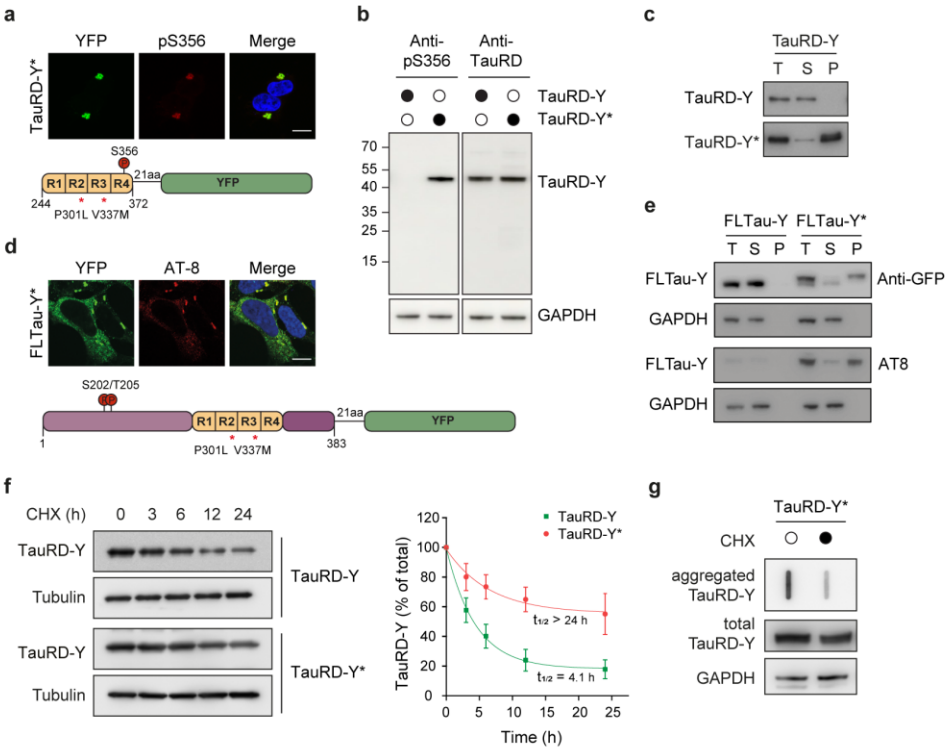

Supplementary Fig. 1: Tau aggregation and clearance in a constitutive expression model.

a Immunofluorescence staining of TauRD-Y* cells with an antibody against Tau phosphorylation at S356 (red) and YFP fluorescence of TauRD-Y (green). Scale bar, 10 µm. **b** Analysis of Tau S356 phosphorylation in lysates of TauRD-Y and TauRD-Y* cells by immunoblotting. Total TauRD-Y was detected using antibody against TauRD. **c** Solubility of TauRD-Y in TauRD-Y and TauRD-Y* cells at steady state, determined by fractionation of cell lysate by centrifugation, followed by immunoblotting with anti-GFP antibody. T, total cell lysate, S, supernatant, P, pellet. **d** Immunofluorescence staining of full-length Tau (FLTau-Y) in aggregate-containing FLTau-Y* cells with AT-8 antibody specific for Tau phosphorylation at S202/T205 (red) and YFP fluorescence of TauRD-Y (green). Scale bar, 10 µm. **e** Solubility of phosphorylated FLTau-Y in FLTau-Y and FLTau-Y* cells at steady state analyzed as in (c). Immunoblotting was with AT-8 antibody (bottom) and anti-GFP (top). GAPDH served as loading control. **f** Turnover of TauRD-Y in TauRD-Y and TauRD-Y* cells upon cycloheximide (CHX) shut-off (CHX; 50 µg/mL). Left, anti-GFP immunoblots to determine TauRD-Y levels. Tubulin served as loading control. Right, exponential fits of CHX chase data and corresponding half-lives ($t_{1/2}$). Mean ± s.d.; n=3. **g** Filter trap analysis of aggregated TauRD-Y upon CHX chase for 24 h. Aggregated and total TauRD-Y levels were determined by anti-GFP immunoblotting. GAPDH served as loading control.

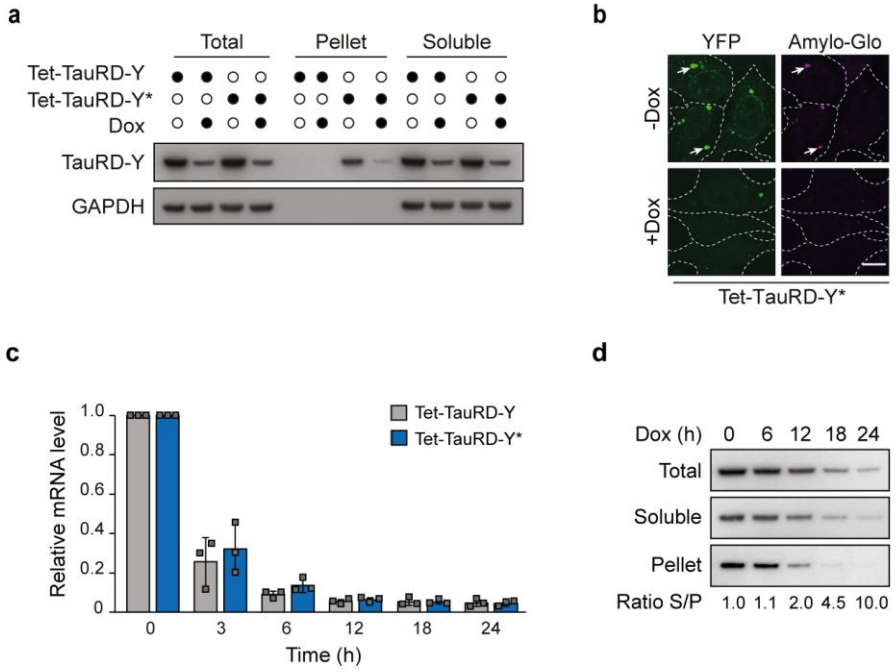

Supplementary Fig. 2: TauRD-Y aggregation and clearance upon inhibition of expression in a Tet-regulated TauRD-Y expression system.

a Solubility of TauRD-Y in Tet-TauRD-Y and Tet-TauRD-Y* cells upon addition of 50 ng/mL doxycycline (Dox) for 24 h. Cell lysates were fractionated as in Supplementary Fig. 1c. TauRD-Y was detected with anti-GFP antibody. GAPDH served as loading control. **b** Representative fluorescence images of Tet-TauRD-Y* cells treated with Dox for 24 h showing staining of TauRD-Y inclusions (green) with Amylo-Glo (magenta). White dashed lines indicate cell boundaries. Scale bar, 10 µm. **c** Quantitative PCR analysis of TauRD-Y mRNA in Tet-TauRD-Y and Tet-TauRD-Y* cells treated with Dox for 0, 3, 6, 12, 18 and 24 h. mRNA levels were normalized to the reference gene *RPS18*. Mean ± s.d.; n=3. **d** Solubility of TauRD-Y in Tet-TauRD-Y* cells upon addition of Dox for the indicated times. Normalized ratios of TauRD-Y in soluble (S) and pellet (P) fractions are stated.

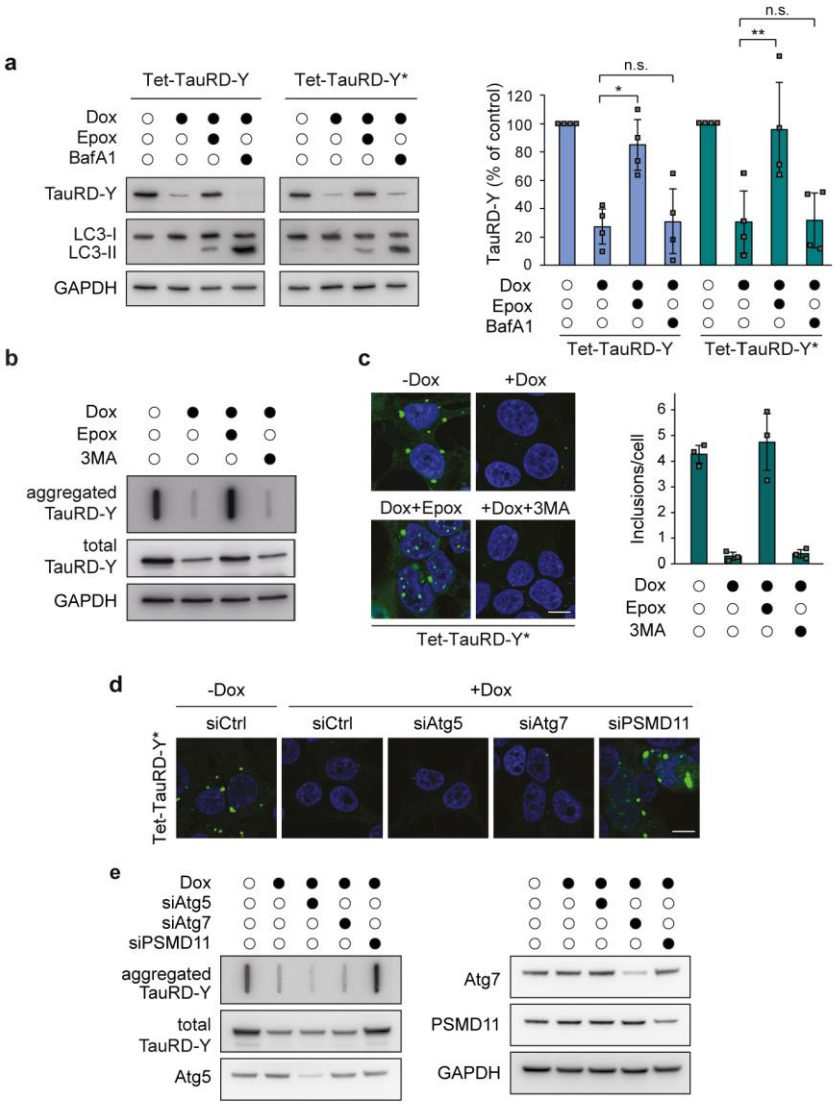

Supplementary Fig. 3: Effect of UPS and autophagy inhibition on TauRD-Y levels and aggregate clearance.

a Analysis of TauRD-Y levels in Tet-TauRD-Y and Tet-TauRD-Y* cells treated for 24 h with doxycycline (Dox; 50 ng/mL) alone or in combination with Epoxomicin (Epox; 50 nM) or

Bafilomycin A1 (BafA1; 50 nM). TauRD-Y and LC3 levels were determined by immunoblotting against GFP and LC3B respectively. GAPDH served as loading control. Mean ± s.d.; n=4. *p<0.05 (Tet-TauRD-Y: + Dox vs + Dox + Epox, p=0.0114), **p<0.01 (Tet-TauRD-Y*: + Dox vs + Dox + Epox, p=0.0026); n.s. non-significant (Tet-TauRD-Y: + Dox vs + Dox + Epox, p= 0.6422; Tet-TauRD-Y*: + Dox vs + Dox + Epox, p= 0.8799) from two-tailed Student's paired t-test. **b** Filter trap analysis of Tet-TauRD-Y* cells treated for 24 h with Dox alone or in combination with Epoxomicin (Epox; 50 nM) or 3-methyladenine (3MA; 5 mM). Aggregated and total TauRD-Y was detected with anti-GFP antibody. **c** Left, representative images of Tet-TauRD-Y* cells treated for 24 h with Dox alone or, in combination with Epoxomicin (Epox; 50 nM) or 3MA (5 mM). Scale bar, 10 μm. Right, quantification of TauRD-Y foci. 100-200 cells analyzed per experiment. Mean ± s.d.; n=3. **d** Representative images of Tet-TauRD-Y* cells transfected with non-targeted (Ctrl) siRNA or siRNA against Atg5 (50 nM), Atg7 (50 nM) and PSMD11 (25 nM). 72 h after transfection, doxycycline (Dox; 50 ng/mL) was added for another 24 h where indicated. Scale bar, 10 μm. **e** Filter trap analysis of Tet-TauRD-Y* cells transfected with siRNAs and treated with Dox as stated in (d). TauRD-Y was detected by immunoblotting with anti-GFP antibody.

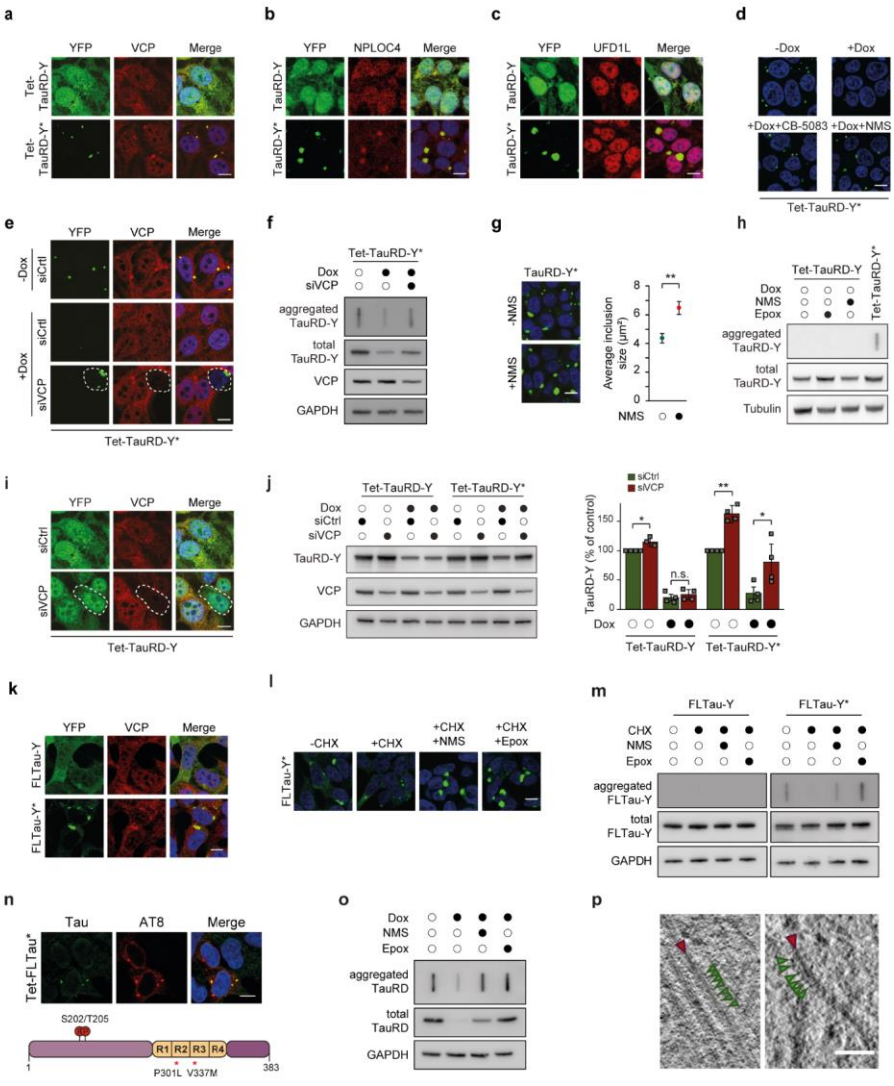

Supplementary Fig. 4: Aggregation specific stabilization of Tau by VCP inactivation.

a Immunofluorescence staining of VCP (red) and YFP fluorescence of TauRD-Y (green) in Tet-TauRD-Y and Tet-TauRD-Y* cells. **b** and **c** Immunofluorescence staining of NPLOC4 (b) (red) and UFD1L (c) (red) in TauRD-Y and TauRD-Y* cells. Scale bars, 10 µm. **d** Representative images of Tet-TauRD-Y* cells treated for 24 h with doxycycline (Dox; 50 ng/mL) alone or in

combination with CB-5083 (1 μM) or NMS-873 (NMS; 2.5 μM). Scale bar, 10 μm. **e** Immunofluorescence staining of VCP (red) in Tet-TauRD-Y* cells treated with non-targeted (Ctrl) or VCP siRNA for 96 h. Doxycycline (Dox; 50 ng/mL) was added for the last 24 h. Dashed lines indicate a cell with reduced VCP levels. Scale bar, 10 μm. **f** Filter trap analysis of aggregated TauRD-Y in Tet-TauRD-Y* lysates treated as in (d). Aggregated and total TauRD-Y was analyzed by anti-GFP immunoblotting. GAPDH served as loading control. **g** Size increase of TauRD-Y inclusions upon VCP inhibition. Representative images of TauRD-Y* cells treated for 24 h with NMS-873 (NMS; 5 μM) and quantification of average inclusion size (μm^2). 200-400 cells analyzed per experiment. Mean ± s.d.; n=5. **$p<0.01$ ($p= 0.0022$) from two-tailed Student's paired t-test. **h** Filter trap analysis of Tet-TauRD-Y cells treated for 24 h with Epoxomicin (Epox; 50 nM) or NMS-873 (NMS; 2.5 μM) where indicated. Tet-TauRD-Y* lysate was used as control. TauRD-Y was detected by immunoblotting with anti-GFP antibody. **i** Immunofluorescence staining of VCP (red) and YFP fluorescence of TauRD-Y (green) in Tet-TauRD-Y cells transfected with non-targeted (Ctrl) or VCP siRNA for 96 h. Dashed lines indicate a cell with reduced VCP levels. Scale bar, 10 μm. **j** Left, analysis of TauRD-Y level in Tet-TauRD-Y and Tet-TauRD-Y* cells transfected for 96 h with non-targeted (Ctrl) or VCP siRNA where indicated. Doxycycline (Dox; 50 ng/mL) was added for the last 24 h. TauRD-Y was detected by immunoblotting with anti-GFP antibody. Right, quantification of TauRD-Y immunoblot. Mean ± s.d.; n=4. *$p<0.05$ (Tet-TauRD-Y - Dox: siCtrl vs siVCP, $p= 0.0218$; Tet-TauRD-Y* + Dox: siCtrl vs siVCP, $p= 0.0156$); **$p<0.01$ (Tet-TauRD-Y* - Dox: siCtrl vs siVCP, $p= 0.0023$); n.s. non-significant (Tet-TauRD-Y + Dox: siCtrl vs siVCP, $p= 0.0539$) from two-tailed paired Student's t-test. **k** Immunofluorescence staining of VCP (red) and YFP fluorescence of FLTau-Y (green) in FLTau-Y and FLTau-Y* cells. Scale bar, 10 μm. **l** Representative images of FLTau-Y* cells treated for 24 h with cycloheximide (CHX; 50 μg/mL) alone or in combination with NMS-873 (NMS; 2.5 μM) or Epoxomicin (Epox; 100 nM). Scale bar, 10 μm. **m** Filter trap analysis of lysates from FLTau-Y and FLTau-Y* cells treated for 24 h with Dox alone or in combination with NMS-873 (NMS; 2.5 μM) or Epoxomicin (Epox; 50 nM). Aggregated and total FLTau-Y levels were determined by immunoblotting against GFP. GAPDH served as loading control. **n** Immunofluorescence staining of full-length Tau (FLTau) in aggregate-containing Tet-FLTau* cells with Tau (green) and Tau S202/T205 phosphorylation specific AT-8 (red) antibody. Scale bar, 10 μm. **o** Filter trap analysis of lysates from Tet-TauRD* cells treated for 24 h with Dox alone or in combination with NMS-873 (NMS; 2.5 μM) or Epoxomicin (Epox; 50 nM). Aggregated and total TauRD levels were determined by immunoblotting against myc and TauRD, respectively. GAPDH served as loading control. **p** Examples of two TauRD-Y fibrils from a representative 1.4 nm thick tomographic slice of a TauRD inclusion from neurons. Red arrows indicate TauRD-Y fibrils and green arrows indicate globular densities along fibrils. Scale bar, 40 nm.

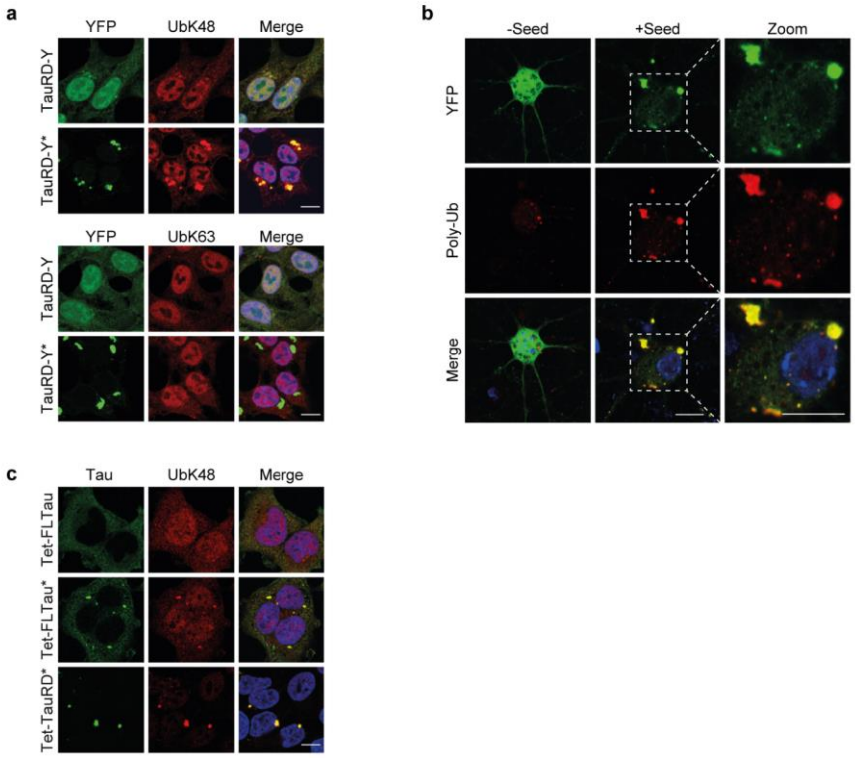

Supplementary Fig. 5: Ubiquitylation of TauRD-Y aggregates.

a Immunofluorescence staining of (top) ubiquitin-K48 (UbK48) (red) and (bottom) ubiquitin K63 (UbK63) (red) chains and YFP fluorescence of TauRD-Y (green) in TauRD-Y and TauRD-Y* cells. Scale bars, 10 µm. **b** Immunofluorescence staining of ubiquitylated proteins (FK2 antibody) (red) in primary neurons expressing TauRD-Y (green) and treated with TauRD containing lysates (+Seed) where indicated. Scale bars, 20 µm. **c** Immunofluorescence staining of ubiquitin-K48 (UbK48) (red) chains and Tau (green) in Tet-FLTau, Tet-FLTau* and Tet-TauRD* cells. FLTau was detected using Tau-5 and TauRD using anti-myc antibody. Scale bar, 10 µm.

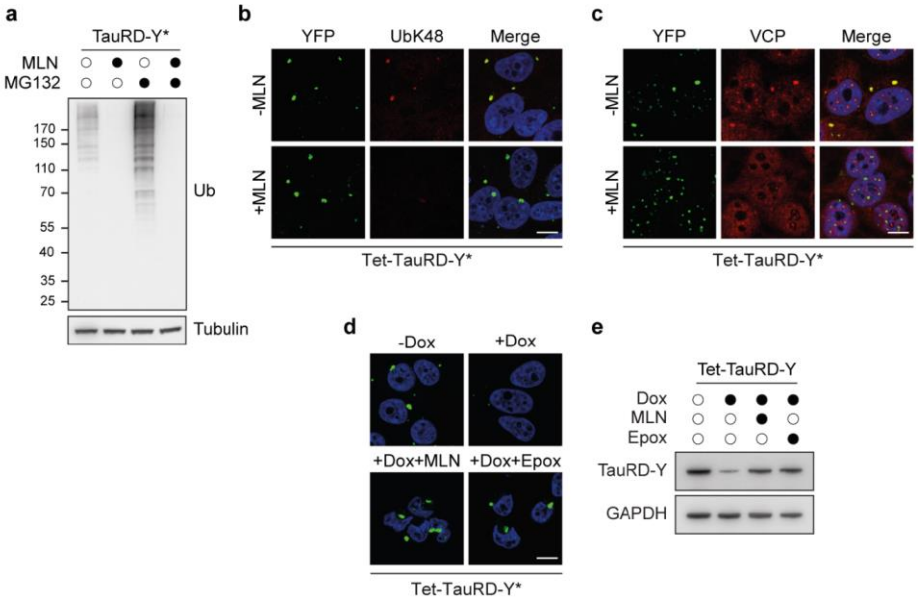

153

154 **Supplementary Fig. 6: Role of ubiquitylation in TauRD-Y disaggregation.**

155 **a** Analysis of ubiquitylated protein levels in lysates of TauRD-Y* cells treated with the ubiquitin
156 activating enzyme E1 inhibitor MLN7243 (MLN; 0.5 µM) alone or in combination with
157 proteasome inhibitor MG132 (1 µM) for 14 h. Ubiquitylated proteins were detected by
158 immunoblotting against ubiquitin. Tubulin served as loading control. **b** Immunofluorescence
159 staining of ubiquitin-K48 chains (UbK48) (red) and **c** VCP (red) in Tet-TauRD-Y* cells treated
160 with MLN7243 (MLN; 0.5 µM) for 12 h. Scale bars, 10 µm. **d** Representative images of Tet-
161 TauRD-Y* cells treated for 24 h with doxycycline (Dox; 50 ng/mL) alone or in combination
162 with MLN7243 (MLN; 0.5 µM) or Epoxomicin (Epox; 50 nM). Scale bar, 10 µm. **e** Analysis of
163 TauRD-Y levels in Tet-TauRD-Y cells treated for 24 h with Dox, MLN7243 and Epoxomicin as
164 in (d). GAPDH served as loading control.
165

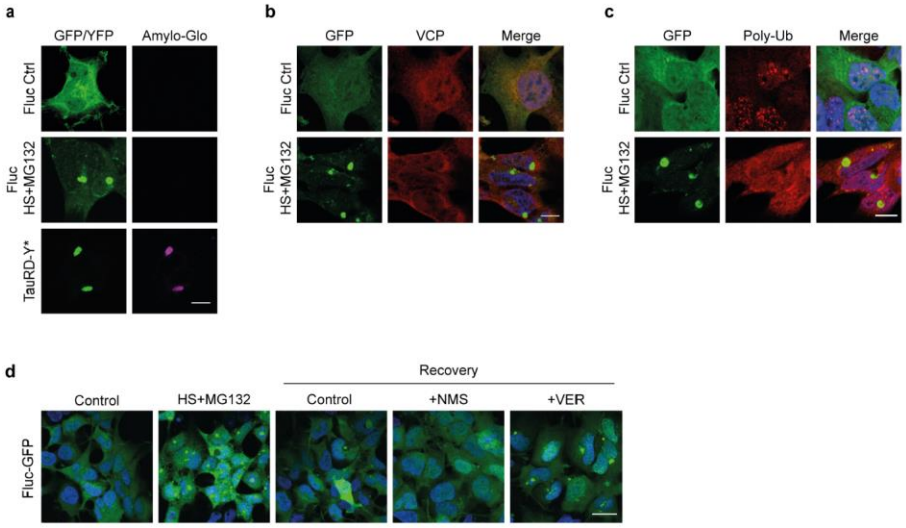

Supplementary Fig. 7: Effect of VCP inhibition on firefly luciferase (Fluc) disaggregation.
a Fluc-GFP expressing cells maintained at 37 °C (Fluc Ctrl) or heat-stressed at 43 °C in presence of 5 µM MG132 for 2 h (Fluc HS) were stained with the amyloid-specific dye Amylo-Glo (magenta). TauRD-Y* cells were used as control. Amylo-Glo fluorescence was imaged with similar exposure settings in all panels. Scale bar, 10 µm. **b** Immunofluorescence staining of VCP (red), and **c** ubiquitylated proteins (FK2 antibody) (red) in Fluc-GFP cells treated as in (a). Scale bars, 10 µm. **d** Effect of VCP and Hsp70 inhibition on Fluc-GFP disaggregation. Fluc-GFP aggregation was induced as in (a). Cells were then shifted to MG132 free media and allowed to recover at 37 °C for 8 h in presence of NMS-873 (NMS; 2.5 µM) and VER-155008 (VER; 10 µM) where indicated. Scale bar, 30 µm.

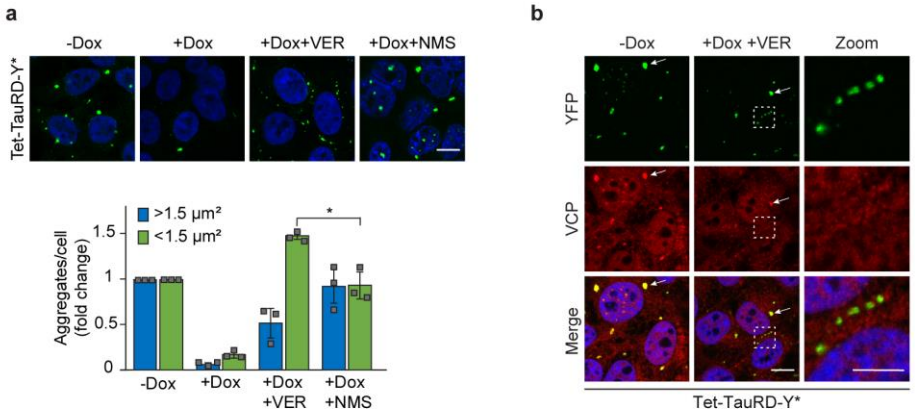

177

178 **Supplementary Fig. 8: Role of Hsp70 in TauRD-Y disaggregation.**

179 **a** Top, Representative images of Tet-TauRD-Y* cells treated for 24 h with doxycycline (Dox; 50
180 ng/mL) alone or in combination with VER-155008 (VER; 10 µM) or NMS-873 (NMS; 2.5 µM).
181 Bottom, quantification of large (>1.5 µm^2) and small (<1.5 µm^2) TauRD-Y foci. Mean ± s.d.;
182 n=3; ~100-200 cells were analyzed per experiment. *p<0.05 (p=0.0435) from two-tailed
183 Student's paired t-test. Scale bar, 10 µm. **b** Immunofluorescence staining of VCP (red) and YFP
184 fluorescence of TauRD-Y (green) in Tet-TauRD-Y* cells treated with a combination of
185 doxycycline (Dox) and VER-155008 (VER) where indicated. White arrow points to large
186 TauRD-Y inclusions co-localizing with VCP. Dashed lines enclose TauRD-Y foci that do not co-
187 localize with VCP. Scale bar, 10 µm. Scale bar zoom, 5 µm.
188

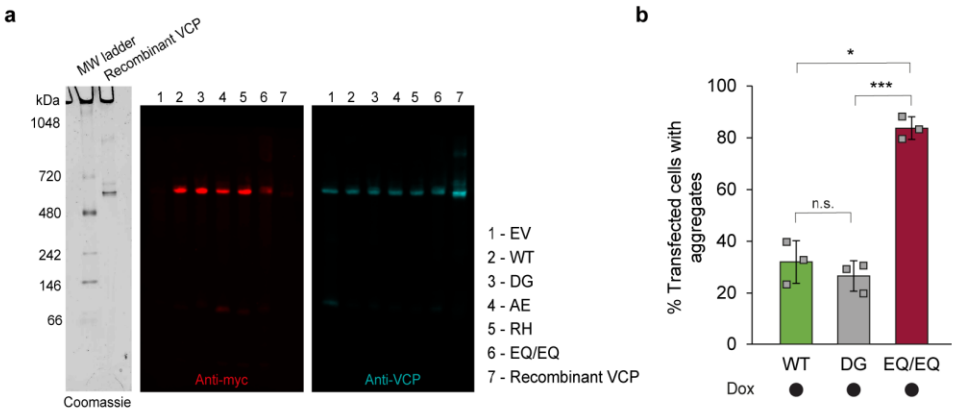

Supplementary Fig. 9: Effect of VCP mutants on Tau disaggregation.

a Native-PAGE analysis of recombinant VCP and lysates from Tet-TauRD-Y* cells transfected with empty vector (EV) and myc-tagged wild type (WT), D395G (DG), A232E (AE), R155H (RH) and E305Q/E578Q (EQ/EQ) VCP constructs. Immunoblot probed against myc (red) and VCP (cyan) is shown. Non-tagged, recombinant VCP was analyzed as control. **b** Quantification of aggregate foci in myc-positive Tet-TauRD-Y* cells transfected with myc-tagged WT, DG and EQ/EQ VCP constructs for 24 h, and treated for another 24 h with doxycycline (Dox; 50 ng/mL). Mean ± s.d.; n=3; > 100 cells analyzed per experiment; *p<0.05 (WT vs EQ/EQ p=0.0192); ***p<0.001 (DG vs EQ/EQ p=0.0008); n.s. non-significant (p=0.5646).

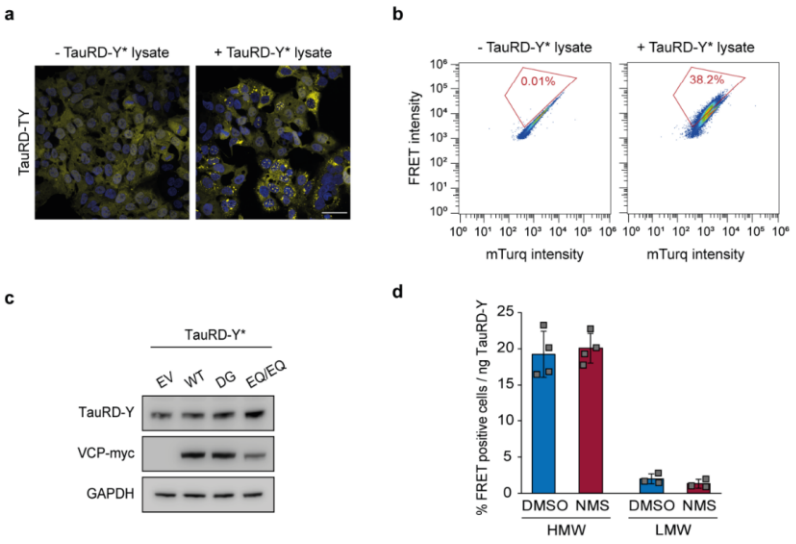

Supplementary Fig. 10: Analysis of seeding-competent TauRD-Y.

a Representative images of TauRD-TY FRET reporter cells treated with TauRD-Y* lysate where indicated showing TauRD-Y florescence in yellow. Scale bar, 40 µm. **b** Representative pseudocolour dot plots for the analysis of FRET positive TauRD-TY cells by flow cytometry upon addition of TauRD-Y* lysate. FRET intensity is plotted against mTurquoise2 (mTurq) intensity and the % of FRET positive cells are indicated in red gates. **c** Analysis of TauRD-Y and VCP-myc levels in TauRD-Y* cells transfected for two days with empty vector (EV) and myc-tagged wild type (WT), D395G (DG) and E305Q/E578Q (EQ/EQ) VCP constructs. TauRD-Y and overexpressed VCP levels were determined by immunoblotting against GFP and myc, respectively. GAPDH served as loading control. **d** Comparison of seeding efficiencies of high molecular weight (HMW) and low molecular weight (LMW) species obtained by size exclusion chromatography of lysates from TauRD-Y* cells treated for 24 h with DMSO or NMS-873 (NMS; 2 µM). Mean ± s.d.; HMW n=4, LMW n=3.

3 Discussion

Although Parkinson's disease was described for the first time in 1817 (Parkinson, 1817) and Lewy bodies were discovered more than 100 years ago (Lewy, 1912), the cellular mechanisms and consequences of protein aggregation in neurodegenerative diseases remain incompletely understood. This may be due to the lack of suitable cellular model systems and biochemical tools as well as to our limited understanding of aggregate structure and interactions of aggregates with cellular components.

While in cell biological studies in the early 2000s protein aggregation was induced by harsh chemical treatments (Ostrerova-Golts *et al.*, 2000; Paxinou *et al.*, 2001), newer models focus on aggregate formation upon seeded aggregation, mimicking the prion-like spread of neurotoxic protein aggregates in patient brains (Volpicelli-Daley, Luk and Lee, 2014). Seeding induces intracellular aggregation of proteins, such as tau and α-syn reliably and allows to study the uptake of the seeds as well as the seeding event *in cellulo.*

By combining this novel seeding approach with cell-biological and ultrastructural methods, we have been able to provide insights into key aspects of the 'aggregation cycle' of neurotoxic protein aggregates. These include the seed uptake, subsequent aggregate formation, ultrastructural information of aggregate architecture and cellular interactions, as well as the dissociation of aggregates by molecular chaperones.

In our first study, we used biochemical and cell-biological methods to analyze the effect of the extracellular chaperone Clusterin on tau and α-syn seed formation and stabilization. We were able to elucidate cellular processes involved in seed uptake as well as seeded aggregation.

When seeds enter the cytosol and templated misfolding of endogenous proteins occurs, large protein aggregates may form. These aggregates can engage cellular components in inappropriate interactions, potentially resulting in cellular toxicity (Hipp, Kasturi and Hartl, 2019). To improve our understanding of aggregate architecture and cellular interactions, we analyzed neuronal α-syn aggregates by cryo-electron tomography (cryo-ET). We were not only able to study the architecture of α-syn

aggregates and their interactions with cellular membranes, but also visualized the uptake of seeds as well as the seeding event *in situ.*

Since α-syn aggregation is neurotoxic, we wanted to analyze cell-biological mechanisms that are involved in counteracting and reverting protein aggregation: In our third study, we used microfluidics combined with spectrometric measurements to determine the molecular mechanisms of α-syn amyloid fibril disaggregation by the Hsp70 machinery *in vitro*.

Hsp70 does not only disaggregate α-syn fibrils efficiently *in vitro*, it is additionally involved in tau amyloid fibril disaggregation in cells, as shown by our fourth study: Here, we found that the AAA+ chaperone VCP together with the Hsp70 machinery disaggregates cellular tau aggregates, thereby creating either tau monomers that are degraded subsequently by the proteasome or small fibril fragments that may serve as new seeds, resulting in another cycle of prion-like seeded aggregation.

Altogether, our studies provide new insights on the 'life cycle' of neurotoxic protein aggregates: We analyze the effect of extracellular chaperones on seeded aggregation, follow the seed uptake and seeding event at unprecedented resolution, characterize cellular interactions of aggregates ultrastructurally and uncover protein disaggregation mechanisms *in vitro* and in cells.

3.1 The extracellular chaperone Clusterin enhances Tau aggregate seeding in a cellular model

The extracellular chaperone Clu has been identified as one of the most common risk factors for LOAD (Harold *et al.*, 2009; Lambert *et al.*, 2009). Until this day the connection between Clu and toxic protein aggregation is not well understood. While some studies observe neuroprotective activity of Clu (Wojtas, Carlomagno, *et al.*, 2020; Wojtas, Sens, *et al.*, 2020), others describe a pathology-enhancing effect (Oda *et al.*, 1995; DeMattos *et al.*, 2002):

'Holdase' chaperones, such as Clu can reduce protein aggregation. By shielding hydrophobic surfaces of aggregating protein species, the chaperones can prevent oligomers and prefibrillar species to engage other cellular components in aberrant

interactions (Wyatt *et al.*, 2013). However, chaperones can also stabilize oligomeric aggregates, possibly resulting in species with higher seeding-competence or toxicity (DeMattos *et al.*, 2002).

Interestingly, in our study, we observed a similar Janus-faced effect of Clu on seeded aggregation: Clu delays the aggregation of α-syn and tau in *in vitro de novo* aggregation reactions, exerting its chaperone function. However, in seeded aggregation experiments, Clu shows a contrary effect. While aggregate seeding with α-syn PFFs co-aggregated with Clu (α-syn/Clu) results in a reduced number of cells containing α-syn aggregates, seeding with tau seeds co-aggregated with Clu (tau/Clu) results in a significantly increased number of cells containing aggregates. Subsequent biochemical and biophysical investigations revealed that Clu stabilizes highly seeding competent oligomeric tau seeds (Yuste-Checa *et al.,* 2021).

In the brain, extracellular aggregates can be cleared via various mechanisms: E.g. by internalization of aggregates by glial cells or neurons. However, it is questionable whether extracellular aggregate clearance by endocytosis is beneficial for cells. On the one hand, the material taken up by the cells can be transferred from endosomes to lysosomes for subsequent degradation (Cao *et al.*, 2019). On the other hand, several studies demonstrated that aggregate seeds disrupt endosomal and lysosomal vesicles and escape into the cytoplasm. Once in contact with the cytosol, the seeds induce the aggregation of the endogenously expressed protein (Jiang *et al.*, 2017; Karpowicz *et al.*, 2017).

Clu-mediated endocytosis of extracellular aggregates may be facilitated by cell surface receptors for Clu, including HSPGs, LRP1/2 (Low density lipoprotein Receptor-related Protein 1 and 2), VLDLR (Very Low Density Lipoprotein Receptor), and the LOAD risk genes scavenger receptors Plexin 4A and TREM2 (Triggering Receptor Expressed on Myeloid cells 2) (Yuste-Checa, Bracher and Hartl, 2022).

TREM2 is a transmembrane glycoprotein that is expressed in microglia, the resident macrophage cells in brain tissue (Bouchon, Dietrich and Colonna, 2000; Neumann and Takahashi, 2007). Notably, TREM2 expression is upregulated in pathological conditions of AD, PD or traumatic brain injury (Lue *et al.*, 2015; Liu *et al.*, 2016; Gratuze, Leyns and Holtzman, 2018). Several genetic mutations have been identified that alter the function of TREM2. The most common mutation, R47H, has a decreased

affinity for lipoprotein ligands ApoE, LDL (Low Density Lipoprotein) or Clu (Guerreiro *et al.*, 2013; Yeh *et al.*, 2016). This could subsequently lead to a decreased uptake of Clu-bound extracellular aggregates, resulting in reduced clearance (Yuste-Checa, Bracher and Hartl, 2022).

LRP1 is not only a receptor for Clu uptake, but also a master regulator for tau endocytosis. A recent study led by the Kosik group employed Clustered Regularly Interspaced Short Palindromic Repeats (CRISPR) based genetic screens to identify cellular receptors involved in tau uptake. The authors showed in seeding experiments that *LRP1* KO reduced the spread of tau aggregates *in vitro* as well as *in vivo* (Rauch *et al.*, 2020). LRP1-mediated tau uptake could therefore be increased by Clu-bound tau aggregates (Yuste-Checa, Bracher and Hartl, 2022).

In our study, we showed that tau seeds as well as tau/Clu seeds enter cells via endocytosis. The incorporated seeds co-localize with Chmp2a (Charged multivesicular body protein 2a) and Gal8 (Galectin 8). Chmp2a is a component of the ESCRT-III complex (Endosomal Sorting Complex Required for Transport III), which is needed for ESCRT-mediated endocytosis (Alqabandi *et al.*, 2021). Gal8 is a marker for disrupted endosomal membranes accumulating on damaged vesicles (Jia *et al.*, 2018). Tau as well as tau/Clu seeds damage endosomal vesicles upon internalization and escape into the cytosol, resulting in seeding of the endogenously expressed tau.

Interestingly, we found that tau and tau/Clu seeds as well as α-syn and α-syn/Clu seeds get internalized by HSPGs. Thus, the mere internalization of the seeds cannot be the cause for the contrasting effects of Clu on tau and α-syn seeded aggregation. A different binding mode of Clu to the amyloidogenic proteins, however, could explain the observed Janus-faced property: While Clu could for example shield hydrophobic patches at the ends of the α-syn fibrils, which are the hubs for fibril growth, it may bind to tau aggregates in a way that renders hydrophobic patches more accessible.

3.2.1 Future perspectives

A recent study reported an exacerbated tau pathology in *CLU* KO-Tau(P301L) mice compared to control Tau(P301L) mice and concluded that Clu is preventing tau aggregation *in vivo* efficiently (Wojtas, Carlomagno, *et al.*, 2020). It is noteworthy that tau pathology in Tau(P301L) mice develops without additional seeding, i.e. tau

aggregation occurs *de novo*. In light of this, it seems important to differentiate between the effect of Clu on *de novo* aggregation and on seeded aggregation. Additionally, the distinct effect of Clu on different amyloidogenic proteins, such as tau, α-syn or Aβ needs to be considered. This goes hand in hand with careful considerations of the mouse or cellular model system and possible compensatory effects of the Clu KO by other apolipoproteins, including ApoE.

To study extracellular chaperones in a humanized model system, 3D organoids could be used. Human stem cells (induced pluripotent stem cells or embryonic stem cells) can be differentiated into specific types of brain cells, such as neurons, astrocytes, oligodendrocytes or microglia. Additionally, 3D cultures allow researchers to mimic the extracellular space between cells, which is a prerequisite to study extracellular proteins (Kim, Koo and Knoblich, 2020).

Investigating the structural differences of aggregate seeds formed with or without Clu seems essential for understanding the Janus-faced effect of Clu on protein aggregation and seeding. Besides low resolution approaches, such as cross-linking mass spectrometry or hydrogen-deuterium exchange, high resolution techniques like cryo-EM, NMR or X-ray crystallography, especially in combination with modeling algorithms, such as AlphaFold 2 (Jumper *et al.*, 2021), can help to resolve the binding interface of Clu and the aggregating protein. This data could provide insight into differences in accessibility of hydrophobic patches on the fibril surface and explain the observed opposing effects of Clu on α-syn and tau seeded aggregation.

3.2 *In situ* architecture of neuronal α-Synuclein inclusions

α-Syn inclusions are the hallmark of various neurodegenerative diseases, such as PD or MSA. The ultrastructure as well as the molecular composition of neuronal α-syn inclusions is, however, still under debate. While previous studies, using conventional EM analysis, suggested that LBs of PD patients consist mainly of fibrillar material, a recent report questions the existence of α-syn fibrils in LBs and defined PD as a lipidopathy. Shahmoradian *et al.* found by room temperature CLEM analysis of *post mortem* PD brain tissue that α-syn inclusions were mainly composed of lipid

membranes and organelles. Although the authors also observed ‘unidentified fibrillar material’ in 14 of the 17 investigated LBs, they suggested that LBs do not consist of amyloid α-syn fibrils, but rather of clustered membranes (Shahmoradian *et al.*, 2019).

Mahul-Mellier *et al.,* who used a seeding-based model system in murine primary neurons to generate LB-like aggregates and analyzed them with room temperature CLEM, also observed membranous organelles as well as fibrillar material. Interestingly, the authors were able to identify the additional fibrillar material as α-syn fibrils. They concluded that LBs are composed of a dense meshwork of α-syn fibrils and membranous organelles (Mahul-Mellier *et al.*, 2020). The observation that α-syn aggregates are enriched with membranous organelles seems to be in agreement with previous *in vitro* work, which showed that monomeric as well as fibrillar α-syn can interact with and bind to lipid bilayers (Grey *et al.*, 2011). α-Syn oligomers penetrate membranes (Fusco *et al.*, 2017) and the addition of phospholipids influences α-syn aggregation kinetics *in vitro* (Galvagnion, 2017).

To analyze the interactions between aggregated α-syn and its cellular environment at high resolution *in situ,* we conducted a cryo-ET study on neuronal LB-like α-syn aggregates (Trinkaus *et al.,* 2021). Cryo-ET has several advantages over conventional EM:

First of all, it forgoes preparation methods, such as dehydration, chemical fixation or embedding of the sample, which alter the cellular architecture and can modify native structures. Instead, cryo-ET samples are fixed by rapid freezing. This process, which is termed ‘vitrification’, keeps the marcomolecules of the sample in their native hydrated state and does not allow any molecular rearrangements (Dubochet *et al.*, 1988).

Secondly, in contrast to conventional microtome sectioning, the thinning of cellular samples is now commonly performed by focused-ion-beam (FIB) milling using gallium ions. FIB milling introduces less cutting artefacts to the sample than microtome sectioning (Rigort *et al.*, 2010).

Thirdly, cellular interactions can be studied in the three-dimensional space, the tomogram. Tomograms are reconstructed from tilt-series that are acquired at areas of interest on the sample. Tomogram segmentations of fibrils and organelles enable the

three-dimensional analysis of interactions between membranes and/or aggregates (Bäuerlein *et al.*, 2017).

For our ultrastructural investigation of α-syn aggregate architecture, we analyzed different types of α-syn aggregates: aggregates formed by GFP-(Green Fluorescent Protein)-labeled α-syn or endogenously expressed α-syn, as well as aggregates seeded with *in vitro* formed PFFs or *post mortem* MSA patient brain aggregates. We observed that in all conditions, the neuronal α-syn aggregates were composed of a meshwork of α-syn fibrils interspersed with various organelles, similar to the LB-like aggregates described by Mahul-Mellier *et al.* 2020.

To analyze the interactions of the α-syn fibrils with the surrounding organelles, we determined the fibril-membrane distance distribution between α-syn fibrils and their nearest membranes. We compared this distribution to a simulated data set, where we randomly moved the experimentally determined fibrils through the volume of the original tomogram. Surprisingly, we did not observe an increased amount of close contacts between the fibrils and membranes in our experimental data compared to the random simulation, indicating that α-syn fibrils do not interact with organelles and membranes directly.

This observation stands in contrast to what was observed for polyglutamine-(polyQ)-expanded huntingtin exon 1 aggregates - a model system for Huntington's disease: PolyQ fibrils were found to interact with membranes directly (Bäuerlein *et al.*, 2017). These interactions induce high curvature regions in the membrane lipid bilayers and have a direct effect on organelle dynamics. Mobility measurements revealed that the ER in close vicinity to the inclusion bodies is less dynamic (Bäuerlein *et al.*, 2017).

Because α-syn has membrane binding properties and was found to interact with vesicles and membranes at the pre-synapse, we sought to investigate whether monomeric or oligomeric α-syn species could lead to organelle clustering within the α-syn aggregates. We therefore compared the intermembrane distance distributions of organelles within α-syn aggregates to those of untransduced, unseeded control neurons. Interestingly, we did not observe any differences in the intermembrane distance distributions, indicating that α-syn does not cluster lipid membranes within neuronal α-syn aggregates.

However, we cannot rule out that at later stages of aggregation or in patient brain, close contacts between fibrils and membranes or between membranes may occur. It has been shown that α-syn in LBs in PD brain can undergo PTMs as well as C- and N-terminal truncations, which may alter its membrane-binding properties (Sorrentino and Giasson, 2020).

Since cryo-EM studies have demonstrated that α-syn fibrils purified from patient brain have distinct protofilament folds, which could not be reproduced *in vitro* (Lövestam *et al.*, 2021), we wanted to compare the structural properties of α-syn fibrils seeded with *in vitro* formed PFFs to those seeded with aggregate material purified from *post mortem* MSA patient brain. Accordingly, we analyzed the fibril persistence length, which is a measure for the bending stiffness of a polymer. Interestingly, we observed that MSA seeded fibrils had a significantly lower persistence length than fibrils seeded with PFFs formed by recombinant α-syn. Although we were not able to resolve the structure of the fibrils by subtomogram averaging, we hypothesized that a different protofilament fold may be the cause for the observed differences in fibril flexibility. This observation is supporting the hypothesis that different strains of seeds result in different types of aggregates (Peng *et al.*, 2018; Peng, Trojanowski and Lee, 2020).

Based on the previous observation, we sought to visually identify the seeds in the aggregates and aimed to observe seeding events *in situ.* In these experiments we used PFFs labeled with gold beads for seeding. Interestingly, seeded fibrils in cells contained short, gold-bead-labeled material at the fibril ends, representing the seeding competent parts of the PFFs used. Since only the ends of the fibrils were labeled with gold beads, we hypothesized that fibril growth occurs unidirectionally. Similar observations have been made in atomic force microscopy (AFM) studies analyzing seeded aggregation of α-syn fibrils *in vitro* (Watanabe-Nakayama *et al.*, 2020).

3.1.1. Future perspectives

Immunofluorescence analyses of PD brain material have revealed that α-syn aggregates ‘age’ over time and grow from loosely packed aggregates into dense inclusions (Moors *et al.*, 2021). Therefore, cryo-ET analyses of aged α-syn aggregates, several months after seeding, could potentially provide new perspectives

on aggregate development and architecture. However, primary neurons do not survive long cultivation times, which makes them an unsuitable model system.

Recent developments in cryo-ET, such as high pressure freezing combined with lift-out FIB-milling (Schaffer *et al.*, 2019), allow the processing of tissue samples. These new methods may be eventually employed to image α-syn aggregates in intact brain tissue at different aggregation stages and in various cell types, such as neurons or oligodendrocytes. Although lift-out FIB milling is a technically challenging low-throughput method (Schaffer *et al.*, 2019), improved process automation and more efficient FIB systems, such as plasma FIBs, will increase the throughput of tissue sample preparation in cryo-ET workflows (Berger *et al.*, 2022).

At the moment, however, the access to intact human brain tissue for scientific purposes is severely limited: Obtaining brain tissue samples proves difficult, as sample preparation (i.e. high pressure freezing) has to be performed immediately after excision of the tissue material, requiring that scientists must be informed about the exact date of the tissue excisions in advance. Therefore, tissue material can only be obtained during planned brain surgeries as part of e.g. cancer therapies or during acts of medically assisted suicide when patients decide to donate the respective tissue material. The latter, however, is restricted to only a few European countries and is associated with complex ethical considerations.

One of the most important hypotheses explaining the intercellular propagation of aggregate strains in different synucleinopathies, is the conformational templating of the seed's protofilament fold inside the cell. To test this hypothesis, it is necessary to solve the structure of the seed and of the seeded fibril inside the cell. Here, single-particle analysis cryo-EM of the seed as well as of the seeded fibril would have to be performed. However, harsh purification steps during cell lysis or ultracentrifugation may introduce structural changes to the fibrils.

Alternatively, cryo-ET in combination with subtomogram averaging may be employed to determine, whether the protofilament fold of the seed is templated during seeded aggregation. However, this approach harbors several difficulties that need to be considered: The spacing between monomers along the amyloid fibril axis is only 4.7 Å (see also chapter 1.4). This implies that, based on the Nyquist-Shannon sampling theorem, an acquisition pixel size of less than 2.35 Å is needed to resolve

the monomer spacing along the fibril axis (Shannon, 1998). This results in two problems: On the one hand, the field of view will be significantly reduced, which decreases information of the cellular environment and leads to a decreased number of particles in the tomographic volume. On the other hand, tomogram reconstruction will become more difficult, since the algorithm used for fiducial-less tilt series alignment has less cellular features to track (Mastronarde and Held, 2017).

However, considering the recent technological developments and improvements of software and hardware, *in situ* subtomogram averaging of amyloid fibrils seems theoretically feasible and could potentially be accomplished in the near future.

3.3 The Hsc70 disaggregation machinery removes monomer units directly from α-synuclein fibril ends

Previous *in vitro* studies investigating the mechanism of Hsp70-dependent α-syn fibril disaggregation, did not conclusively demonstrate what kind of α-syn species (monomers or small oligomers) are removed from fibril ends. Both, fragmentation and depolymerization have been observed, however the relative contributions of the two mechanisms proved difficult to assess (Gao *et al.*, 2015; Wentink *et al.*, 2020, see chapter 1.12.1).

We therefore aimed to provide more evidence on the exact mode of fibril disaggregation. By employing microfluidic measurements combined with chemical kinetics, we showed that the Hsp70 machinery is removing α-syn monomers from the fibril ends and that fibril fragmentation makes little contribution to the disaggregation reaction (Schneider *et al*., 2021).

In our experimental setup, we incubated α-syn fibrils with the Hsc70, DnajB1 and Apg2 chaperone system and analyzed the disaggregation by ThT measurements as well as by diffusional sizing at different time points. The size of the observed α-syn species was calculated based on the recorded diffusion profiles. During the disaggregation reaction, two diffusing species were observed – one with a radius of ~350 nm, which declined in abundance over time and corresponds to the α-syn fibrils and another one

with a hydrodynamic radius of ~3 nm, which increased in abundance over time and corresponds to α-syn monomers.

By combining our experimental data with insights from previous studies (Gao *et al.*, 2015; Wentink *et al.*, 2020; see Chapter 1.12.2), we were able to describe a more detailed molecular mechanism of α-syn fibril disaggregation by the Hsp70 chaperone machinery: In a first step, DnajB1 is binding to the α-syn fibrils, most likely to the α-syn C-terminus that is protruding from the fibril core (Wentink *et al.*, 2020). Hsc70 is subsequently recruited to the fibrils by DnajB1. Once Hsc70 is bound, ATP is hydrolyzed and DnajB1 dissociates from the fibrils. More Hsc70 molecules are binding to the fibrils and Apg2 joins the complex. Apg2 may reshuffle Hsc70 proteins, which results in a high Hsc70 concentration at the fibril ends. At the end of the reaction cycle, α-syn monomers are dissociated from the fibrils, which is directly coupled to the dissociation of ADP from Hsc70 and the disassembly of the chaperone machinery.

Our proposed mechanism implicates that during disaggregation, fibril fragmentation is largely avoided, preventing the formation of small fibrillar species that could serve as potential seeds during aggregate propagation. Since the mechanism of the disaggregation reaction has only been studied *in vitro*, more detailed follow-up studies have to be conducted in cells.

3.3.1 Future perspectives

So far, only little is known about the amyloid fibril disaggregation activities of Hsp70 *in cellulo* and previous reports seem contradictory: A recent study by the Nussbaum-Krammer and Bukau groups reported that the Hsp110/Hsp70 machinery generates seeding competent α-syn species in *C. elegans* (Tittelmeier, 2020). Tittelmeier *et al.* observed that upon knock down of Hsp110, a reduced amount of α-syn-YFP (Yellow Fluorescent Protein) foci forms in *C. elegans* muscle tissue (Tittelmeier, 2020). Contrary, the Chandra group observed a protective effect of Hsp110 against α-syn seeded aggregation in mouse brain (Taguchi *et al.*, 2019). Taguchi *et al.* showed that overexpression of Hsp110 protects neurons in mouse brain from α-syn seeded aggregation. Upon overexpression of Hsp110, the spread of injected α-syn aggregates is decreased (Taguchi *et al.*, 2019).

Differences in the model systems used may be responsible for these seemingly contradictory observations: While α-syn aggregates readily in *C. elegans* and *de novo* aggregate formation can be observed, the mouse model is dependent on α-syn seeded aggregation with PFFs. More research needs to be conducted in cells to elucidate the effects of the Hsp70 system on aggregate formation and seeding.

3.4 The AAA+ chaperone VCP disaggregates Tau fibrils and generates aggregate seeds

In *S. cerevisiae,* prion fibril disaggregation is mediated by the AAA+ chaperone Hsp104 (see Chapter 1.12.3). Metazoan cells, however, do not express Hsp104 homologues. Recent studies identified the AAA+ ATPase VCP as a potential metazoan disaggregase (Ghosh, Roy and Ranjan, 2018; Darwich *et al.*, 2020), but the exact cell-biological mechanism of VCP-mediated disaggregation of amyloid fibrils remained elusive. In our study, we examined how human embryonic kidney cells and primary murine neurons dissociate tau aggregates and which components are required for the disaggregation reaction (Saha *et al.,* 2022).

To identify factors involved in the disaggregation of tau fibrils, a mass-spectrometric analysis of immunoprecipitated tau-YFP aggregates was conducted. VCP together with its cofactors Npl4 and Ufd1, as well as several subunits of the proteasome were identified as interactors of the aggregates. Subsequent biochemical and cell-biological experiments showed that indeed VCP, in cooperation with the proteasome, is required for the disaggregation reaction.

Unlike Hsp104, VCP requires ubiquitination of its substrate. We found that tau aggregates were labeled with K48-linked ubiquitin chains. Upon chemical inhibition of the E1 ubiquitin enzymes, tau aggregates were no longer ubiquitinated, which prevented disaggregation by VCP and stabilized the aggregates.

Another difference between Hsp104 and VCP concerns the interaction with Hsp70. While Hsp104 interacts with Hsp70 via its M-domain (Sielaff and Tsai, 2010), VCP lacks this domain and has not been found to interact with Hsp70 directly. Hsp70

function is, however, important for the disaggregation reaction of tau aggregates, since inhibition of Hsp70 during the reaction results in accumulation of small tau aggregates that do not get dissolved. We hypothesized that Hsp70 may act downstream of VCP to disaggregate small aggregate species produced by VCP action.

VCP gene mutations are associated with protein misfolding diseases, including AD, PD, MSP and FTD (Tang and Xia, 2016). Darwich *et al.* described a *VCP* gene mutation (D395G) that is directly linked to a disease termed 'vacuolar tauopathy' (Darwich *et al.*, 2020). Vacuolar tauopathy is characterized by vacuolar structures in the temporal and visual cortex and NFTs in the frontal, motor and cingulate cortex. The mutation D395G is located in the lid subdomain of the D1 ATPase and results in a destabilization and decreased function of VCP. The authors found that upon overexpression of the D395G *VCP* mutant, seeded tau aggregation in human embryonic kidney cells is increased (Darwich *et al.*, 2020). Surprisingly, in our study, the D395G mutant does not have a significant effect on the disaggregation reaction.

This result might be explained by differences in the experimental set-up: While Darwich *et al.* expressed the *VCP* mutant prior to aggregate seeding, we first induced aggregation and expressed the mutant subsequently. Expression of the mutant prior to seeded aggregation might change the seeding event itself: A recent study described a direct relationship between VCP function and seeded aggregation of α-syn and TDP-43 (Transactive response DNA binding protein of 43 kDa) (Zhu *et al.*, 2022). Upon chemical inhibition of VCP, the amount of α-syn and TDP-43 seeded aggregation was increased in Förster resonance energy transfer (FRET) biosensor cells as well as in mouse models. The authors hypothesized that the observed effect might be due to VCP's role in lysophagy: α-Syn and TDP-43 seeds enter the cytoplasm through damaged endolysosomes. To avoid the escape of the seeds through damaged lysosomes, a constant turnover of these organelles and the degradation of dysfunctional ones is required. Interestingly, VCP plays a role in the degradation of damaged lysosomes by autophagy (Papadopoulos *et al.*, 2017).

Remarkably, VCP does not only extract tau monomers from the amyloid fibrils, but also forms seeding competent smaller tau aggregates as a byproduct. These smaller species may occur during the disaggregation reaction due to fragmentation of the amyloid fibrils and could be potential substrates for downstream chaperone

machineries or the proteasome. If these small aggregates are not cleared from the cytoplasm directly, they can induce additional seeded aggregation. It remains to be seen whether VCP can be targeted for potential pharmacological intervention with tauopathies.

3.4.1. Future perspectives

To elucidate the exact molecular mechanism of VCP-mediated disaggregation of tau aggregates, *in vitro* disaggregation reactions need to be performed. The kinetics of the reaction could be determined by measuring ThT fluorescence and the structural basis of the interaction between VCP, its cofactors, the tau amyloid fibrils and the ubiquitin chains could be explored by cryo-EM and cryo-ET. One interesting aspect for future study is the conformation of AAA+ ATPases that are acting on the fibrils versus those that are unbound. Differences in the nucleotide state as well as in the arrangement of the hexameric subunits could be of special interest in understanding how AAA+ chaperones dissociate amyloid fibrils.

To reconstitute the disaggregation reaction *in vitro*, all participating proteins need to be purified, the tau fibrils need to be formed and then ubiquitinated. So far, however, the E3 ligase that is ubiquitinating tau aggregates *in cellulo* has not yet been identified. A genetic knock-out screen in combination with immunofluorescence or immunoblot analyses may help to identify this E3 ligase.

4 Abbreviations

Å	Ångström
aa	Amino acid
AAA+	ATPases associated with diverse cellular activities
Aβ	Amyloid-β
ACD	α-Crystalline core domain
AD	Alzheimer's disease
ADP	Adenosine-di-phosphate
AFM	Atomic force microscopy
Amg	Amygdala
APG2	Heat shock 70-related protein APG-2
APLP1	Amyloid precursor-like protein 1
APOE	Apolipoprotein E
APOJ	Apolipoprotein J
APP	Amyloid-beta precursor protein
ATG	Autophagy-related protein
ATP	Adenosine-tri-phosphate
BSE	Bovine spongiform encephalopathy
C	Celsius
C. elegans	*Caenorhabditis elegans*
CB	Cerebellum
CBD	Corticobasal degeneration
CHCHD2	Coiled-coil-helix-coiled-coil-helix domain containing 1
Chmp2a	Charged multivesicular body protein 2a
CJD	Creuzfeld-Jakob-disease
CLEM	Correlative light electron microscopy
ClpB	Caseinolytic peptidase B protein homolog
Clu	Clusterin
CNS	Central nervous system

CRISPR	Clustered regularly interspaced short palindromic repeats
cryo-EM	Cryo-electron microscopy
cryo-ET	Cryo-electron tomography
CSF	Cerebral spinal fluid
CTD	C-terminal domain
CTE	Chronic traumatic encephalopathy
C-terminus	Carboxy terminus
Ctx	Cortex
Da	Dalton
DBS	Deep brain stimulation
DJ1	Daisuke-Junko-1
DLB	Dementia with Lewy bodies
DNA	Deoxyribonucleic acid
DNAJB1	DnaJ heat shock protein family member B1
DPBS	Dulbecco’s phosphate buffered saline
E1	Ubiquitin activating enzyme
E2	Ubiquitin conjugating enzyme
E3	Ubiquitin ligating enzyme
E. coli	*Escherichia coli*
ECS	Extracellular space
eIF4G1	Eukaryotic translation initiation factor 4 gamma 1
EM	Electron microscopy
ER	Endoplasmic reticulum
ERAD	ER-associated degradation
ESCRT	Endosomal sorting complex required for transport
FIB	Focused ion beam
FRET	Förster resonance energy transfer
FTD	Frontotemporal degeneration
FTDP-17	Frontotemporal dementia and parkinsonism linked to chromosome 17
GABARAP	Gamma-aminobutyric acid receptor-associated protein

Gal8	Galectin 8
GBA1	Glucosylceramidase beta 1
GCI	Glial cell cytoplasmic inclusion
GFP	Green fluorescent protein
GFTs	Gliofibrillary tangles
GRPE	Gro-P like protein E
GTP	Guanosine-tri-phosphate
GWAS	Genome-wide association studies
H-bond	Hydrogen-bond
HECT	Homologous to the EAP6 carboxyl terminus
Hsc70	Heat shock cognate 71 KDa protein
Hsp	Heat shock protein
HSPG	Heparan sulfate proteoglycan
IBMPFD	Inclusion bodies myopathy Paget disease and frontotemporal dementia
IDP	Intrinsically disordered protein
K (Ubi)	Ubiquitination
KO	Knock out
LAG3	Lymphocyte activation gene 3
LB	Lewy body
LC3	Light chain 3
LDL	Low density lipoprotein
L-DOPA	Levodopa
LIR	LC3 interacting region
LOAD	Late onset Alzheimer’s disease
LRP1 / 2	Low density lipoprotein receptor-related protein 1 and 2
LRRK2	Leucin rich repeat kinase 2
MAD	Mitochondria-associated degradation
MAPT	Microtubule binding protein tau
MD	Middle domain
MSA	Multiple system atrophy
MSP	Multisystem proteinopathies

MT	Microtubule
MTBD	Microtubule binding domain
NAC	Non-Aβ-component of AD amyloid
NBD	Nucleotide binding domain
NBR1	Neighbor of BRCA1 gene 1 protein
N-domain	N-terminal domain
NEF	Nucleotide exchange factor
NFTs	Neurofibrillary tangles
nm	Nanometer
NMR	Nuclear magnetic resonance
Npl4	Nuclear protein localization protein 4 homolog
NTD	N-terminal domain
N-terminus	Amino terminus
p62	Ubiquitin-binding protein p62 / Sequestosome-1
PD	Parkinson’s disease
PFFs	Preformed fibrils
PHF	Paired helical filaments
PiD	Pick’s disease
PINK1	PTEN-induced putative kinase 1
PMCA	Protein misfolding cyclic amplification
PQC	Protein quality control
PRKN	Parkin RBR E3 ubiquitin protein ligase
PrP^{C}	Prion protein, cellular
PrP^{SC}	Prion protein, scrapie form
PRPN	Prion protein (gene)
PSEN 1 / 2	Persenilin 1 and 2
PTM	Posttranslational modification
RAD	Ribosome-associated degradation
REM	Rapid eye movement
RING	Really interesting new gene
RNA	Ribonucleic acid
ROS	Reactive oxygen species

RPN	Regulatory particle of non-ATPase
RPT	Regulatory particle of triple-ATPase
S	Svedberg
SBD	Substrate binding domain
S. cerevisiae	*Saccharomyces cerevisiae*
SDS	Sodium-dodecyl-sulfate
SDS-PAGE	Sodium dodecylsulfate polyacrylamide gel electrophoresis
SF	Straight filament
sHsp	Small heat shock protein
SN	*Substantia nigra*
SNCA	α-Synuclein, α-Syn
SORL1	Sortilin related receptor 1
Sup35	Eukaryotic peptide chain release factor GTP-binding subunit
Tau	MAPT – MT-associated protein tau
TDP-43	Transactive response DNA binding protein of 43 kDa
ThT	Thioflavin T
TREM2	Triggering receptor expressed on myeloid cells 2
UBA	Ubiquitin associated
UBX	Ubiquitin X regulatory
Ufd1	Ubiquitin fusion degradation protein 1 homolog
UPS	Ubiquitin proteasome system
Ure2	Transcriptional regulator URE2
VCP	Vasolin containing protein
VLDLR	Very low density lipoprotein receptor
VPS35	Vascular protein sorting 35
wt	Wild type
YFP	Yellow fluorescent protein

5 Literature

Adams, J. (2003) ‘The proteasome: structure, function, and role in the cell’, *Cancer Treatment Reviews*, 29, pp. 3–9.

Alam, P. *et al.* (2019) ‘α-synuclein oligomers and fibrils: a spectrum of species, a spectrum of toxicities’, *Journal of Neurochemistry*, 150(5), pp. 522–534.

Alberts, B. *et al.* (2002) *Molecular Biology of the Cell*. 4th edn. Garland Science.

Alqabandi, M. *et al.* (2021) ‘The ESCRT-III isoforms CHMP2A and CHMP2B display different effects on membranes upon polymerization’, *BMC Biology*, 19(1), p. 66.

Appel-Cresswell, S. *et al.* (2013) ‘Alpha-synuclein p.H50Q, a novel pathogenic mutation for Parkinson’s disease’, *Movement Disorders*, 28(6), pp. 811–813.

Arima, K. *et al.* (1998) ‘Immunoelectron-microscopic demonstration of NACP/α-synuclein-epitopes on the filamentous component of Lewy bodies in Parkinson’s disease and in dementia with Lewy bodies’, *Brain Research*, 808(1), pp. 93–100.

Armstrong, M.J. and Okun, M.S. (2020) ‘Diagnosis and Treatment of Parkinson Disease: A Review’, *JAMA*, 323(6), pp. 548–560.

Bakthisaran, R., Tangirala, R. and Rao, Ch.M. (2015) ‘Small heat shock proteins: Role in cellular functions and pathology’, *Biochimica et Biophysica Acta (BBA) - Proteins and Proteomics*, 1854(4), pp. 291–319.

Balch, W.E. *et al.* (2008) ‘Adapting proteostasis for disease intervention’, *Science (New York, N.Y.)*, 319(5865), pp. 916–919.

Balchin, D., Hayer-Hartl, M. and Hartl, F.U. (2016) ‘In vivo aspects of protein folding and quality control’, *Science*, 353(6294):aac4354

Bartels, T., Choi, J.G. and Selkoe, D.J. (2011) ‘α-Synuclein occurs physiologically as a helically folded tetramer that resists aggregation’, *Nature*, 477(7362), pp. 107–110.

Bature, F. *et al.* (2017) ‘Signs and symptoms preceding the diagnosis of Alzheimer’s disease: a systematic scoping review of literature from 1937 to 2016’, *BMJ Open*, 7(8), p. e015746.

Bäuerlein, F.J.B. *et al.* (2017) ‘In Situ Architecture and Cellular Interactions of PolyQ Inclusions’, *Cell*, 171(1), pp. 179-187.e10.

Benaki, D.C. *et al.* (1998) ‘Laser-Raman and FT-IR spectroscopic studies of peptide-analogues of silkmoth chorion protein segments’, *International Journal of Biological Macromolecules*, 23(1), pp. 49–59.

Benazzouz, A. *et al.* (2014) ‘Involvement of dopamine loss in extrastriatal basal ganglia nuclei in the pathophysiology of Parkinson’s disease’, *Frontiers in Aging Neuroscience*, 6, p. 87.

Bennhold, H. (1922) ‘Eine spezifische Amyloid Färbung mit Kongorot.’ Münchener Medizinische Wochenschrift, 69, pp. 1537-1538.

Berger, C. *et al.* (2022) ‘Plasma FIB milling for the determination of structures in situ’. bioRxiv, p. 2022.08.01.502333.

Berriman, J. *et al.* (2003) ‘Tau filaments from human brain and from in vitro assembly of recombinant protein show cross-β structure’, *Proceedings of the National Academy of Sciences of the United States of America*, 100(15), pp. 9034–9038.

Bettens, K. *et al.* (2015) ‘Reduced secreted clusterin as a mechanism for Alzheimer-associated CLU mutations’, *Molecular Neurodegeneration*, 10, p. 30.

Billingsley, K.J. *et al.* (2018) ‘Genetic risk factors in Parkinson’s disease’, *Cell and tissue research*, 373(1), pp. 9–20.

Blauwendraat, C. *et al.* (2019) ‘Parkinson’s disease age at onset genome-wide association study: Defining heritability, genetic loci, and α-synuclein mechanisms’, *Movement Disorders: Official Journal of the Movement Disorder Society*, 34(6), pp. 866–875.

Bolen, D.W. and Rose, G.D. (2008) ‘Structure and Energetics of the Hydrogen-Bonded Backbone in Protein Folding’, *Annual Review of Biochemistry*, 77(1), pp. 339–362.

Bouchon, A., Dietrich, J. and Colonna, M. (2000) ‘Cutting Edge: Inflammatory Responses Can Be Triggered by TREM-1, a Novel Receptor Expressed on Neutrophils and Monocytes’, *The Journal of Immunology*, 164(10), pp. 4991–4995.

Boyer, D.R. *et al.* (2019) ‘Structures of fibrils formed by α-synuclein hereditary disease mutant H50Q reveal new polymorphs’, *Nature Structural & Molecular Biology*, 26(11), pp. 1044–1052.

Braak, H. *et al.* (2003) ‘Staging of brain pathology related to sporadic Parkinson’s disease’, *Neurobiology of Aging*, 24(2), pp. 197–211.

Braak, H. and Braak, E. (1991) ‘Neuropathological stageing of Alzheimer-related changes’, *Acta Neuropathologica*, 82(4), pp. 239–259.

Breydo, L., Wu, J.W. and Uversky, V.N. (2012) ‘α-Synuclein misfolding and Parkinson’s disease’, *Biochimica et Biophysica Acta (BBA) - Molecular Basis of Disease*, 1822(2), pp. 261–285.

Brockwell, D.J. and Radford, S.E. (2007) ‘Intermediates: ubiquitous species on folding energy landscapes?’, *Current Opinion in Structural Biology*, 17(1), pp. 30–37.

Bukau, B. and Horwich, A.L. (1998) ‘The Hsp70 and Hsp60 Chaperone Machines’, *Cell*, 92(3), pp. 351–366.

Burré, J. *et al.* (2013) ‘Properties of native brain α-synuclein’, *Nature*, 498(7453), pp. E4–E6.

Burré, J. (2015) ‘The Synaptic Function of α-Synuclein’, *Journal of Parkinson’s Disease*, 5(4), pp. 699–713.

Caceres, A. and Kosik, K.S. (1990) ‘Inhibition of neurite polarity by tau antisense oligonucleotides in primary cerebellar neurons’, *Nature*, 343(6257), pp. 461–463.

Calero, M. *et al.* (2000) ‘Apolipoprotein J (clusterin) and Alzheimer’s disease’, *Microscopy Research and Technique*, 50(4), pp. 305–315.

Cao, J. *et al.* (2019) ‘Endo-lysosomal pathway and ubiquitin-proteasome system dysfunction in Alzheimer’s disease pathogenesis’, *Neuroscience letters*, 703, pp. 68–78.

Capouch, S.D., Farlow, M.R. and Brosch, J.R. (2018) ‘A Review of Dementia with Lewy Bodies’ Impact, Diagnostic Criteria and Treatment’, *Neurology and Therapy*, 7(2), pp. 249–263.

Carnazza, K.E. *et al.* (2020) *BETA- AND GAMMA-SYNUCLEINS MODULATE SYNAPTIC VESICLE-BINDING OF ALPHA-SYNUCLEIN*. preprint Biorxiv. Neuroscience. e2012435118

Carver, J.A. *et al.* (2017) ‘The functional roles of the unstructured N- and C-terminal regions in αB-crystallin and other mammalian small heat-shock proteins’, *Cell Stress and Chaperones*, 22(4), pp. 627–638.

Cascella, R. *et al.* (2021) ‘The release of toxic oligomers from α-synuclein fibrils induces dysfunction in neuronal cells’, *Nature Communications*, 12(1), p. 1814.

Chau, V. *et al.* (1989) ‘A Multiubiquitin Chain Is Confined to Specific Lysine in a Targeted Short-Lived Protein’, *Science*, 243(4898), pp. 1576–1583.

Chen, S.W. *et al.* (2015) ‘Structural characterization of toxic oligomers that are kinetically trapped during α-synuclein fibril formation’, *Proceedings of the National Academy of Sciences*, 112(16), pp. E1994–E2003.

Chernoff, Y.O. *et al.* (1995) ‘Role of the Chaperone Protein Hsp104 in Propagation of the Yeast Prion-Like Factor [psi+]’, *Science* 1995 May 12;268(5212):880-4. pp. 880-884

Chernova, T.A., Wilkinson, K.D. and Chernoff, Y.O. (2017) ‘Prions, Chaperones, and Proteostasis in Yeast’, *Cold Spring Harbor Perspectives in Biology*, 9(2), p. a023663.

Ciechanover, A. *et al.* (1980) ‘ATP-dependent conjugation of reticulocyte proteins with the polypeptide required for protein degradation’, *Proceedings of the National Academy of Sciences of the United States of America*, 77(3), pp. 1365–1368.

Clayton, D.F. and George, J.M. (1998) ‘The synucleins: a family of proteins involved in synaptic function, plasticity, neurodegeneration and disease’, *Trends in Neurosciences*, 21(6), pp. 249–254.

Collard, M.W. and Griswold, M.D. (1987) ‘Biosynthesis and molecular cloning of sulfated glycoprotein 2 secreted by rat Sertoli cells’, *Biochemistry*, 26(12), pp. 3297–3303.

Collins, G.A. and Goldberg, A.L. (2017) ‘The Logic of the 26S Proteasome’, *Cell*, 169(5), pp. 792–806.

Cooney, I. *et al.* (2019) ‘Structure of the Cdc48 segregase in the act of unfolding an authentic substrate’, *Science (New York, N.Y.)*, 365(6452), pp. 502–505.

Cremades, N., Chen, S.W. and Dobson, C.M. (2017) ‘Chapter Three - Structural Characteristics of α-Synuclein Oligomers’, in M. Sandal (ed.) *International Review of Cell and Molecular Biology*. Academic Press (Early Stage Protein Misfolding and Amyloid Aggregation), pp. 79–143.

Culvenor, J.G. *et al.* (1999) ‘Non-Aβ Component of Alzheimer’s Disease Amyloid (NAC) Revisited: NAC and α-Synuclein Are Not Associated with Aβ Amyloid’, *The American Journal of Pathology*, 155(4), pp. 1173–1181.

Dai, M.-H. *et al.* (2017) ‘The genes associated with early-onset Alzheimer’s disease’, *Oncotarget*, 9(19), pp. 15132–15143.

Danzer, K.M. *et al.* (2007) 'Different species of alpha-synuclein oligomers induce calcium influx and seeding', *The Journal of Neuroscience: The Official Journal of the Society for Neuroscience*, 27(34), pp. 9220–9232.

Darwich, N.F. *et al.* (2020) 'Autosomal dominant VCP hypomorph mutation impairs disaggregation of PHF-tau', *Science*, 370(6519), p. eaay8826.

Darwin, K.H. (2009) 'Prokaryotic ubiquitin-like protein (Pup), proteasomes and pathogenesis', Nature Reviews Microbiology, 7(7), pp. 485–491.

Daugaard, M., Rohde, M. and Jäättelä, M. (2007) 'The heat shock protein 70 family: Highly homologous proteins with overlapping and distinct functions', *FEBS Letters*, 581(19), pp. 3702–3710.

De Silva, H.V. *et al.* (1990) 'Apolipoprotein J: structure and tissue distribution', *Biochemistry*, 29(22), pp. 5380–5389.

DeMattos, R.B. *et al.* (2002) 'Clusterin promotes amyloid plaque formation and is critical for neuritic toxicity in a mouse model of Alzheimer's disease', *Proceedings of the National Academy of Sciences*, 99(16), pp. 10843–10848.

Despres, C. *et al.* (2017) 'Identification of the Tau phosphorylation pattern that drives its aggregation', *Proceedings of the National Academy of Sciences of the United States of America*, 114(34), pp. 9080–9085.

Diaz-Espinoza, R. (2021) 'Recent High-Resolution Structures of Amyloids Involved in Neurodegenerative Diseases', *Frontiers in Aging Neuroscience*, 13, p. 782617.

Dikic, I. and Elazar, Z. (2018) 'Mechanism and medical implications of mammalian autophagy', *Nature Reviews Molecular Cell Biology*, 19(6), pp. 349–364.

Dill, K.A. (1990) 'Dominant forces in protein folding', *Biochemistry*, 29(31), pp. 7133–7155.

Dittmar, G. and Winklhofer, K.F. (2020) ‘Linear Ubiquitin Chains: Cellular Functions and Strategies for Detection and Quantification’, *Frontiers in Chemistry*, 7, p. 915.

Dobson, C.M., Šali, A. and Karplus, M. (1998) ‘Protein Folding: A Perspective from Theory and Experiment’, *Angewandte Chemie International Edition*, 37(7), pp. 868–893.

Dragovic, Z. *et al.* (2006) ‘Molecular chaperones of the Hsp110 family act as nucleotide exchange factors of Hsp70s’, *The EMBO Journal*, 25(11), pp. 2519–2528.

Dubochet, J. *et al.* (1988) ‘Cryo-electron microscopy of vitrified specimens’, *Quarterly Reviews of Biophysics*, 21(2), pp. 129–228.

Duennwald, M.L., Echeverria, A. and Shorter, J. (2012) ‘Small Heat Shock Proteins Potentiate Amyloid Dissolution by Protein Disaggregases from Yeast and Humans’, *PLOS Biology*, 10(6), p. e1001346.

Dunker, A.K. *et al.* (2001) ‘Intrinsically disordered protein’, *Journal of Molecular Graphics and Modelling*, 19(1), pp. 26–59.

Elbaum-Garfinkle, S. *et al.* (2014) ‘Tau mutants bind tubulin heterodimers with enhanced affinity’, *Proceedings of the National Academy of Sciences*, 111(17), pp. 6311–6316.

Eliezer, D. *et al.* (2001) ‘Conformational properties of α-synuclein in its free and lipid-associated states11Edited by P. E. Wright’, *Journal of Molecular Biology*, 307(4), pp. 1061–1073.

Elsasser, S. *et al.* (2002) ‘Proteasome subunit Rpn1 binds ubiquitin-like protein domains’, *Nature Cell Biology*, 4(9), pp. 725–730.

Elsasser, S. *et al.* (2004) ‘Rad23 and Rpn10 Serve as Alternative Ubiquitin Receptors for the Proteasome*’, *Journal of Biological Chemistry*, 279(26), pp. 26817–26822.

Emanuele, M. and Chieregatti, E. (2015) ‘Mechanisms of Alpha-Synuclein Action on Neurotransmission: Cell-Autonomous and Non-Cell Autonomous Role’, *Biomolecules*, 5(2), pp. 865–892.

Emmenegger, M. *et al.* (2021) ‘LAG3 is not expressed in human and murine neurons and does not modulate α-synucleinopathies’, *EMBO molecular medicine*, 13(9), p. e14745.

Falcon, B. *et al.* (2018) ‘Structures of filaments from Pick’s disease reveal a novel tau protein fold’, *Nature*, 561(7721), pp. 137–140.

Falcon, B. *et al.* (2019) ‘Novel tau filament fold in chronic traumatic encephalopathy encloses hydrophobic molecules’, *Nature*, 568(7752), pp. 420–423.

Ferrari, V. *et al.* (2022) ‘Valosin Containing Protein (VCP): A Multistep Regulator of Autophagy’, *International Journal of Molecular Sciences*, 23(4), p. 1939.

Filippini, A. *et al.* (2021) ‘Extracellular clusterin limits the uptake of α-synuclein fibrils by murine and human astrocytes’, *Glia*, 69(3), pp. 681–696.

Fitzpatrick, A.W.P. *et al.* (2017) ‘Cryo-EM structures of tau filaments from Alzheimer’s disease’, *Nature*, 547(7662), pp. 185–190.

Fonseca-Ornelas, L. *et al.* (2017) ‘Small-Molecule-Induced Soluble Oligomers of α-Synuclein with Helical Structure’, *Chemistry – A European Journal*, 23(53), pp. 13010–13014.

Forno, L.S. (1996) ‘Neuropathology of Parkinson’s Disease’, *Journal of Neuropathology & Experimental Neurology*, 55(3), pp. 259–272.

Foster, E.M. et al. (2019) ‘Clusterin in Alzheimer’s Disease: Mechanisms, Genetics, and Lessons From Other Pathologies’, Frontiers in Neuroscience, 13. Available at: https://www.frontiersin.org/articles/10.3389/fnins.2019.00164

Freilich, R. *et al.* (2018) ‘Competing protein-protein interactions regulate binding of Hsp27 to its client protein tau’, *Nature Communications*, 9(1), p. 4563.

Fujiwara, H. *et al.* (2002) ‘α-Synuclein is phosphorylated in synucleinopathy lesions’, *Nature Cell Biology*, 4(2), pp. 160–164.

Fusco, G. *et al.* (2017) ‘Structural basis of membrane disruption and cellular toxicity by α-synuclein oligomers’, *Science*, 358(6369), pp. 1440–1443.

Gai, W.P. *et al.* (2003) ‘α-synuclein fibrils constitute the central core of oligodendroglial inclusion filaments in multiple system atrophy’, *Experimental Neurology*, 181(1), pp. 68–78.

Galvagnion, C. (2017) ‘The Role of Lipids Interacting with α-Synuclein in the Pathogenesis of Parkinson’s Disease’, *Journal of Parkinson’s Disease*, 7(3), pp. 433–450.

Gao, X. *et al.* (2015) ‘Human Hsp70 Disaggregase Reverses Parkinson’s-Linked α-Synuclein Amyloid Fibrils’, *Molecular Cell*, 59(5), pp. 781–793.

Gerards, W.L. *et al.* (1998) ‘Structure and assembly of the 20S proteasome’, *Cellular and molecular life sciences: CMLS*, 54(3), pp. 253–262.

Ghetti, B. *et al.* (1996) ‘Prion protein amyloidosis’, *Brain Pathology (Zurich, Switzerland)*, 6(2), pp. 127–145.

Ghosh, D.K., Roy, A. and Ranjan, A. (2018) ‘The ATPase VCP/p97 functions as a disaggregase against toxic Huntingtin-exon1 aggregates’, *FEBS Letters*, 592(16), pp. 2680–2692.

Giasson, B.I. *et al.* (2001) ‘A Hydrophobic Stretch of 12 Amino Acid Residues in the Middle of α-Synuclein Is Essential for Filament Assembly*’, *Journal of Biological Chemistry*, 276(4), pp. 2380–2386.

Goedert, M., Eisenberg, D.S. and Crowther, R.A. (2017) ‘Propagation of Tau Aggregates and Neurodegeneration’, *Annual Review of Neuroscience*, 40(1), pp. 189–210.

Goedert, M. and Jakes, R. (1990) ‘Expression of separate isoforms of human tau protein: correlation with the tau pattern in brain and effects on tubulin polymerization.’, *The EMBO Journal*, 9(13), pp. 4225–4230.

Goedert, M. and Jakes, R. (2005) ‘Mutations causing neurodegenerative tauopathies’, *Biochimica et Biophysica Acta (BBA) - Molecular Basis of Disease*, 1739(2), pp. 240–250.

Goldknopf, I.L. and Busch, H. (1977) ‘Isopeptide linkage between nonhistone and histone 2A polypeptides of chromosomal conjugate-protein A24’, *Proceedings of the National Academy of Sciences*, 74(3), pp. 864–868.

Goldman, J.E. *et al.* (1983) ‘Lewy bodies of Parkinson’s disease contain neurofilament antigens’, *Science*, 221(4615), pp. 1082–1084.

Goldstein, G. *et al.* (1975) ‘Isolation of a polypeptide that has lymphocyte-differentiating properties and is probably represented universally in living cells’, *Proceedings of the National Academy of Sciences of the United States of America*, 72(1), pp. 11–15.

Golenhofen, G. and Bartelt-Kirbach, B.-K. (2016) ‘The Impact of Small Heat Shock Proteins (HspBs) in Alzheimer’s and Other Neurological Diseases’, *Current Pharmaceutical Design*, 22(26), pp. 4050–4062.

Gratuze, M., Leyns, C.E.G. and Holtzman, D.M. (2018) ‘New insights into the role of TREM2 in Alzheimer’s disease’, *Molecular Neurodegeneration*, 13(1), p. 66.

Grey, M. *et al.* (2011) ‘Membrane Interaction of α-Synuclein in Different Aggregation States’, *Journal of Parkinson’s Disease*, 1(4), pp. 359–371.

Grice, G.L. and Nathan, J.A. (2016) ‘The recognition of ubiquitinated proteins by the proteasome’, *Cellular and Molecular Life Sciences*, 73(18), pp. 3497–3506.

Groll, M. *et al.* (1997) ‘Structure of 20S proteasome from yeast at 2.4Å resolution’, *Nature*, 386(6624), pp. 463–471.

Grosas, A.B. *et al.* (2020) 'The Aggregation of αB-Crystallin under Crowding Conditions Is Prevented by αA-Crystallin: Implications for α-Crystallin Stability and Lens Transparency', *Journal of Molecular Biology*, 432(20), pp. 5593–5613.

Grozdanov, V. and Danzer, K.M. (2018) 'Release and uptake of pathologic alpha-synuclein', *Cell and Tissue Research*, 373(1), pp. 175–182.

Grundke-Iqbal, I. *et al.* (1986) 'Abnormal phosphorylation of the microtubule-associated protein tau (tau) in Alzheimer cytoskeletal pathology', *Proceedings of the National Academy of Sciences of the United States of America*, 83(13), pp. 4913–4917.

Guerreiro, R. *et al.* (2013) 'TREM2 Variants in Alzheimer's Disease', *New England Journal of Medicine*, 368(2), pp. 117–127.

Guerrero-Ferreira, R. *et al.* (2018) 'Cryo-EM structure of alpha-synuclein fibrils', *eLife*. Edited by J. Kuriyan et al., 7, p. e36402.

Guo, J.L. *et al.* (2016) 'Unique pathological tau conformers from Alzheimer's brains transmit tau pathology in nontransgenic mice', *The Journal of Experimental Medicine*, 213(12), pp. 2635–2654.

Guo, T., Noble, W. and Hanger, D.P. (2017) 'Roles of tau protein in health and disease', *Acta Neuropathologica*, 133(5), pp. 665–704.

Hanes, J. *et al.* (2009) 'Rat tau proteome consists of six tau isoforms: implication for animal models of human tauopathies', *Journal of Neurochemistry*, 108(5), pp. 1167–1176.

Hansen, C. *et al.* (2011) 'α-Synuclein propagates from mouse brain to grafted dopaminergic neurons and seeds aggregation in cultured human cells', *The Journal of Clinical Investigation*, 121(2), pp. 715–725.

Harold, D. *et al.* (2009) 'Genome-wide association study identifies variants at CLU and PICALM associated with Alzheimer's disease', *Nature Genetics*, 41(10), pp. 1088–1093.

Hartl, F.U. (1996) ‘Molecular chaperones in cellular protein folding’, *Nature*, 381(6583), pp. 571–580.

Hartl, F.U., Bracher, A. and Hayer-Hartl, M. (2011) ‘Molecular chaperones in protein folding and proteostasis’, *Nature*, 475(7356), pp. 324–332.

Hashimoto, M. *et al.* (2004) ‘The Role of alpha-synuclein assembly and metabolism in the pathogenesis of Lewy body disease’, *Journal of molecular neuroscience: MN*, 24(3), pp. 343–352.

Haslbeck, M. *et al.* (2005) ‘Some like it hot: the structure and function of small heat-shock proteins’, *Nature Structural & Molecular Biology*, 12(10), pp. 842–846.

Haslbeck, M., Weinkauf, S. and Buchner, J. (2015) ‘Regulation of the Chaperone Function of Small Hsps’, in R.M. Tanguay and L.E. Hightower (eds) *The Big Book on Small Heat Shock Proteins*. Cham: Springer International Publishing (Heat Shock Proteins), pp. 155–178.

Heo, J.-M. *et al.* (2010) ‘A Stress-Responsive System for Mitochondrial Protein Degradation’, *Molecular Cell*, 40(3), pp. 465–480.

Hershko, A. *et al.* (1980) ‘Proposed role of ATP in protein breakdown: conjugation of protein with multiple chains of the polypeptide of ATP-dependent proteolysis’, *Proceedings of the National Academy of Sciences*, 77(4), pp. 1783–1786.

Hershko, A. and Ciechanover, A. (1998) ‘The Ubiquitin System’, *Annual Review of Biochemistry*, 67(1), pp. 425–479.

Hipp, M.S., Kasturi, P. and Hartl, F.U. (2019) ‘The proteostasis network and its decline in ageing’, *Nature Reviews Molecular Cell Biology*, 20(7), pp. 421–435.

Hoehn, M.M. and Yahr, M.D. (1967) ‘Parkinsonism: onset, progression, and mortality’, *Neurology*, 17(5), pp. 427–427.

Hoffman-Zacharska, D. *et al.* (2013) 'Novel A18T and pA29S substitutions in α-synuclein may be associated with sporadic Parkinson's disease', *Parkinsonism & Related Disorders*, 19(11), pp. 1057–1060.

Holmes, B.B. *et al.* (2013) 'Heparan sulfate proteoglycans mediate internalization and propagation of specific proteopathic seeds', *Proceedings of the National Academy of Sciences of the United States of America*, 110(33), pp. E3138-3147.

Hong, M. *et al.* (1998) 'Mutation-Specific Functional Impairments in Distinct Tau Isoforms of Hereditary FTDP-17', *Science*, 282(5395), pp. 1914–1917.

Huibregtse, J.M. *et al.* (1995) 'A family of proteins structurally and functionally related to the E6-AP ubiquitin-protein ligase.', *Proceedings of the National Academy of Sciences*, 92(7), pp. 2563–2567.

Ilie, I.M. and Caflisch, A. (2019) 'Simulation Studies of Amyloidogenic Polypeptides and Their Aggregates', Chemical Reviews, 119(12), pp. 6956–6993. Available at: https://doi.org/10.1021/acs.chemrev.8b00731.

Irwin, D.J. and Hurtig, H.I. (2018) 'The Contribution of Tau, Amyloid-Beta and Alpha-Synuclein Pathology to Dementia in Lewy Body Disorders', *Journal of Alzheimer's disease & Parkinsonism*, 8(4), p. 444.

Iwata, A. *et al.* (2003) 'Alpha-synuclein degradation by serine protease neurosin: implication for pathogenesis of synucleinopathies', *Human Molecular Genetics*, 12(20), pp. 2625–2635.

Jeganathan, S. *et al.* (2006) 'Global Hairpin Folding of Tau in Solution', *Biochemistry*, 45(7), pp. 2283–2293.

Jia, J. *et al.* (2018) 'Galectins control mTOR in response to endomembrane damage', *Molecular cell*, 70(1), pp. 120-135.e8.

Jiang, J. *et al.* (2007) 'Structural Basis of J Cochaperone Binding and Regulation of Hsp70', *Molecular cell*, 28(3), pp. 422–433.

Jiang, P. *et al.* (2017) ‘Impaired endo-lysosomal membrane integrity accelerates the seeding progression of α-synuclein aggregates’, *Scientific Reports*, 7(1), p. 7690.

Jin, L. *et al.* (2008) ‘Mechanism of Ubiquitin-Chain Formation by the Human Anaphase-Promoting Complex’, *Cell*, 133(4), pp. 653–665.

Johansen, K.K. *et al.* (2018) ‘A Case of Parkinson’s Disease with No Lewy Body Pathology due to a Homozygous Exon Deletion in Parkin’, *Case Reports in Neurological Medicine*, 2018, p. 6838965.

de Jong, W.W., Caspers, G.-J. and Leunissen, J.A.M. (1998) ‘Genealogy of the α-crystallin—small heat-shock protein superfamily’, *International Journal of Biological Macromolecules*, 22(3), pp. 151–162.

Jumper, J. *et al.* (2021) ‘Highly accurate protein structure prediction with AlphaFold’, *Nature*, 596(7873), pp. 583–589.

Kadavath, H. *et al.* (2015) ‘Tau stabilizes microtubules by binding at the interface between tubulin heterodimers’, *Proceedings of the National Academy of Sciences*, 112(24), pp. 7501–7506.

Kampinga, H.H. *et al.* (2009) ‘Guidelines for the nomenclature of the human heat shock proteins’, *Cell Stress and Chaperones*, 14(1), pp. 105–111.

Kampinga, H.H. and Craig, E.A. (2010) ‘The HSP70 chaperone machinery: J proteins as drivers of functional specificity’, *Nature Reviews Molecular Cell Biology*, 11(8), pp. 579–592.

Karpowicz, R.J. *et al.* (2017) ‘Selective imaging of internalized proteopathic α-synuclein seeds in primary neurons reveals mechanistic insight into transmission of synucleinopathies’, *The Journal of Biological Chemistry*, 292(32), pp. 13482–13497.

Kauzmann, W. (1959) ‘Some Factors in the Interpretation of Protein Denaturation11The preparation of this article has been assisted by a grant from

the National Science Foundation.', in C.B. Anfinsen et al. (eds) *Advances in Protein Chemistry*. Academic Press, pp. 1–63.

Kidd, M. (1963) 'Paired Helical Filaments in Electron Microscopy of Alzheimer's Disease', *Nature*, 197(4863), pp. 192–193.

Kim, J., Koo, B.-K. and Knoblich, J.A. (2020) 'Human organoids: model systems for human biology and medicine', *Nature Reviews Molecular Cell Biology*, 21(10), pp. 571–584.

Kim, Y.E. *et al.* (2013) 'Molecular chaperone functions in protein folding and proteostasis', *Annual Review of Biochemistry*, 82, pp. 323–355.

Kirkin, V. *et al.* (2009) 'A Role for NBR1 in Autophagosomal Degradation of Ubiquitinated Substrates', *Molecular Cell*, 33(4), pp. 505–516.

Kisselev, A.F. *et al.* (1999) 'The sizes of peptides generated from protein by mammalian 26 and 20 S proteasomes. Implications for understanding the degradative mechanism and antigen presentation', *The Journal of Biological Chemistry*, 274(6), pp. 3363–3371.

Köllensperger, M. *et al.* (2010) 'Presentation, diagnosis, and management of multiple system atrophy in Europe: Final analysis of the European multiple system atrophy registry', *Movement Disorders*, 25(15), pp. 2604–2612.

Komander, D. (2009) 'The emerging complexity of protein ubiquitination', *Biochemical Society Transactions*, 37(Pt 5), pp. 937–953.

Kordek, R. *et al.* (1999) 'Deposition of the prion protein (PrP) during the evolution of experimental Creutzfeldt-Jakob disease', *Acta Neuropathologica*, 98(6), pp. 597–602.

Kordower, J.H. *et al.* (2008) 'Lewy body-like pathology in long-term embryonic nigral transplants in Parkinson's disease', *Nature Medicine*, 14(5), pp. 504–506.

Krüger, R. *et al.* (1998) 'AlaSOPro mutation in the gene encoding α-synuclein in Parkinson's disease', *Nature Genetics*, 18(2), pp. 106–108.

Kuzuhara, S. *et al.* (1988) 'Lewy bodies are ubiquitinated - A light and electron microscopic immunocytochemical study', *Acta Neuropathologica*, 75(4), pp. 345–353.

Ladogana, A. and Kovacs, G.G. (2018) 'Chapter 13 - Genetic Creutzfeldt–Jakob disease', in M. Pocchiari and J. Manson (eds) *Handbook of Clinical Neurology*. Elsevier (Human Prion Diseases), pp. 219–242.

Lambert, J.-C. *et al.* (2009) 'Genome-wide association study identifies variants at CLU and CR1 associated with Alzheimer's disease', *Nature Genetics*, 41(10), pp. 1094–1099.

Lashuel, H.A. *et al.* (2013) 'The many faces of α-synuclein: from structure and toxicity to therapeutic target', *Nature Reviews Neuroscience*, 14(1), pp. 38–48.

Lashuel, H.A. (2020) 'Do Lewy bodies contain alpha-synuclein fibrils? and Does it matter? A brief history and critical analysis of recent reports', *Neurobiology of Disease*, 141, p. 104876.

Lautenschläger, J. *et al.* (2018) 'C-terminal calcium binding of α-synuclein modulates synaptic vesicle interaction', *Nature Communications*, 9(1), p. 712.

Lesage, S. *et al.* (2013) 'G51D α-synuclein mutation causes a novel Parkinsonian–pyramidal syndrome', *Annals of Neurology*, 73(4), pp. 459–471.

LeVine, H. (1993) 'Thioflavine T interaction with synthetic Alzheimer's disease beta-amyloid peptides: detection of amyloid aggregation in solution', *Protein Science: A Publication of the Protein Society*, 2(3), pp. 404–410.

Levinthal, C. (1968) 'Are there pathways for protein folding?', *Journal de Chimie Physique*, 65, pp. 44–45.

Lewy, F. (1912) 'Paralysis agitans. I', *Pathologische Anatomie. Handbuch der Neurologie,* pp. 920-933.

Li, B. *et al.* (2018) 'Cryo-EM of full-length α-synuclein reveals fibril polymorphs with a common structural kernel', *Nature Communications*, 9(1), p. 3609.

Li, Y. *et al.* (2018) ‘Amyloid fibril structure of α-synuclein determined by cryo-electron microscopy’, *Cell Research*, 28(9), pp. 897–903.

Liebman, S.W. and Chernoff, Y.O. (2012) ‘Prions in Yeast’, *Genetics*, 191(4), pp. 1041–1072.

Liu, F. and Gong, C.-X. (2008) ‘Tau exon 10 alternative splicing and tauopathies’, *Molecular Neurodegeneration*, 3(1), p. 8.

Liu, G. *et al.* (2016) ‘Convergent Genetic and Expression Datasets Highlight TREM2 in Parkinson’s Disease Susceptibility’, *Molecular Neurobiology*, 53(7), pp. 4931–4938.

Long, H. *et al.* (2021) ‘Wild-type α-synuclein inherits the structure and exacerbated neuropathology of E46K mutant fibril strain by cross-seeding’, *Proceedings of the National Academy of Sciences*, 118(20), p. e2012435118.

Lorick, K.L. *et al.* (1999) ‘RING fingers mediate ubiquitin-conjugating enzyme (E2)-dependent ubiquitination’, *Proceedings of the National Academy of Sciences*, 96(20), pp. 11364–11369.

Lövestam, S. *et al.* (2021) ‘Seeded assembly in vitro does not replicate the structures of α-synuclein filaments from multiple system atrophy’, *FEBS Open Bio*, 11(4), pp. 999–1013.

Lue, L.-F. *et al.* (2015) ‘TREM2 Protein Expression Changes Correlate with Alzheimer’s Disease Neurodegenerative Pathologies in Post-Mortem Temporal Cortices’, *Brain Pathology*, 25(4), pp. 469–480.

Luk, K.C. *et al.* (2009) ‘Exogenous α-synuclein fibrils seed the formation of Lewy body-like intracellular inclusions in cultured cells’, *Proceedings of the National Academy of Sciences*, 106(47), pp. 20051–20056.

Luk, K.C. *et al.* (2012) ‘Pathological α-synuclein transmission initiates Parkinson-like neurodegeneration in nontransgenic mice’, *Science (New York, N.Y.)*, 338(6109), pp. 949–953.

Lunati, A., Lesage, S. and Brice, A. (2018) ‘The genetic landscape of Parkinson’s disease’, *Revue Neurologique*, 174(9), pp. 628–643.

Magnani, E. *et al.* (2007) ‘Interaction of tau protein with the dynactin complex’, *The EMBO journal*, 26(21), pp. 4546–4554.

Mahul-Mellier, A.-L. *et al.* (2020) ‘The process of Lewy body formation, rather than simply α-synuclein fibrillization, is one of the major drivers of neurodegeneration’, *Proceedings of the National Academy of Sciences*, 117(9), pp. 4971–4982.

Maji, S.K. *et al.* (2009) ‘Functional amyloids as natural storage of peptide hormones in pituitary secretory granules’, *Science (New York, N.Y.)*, 325(5938), pp. 328–332.

Makin, O.S. and Serpell, L.C. (2005) ‘Structures for amyloid fibrils’, *The FEBS Journal*, 272(23), pp. 5950–5961.

Manzanza, N. de O., Sedlackova, L. and Kalaria, R.N. (2021) ‘Alpha-Synuclein Post-translational Modifications: Implications for Pathogenesis of Lewy Body Disorders’, *Frontiers in Aging Neuroscience*, 13, p. 690293.

Mao, X. *et al.* (2016) ‘Pathological α-synuclein transmission initiated by binding lymphocyte-activation gene 3’, *Science (New York, N.Y.)*, 353(6307), p. aah3374.

Masliah, E. *et al.* (1996) ‘Altered presynaptic protein NACP is associated with plaque formation and neurodegeneration in Alzheimer’s disease.’, *The American Journal of Pathology*, 148(1), pp. 201–210.

Mastronarde, D.N. and Held, S.R. (2017) ‘Automated Tilt Series Alignment and Tomographic Reconstruction in IMOD’, *Journal of structural biology*, 197(2), pp. 102–113.

Masuda-Suzukake, M. *et al.* (2013) ‘Prion-like spreading of pathological α-synuclein in brain’, *Brain*, 136(4), pp. 1128–1138.

May, P.C. *et al.* (1990) ‘Dynamics of gene expression for a hippocampal glycoprotein elevated in Alzheimer’s disease and in response to experimental lesions in rat’, *Neuron*, 5(6), pp. 831–839.

Mayer, M.P. (2010) ‘Gymnastics of Molecular Chaperones’, *Molecular Cell*, 39(3), pp. 321–331.

Mayer, M.P. and Bukau, B. (2005) ‘Hsp70 chaperones: Cellular functions and molecular mechanism’, *Cellular and Molecular Life Sciences*, 62(6), p. 670.

McDowell, G.S. and Philpott, A. (2013) ‘Non-canonical ubiquitylation: Mechanisms and consequences’, *The International Journal of Biochemistry & Cell Biology*, 45(8), pp. 1833–1842.

Meisl, G. *et al.* (2016) ‘Molecular mechanisms of protein aggregation from global fitting of kinetic models’, *Nature Protocols*, 11(2), pp. 252–272.

Metzger, M.B., Hristova, V.A. and Weissman, A.M. (2012) ‘HECT and RING finger families of E3 ubiquitin ligases at a glance’, *Journal of Cell Science*, 125(3), pp. 531–537.

Meyer, H. and Weihl, C.C. (2014) ‘The VCP/p97 system at a glance: connecting cellular function to disease pathogenesis’, *Journal of Cell Science*, 127(Pt 18), pp. 3877–3883.

MICHEL, D. *et al.* (1997) ‘Stress-induced transcription of the clusterin/apoJ gene’, *Biochemical Journal*, 328(1), pp. 45–50.

Mogk, A., Bukau, B. and Kampinga, H.H. (2018) ‘Cellular Handling of Protein Aggregates by Disaggregation Machines’, *Molecular Cell*, 69(2), pp. 214–226.

Moors, T.E. *et al.* (2021) ‘The subcellular arrangement of alpha-synuclein proteoforms in the Parkinson’s disease brain as revealed by multicolor STED microscopy’, *Acta Neuropathologica*, 142(3), pp. 423–448.

Neumann, H. and Takahashi, K. (2007) ‘Essential role of the microglial triggering receptor expressed on myeloid cells-2 (TREM2) for central nervous tissue immune homeostasis’, *Journal of Neuroimmunology*, 184(1), pp. 92–99.

Ngolab, J. *et al.* (2017) ‘Brain-derived exosomes from dementia with Lewy bodies propagate α-synuclein pathology’, *Acta Neuropathologica Communications*, 5(1), p. 46.

Nickell, S. *et al.* (2007) ‘Automated cryoelectron microscopy of “single particles” applied to the 26S proteasome’, *FEBS Letters*, 581(15), pp. 2751–2756.

Nielsen, M.S. *et al.* (2001) ‘Ca2+ Binding to α-Synuclein Regulates Ligand Binding and Oligomerization*’, *Journal of Biological Chemistry*, 276(25), pp. 22680–22684.

Nilsson, M.R. (2004) ‘Techniques to study amyloid fibril formation in vitro’, *Methods (San Diego, Calif.)*, 34(1), pp. 151–160.

Oda, T. *et al.* (1995) ‘Clusterin (apoJ) Alters the Aggregation of Amyloid β-Peptide (Aβ1-42) and Forms Slowly Sedimenting Aβ Complexes That Cause Oxidative Stress’, *Experimental Neurology*, 136(1), pp. 22–31.

Ostrerova-Golts, N. *et al.* (2000) ‘The A53T α-Synuclein Mutation Increases Iron-Dependent Aggregation and Toxicity’, *Journal of Neuroscience*, 20(16), pp. 6048–6054.

Ozawa, T. *et al.* (2004) ‘The spectrum of pathological involvement of the striatonigral and olivopontocerebellar systems in multiple system atrophy: clinicopathological correlations’, *Brain: A Journal of Neurology*, 127(Pt 12), pp. 2657–2671.

Padhy, B. *et al.* (2017) ‘Pseudoexfoliation and Alzheimer’s associated CLU risk variant, rs2279590, lies within an enhancer element and regulates CLU, EPHX2 and PTK2B gene expression’, *Human Molecular Genetics*, 26(22), pp. 4519–4529.

Paleologou, K.E. *et al.* (2010) ‘Phosphorylation at S87 is enhanced in synucleinopathies, inhibits alpha-synuclein oligomerization, and influences synuclein-membrane interactions’, *The Journal of Neuroscience: The Official Journal of the Society for Neuroscience*, 30(9), pp. 3184–3198.

Panda, D. *et al.* (2003) ‘Differential regulation of microtubule dynamics by three- and four-repeat tau: Implications for the onset of neurodegenerative disease’, *Proceedings of the National Academy of Sciences*, 100(16), pp. 9548–9553.

Pankiv, S. *et al.* (2007) ‘p62/SQSTM1 Binds Directly to Atg8/LC3 to Facilitate Degradation of Ubiquitinated Protein Aggregates by Autophagy*’, *Journal of Biological Chemistry*, 282(33), pp. 24131–24145.

Papadopoulos, C. *et al.* (2017) ‘VCP/p97 cooperates with YOD1, UBXD1 and PLAA to drive clearance of ruptured lysosomes by autophagy’, *The EMBO Journal*, 36(2), pp. 135–150.

Papp, M.I., Kahn, J.E. and Lantos, P.L. (1989) ‘Glial cytoplasmic inclusions in the CNS of patients with multiple system atrophy (striatonigral degeneration, olivopontocerebellar atrophy and Shy-Drager syndrome)’, *Journal of the Neurological Sciences*, 94(1), pp. 79–100.

Papp, M.I. and Lantos, P.L. (1994) ‘The distribution of oligodendroglial inclusions in multiple system atrophy and its relevance to clinical symptomatology’, *Brain*, 117(2), pp. 235–243.

Parihar, M.S. *et al.* (2009) ‘Alpha-synuclein overexpression and aggregation exacerbates impairment of mitochondrial functions by augmenting oxidative stress in human neuroblastoma cells’, *The International Journal of Biochemistry & Cell Biology*, 41(10), pp. 2015–2024.

Parkinson, J. (2002) ‘An Essay on the Shaking Palsy’, *The Journal of Neuropsychiatry and Clinical Neurosciences*, 14(2), pp. 223–236.

Parsell, D.A. *et al.* (1994) ‘Protein disaggregation mediated by heat-shock protein Hspl04’, *Nature*, 372(6505), pp. 475–478.

Pasanen, P. *et al.* (2014) ‘A novel α-synuclein mutation A53E associated with atypical multiple system atrophy and Parkinson’s disease-type pathology’, *Neurobiology of Aging*, 35(9), p. 2180.e1-2180.e5.

Pauling, L. and Corey, R.B. (1951) ‘The Pleated Sheet, A New Layer Configuration of Polypeptide Chains’, *Proceedings of the National Academy of Sciences*, 37(5), pp. 251–256.

Pauling, L., Corey, R.B. and Branson, H.R. (1951) ‘The structure of proteins: Two hydrogen-bonded helical configurations of the polypeptide chain’, *Proceedings of the National Academy of Sciences*, 37(4), pp. 205–211.

Paxinou, E. *et al.* (2001) ‘Induction of alpha-synuclein aggregation by intracellular nitrative insult’, *The Journal of Neuroscience: The Official Journal of the Society for Neuroscience*, 21(20), pp. 8053–8061.

Peeraer, E. *et al.* (2015) ‘Intracerebral injection of preformed synthetic tau fibrils initiates widespread tauopathy and neuronal loss in the brains of tau transgenic mice’, *Neurobiology of Disease*, 73, pp. 83–95.

Peng, C. *et al.* (2018) ‘Cellular Milieu Imparts Distinct Pathological α-Synuclein Strains in α-Synucleinopathies’, *Nature*, 557(7706), pp. 558–563.

Peng, C., Gathagan, R.J. and Lee, V.M.-Y. (2018) ‘Distinct α-Synuclein strains and implications for heterogeneity among α-Synucleinopathies’, *Neurobiology of Disease*, 109, pp. 209–218.

Peng, C., Trojanowski, J.Q. and Lee, V.M.-Y. (2020) ‘Protein transmission in neurodegenerative disease’, *Nature Reviews Neurology*, 16(4), pp. 199–212.

Polier, S. *et al.* (2008) ‘Structural Basis for the Cooperation of Hsp70 and Hsp110 Chaperones in Protein Folding’, *Cell*, 133(6), pp. 1068–1079.

Pollanen, M.S., Dickson, D.W. and Bergeron, C. (1993) ‘Pathology and Biology of the Lewy Body’, *Journal of Neuropathology & Experimental Neurology*, 52(3), pp. 183–191.

Polymeropoulos, M.H. *et al.* (1997) ‘Mutation in the α-Synuclein Gene Identified in Families with Parkinson’s Disease’, *Science*, 276(5321), pp. 2045–2047.

Poon, S. *et al.* (2000) ‘Clusterin Is an ATP−Independent Chaperone with Very Broad Substrate Specificity that Stabilizes Stressed Proteins in a Folding-Competent State’, *Biochemistry*, 39(51), pp. 15953–15960.

Purro, S.A. *et al.* (2018) ‘Transmission of amyloid-β protein pathology from cadaveric pituitary growth hormone’, *Nature*, 564(7736), pp. 415–419.

Quraishe, S. *et al.* (2008) ‘Expression of the small heat shock protein family in the mouse CNS: Differential anatomical and biochemical compartmentalization’, *Neuroscience*, 153(2), pp. 483–491.

Ramachandran, G.N., Ramakrishnan, C. and Sasisekharan, V. (1963) ‘Stereochemistry of polypeptide chain configurations’, *Journal of Molecular Biology*, 7(1), pp. 95–99.

Rauch, J.N. *et al.* (2020) ‘LRP1 is a master regulator of tau uptake and spread’, *Nature*, 580(7803), pp. 381–385.

Raviol, H. *et al.* (2006) ‘Chaperone network in the yeast cytosol: Hsp110 is revealed as an Hsp70 nucleotide exchange factor’, *The EMBO Journal*, 25(11), pp. 2510–2518.

Rigort, A. *et al.* (2010) ‘Micromachining tools and correlative approaches for cellular cryo-electron tomography’, *Journal of Structural Biology*, 172(2), pp. 169–179.

Rosenzweig, R. *et al.* (2019) ‘The Hsp70 chaperone network’, *Nature Reviews Molecular Cell Biology*, 20(11), pp. 665–680.

Ryan, M.T. and Pfanner, N. (2001) ‘Hsp70 proteins in protein translocation’, in *Advances in Protein Chemistry*. Academic Press (Protein Folding in the Cell), pp. 223–242.

Saha, I. *et al.* (2022) *The AAA+ chaperone VCP disaggregates Tau fibrils and generates aggregate seeds*. preprint Biorxiv. Cell Biology. https://doi.org/10.1101/2022.02.18.481043

Saman, Sudad *et al.* (2012) 'Exosome-associated tau is secreted in tauopathy models and is selectively phosphorylated in cerebrospinal fluid in early Alzheimer disease', *The Journal of Biological Chemistry*, 287(6), pp. 3842–3849.

Sanchez, Y. and Lindquist, S.L. (1990) 'HSP104 required for induced thermotolerance', *Science (New York, N.Y.)*, 248(4959), pp. 1112–1115.

Sanders, D.W. *et al.* (2014) 'Distinct tau prion strains propagate in cells and mice and define different tauopathies', *Neuron*, 82(6), pp. 1271–1288.

Santhanagopalan, I. *et al.* (2018) 'It takes a dimer to tango: Oligomeric small heat shock proteins dissociate to capture substrate', *The Journal of Biological Chemistry*, 293(51), pp. 19511–19521.

dos Santos, L.R. *et al.* (2020) 'The combined risk effect among BIN1, CLU, and APOE genes in Alzheimer's disease', *Genetics and Molecular Biology*, 43(1), p. e20180320.

Schaffer, M. *et al.* (2019) 'A cryo-FIB lift-out technique enables molecular-resolution cryo-ET within native Caenorhabditis elegans tissue', *Nature Methods*, 16(8), pp. 757–762.

Scheffner, M., Nuber, U. and Huibregtse, J.M. (1995) 'Protein ubiquitination involving an E1–E2–E3 enzyme ubiquitin thioester cascade', *Nature*, 373(6509), pp. 81–83.

Scheres, S.H. *et al.* (2020) 'Cryo-EM structures of tau filaments', *Current Opinion in Structural Biology*, 64, pp. 17–25.

Schmid, A.W. *et al.* (2013) 'Alpha-synuclein Post-translational Modifications as Potential Biomarkers for Parkinson Disease and Other Synucleinopathies', *Molecular & Cellular Proteomics*, 12(12), pp. 3543–3558.

Schneider, M.M. *et al.* (2021) ‘The Hsc70 disaggregation machinery removes monomer units directly from α-synuclein fibril ends’, *Nature Communications*, 12(1), p. 5999.

Schuermann, J.P. *et al.* (2008) ‘Structure of the Hsp110:Hsc70 Nucleotide Exchange Machine’, *Molecular Cell*, 31(2), pp. 232–243.

Schweighauser, M. *et al.* (2020) ‘Structures of α-synuclein filaments from multiple system atrophy’, *Nature*, 585(7825), pp. 464–469.

Shahmoradian, S.H. *et al.* (2019) ‘Lewy pathology in Parkinson’s disease consists of crowded organelles and lipid membranes’, *Nature Neuroscience*, 22(7), pp. 1099–1109.

Shahnawaz, M. *et al.* (2020) ‘Discriminating α-synuclein strains in Parkinson’s disease and multiple system atrophy’, *Nature*, 578(7794), pp. 273–277.

Shannon, C.E. (1998) ‘Communication in the Presence of Noise’, *PROCEEDINGS OF THE IEEE*, 86(2), p. 11.

Shelton, L.B. *et al.* (2017) ‘Hsp90 activator Aha1 drives production of pathological tau aggregates’, *Proceedings of the National Academy of Sciences*, 114(36), pp. 9707–9712.

Shi, M. *et al.* (2014) ‘Plasma exosomal α-synuclein is likely CNS-derived and increased in Parkinson’s disease’, *Acta neuropathologica*, 128(5), pp. 639–650.

Shiber, A. and Ravid, T. (2014) ‘Chaperoning Proteins for Destruction: Diverse Roles of Hsp70 Chaperones and their Co-Chaperones in Targeting Misfolded Proteins to the Proteasome’, Biomolecules, 4(3), pp. 704–724. Available at: https://doi.org/10.3390/biom4030704.

Sielaff, B. and Tsai, F.T.F. (2010) ‘The M-domain controls Hsp104 protein remodeling activity in an Hsp70/Hsp40-dependent manner’, *Journal of Molecular Biology*, 402(1), pp. 30–37.

Singleton, A.B. *et al.* (2003) ‘α-Synuclein Locus Triplication Causes Parkinson’s Disease’, *Science*, 302(5646), pp. 841–841.

Sorrentino, Z.A. *et al.* (2018) ‘Physiological C-terminal truncation of α-synuclein potentiates the prion-like formation of pathological inclusions’, *Journal of Biological Chemistry*, 293(49), pp. 18914–18932.

Sorrentino, Z.A. and Giasson, B.I. (2020) ‘The emerging role of α-synuclein truncation in aggregation and disease’, *Journal of Biological Chemistry*, 295(30), pp. 10224–10244.

Spillantini, M. *et al.* (1998) ‘Filamentous α-synuclein inclusions link multiple system atrophy with Parkinson’s disease and dementia with Lewy bodies’, *Neuroscience Letters*, 251(3), pp. 205–208.

Spillantini, M.G. *et al.* (1997) ‘α-Synuclein in Lewy bodies’, *Nature*, 388(6645), pp. 839–840.

Spillantini, M.G. *et al.* (1998) ‘α-Synuclein in filamentous inclusions of Lewy bodies from Parkinson’s disease and dementia with Lewy bodies’, *Proceedings of the National Academy of Sciences*, 95(11), pp. 6469–6473.

Spires-Jones, T.L., Attems, J. and Thal, D.R. (2017) ‘Interactions of pathological proteins in neurodegenerative diseases’, *Acta Neuropathologica*, 134(2), pp. 187–205.

Srinivasan, E. *et al.* (2021) ‘Alpha-Synuclein Aggregation in Parkinson’s Disease’, *Frontiers in Medicine*, 8.

Stöckl, M.T., Zijlstra, N. and Subramaniam, V. (2013) ‘α-Synuclein Oligomers: an Amyloid Pore?’, *Molecular Neurobiology*, 47(2), pp. 613–621.

Stolz, A. *et al.* (2011) ‘Cdc48: a power machine in protein degradation’, *Trends in Biochemical Sciences*, 36(10), pp. 515–523.

Strang, K.H. *et al.* (2018) ‘Distinct differences in prion-like seeding and aggregation between Tau protein variants provide mechanistic insights into tauopathies’, *The Journal of Biological Chemistry*, 293(7), pp. 2408–2421.

Strang, K.H., Golde, T.E. and Giasson, B.I. (2019) ‘MAPT mutations, tauopathy, and mechanisms of neurodegeneration’, *Laboratory Investigation*, 99(7), pp. 912–928.

Sunde, M. *et al.* (1997) ‘Common core structure of amyloid fibrils by synchrotron X-ray diffraction11Edited by F. E. Cohen’, *Journal of Molecular Biology*, 273(3), pp. 729–739.

Swatek, K.N. and Komander, D. (2016) ‘Ubiquitin modifications’, *Cell Research*, 26(4), pp. 399–422.

Sweeny, E.A. and Shorter, J. (2016) ‘Mechanistic and Structural Insights into the Prion-Disaggregase Activity of Hsp104’, *Journal of Molecular Biology*, 428(9), pp. 1870–1885.

Szymanski, M. *et al.* (2011) ‘Alzheimer’s risk variants in the clusterin gene are associated with alternative splicing’, *Translational Psychiatry*, 1, p. e18.

Taguchi, Y.V. *et al.* (2019) ‘Hsp110 mitigates α-synuclein pathology in vivo’, *Proceedings of the National Academy of Sciences*, 116(48), pp. 24310–24316.

Tan, J.M.M. *et al.* (2008) ‘Lysine 63-linked ubiquitination promotes the formation and autophagic clearance of protein inclusions associated with neurodegenerative diseases’, *Human Molecular Genetics*, 17(3), pp. 431–439.

Tang, W.K. and Xia, D. (2016) ‘Mutations in the Human AAA+ Chaperone p97 and Related Diseases’, *Frontiers in Molecular Biosciences*, 3, p. 79.

Tanner, C.M. and Goldman, S.M. (1996) ‘EPIDEMIOLOGY OF PARKINSON’S DISEASE’, *Neurologic Clinics*, 14(2), pp. 317–335.

Taylor, J.-P. et al. (2017) ‘Cholinergic Pathology in Dementia with Lewy Bodies’, in K. Kosaka (ed.) Dementia with Lewy Bodies: Clinical and Biological Aspects. Tokyo: Springer Japan, pp. 23–39. Available at: https://doi.org/10.1007/978-4-431-55948-1_3.

Tittelmeier (2020) ‘The HSP110/HSP70 disaggregation system generates spreading-competent toxic α-synuclein species’, *The EMBO Journal*, 39(13), p. e103954.

Toyama, B.H. and Weissman, J.S. (2011) ‘Amyloid Structure: Conformational Diversity and Consequences’, *Annual Review of Biochemistry*, 80(1), pp. 557–585.

Trinkaus, V.A. *et al.* (2021) ‘In situ architecture of neuronal α-Synuclein inclusions’, *Nature Communications*, 12(1), p. 2110.

Trojanowski, J.Q. and Lee, V.M.-Y. (1998) ‘Aggregation of neurofilament and α-synuclein proteins in Lewy bodies: Implications for the pathogenesis of Parkinson disease and Lewy body dementia’, *Archives of Neurology*, 55(2), pp. 151–152.

Tysnes, O.-B. and Storstein, A. (2017) ‘Epidemiology of Parkinson’s disease’, *Journal of Neural Transmission (Vienna, Austria: 1996)*, 124(8), pp. 901–905.

Uéda, K. *et al.* (1993) ‘Molecular cloning of cDNA encoding an unrecognized component of amyloid in Alzheimer disease’, *Proceedings of the National Academy of Sciences*, 90(23), pp. 11282–11286.

Uversky, V.N. (2015) ‘Intrinsically disordered proteins and their (disordered) proteomes in neurodegenerative disorders’, *Frontiers in Aging Neuroscience*, 7.

Van Swieten, J.C. *et al.* (1999) ‘Phenotypic variation in hereditary frontotemporal dementia with tau mutations’, *Annals of Neurology*, 46(4), pp. 617–626.

Vasili, E., Dominguez-Meijide, A. and Outeiro, T.F. (2019) ‘Spreading of α-Synuclein and Tau: A Systematic Comparison of the Mechanisms Involved’, *Frontiers in Molecular Neuroscience*, 12, p. 107.

Verma, R. *et al.* (2013) ‘Cdc48/p97 promotes degradation of aberrant nascent polypeptides bound to the ribosome’, *eLife*. Edited by I. Dikic, 2, p. e00308.

Villar-Piqué, A., Lopes da Fonseca, T. and Outeiro, T.F. (2016) ‘Structure, function and toxicity of alpha-synuclein: the Bermuda triangle in synucleinopathies’, *Journal of Neurochemistry*, 139(S1), pp. 240–255.

Volpicelli-Daley, L.A., Luk, K.C. and Lee, V.M.-Y. (2014) ‘Addition of exogenous α-Synuclein Pre-formed fibrils to Primary Neuronal Cultures to seed recruitment of endogenous α-Synuclein to Lewy body and Lewy Neurite-like aggregates’, *Nature protocols*, 9(9), pp. 2135–2146.

Vos, M.J. *et al.* (2008) ‘Structural and Functional Diversities between Members of the Human HSPB, HSPH, HSPA, and DNAJ Chaperone Families’, *Biochemistry*, 47(27), pp. 7001–7011.

Walther, D.M. *et al.* (2015) ‘Widespread Proteome Remodeling and Aggregation in Aging C. elegans’, *Cell*, 161(4), pp. 919–932.

Walz, J. *et al.* (1998) ‘26S Proteasome Structure Revealed by Three-dimensional Electron Microscopy’, *Journal of Structural Biology*, 121(1), pp. 19–29.

Wang, Q., Song, C. and Li, C.-C.H. (2004) ‘Molecular perspectives on p97–VCP: progress in understanding its structure and diverse biological functions’, *Journal of Structural Biology*, 146(1), pp. 44–57.

Wang, W. *et al.* (2011) ‘A soluble α-synuclein construct forms a dynamic tetramer’, *Proceedings of the National Academy of Sciences*, 108(43), pp. 17797–17802.

Watanabe-Nakayama, T. *et al.* (2020) ‘Self- and Cross-Seeding on α-Synuclein Fibril Growth Kinetics and Structure Observed by High-Speed Atomic Force Microscopy’, *ACS Nano*, 14(8), pp. 9979–9989.

Webb, J.L. *et al.* (2003) ‘α-Synuclein Is Degraded by Both Autophagy and the Proteasome*’, *Journal of Biological Chemistry*, 278(27), pp. 25009–25013.

Webster, J.M. *et al.* (2019) 'Small Heat Shock Proteins, Big Impact on Protein Aggregation in Neurodegenerative Disease', *Frontiers in Pharmacology*, 10.

Weinreb, P.H. *et al.* (1996) 'NACP, a protein implicated in Alzheimer's disease and learning, is natively unfolded', *Biochemistry*, 35(43), pp. 13709–13715.

Weinstein, G. *et al.* (2016) 'Plasma clusterin levels and risk of dementia, Alzheimer's disease, and stroke', *Alzheimer's & Dementia: Diagnosis, Assessment & Disease Monitoring*, 3(1), pp. 103–109.

Wendler, P. *et al.* (2009) 'Motor Mechanism for Protein Threading through Hsp104', *Molecular Cell*, 34(1), pp. 81–92.

Wenning, G.K. *et al.* (2013) 'The natural history of multiple system atrophy: a prospective European cohort study', *The Lancet Neurology*, 12(3), pp. 264–274.

Wentink, A.S. *et al.* (2020) 'Molecular dissection of amyloid disaggregation by human HSP70', *Nature*, 587(7834), pp. 483–488.

Whiten, D.R. *et al.* (2018) 'Single-Molecule Characterization of the Interactions between Extracellular Chaperones and Toxic α-Synuclein Oligomers', *Cell Reports*, 23(12), pp. 3492–3500.

Wickner, R.B. (2016) 'Yeast and Fungal Prions', Cold Spring Harbor Perspectives in Biology, 8(9), p. a023531. Available at: https://doi.org/10.1101/cshperspect.a023531.

Will, R. (2004) 'Variant Creutzfeldt-Jakob disease', *Folia Neuropathologica*, 42 Suppl A, pp. 77–83.

Will, R.G. *et al.* (1996) 'A new variant of Creutzfeldt-Jakob disease in the UK', *Lancet (London, England)*, 347(9006), pp. 921–925.

Winner, B. *et al.* (2011) 'In vivo demonstration that alpha-synuclein oligomers are toxic', *Proceedings of the National Academy of Sciences of the United States of America*, 108(10), pp. 4194–4199.

Wojtas, A.M., Sens, J.P., *et al.* (2020) ‘Astrocyte-derived clusterin suppresses amyloid formation in vivo’, *Molecular Neurodegeneration*, 15(1), p. 71.

Wojtas, A.M., Carlomagno, Y., *et al.* (2020) ‘Clusterin ameliorates tau pathology in vivo by inhibiting fibril formation’, *Acta Neuropathologica Communications*, 8(1), p. 210.

Wolf, E. (2012) ‘Fehldiagnose Morbus Parkinson: Kasuistik einer Patientin mit Multisystematrophie-P, deren Erst-Diagnose fälschlicherweise Mb. Parkinson gelautet hatte’, *Psychopraxis*, 15(4), pp. 19–22.

Wyatt, A.R. *et al.* (2013) ‘Extracellular Chaperones and Proteostasis’, *Annual Review of Biochemistry*, 82(1), pp. 295–322.

Yeh, F.L. *et al.* (2016) ‘TREM2 Binds to Apolipoproteins, Including APOE and CLU/APOJ, and Thereby Facilitates Uptake of Amyloid-Beta by Microglia’, *Neuron*, 91(2), pp. 328–340.

Yerbury, J.J. *et al.* (2007) ‘The extracellular chaperone clusterin influences amyloid formation and toxicity by interacting with prefibrillar structures’, *The FASEB Journal*, 21(10), pp. 2312–2322.

Young, J.C., Barral, J.M. and Ulrich Hartl, F. (2003) ‘More than folding: localized functions of cytosolic chaperones’, *Trends in Biochemical Sciences*, 28(10), pp. 541–547.

Yuste-Checa, P. *et al.* (2021) ‘The extracellular chaperone Clusterin enhances Tau aggregate seeding in a cellular model’, *Nature Communications*, 12(1), p. 4863.

Yuste-Checa, P., Bracher, A. and Hartl, F.U. (2022) ‘The chaperone Clusterin in neurodegeneration−friend or foe?’, *BioEssays*, 44(7), p. 2100287.

Zarranz, J.J. *et al.* (2004) ‘The new mutation, E46K, of α-synuclein causes parkinson and Lewy body dementia’, *Annals of Neurology*, 55(2), pp. 164–173.

Zatloukal, K. *et al.* (2002) ‘p62 Is a Common Component of Cytoplasmic Inclusions in Protein Aggregation Diseases’, *The American Journal of Pathology*, 160(1), pp. 255–263.

Zhang, S. *et al.* (2021) ‘Mechanistic basis for receptor-mediated pathological α-synuclein fibril cell-to-cell transmission in Parkinson’s disease’, *Proceedings of the National Academy of Sciences of the United States of America*, 118(26), p. e2011196118.

Zhang, W. *et al.* (2020) ‘Novel tau filament fold in corticobasal degeneration’, *Nature*, 580(7802), pp. 283–287.

Zhu, J. *et al.* (2022) ‘VCP suppresses proteopathic seeding in neurons’, *Molecular Neurodegeneration*, 17(1), p. 30.

Zhuravleva, A. and Gierasch, L.M. (2011) ‘Allosteric signal transmission in the nucleotide-binding domain of 70-kDa heat shock protein (Hsp70) molecular chaperones’, *Proceedings of the National Academy of Sciences*, 108(17), pp. 6987–6992.

Zwanzig, R., Szabo, A. and Bagchi, B. (1992) ‘Levinthal’s paradox.’, *Proceedings of the National Academy of Sciences*, 89(1), pp. 20–22.